



UNIVERSIDADE DE SANTIAGO DE COMPOSTELA
FACULTADE DE FÍSICA
DEPARTAMENTO DE FÍSICA DE PARTÍCULAS

PRECISION DETERMINATION OF THE S-WAVE
 $\pi\pi$ ISOSPIN SCATTERING LENGTH DIFFERENCE
 $|a_0 - a_2|$ IN THE DIRAC EXPERIMENT

Antonio Romero Vidal

Bernardo Adeva Andany
Catedrático da área de Física atómica, molecular e nuclear

INFORMA

que a memoria titulada

Precision Determination of the S-wave $\pi\pi$ Isospin Scattering Length Difference $|a_0 - a_2|$ in the DIRAC Experiment

foi realizada por D. Antonio Romero Vidal
no **Departamento de Física de Partículas**
da **Universidade de Santiago de Compostela**
baixo a súa dirección, e constitúe o traballo de tese que
presenta para optar ó Grao de Doutor en Ciencias Físicas.

Santiago de Compostela, a 14 de Decembro de 2007.

Asdo. Bernardo Adeva Andany

Asdo. Antonio Romero Vidal

Agradecementos

Para comezar gustaríame darlle as gracias a Bernardo Adeva pola oportunidade ofrecida para traballar nun experimento de física de partículas de alto nivel, onde me formei non só como físico senón tamén como persoa.

Gracias á xente que me axudou dende un principio como Juan Saborido, Manuel Sánchez e Marcos Seco por toda a axuda ofrecida, sen a cal o traballo diario sería moito máis difícil, por non dicir imposible. E tamén ós membros do CESGA e en especial a Carlos Fernández por prestarme sempre a súa axuda cando a necesitaba.

Agradecer tamén a Pentia pola súa amabilidade e simpatía durante as miñas estancias no CERN. A Carlo Guaraldo e Catalina Petrascu, tamén pola súa amabilidade e por apostar por min. Á xente que coñecín no CERN, Óscar, Benja, Ausias, Julito, Sam e outros moitos cos que pasei moitas e moi variadas aventuras.

Ós meus compañeiros de carreira, especialmente a Juan Pardo, sen o cal quizáis hoxe non estaría traballando nisto. Ós meus compañeiros na etapa de tese, empezando por Otón por toda a súa axuda e por se-lo compañeiro perfecto, a Cris, Javi, Mariñas, Lucas, Leticia e outra moita xente que me rodeou durante estes anos e cos que disfrutei tanto do día a día.

Gracias a tódolos meus amigos cos que compartín tanto tempo durante, antes e despois da carreira: Pablo, Toño, Gabriel, Samuel, Raquel, Juan, Nacho, Miguel, Carletis, Gus, Moncho, a toda a xente da charanga, grupo e banda, e xa paro de contar porque a lista é interminable.

A meus pais, por deixarme sempre a opción de elixir o meu camiño e a meus irmáns. E como non a Marga, por apoiarme e facer que estes últimos meses fosen do máis intenso.

0

Contents

Resumo	5
1 The DIRAC Experiment	11
1.1 Introduction	11
1.2 Chiral Perturbation Theory and QCD	12
1.2.1 $\pi\pi$ scattering	13
1.3 Pionium lifetime in QCD and QED	15
1.3.1 Photon decays of pionium	21
1.4 Pionium production	21
1.5 Propagation inside the target	23
1.6 Pionium lifetime	25
1.7 DIRAC spectrometer	26
1.7.1 The MSGC/GEM detector	28
1.7.2 The Scintillating Fibre Detector	29
1.7.3 The Ionisation Hodoscope	32
1.7.4 Magnet	34
1.7.5 Drift Chambers	34
1.7.6 Time-of-Flight detector	38
1.7.7 The Horizontal Hodoscopes	41
1.7.8 The Cerenkov Counters	42
1.7.9 The Preshower and Muon Detectors	43
1.8 Trigger system	46
1.8.1 First level trigger (T1)	47
1.8.2 Drift chamber processor (T4)	48

1.8.3	Trigger performances	50
1.9	Analysis method	51
1.9.1	Data selection	51
1.9.2	Reconstruction method	52
1.9.3	Monte Carlo simulation	53
1.9.4	Analysis of Q-spectrum	56
1.9.5	Accidental pairs	58
1.9.6	K-factors and break-up probability	61
1.9.7	K^+K^- background	63
1.9.8	Q_L acceptance correction	65
1.9.9	Target impurity correction	66
2	Upstream Detectors Alignment	69
2.1	Angle alignment.	70
2.2	Position alignment	73
2.3	Beam position	74
3	SFD Efficiency Using MSGC-GEM for 2001 Data	77
3.1	Tracking procedure and results	78
3.2	Monte Carlo simulation of MSGC background noise	83
3.3	Conclusions	84
4	Multiple Scattering in Upstream Detectors	89
4.1	Vertex resolution analysis	90
4.2	Checks on systematic effects	95
4.2.1	Track fitting procedure	96
4.2.2	MSGC clusterisation	97
4.2.3	MSGC background	98
4.2.4	SFD background	99
4.2.5	Beam spotsize and accidental pairs	112
4.2.6	Long lifetime particles	113
4.3	Conclusions	114

5	Study of Kaon Contamination in DIRAC	119
5.1	Determination of the $K^\pm\pi^\mp/\pi^+\pi^-$ ratio	119
5.2	Measurement of K^+K^- at $2.9\text{ GeV}/c$	133
5.2.1	Results from method A	135
5.2.2	Results from method B	138
5.3	Analysis of $K^+K^-/\pi^+\pi^-$ at high momentum	148
5.3.1	Comparison with UrQMD Monte Carlo	153
5.3.2	The K^-p signal	160
5.4	Summary and conclusions	163
6	Pionium Lifetime using 2002 and 2003 Data	165
6.1	Global fit analysis	165
6.2	Momentum-dependent analysis	182
6.2.1	Fit results	182
6.3	Break-up probability measurement	200
7	Pionium Lifetime and $a_0 - a_2$	203
7.1	Summary of corrections	203
7.2	Combined global fit analysis	203
7.2.1	Dependence on the Q_L upper limit	206
7.3	Momentum-dependent analysis	218
7.4	Systematic error	237
7.5	Lifetime and $ a_0 - a_2 $ measurement	239
8	Summary of results and conclusions	241

Resumo

A tese aquí presentada está baseada na análise de datos do experimento DIRAC (Dimeson Relativistic Atom Complex) do CERN (Laboratorio Europeo de Física de Partículas).

O obxectivo de experimento DIRAC non é outro que a determinación da vida media do estado fundamental do átomo piónico ou *pionium*, τ_{1s} , formado por un pión con carga eléctrica positiva π^+ en un pión con carga eléctrica negativa π^- cunha precisión mellor ca un 10%. O inverso da vida media está directamente relacionado co cadrado da diferenza entre as lonxitudes de dispersión de isospin $l=0$ e $l=2$ a través dunha relación moi exacta:

$$\Gamma_{1s} = \frac{1}{\tau_{1s}} = C|a_0 - a_2|^2 \quad (1)$$

Como se verá nesta tese, a vida media vai ser medida cun 7% de precisión, mellorando as expectativas orixinais do experimento, e que nos levará a medir $|a_0 - a_2|$ cun 3.5% de precisión.

A Teoría de Perturbacións Chiral (CHPT) foi creada para estudar a Cromodinámica Cuántica a baixa enerxía. Esta teoría predice unha vida media para o *pionium* $\tau_{1s} = 2.9 \pm 0.1 \text{ fs}$ e un valor para $|a_0 - a_2|m_\pi$ de 0.265 ± 0.004 , onde m_π é a masa do pión cargado.

DIRAC supón unha proba para a Teoría de Perturbacións Chiral, pois unha discrepancia entre o experimento e dita teoría levaríanos a dicir que a CHPT non se comporta correctamente.

A determinación de τ_{1s} é posible debido ó coñecemento da relación entre τ_{1s} e a Probabilidade de ruptura (P_{Br}) do átomo no branco en cuestión (neste caso un branco de Níquel de 98 micras de grosor) sacada mediante a utilización dun método de Monte Carlo gracias ó preciso coñecemento das seccións eficaces de interacción do átomo co branco. A P_{Br} é a cantidade que se pode medir directamente en DIRAC. Esta P_{Br} depende das características do branco así como da enerxía do feixe de protóns incidentes no branco, pero tanto τ_{1s} coma $|a_0 - a_2|$ son cantidades constantes que non dependen da situación experimental.

O método utilizado por DIRAC baséase na detección de pares de pións

procedentes da ruptura do *pionium* no branco tras interaccionar cos núcleos dos átomos de Níquel deste e que chamaremos Pares atómicos (AT). Estes pares de pións son moi característicos posto que salen do branco cun ángulo moi pequeno, menor ca 3 mrad e cun momento relativo (Q) no sistema de centro de masas (CMS) tamén moi pequeno, menor ca $3 \text{ MeV}/c$. Esos pares de pións son detectados, no espectro de Q , sobre un fondo de pares de pións con distintas características:

- *Pares Coulombianos* (CC). Son producidos na mesma colisión protón-núcleo trala fragmentación de resonancias de vida media curta e posúen interacción de Coulomb no estado final.
- *Pares Non Coulombianos* (NC). Producidos na mesma colisión protón-núcleo onde polo menos un dos pións ven dunha resonancia de vida media longa. Estes pares non posúen interacción de Coulomb no estado final.
- *Pares Accidentais* (AC). Producidos en diferentes colisións protón-núcleo. Non teñen interacción coulombiana no estado final.

Para poder ve-los pares atómicos sobre o fondo de CC+NC+AC foi necesario a construción dun espectrómetro de dobre brazo con moita precisión na media do Q dos pares. A resolución do espectrómetro é duns $0.5 \text{ MeV}/c$ no momento relativo lonxitudinal no sistema centro de de masas (Q_L) e duns $0.1 \text{ MeV}/c$ para o momento relativo transversal no sistema de centro de masas (Q_T). Un feixe de protóns de momento $24 \text{ GeV}/c$ lánzase contra o branco de Níquel de 98 micras e tra-lo branco atópanse os detectores MSGC/GEM (Cámaras de Micropistas de Gas), cunha resolución na posición dunhas 60 micras, e os detectors SFD (Detectores de Fibras centelleantes), cunha resolución dunhas 120 micras. Estes dous detectores son usados para o sistema de trazado, sendo o MSGC/GEM o encargado, en última instancia de medi-lo ángulo entre partículas, quedando a SFD relegado a un uso de selección de trazas, e non é utilizado na medida da posición. Despois destes dous detectores atópanse situados os IH (Hodoscopios de Ionización) que serven para separar pares de partículas a moi baixo ángulo cando non

puido ser resolto polo sistema MSGC/GEM-SFD mediante a esixencia de dobre ionización. Tra-lo IH está situado o imán, cuxo campo magnético se coñece con moita precisión, o cal é necesario para calcula-lo momento das partículas no sistema de laboratorio. Despois do imán están as DC (Cámaras de deriva) para reconstruí-las trazas despois deste, e os VH e HH (Hodoscopios Verticais e Hodoscopios Horizontais) os cales son usados no sistema de selección de sucesos e que teñen unha resolución duns 170 ps . Serven para discriminar sucesos que veñen de distintas interaccións protón-núcleo. E por último atópanse situados os CH (Contadores Cherenkov), PSH (Detectores de Precascada) e os MU (Detectores de muóns) que serven para discrimina-los electróns no caso dos dous primeiros e os muóns no caso dos últimos.

Para calcula-la P_{Br} é necesario o coñecemento coa maior precisión posible do número de átomos e o número de Pares Coulombianos para un corte de momento relativo dado. Para obter estas cantidades creouse un programa chamado GEANT-DIRAC e que se basa en GEANT, no cal se describe a xeometría do espectrómetro. Aparte deste programa xenéranse pares de pións coas características cinemáticas dos catro tipos de pares de pións vistos antes (AT,CC,NC,AC), e fanse pasar polo código de GEANT-DIRAC para simula-la aceptación do espectrómetro. Estes catro tipos de Monte Carlo son utilizados para, mediante unha combinación lineal substraer-lo número de átomos e número de Pares Coulombianos, cantidades que se usan para determina-la P_{Br} , e que nos leva directamente á medida da vida media.

Na actualidade existen dúas determinacións de τ_{1s} no experimento DIRAC como resultado da análise dos datos correspondentes ó ano 2001, unha na cal se utilizou toda a información dos detectores do espectrómetro de DIRAC e que se corresponde co resultado final de memoria de tese de Otón Vázquez Doce, obtendo $\tau_{1s} = 2.58^{+0.26}_{-0.22}(stad) \ ^{+0.15}_{-0.14}(sist) \ fs$ e outro no que os detectores MSGC/GEM foron deixados fóra do proceso de creación e selección de trazas, no que se obtén $\tau_{1s} = 2.91^{+0.45}_{-0.38}(stad) \ ^{+0.19}_{-0.49}(sist) \ fs$ onde tanto os erros sistemáticos coma os estadísticos son maiores, os primeiros debidos principalmente a un maior descoñecemento da dispersión múltiple dos pións ó paso polos detectores situados entre o branco e o imán. E os segundos debido á utilización dun método de axuste que claramente da peores resultados

xa que ámbalas dúas mostras de datos son practicamente iguais.

Nesta tese inclúense na análise os datos correspondentes ó período dos anos 2002 e 2003, o cal por si mesmo nos leva a mellorar de forma apreciable o erro estadístico, pero tamén se fai unha análise máis profunda dos erros sistemáticos, como por exemplo o coñecemento da contaminación de pares K^+K^- dentro da mostra de $\pi^+\pi^-$, así como a capacidade de poder discriminar correccións debidas ó tamaño finito dos núcleos do branco.

Para chegar ó resultado final foi necesario pasar por unha serie de pasos intermedios, como foron o alineamento dos Detectores de antes do imán, o estudio da eficiencia e comportamento do SFD utilizando o MSGC/GEM, o estudio da dispersión múltiple nos detectores de antes do imán, un preciso estudio da contaminación de kaóns na mostra de pións e finalmente a análise da vida media utilizando datos do 2002 e 2003 por un lado e coa mostra completa, sumando os datos recolleitos no 2001 e que nos leva finalmente ás conclusións.

O alineamento dos detectores de despois do imán foi feito mediante un método iterativo. O programa ARIANE utilízase para o proceso de reconstrución de sucesos. Para comezar, defínese o concepto de resíduo (para os detectores MSGC/GEM e SFD) como a diferenza entre a extrapolación dunha traza dada sobre o plano en cuestión e a sinal dese plano asociada a dita traza. O método trátase de move-la orientación dos detectores e a posición dun dos bordes ata que as distribucións de resíduos estén centradas en cero en que a anchura de dita distribución sexa mínima. Isto conséguese e ademáis móstrase a posición calculada do feixe de protóns como resultado da extrapolación das trazas usadas ata o plano do branco.

Para estudia-la eficiencia do detector SFD o que se fai é seleccionar trazas reconstruídas co sistema MSGC/GEM-SFD e borra-las sinais do plano en cuestión do detector SFD. As trazas reconstruídas son extrapoladas a dito plano e no entorno búscase pola existencia de sinal. Desta forma podemos facer un estudio da probabilidade de atopar 0,1 ou 2 sinais para cada par de trazas. O estudio realízase comparando os resultados atopados nos datos con varios tipos de Monte Carlos no que se cambiaron varios parámetros da simulación tales como eficiencias dos detectores e multiplicidade de sinais en cada plano. Como resultado final atópase que o SFD ten unha eficiencia de

prácticamente un 98%.

O estudio da dispersión múltiple nos detectores situados antes do imán realízase tamén utilizando o sistema MSGC/GEM-SFD. Neste caso trátase de averiguar se a cantidade de materia que hai na simulación de GEANT-DIRAC é ou non correcta. Utilizando ARIANE para reconstruí-las trazas, extrapolamos estas ata a posición do vértice e calculámo-a distancia entre ámba-las dúas. Deste xeito obtemos unha distribución para datos reais e outra para o Monte Carlo GEANT-DIRAC. Mediante unha análise dependente do momento vemos como a anchura da distribución do Monte Carlo é un 15% menor, o cal nos leva a afirmar que a cantidade de materia dos detectores de antes do imán está subestimada en GEANT-DIRAC nun 15% cun erro dun 1%, o cal é un logro moi importante dentro do experimento dado que en principio se cría que este ía ser un dos erros sistemáticos máis importante e finalmente se demostrou que é practicamente nulo. Fíxose un estudio dos cambios na distribución debido a variacións no procedemento de axuste das trazas, nas distribucións de carga nas MSGC/GEM e tamén na multiplicidade de sinais neste detector e no SFD, o que demostrou a fiabilidade da medida. Finalmente, calculámo-la anchura do feixe de protóns tanto na proxección X coma na Y comparando as distribucións para datos accidentais e non accidentais, xa que ambas distribucións discrepan polo feito de que a anchura dos pares accidentais ven dada por tres factores, como son a resolución dos detectores, a dispersión múltiple neles e a anchura do feixe de protóns, mentres que para os pares non accidentais só os dous primeiros contribúen xa que os dous pións veñen do mesmo punto matemático debido a que proceden da mesma interacción protón-núcleo, e en cambio os accidentais non.

Finalmente, e antes de entrar na análise directa da vida media, fíxose un estudio da contaminación de kaóns en DIRAC. Para empezar utilizouse a información dos detectores VH para encontrar pares $K\pi$ debido a que partículas máis pesadas tardan máis en chegar ata os VH. Observouse que a cantidade de $K^+\pi^-$ é maior que a de $K^-\pi^+$ en máis dun factor 2. Despois, e utilizando os datos reais dos anos 2001, 2002 e 2003 usouse toda a información de tempos dispoñibles na SFD, IH e VH para poder calcula-los tempos de voo das partículas dende a zona de antes do imán ata a zona de despois

do imán e poder traducir estes tempos a masas cadradas e atopar a sinal de pares K^+K^- . Para chegar a este obxectivo utilizáronse dous métodos, nun dos cales se utilizaban tódolos tempos para ser promediados, e outro onde os tempos dos IH se utilizaban como veto para limpa-la sinal de K^+K^- . Ámbolos dous métodos dan un resultado moi compatible e que finalmente nos leva a afirmar que a contaminación de K^+K^- sobre a mostra de $\pi^+\pi^-$ a un momento de $2.9 \text{ GeV}/c$ é de 2.38×10^{-3} . En DIRAC existen datos seleccionados para ver pares pK^- procedentes do $\Lambda(1116)$ e que seleccionan pares de partículas con momentos moi distintos (a partícula negativa ten un momento do orden de $4 \text{ GeV}/c$ mentres o da positiva é da orde de $2 \text{ GeV}/c$). Esta diferenza de momento permítenos utiliza-la diferenza de tempo entre os detectores de antes do imán e os VH para encontrar pares de partículas de mesma masa, neste caso pares K^+K^- e desta maneira obter un segundo punto da contaminación de K^+K^- sobre $\pi^+\pi^-$ a alto momento. Tanto a contaminación de pares $K\pi$ como a de pares KK foi calculada usando o Monte Carlo UrQMD amosando un gran acordo, non tanto na cantidade, pero si na derivada con respecto ó momento. Para finalizar tamén foi posible, elixindo os cortes apropiados nas masas cadradas calculadas coas diferenzas de tempo entre os IH e os VH, atopar unha sinal K^-p aínda que neste caso non se calculou a contaminación en relación á cantidade de pares $\pi^+\pi^-$ posto que estes pares non teñen influencia na mediada de DIRAC.

E para finalizar realizouse a análise para os datos do 2002 e 2003 e despois integrouse coa mostra xa analizada do 2001. Desta maneira, atopáronse un total de 17005 pares atómicos produto da ruptura do átomo no branco, cuxo espectro de ionización foi determinado con precisión nas proxeccións transversa e lonxitudinal do momento relativo no centro de masas.

A vida media do estado $1s$ do *pionium* foi determinada para a mostra completa de datos, resultando ser $\tau_{1s} = 2.58^{+0.19}_{-0.18} \text{ fs}$ usando un método de extrapolación á zona na que se atopan os pares atómicos e sen facer ningunha presunción sobre a física das colisións proton-Níquel.

Debido á existencia dun calculo riguroso en QCD e QED, a vida media do *pionium* foi convertida nunha medida dun 3.5% da diferenza nas lonxitudes de dispersión de Isospin 0 e 2, $|a_0 - a_2|$ para o proceso $\pi^+\pi^- \rightarrow \pi^0\pi^0$ no umbral, co resultado de $|a_0 - a_2|m_\pi = 0.279 \pm 0.010$.

Chapter 1

The DIRAC Experiment

1.1 Introduction

The DIRAC experiment [1] aims to make a precision measurement of the difference between the isoscalar a_0 and isotensor a_2 S-wave scattering lengths. There exists a precise (1.5%) relationship, accurate to next-to-leading order in the quiral expansion of QCD and QED, between $|a_0 - a_2|$ and the lifetime τ of the $1s \pi^+ \pi^-$ (pionium) bound states : $1/\tau = C|a_0 - a_2|^2$ [2]. In order to determine $|a_0 - a_2|$ down to , for instance 5%, the lifetime has to be measured with 10% accuracy. On the other hand, pion scattering lengths have been calculated in the framework of Chiral Perturbation Theory (CHPT) with at least the same level of accuracy [3], and for this reason DIRAC represents an important test to validate or disprove this theory. Should CHPT have to be abandoned, and a generalized CHPT be adopted [4], the physics consequences would be far-reaching, specially in what concerns the QCD quiral $\bar{q}q$ condensate, which rules QCD spontaneous chiral symmetry breaking in vacuum. In fact, this parameter also plays an relevant role in cosmological models.

As we shall see in this thesis, the experimental measurement by DIRAC actually exceeds the anticipated level of precision, and reaches 3.5% in the S-wave scattering length difference, improving the previous DIRAC results [5] [6] [7].

1.2 Chiral Perturbation Theory and QCD

The Standard Model (SM) comprises our understanding of the strong and electroweak interactions. The strong part of the SM, quantum chromodynamics (QCD) exhibits two distinct features, asymptotic freedom and colour confinement. At large momentum transfer ($Q > 1 \text{ GeV}/c$), QCD is essentially a perturbation theory and it has been tested in many reactions. In this region, quarks are considered massless, and then the QCD Lagrangian is invariant under the Chiral $SU(2)_L \times SU(2)_R$ transformations, or $SU(3)_L \times SU(3)_R$ if we also consider the strange quark mass m_s negligible. On the other hand, the observed hadron spectrum with no mass degenerate hadron multiplets with opposite parity, suggests that the ground state of the theory is asymmetric under the action of either of these two groups. This phenomenon, which is due to non-zero vacuum expectation values of $\bar{q}q$ quark operators, is known in the literature as spontaneous breakdown of chiral symmetry. It plays a role in QCD similar to that of the Higgs field in the electroweak sector, that also spontaneously breaks the electroweak gauge symmetry.

Because the broken symmetry is continuous, there exist three (in the case of $SU(2)$) massless pseudoscalar particles in the spectrum, or Goldstone bosons. The three lightest hadrons π^+, π^-, π^0 indeed are pseudoscalars but they are not massless as Goldstone bosons are. This is attributed to the fact that the full QCD Lagrangian is not chiral invariant, since quark masses break the $SU(2)_L \times SU(2)_R$ symmetry and the pions appear with mass $m_\pi \sim 135 \text{ MeV}/c$.

Chiral Perturbation Theory (ChPT) was created by S. Weinberg [8] and since then it has been converted into a very powerful tool [9] [10] to describe the low energy region (low momentum transfer, $Q < 100 \text{ MeV}/c$) for hadron interactions. ChPT is an effective theory formulated in terms of the physical pion fields instead of quark and gluon degrees of freedom. It is mathematically equivalent to QCD and it provides a systematic way to evaluate S-matrix elements at low energies.

Excellent reviews of ChPT can be found for example in references [11] [12].

1.2.1 $\pi\pi$ scattering

Pion-pion scattering has always been a main testing ground for ChPT, because it directly handles the behaviour of the Goldstone bosons, which are the essence of the theory. Rather than trying to review here the extensive literature on the subject, we focus on a recent contribution by H. Leutwyler [13], which summarizes the status of our knowledge of the s-wave isospin scattering lengths a_0 and a_2 , both from the theoretical and experimental points of view. It is illustrated in figure 1.1, borrowed from this reference.

The corrections to Weinberg's low energy theorems [14] for a_0 and a_2 (see left dot in figure 1.1) have been worked out to first non-leading order [15] (middle dot), and those of next-to-next-to-leading order are also known [16] (dot on the right). When the chiral perturbation series is matched to dispersive representations of the amplitude arising from low energy theorems, very accurate predictions for the scattering lengths are obtained [15] (see the small ellipse in figure 1.1).

In most production experiments, the two pions in the final state are accompanied by other hadrons, which often makes the analysis model-dependent. Some exceptions to this case are $e^+e^- \rightarrow \pi^+\pi^-$, $\tau \rightarrow \nu\pi\pi$ and $K \rightarrow e\nu\pi\pi$ (K_{4e4}). In the latter process the $K \rightarrow \pi\pi$ form factors allow a measurement of the phase difference between s and p waves, $\delta_0^0 - \delta_1^1$. The ellipse labelled E865 [17] in figure 1.1 shows the constraint imposed on a_0 and a_2 by the K_{4e4} data collected at Brookhaven.

Some improvements are obtained when the latter data and other from various hadron experiments are combined in a model-independent analysis of the $\pi\pi$ partial-wave amplitudes using dispersion relations. The area labelled PY in figure 1.1 shows the results of this analysis [18] when projected onto the (a_0, a_2) plane. Also shown in figure 1.1 are the two ellipses corresponding to 1σ and 2σ contours from the analysis of authors in reference [19].

A new player in the field was incorporated after the brilliant idea by N. Cabibbo [20] of utilizing the cusp observed by the NA48/2 experiment at CERN in the decay $K^\pm \rightarrow \pi^\pm\pi^0\pi^0$, to measure the difference $a_0 - a_2$. However the presence of three final state pions still entails a level of complexity in the analysis that cannot be minimized, when one gets to the

percent level accuracy. The original authors have estimated an intrinsic theoretical uncertainty of 5% [21], despite the very precise experimental data. New studies have been made since then on the theory side [22], [23]. Results from this input are shown in figure 1.1 under the label NA48/2 $K3\pi$. The same group has investigated a very large sample of K_{4e_4} decays [24] also indicated in figure 1.1 by the broad vertical band.

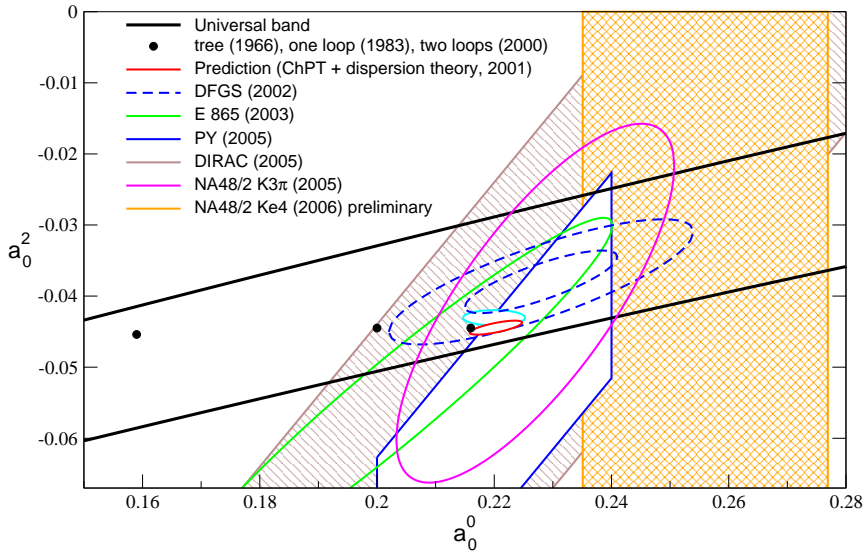


Figure 1.1: S wave scattering lengths: theoretical results.

In this thesis, we are going to report on a different kind of experimental measurement of the $\pi\pi$ scattering lengths [1]. As far as the reaction channel is concerned, it can hardly be more direct, since the two-body process $\pi^+\pi^- \rightarrow \pi^0\pi^0$ is decoupled in time from any other background reaction, and it takes place practically at rest. The DIRAC experiment consists of forming pionium states (electromagnetically bound $\pi^+\pi^-$) using a high energy proton beam, and measuring the atom lifetime by observing its survival probability, or ionization yield, in a very thin metal foil.

1.3 Pionium lifetime in QCD and QED

A precision measurement of pionium lifetime as a means to determine the $\pi\pi$ isospin scattering length difference $|a_0 - a_2|$ is the fundamental objective of the DIRAC experiment at CERN [1]. In fact, as we have seen above, the difference $|a_0 - a_2|$ is calculable in Chiral Perturbation Theory (ChPT), and it is very sensitive to the value of the quark condensate in QCD [4], and thus to the manner in which chiral symmetry is spontaneously broken.

We shall briefly review in this section the theoretical understanding of how such determination can be achieved to the percent level, and mention some of the subtleties involved in it.

The authors of reference [25] have recently pointed out that a considerable step forward in the precision calculation of the spectrum of hadronic atoms took place when the non-relativistic effective Lagrangian approach was introduced for the study of bound states, originally in the framework of QED [26]. When using such approach, the calculation of the pionium atom spectrum can be treated separately from the chiral expansion. This actually becomes possible because of the large difference of the relevant momentum scales: whereas the characteristic momenta in ChPT are of order of the pion mass, the typical bound state momentum is the inverse of the Bohr radius, which prompts the successful use of the non-relativistic Lagrangian approach for the analysis of the bound state.

Let us summarize how this concept is applied to the pionium state, following the original publications [27],[28],[29] by J. Gasser, V.E. Lyubovitskij, A. Rusetsky and A. Gall (GLRG).

GLRB have made a rigorous analysis of pionium $\pi^0\pi^0$ width using a non-relativistic lagrangian (NRL), in association with quantum mechanics perturbation theory (Feshbach formalism of the Rayleigh-Schrödinger theory). The non-relativistic Lagrangian \mathcal{L} contains all terms needed to evaluate the decay width $\Gamma_{\pi^0\pi^0}$ up to and including terms of order $\alpha^{9/2}$.

At this order of precision, $\mathcal{L} = \mathcal{L}_0 + \mathcal{L}_D + \mathcal{L}_C + \mathcal{L}_S$ consists of a free Lagrangian for charged and neutral pions (\mathcal{L}_0), a disconnected piece providing the correct relativistic relation between the energies and momenta of the pions (\mathcal{L}_D), a Coulomb interaction piece (\mathcal{L}_C), and a connected piece (\mathcal{L}_S),

which contains local four-pion interaction vertices, defined by the expressions:

$$\begin{aligned}
\mathcal{L}_0 &= \sum_{i=\pm,0} \pi_i^\dagger \left(i\partial_t - M_{\pi_i} + \frac{\Delta}{2M_{\pi_i}} \right) \pi_i, \\
\mathcal{L}_D &= \sum_{i=\pm,0} \pi_i^\dagger \left(\frac{\Delta^2}{8M_{\pi_i}^3} + \dots \right) \pi_i, \\
\mathcal{L}_C &= -4\pi\alpha(\pi_-^\dagger \pi_-) \Delta^{-1} (\pi_+^\dagger \pi_+) + \dots, \\
\mathcal{L}_S &= c_1 \pi_+^\dagger \pi_-^\dagger \pi_+ \pi_- + c_2 [\pi_+^\dagger \pi_-^\dagger (\pi_0)^2 + \text{h.c.}] + c_3 (\pi_0^\dagger \pi_0)^2 \\
&\quad + c_4 [\pi_+^\dagger \overleftrightarrow{\Delta} \pi_-^\dagger (\pi_0)^2 + \pi_+^\dagger \pi_-^\dagger \pi_0 \overleftrightarrow{\Delta} \pi_0 + \text{h.c.}] + \dots,
\end{aligned} \tag{1.1}$$

where π_i are the isospin components of the pion fields, and Δ^{-1} denotes the inverse of the Laplacian. The couplings c_i are determined by matching to the relativistic pion scattering theory.

The authors show [29] that the above Lagrangian provides a rigorous description of low-energy interactions of pions and photons, at order α . It is actually the restriction at the non-relativistic limit of the most general Lagrangian including all possible operators (an infinite tower with increasing mass dimension) allowed by the symmetries, the building blocks being the covariant derivatives of the charged and neutral pion fields, as well as Maxwell's equations. Transverse photons contribute neither to the decay width at $O(\alpha^{9/2})$, nor to the matching condition at threshold, and that allows to eliminate Coulomb photons by using the equations of motion, leading to the Lagrangian 1.1.

The real and imaginary parts of the pole positions (z) that describe the bound states in the Rayleigh-Schrödinger formalism mentioned above can be calculated by means of an iterative procedure applied to a perturbed potential, which is unambiguously derived from the non-relativistic Lagrangian, to the required precision. As a result of this analysis, the $\pi^0\pi^0$ pionium width ($\Gamma_{\pi^0\pi^0} = -2\text{Im}z$) can be expressed in terms of the four low energy constants, namely c_1, c_2, c_3, c_4 , with precision that includes all terms of $O(\alpha^{9/2})$. The final expression is:

$$\Gamma_{2\pi^0} = -\frac{\alpha^3 M_{\pi^+}^3}{4\pi} \text{Im}w \left(1 + \frac{\alpha M_{\pi^+}^2}{4\pi} \xi \text{Re}w \right) + \dots,$$

$$\begin{aligned}
\xi &= 2 \ln \alpha - 3 + \Lambda + \ln \frac{M_{\pi^+}^2}{\mu^2}, \\
\Lambda &= (\mu^2)^{d-3} [(d-3)^{-1} - \Gamma'(1) - \ln 4\pi], \\
\text{Im}w &= -\frac{M_{\pi^0}}{2\pi} \rho^{1/2} \left(1 + \frac{5\rho}{8M_{\pi^0}^2}\right) (c_2 - 2\rho c_4)^2 \\
&\times \left(1 - \rho \frac{M_{\pi^0}^2 c_3^2}{4\pi^2}\right), \quad \text{Re}w = -c_1,
\end{aligned} \tag{1.2}$$

where $\rho = 2M_{\pi^0}(M_{\pi^+} - M_{\pi^0} - \frac{1}{8}\alpha^2 M_{\pi^0})$, μ is the renormalization scale and d is the number of space dimensions.

The same NRL can be used to study the on-shell amplitude at threshold for the process $\pi^+\pi^- \rightarrow \pi^0\pi^0$, in the presence of photons. Specifically, it is shown that the analytic structure of this amplitude at order α , once the divergent Coulomb phase is split off, can be written as:

$$\text{Re}T_{NR}^{00;\pm}(\mathbf{p}) = \frac{B_1}{|\mathbf{p}|} + B_2 \ln \frac{2|\mathbf{p}|}{M_{\pi^+}} + \frac{1}{4M_{\pi^+}^2} \text{Re}A_{\text{thr}}^{+-00} + o(\mathbf{p}), \tag{1.3}$$

where \mathbf{p} is the $\pi^+\pi^-$ relative momentum in the center-of-mass frame and $\text{Re}A_{\text{thr}}^{+-00}$ represents the non-singular part of the amplitude at threshold.

The singular contributions of the first two terms are generated by the exchange of one Coulomb photon, according to the Feynmann diagrams (a) and (b) in figure 1.2, respectively. The B_1 and B_2 coefficients (which are of order α), as well as the non-singular term $\text{Re}A_{\text{thr}}^{+-00}$, can be matched to the low energy constants of the NRL. In particular $\text{Re}A_{\text{thr}}^{+-00}$ can be related to the constants c_1, c_2, c_3, c_4 as follows:

$$\begin{aligned}
\frac{1}{4M_{\pi^+}^2} \text{Re}A_{\text{thr}}^{+-00} &= 2c_2 - 4M_{\pi^0}^2 \kappa \left(c_4 + \frac{c_2 c_3^2}{8\pi^2} M_{\pi^0}^2\right) \\
&+ \frac{\alpha M_{\pi^+}^2}{4\pi} \left(1 - \Lambda - \ln \frac{M_{\pi^+}^2}{\mu^2}\right) c_1 c_2.
\end{aligned} \tag{1.4}$$

where $\kappa = (M_{\pi^+}^2/M_{\pi^0}^2) - 1$ and Λ was defined in (1.2). The constants c_1 and c_3 can be expressed, at order zero in α , in terms of the isospin scattering lengths a_0 and a_2 as follows:

$$\begin{aligned}
c_1 &= (4\pi/3)(2a_0 + a_2)/M_{\pi^+}^2 + O(\alpha) \\
c_2 &= (2\pi/3)(a_0 + 2a_2)/M_{\pi^+}^2 + O(\alpha)
\end{aligned}
\tag{1.5}$$

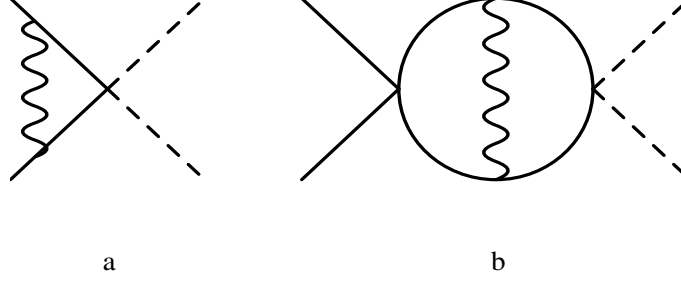


Figure 1.2: Diagrams that generate a singular behavior of the $\pi^+\pi^- \rightarrow \pi^0\pi^0$ scattering amplitude at threshold in the relativistic theory: (a) vertex correction, (b) internal exchange of the photon. Solid lines represent charged pions and dotted lines neutral pions.

Formulae (1.2) and (1.4) lead us to the following expression, accurate with precision $\alpha^{9/2}$:

$$\Gamma_{2\pi^0} = \frac{2}{9} \alpha^3 p^* \mathcal{A}^2 (1 + K),
\tag{1.6}$$

with $p^* = (M_{\pi^+}^2 - M_{\pi^0}^2 - \frac{1}{4}M_{\pi^+}^2\alpha^2)^{1/2}$, and

$$\begin{aligned}
\mathcal{A} &= -\frac{3}{32\pi} \text{Re}A_{\text{thr}}^{+-00} + o(\alpha), \\
K &= \frac{\kappa}{9} (a_0 + 2a_2)^2 - \frac{2\alpha}{3} (\ln \alpha - 1) (2a_0 + a_2) + o(\alpha).
\end{aligned}
\tag{1.7}$$

The ultra-violet divergent contributions that appear at $O(\alpha^{9/2})$ both in the analysis of $\Gamma_{\pi^0\pi^0}$ and $\text{Re}A_{\text{thr}}^{+-00}$, with opposite signs, through the respective terms $\Lambda + \ln(M_{\pi^+}^2/\mu^2)$, are again rooted into the diagram (b) of figure

1.2, and they are actually removed by the renormalization procedure in the scattering process $\pi^+\pi^- \rightarrow \pi^0\pi^0$. We have checked ¹ that indeed expression (1.6) is verified with precision $\alpha^{9/2}$.

The above result is of fundamental importance, because it provides a rigorous and accurate relationship between two physical quantities, namely the pionium $\pi^0\pi^0$ width, subject to precision measurement by DIRAC, and the non-singular piece of the relativistic scattering amplitude at threshold for the process $\pi^+\pi^- \rightarrow \pi^0\pi^0$. In its derivation only the NRL (exact at $O(\alpha^{9/2})$), and standard non-relativistic quantum mechanics perturbation theory have been used. It is worth noting that, in particular, ChPT has not been used in this approach.

Given the fact that the quantities a_0 and a_2 are calculable in ChPT, GLRB have used this theory to disentangle the isospin-breaking corrections at $O(\alpha^{9/2})$, in order to single out the leading contribution to $\text{Re}A_{\text{thr}}^{+-00}$, which is certainly $a_0 - a_2$. In fact, already expression (1.7) is normalized such that in the isospin limit ($\alpha = 0$) we have $\mathcal{A} = a_0 - a_2$.

ChPT can now be invoked in order to extract the $\pi\pi$ scattering lengths from the experimental information on the width, and the amplitude \mathcal{A} can be expanded as²:

$$\mathcal{A} = a_0 - a_2 + h_1 (m_d - m_u)^2 + h_2 \alpha + o(\delta), \quad (1.8)$$

where δ now stands for either α or the quark mass difference $m_u - m_d$. The above expression actually *defines* the strong $\pi\pi$ scattering lengths evaluated in QCD at $\alpha = 0$, $m_u - m_d = 0$. Note the coefficients h_1 and h_2 are not changed when taking the isospin symmetry limit.

The coefficients h_i are then evaluated in the framework of standard ChPT. The result for h_1 at order e^2p^2 is known in the literature [30] and it is negligible at order α . We have $h_1 = O(\hat{m})$, with $\hat{m} = m_u + m_d$. The coefficient h_2 contains two parts $h_2 = h_\Delta + h_\gamma + O(\hat{m})$ [30]. As a

¹we thank Marcos Seco and the authors for helping us using MATHEMATICA for this purpose.

²in QCD the scattering amplitude $\pi^+\pi^- \rightarrow \pi^0\pi^0$ does not contain terms linear in the quark mass difference $m_u - m_d$.

consequence of this analysis , the pionium decay width can be expressed in the form :

$$\Gamma_{2\pi^0} = \frac{2}{9} \alpha^3 p^* (a_0 - a_2 + \epsilon)^2 (1 + K), \quad (1.9)$$

with

$$\begin{aligned} \epsilon &= \alpha h_\Delta + \alpha h_\gamma + \dots \\ &= \frac{3\Delta_\pi^{e.m.}}{32\pi F_\pi^2} \left\{ 1 + \frac{M_{\pi^+}^2}{12\pi^2 F_\pi^2} \left[\frac{23}{8} + \bar{l}_1 + \frac{3}{4} \bar{l}_3 + \frac{3}{2} \bar{l}_4 \right] \right\} \\ &+ \frac{3\alpha M_{\pi^+}^2}{256\pi^2 F_\pi^2} (P(K_i) - 8Z\bar{l}_4) + \dots . \end{aligned} \quad (1.10)$$

where

$$\begin{aligned} P(K_i) &= \frac{128\pi^2}{3} \left(-6(K_1^r + K_3^r) + 3K_4^r - 5K_5^r + K_6^r + 6(K_8^r + K_{10}^r + K_{11}^r) \right) \\ &- (18 + 28Z) \ln \frac{M_{\pi^+}^2}{\mu^2} - 2Z \left(\ln \frac{m_s B_0}{\mu^2} + 1 \right) - 30. \end{aligned} \quad (1.11)$$

the ellipses denote terms of order $O(\hat{m}(m_d - m_d)^2, \alpha \hat{m}^2)$ and higher, which are negligible. \bar{l}_i denote the running coupling constants l_i^r at scale $\mu = M_{\pi^+}$. K_i^r denote the electromagnetic low energy constants in $SU(3) \times SU(3)$ ChPT. Both Z and $\Delta_\pi^{e.m.}$ are defined in the chiral limit :

$$\Delta_\pi^{e.m.} = \Delta_\pi|_{m_u=m_d}, \quad Z = \frac{\Delta_\pi}{8\pi\alpha F^2} \Big|_{m_u=m_d=0}. \quad (1.12)$$

where $\Delta_\pi = M_{\pi^+}^2 - M_{\pi^0}^2$. B_0 is related to the chiral condensate in $SU(3) \times SU(3)$ and m_s denotes the strange quark mass [10].

The detailed numerical analysis of equations (1.11) and (1.12) has been carried out by GLRB in references [28] , [29] , and more recently summarized in reference [25]. According to it, we have:

$$\epsilon = (0.58 \pm 0.16) \cdot 10^{-2}, \quad K = 1.07 \cdot 10^{-2}. \quad (1.13)$$

We will use expression (1.9) for our $|a_0 - a_2|$ measurement with the indicated values of ϵ and K , as then main theoretical input in this thesis. Formula 1.9 can also be recast [29] under the form:

$$\Gamma_{2\pi^0} = \frac{2}{9} \alpha^3 p^* (a_0 - a_2)^2 (1 + \delta_T), \quad (1.14)$$

with $\delta_T = (5.8 \pm 1.2) \times 10^{-2}$.

1.3.1 Photon decays of ponium

In the s-wave, ponium decays overwhelmingly into $\pi^0\pi^0$. Let us briefly comment on the high order contributions that lead to photons in the final state.

At leading order the decay width into $\pi^0\pi^0$ counts at $O(\alpha^{7/2})$. Next-to-leading isospin breaking corrections are of order $\alpha^{9/2}$, as we have seen. The anomaly-induced decay into $\pi^0\gamma$ cannot proceed in the s-wave (due to C-invariance) [29], and the decay into $\gamma\gamma$ starts at order $O(\alpha^5)$ [31], and at least at the same order $O(\alpha^5)$ starts the decay into $\pi^0\pi^0\gamma\gamma$ [29]. At order $O(\alpha^{9/2})$, the multi-photon final states of the type $\pi^0\pi^0\gamma$ do not contribute either [32]. In consequence, at $O(\alpha^{9/2})$ only ponium decay into $\pi^0\pi^0$ final state needs to be taken into account.

1.4 Ponium production

The differential production cross section of ponium atoms only occurs in S -states [33], and can be expressed as:

$$\frac{d\sigma_A^n}{d\vec{p}_A} = (2\pi)^3 \frac{E_A}{M_A} |\Psi_n^C(\vec{r}^* = 0)|^2 \frac{d^2\sigma_s^0}{d\vec{p}_+ d\vec{p}_-} \Big|_{\vec{p}_+ = \vec{p}_-} \quad (1.15)$$

with \vec{p}_A , E_A and M_A the momentum, energy and mass of the atom in the lab frame, respectively, and \vec{p}_+ , \vec{p}_- the momenta of the charged pions. The square of the Coulomb atomic wave function for zero distance \vec{r}^* between them in the center of mass system is $|\Psi_n^C(0)|^2 = p_B^3/\pi n^3$, where $p_B = m_\pi\alpha/2$ is the Bohr momentum of the pions and m_π the pion mass.

Final state interaction also transforms the ‘‘unphysical’’ cross section σ_s^0 into a real one for Coulomb correlated pairs, σ_C [34, 35]:

$$\frac{d^2\sigma_C}{d\vec{p}_+d\vec{p}_-} = |\Psi_{-\vec{k}^*}^C(\vec{r}^*)|^2 \frac{d^2\sigma_s^0}{d\vec{p}_+d\vec{p}_-}, \quad (1.16)$$

where $\Psi_{-\vec{k}^*}^C(\vec{r}^*)$ is the continuum wave function and $2\vec{k}^* \equiv \vec{q}$ with \vec{q} being the relative momentum of the π^+ and π^- in the CMS³. $|\Psi_{-\vec{k}^*}^C(\vec{r}^*)|^2$ describes the Coulomb correlation and at $r^* = 0$ coincides with the Gamov-Sommerfeld factor $A_C(q)$ with $q = |\vec{q}|$ [35]:

$$A_C(q) = \frac{2\pi m_\pi\alpha/q}{1 - \exp(-2\pi m_\pi\alpha/q)}. \quad (1.17)$$

Charged pions with opposite charge emerging from a high energy proton-nucleus collision are produced directly or originate from strong short-lived (ρ, ω, K^*, \dots) or electroweak long-lived ($\eta, \eta', K_s^0, \dots$) sources. Pion pairs from short-lived sources undergo Coulomb final state interaction and may therefore form atoms⁴, since the region of production is very small as compared to the Bohr radius of the atom ($r_B = 387 fm$). The total pion spectrum is formed by four type of pion pairs:

- *Atomic Pairs*. Coulomb bound state of two pions (pionium) produced in one proton-nucleus collision.
- *Coulomb Pairs*. Produced in one proton-nucleus collision from fragmentation or short-lived resonances and exhibit Coulomb interaction in the final state.

³For the sake of clarity we use the symbol Q for the experimentally reconstructed and q for the physical relative momentum.

⁴the contribution to the pionium production of long-lived sources was neglected as it is under the 1% level.

- *Non Coulomb Pairs* (or *Long – lived Pairs*). Produced in one proton-nucleus collision where at least one pion comes from a long-lived resonance. They do not exhibit Coulomb interaction in the final state.
- *Accidental Pairs*. The two charged particles are produced in two different proton-nucleus collisions. They do not exhibit Coulomb interaction in the final state.

In figure 1.3 we show the precision time difference measured by the TOF detectors (Vertical Hodoscopes). The $1ns$ coincidence peak (prompt pairs) is formed by atomic pairs, Coulomb pairs and non-Coulomb pairs, apart from a fraction of accidental pairs that can be easily extrapolated. The peak width ($\sim 170 ps$) is determined by detector resolution. Proton background can be appreciated in the peak asymmetry. Pairs in the colored lateral band are accidental pairs.

1.5 Propagation inside the target

After production, the pionium atoms propagate inside the target foil, interacting mostly with the electromagnetic field of the target atoms. Therefore pionium can undergo one of the three following processes [36] [1], one mediated by strong forces, and the other two of electromagnetic nature:

- Annihilation into $\pi^0\pi^0$
- Ionization (break up) by the target nuclei into $\pi^+\pi^-$
- Excitation/de-excitation to higher/lower principal quantum number levels

The relation

$$1 = P_{Br} + P_{ann} + P_{dsc} \quad (1.18)$$

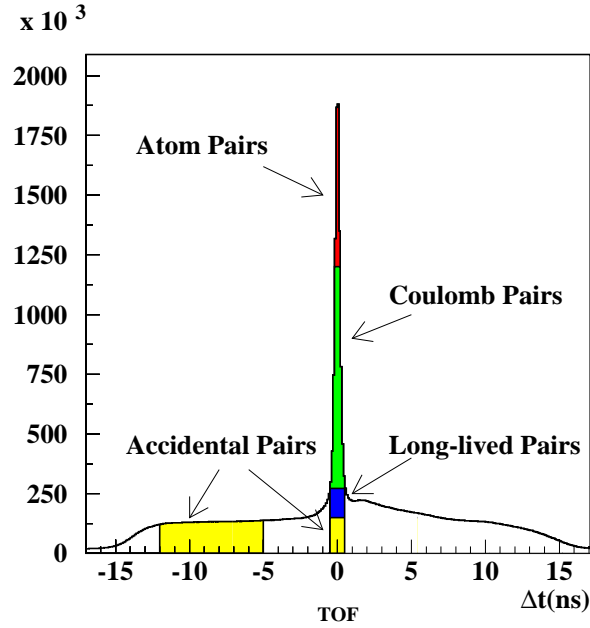


Figure 1.3: Time difference between positive and negative particles measured by the Time-of-Flight detector in 2002. *Red*: Atom pairs, *green*: Coulomb pairs, *blue*: Long-lived pairs, and *yellow*: Accidental pairs.

is obviously satisfied being P_{Br} the pionium breakup probability, P_{ann} the annihilation probability, and P_{dsc} stands for the probability of the atom leaving the target in a discrete state.

Using a high-Z and thin target, the pionium ionization probability competes mainly with the annihilation process, so that P_{dsc} is highly reduced.

The $\pi^+\pi^-$ pairs coming from pionium break-up (atomic pairs) exhibit specific kinematical features which allow to identify them experimentally. For thin targets ($10^{-3}X_0$), due to the very small momentum transfer induced by the electric field near the target nuclei, the signal of atomic pairs is detected by DIRAC spectrometer as an excess with respect to Coulomb-correlated pairs at very low center-of-mass momentum, $Q < 3MeV/c$, with a yield of $\sim 10\%$ in this Q interval.

1.6 Pionium lifetime

The breakup probability is a function of the atom momentum and depends on the dynamics of the pionium interaction with the target atoms and on the pionium lifetime. For a given target atomic number and thickness, the theoretical breakup probability for pionium is calculated [36] with a relative error of less than 1% [37] thanks to the detailed knowledge of the cross-sections involved in the process, which is purely electromagnetic, in which Born and Glauber approximations are used [38][39][40].

This breakup probability is uniquely linked to the atom lifetime [33]. In Fig.1.4 the P_{Br} as a function of the lifetime is displayed for a 98 μm Ni target, which was the foil thickness installed in DIRAC during the 2002 and 2003 data taking period.

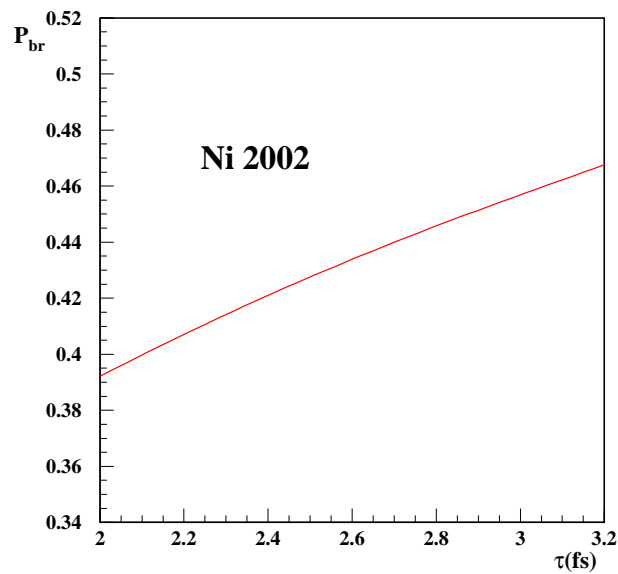


Figure 1.4: Breakup probability as a function of pionium lifetime for a 98 μm Nickel target.

Measuring P_{Br} thus allows to determine the lifetime of ponium. In DIRAC the breakup probability can be measured experimentally as the ratio of the detected number of atomic pairs (n_A) over the total number of produced atoms (N_A):

$$P_{Br} = \frac{n_A}{N_A} \quad (1.19)$$

The total number of produced $\pi^+\pi^-$ atoms is related by an exact expression to the number of free pion pairs with low relative momenta, so that the breakup probability can be measured with DIRAC experimental method.

1.7 DIRAC spectrometer

In this section, the general characteristics, design and working performances of the apparatus are explained.

Pion pairs $\pi^+\pi^-$ emerging from break-up of ponium have a low relative momentum in their centre of mass system ($Q < 3 \text{ MeV}/c$), very small opening angle ($\theta < 3 \text{ mrad}$) and nearly identical energies in the laboratory frame. A high resolution magnetic spectrometer is then required [41] to split up the pairs and measure their relative momentum with sufficient precision to detect the ponium signal superimposed on the substantial background of “free” $\pi^+\pi^-$ pairs produced in inclusive proton-nucleus interactions.

The DIRAC experimental setup, located at the T8 proton beam line (with energy of 20 or 24 GeV/c) in the East Hall of the PS accelerator at CERN, became operational at the end of 1998 and has been collecting data since the middle of 1999. A general view of the spectrometer and a list of the setup components ordered along the proton beam direction are shown in Fig.1.5, consisting of beam line, target station, secondary vacuum channel, spectrometer dipole magnet and detectors placed upstream and downstream of the magnet.

Protons are extracted in spills of $\sim 400\text{--}500 \text{ ms}$ duration from the PS to the T8 beam line using a slow ejection mode [42]. During data taking, between 1 to 5 cycles per PS super-cycle of $14.4 \div 19.2 \text{ s}$ duration are

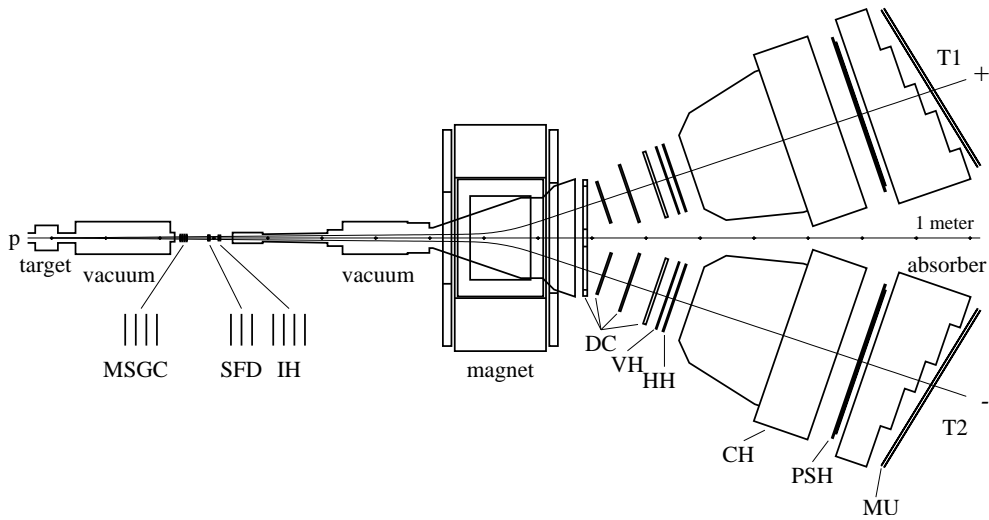


Figure 1.5: Top view representation of the DIRAC setup.

delivered to DIRAC. The proton beam intensity was set to $\sim 10^{11}$ protons per spill, depending on the target used.

The target station houses a device with 12 holders for the targets. The data analyzed in this work was collected during 2002 and 2003 data taking using two a Ni target with $98 \mu\text{m}$ thicknesses. The DIRAC experiment is sensitive to particles outside the beam core (halo), because the target is very thin and the upstream detectors are placed very close to the primary proton beam. Special optics has been designed to decrease the background halo to a negligible level. The ratio of detector counting rates with the target in place to those with an empty holder was measured to be ~ 25 .

Free and atomic $\pi^+\pi^-$ pairs produced in the target enter a secondary particle channel which is tilted upwards by 5.7° with respect to the proton beam (as indicated in Fig.1.5) to avoid background in the detectors. It consists of two vacuum cylindrical volumes, one immediately downstream the target station, and a second one located at ~ 3.5 m from the target between the spectrometer magnet poles. Secondary particles exit this tube through a 200 mm diameter window, made of $250 \mu\text{m}$ thick mylar film. The angular aperture of the secondary particle channel is determined by the

collimator resulting in a solid angle acceptance of $1.2 \cdot 10^{-3}$ sr.

Downstream the target the proton beam travels in a vacuum channel below the spectrometer. Before it is finally absorbed by a beam dump with a dedicated radiation shielding, in order to decrease the background gamma and neutron fluxes towards the detectors [43]. The downstream detectors are shielded in addition from background secondary particles produced at the primary proton beam pipe and surrounding elements by a 1 m thick iron wall that physically separates the upstream detector region from the rest. Collimators are inserted around the primary proton beam pipe and the secondary particle channel. A concrete radiation shielding encloses the whole DIRAC experimental apparatus to protect the surrounding East Hall in respect of the CERN safety regulations.

The secondary particle channel is endowed with a real spectrometer arm. This upstream arm consists of two tracking devices, the microstrip gas chambers (MSGC/GEM) and the scintillating fibre detector (SFD). They are used to improve resolution on the longitudinal and transverse components of the relative momentum of pion pairs, by unambiguously measuring the pair opening angle. The detection capability is increased for small angle tracks by an Ionisation Hodoscope (IH) is located past the SFD following the proton beam direction. A real picture of the above-mentioned detectors, as they are installed between the first vacuum chamber and the secondary particle channel, can be seen in Fig.1.6.

Downstream the spectrometer magnet the setup splits into two identical arms for detection and identification of positive and negative charged particles. The half opening angle between the two arms is 19° . Along each arm the following detectors are located: drift chamber system (DC), vertical hodoscope (VH), horizontal hodoscopes (HH), gas cerenkov counter (CH), preshower detector (PSH) and muon detector (MU).

1.7.1 The MSGC/GEM detector

It performs particle tracking at a distance of 2.4 m from the interaction point. In order to resolve two-particle ambiguities by means of stereo angles, four planes of a proportional gas detector with a single-hit space resolution

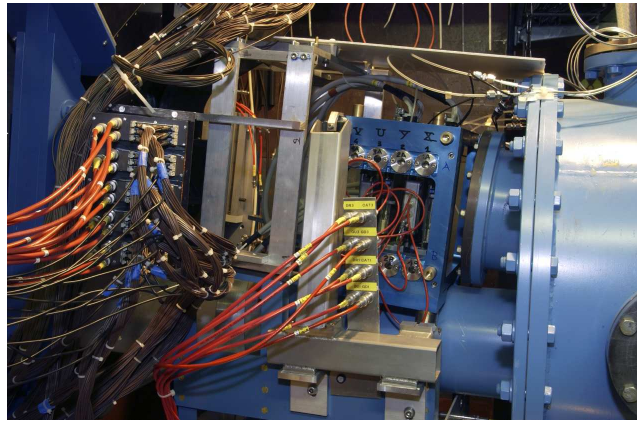


Figure 1.6: Photography of the three detectors installed upstream the magnet, between the first vacuum chamber (right-hand side) and the secondary particle channel. From right to left, the MSGC/GEM, SFD and IH detectors can be found. The primary proton beam line can be appreciated at the bottom.

of $\sim 50 \mu\text{m}$ are installed. It achieves an experimental double track resolution better than 0.3 mm. , limited by detector pitch and clustering. Because of its particular importance for upstream tracking, a more complete description of the MSGC/GEM will be done in the following chapters.

1.7.2 The Scintillating Fibre Detector

The Scintillating Fibre Detector (SFD) is used together with the MSGC/GEM detector, for upstream tracking, and it provides topological trigger capabilities [44] for rejection of pairs with relative distance larger than 9 mm. It also provides time information for upstream tracking.

The SFD consists of two perpendicular fibre planes to measure the X and Y coordinates of incident particles⁵, as the deposited energy from the particles is transformed into light.

⁵A third upgraded SFD-U plane rotated 45° relative to X and Y was added for 2002 and 2003 periods.

The SFD covers a $105 \times 105 \text{ mm}^2$ area. Each detector plane is composed of 240 column channels with $440 \mu\text{m}$ pitch, each consisting of a stack of 5 fibres in depth, measuring each one from 70 to 150 mm, as seen in Fig.1.7. Fibres forming one sensitive column are connected via a light guide into one channel of position-sensitive photomultiplier (PSPM), with a total of 15 photomultipliers of 16 channels each.

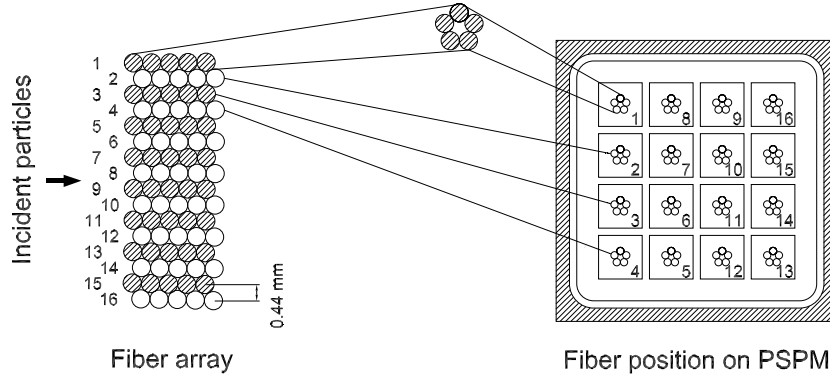


Figure 1.7: The SFD principal structure. A 16-channel fragment is shown.

A dedicated electronic circuit Peak Sensing Circuit (PSC) has been custom developed to provide signal discrimination with dynamic rejection of cross-talk in adjacent channels using the peak-sensing technique [45]. Discrimination of a channel is given by the condition $2A_i - A_{i-1} - A_{i+1} > A_{thr}$, where A_i are channel signal amplitudes and A_{thr} defines the threshold value.

For time correlated particle pairs (up to $\sim 5 \text{ ns}$ time difference) with distance more than one fibre pitch, the PSC algorithm provides efficient detection, avoiding cross-talk and rejecting noise. However, when adjacent fibre columns are crossed by two particles simultaneously, then the PSC algorithm leads to a suppression (with 50% probability) of the detected yield of double track events, and one of the hits is lost. For time difference greater than 5 ns the PSC behaves as an ordinary leading edge discriminator.

The upstream detectors performance is compromised by the high particle flux originated by the proximity of the proton beam line and collimators.

The level of optical cross talk among the PSPM channels due to escape

of ultraviolet light from one fibre column to the adjacent one, together with noise was found to be $\sim 2\%$. The detection efficiency is high (larger than 97% as we shall see) and the average hit multiplicity is near 5 in the 50 ns time window of TDC. Each detector fibre is equipped with a TDC channel which provides time tagging essential for upstream tracking.

Readout supplies time information in digital form TDC. The raw time spectra, obtained from e^+e^- and $\pi^+\pi^-$ events, are shown in Fig. 1.8 for two arbitrary SFD channels. After off-line deconvolution of the trigger time jitter the resolution of the SFD is found to be $\sigma=0.8$ ns. Single track resolution is defined by fibre column pitch of $440 \mu\text{m}$.

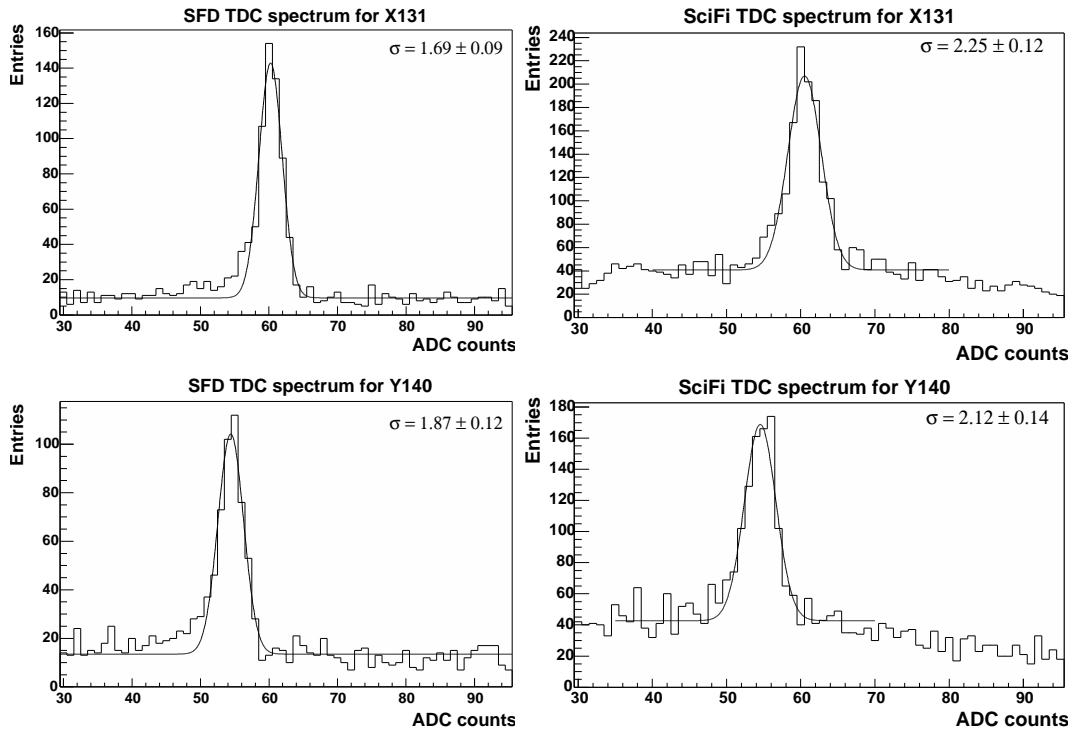


Figure 1.8: SFD raw time spectra for e^+e^- (left) and for $\pi^+\pi^-$ (right) trigger data. The horizontal scale is in TDC channels, the channel width is 0.5 ns.

1.7.3 The Ionisation Hodoscope

Since charged pions originated from pionium breakup cross the upstream detectors at rather small relative distances, a dedicated Ionisation Hodoscope [46] has been built to separate the double ionisation signal produced by close pion pairs incident on the same scintillating slab, from single ionisation signals produced by one particle. In this way, uncertainties resulting from pairs with relative distance less than the double track resolution are significantly reduced. In addition, the IH takes part of the trigger system of DIRAC.

IH detector is a scintillation hodoscope consisting of 4 planes of $11 \times 11 \text{ cm}^2$ sensitive area (Fig. 1.9) placed 3 m downstream the target. Two planes (X-A and X-B) vertically oriented, and the other two with horizontal slabs (Y-A and Y-B), being planes with the same slab orientation shifted by a half-slab-width with respect to each other. Each plane is assembled from 16 plastic scintillating. The slabs are 11 cm long, 7 mm wide and 1 mm thick. They are connected to the PM photocathodes via 2 mm thick and 7 mm wide lucite light guides.

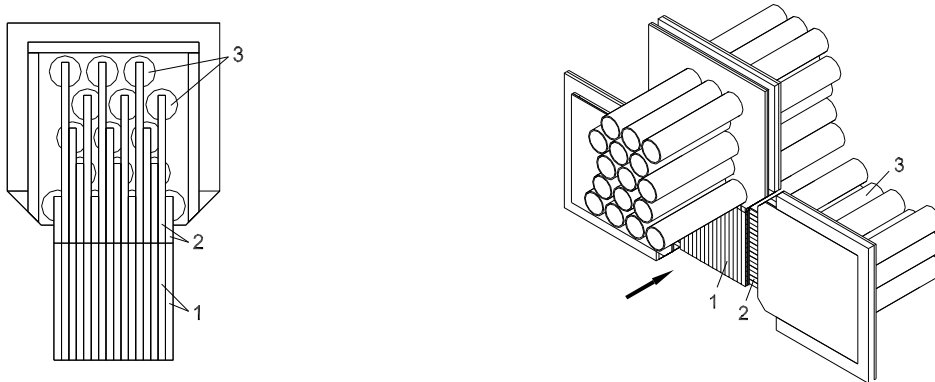


Figure 1.9: *Design and isometric view of the IH scintillation plane (1 – scintillators, 2 – light-guides, 3 – photomultipliers).*

The front and rear surfaces of a slab are covered by a millipore film [47] for efficient light collection. At the lateral surface of the slab, light is reflected

by a 30 μm mylar film in order to minimise the gaps between adjacent slabs, which is less than 70 μm wide.

Scintillation light is detected by photomultipliers. Photocathodes are in optical contact with the wide side of a light guide instead of the traditional butt-end readout, improving the light collection efficiency.

Signal amplitude and time are digitised by ADC and TDC modules, respectively. The time resolution of the IH detector is better than 1 ns. The typical response of one IH channel to close particle pairs incident on one scintillating slab and to single particle is shown in Fig.1.10. If a threshold is set to retain 95% of the double ionisation signal from pairs, the contamination from single particle amplitudes is less than 15% (Fig.1.11).

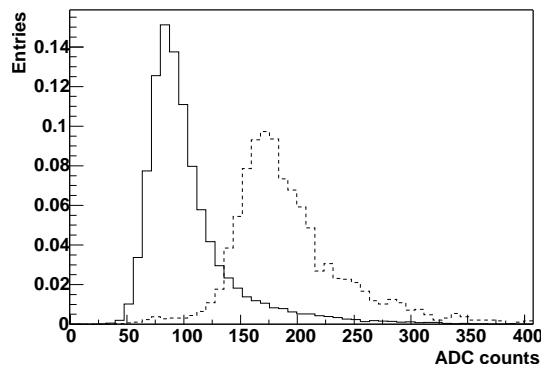


Figure 1.10: Typical ADC spectra for single (solid line) and double (dashed line) ionisation loss from particles crossing one IH scintillating slab.

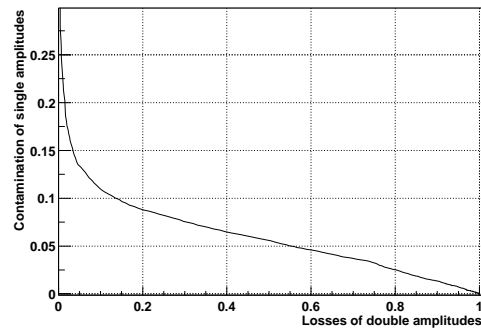


Figure 1.11: Contamination of single ionisation amplitudes as a function of losses of double ionisation as obtained from the analysis of the spectra of Fig. 1.10.

1.7.4 Magnet

The magnet separates positive and negative particles coming from upstream area, being the two downstream arms placed at arms $\pm 19^\circ$ relative to the central axis. Magnetic field ($B=1.65$ T, field integral $BL = 2.2$ T·m) has been parametrized. The dipole magnet has an aperture of 1.55×0.50 m² ($W \times H$) and measures $0.5 \times 1.5 \times 1.1$ m. To reduce the stray field, two magnetic screens are fixed near its entrance and exit.

1.7.5 Drift Chambers

The drift chamber system is used to perform particle tracking downstream the dipole magnet. These are gas detectors with periodic cell structure giving spatial and time (by means of the drift time) information, used in the T4 level trigger.

A two-arm solution has been chosen, except for the first chamber which is a single large module (DC-1) designed with two separated sensitive areas. This chamber provides 6 successive measurements of the particle trajectory along the coordinates X, Y, W, X, Y, W, where W is a stereo angle with inclination 11.3° with respect to the X-coordinate. Each of the two arms

consists of 3 chamber modules, of identical design, measuring coordinates X, Y (DC-2), X, Y (DC-3) and X, Y, X, Y (DC-4) following the direction of the outgoing particle. The dimensions are $0.8 \times 0.4 \text{ m}^2$ for DC-1 sensitive areas, $0.8 \times 0.4 \text{ m}^2$ for DC-2, $1.12 \times 0.4 \text{ m}^2$ for DC-3, and DC-4 is $1.28 \times 0.4 \text{ m}^2$. DC-1 is instrumented with 800 electronic channels, and both arms together contain 1216 electronic channels.

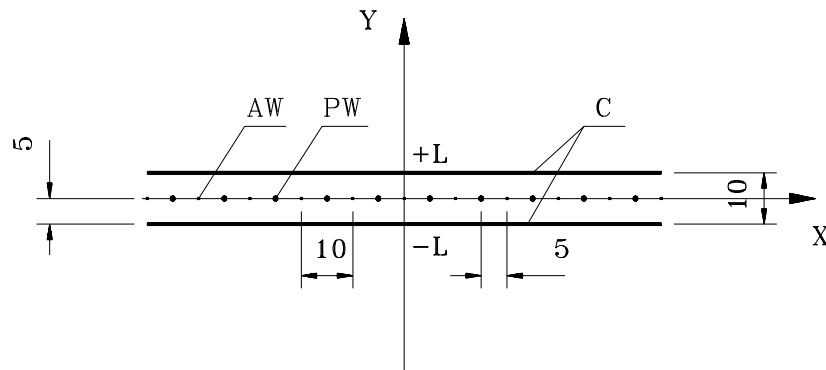


Figure 1.12: Schematic view of the wire chamber electrodes: *AW* – anode wires, *PW* – potential wires, *C* – cathode foils. Dimensions are in mm.

The distance between the center of the first half of DC1 and the center of DC4 provides a lever-arm of 1.6 m along the average particle path, having uniform spacing of chambers DC-2 and DC-3 along this path. Six measurement points, together with a sufficiently long lever arm, allows to accurately reconstruct the downstream tracks.

A schematic drawing of the sensitive element is shown in Fig. 1.12. As seen in the figure, a sensitive area, corresponding to each anode wire and limited by the cathode planes and potential wires, has a square ($10 \times 10 \text{ mm}^2$) shape. Cathode plane foils provide stable chamber operation and, being thin, add only small amount of material along the particle path. A rather large diameter of the anode wires has been chosen in order to operate the chambers at high current avalanche amplification mode.

The chamber design is shown in Fig. 1.13 for the case of the DC-2 module. The module is a stack of aluminium and fibreglass frames fixed by screws with rubber o-rings glued to provide gas tightness. The design of module DC-1 differs from this description. The main difference, illustrated

in Fig. 1.14, consists in the fact that DC-1 comprises, in a single gas volume, two sets of sensitive planes, placed symmetrically to the left and right hand side of the spectrometer axis. The middle zone, strongly irradiated, is made insensitive to the particle flux. The limiting edge of the sensitive zones can be varied. This design of the DC-1 module ensures little amount of material, by avoiding frames in the small angle region.

The readout electronics of the drift chambers, which is a custom-made system [48], provides data readout into the data collection memories and input to the trigger processor. The sensitive wire signals are digitised by TDC counters, which are plugged in the connectors mounted onto the chamber frames, and are connected to the Drift Chamber Processor (DCP) and VME buffer memory. This solution results in reduced number of electronic units, small number of cables and high noise immunity. The data of an event are stored in local data buffers until the higher level trigger decision is issued.

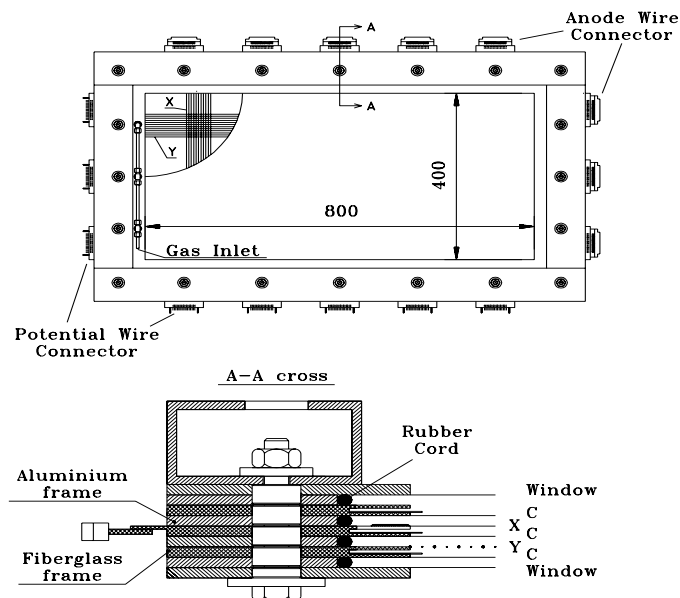


Figure 1.13: Design of the DC-2 module. Top: general view. Bottom: structure of the frame stack; X – X-plane, Y – Y-plane, C – cathode foils.

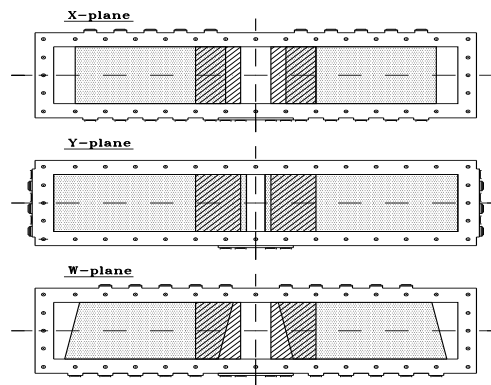


Figure 1.14: Schematic view of the *DC-1* module. Dotted areas show the sensitive regions of the *X*-, *Y*- and *W*-planes. Hatched areas mark the zones of the cathode strips which allow to change the width of the insensitive area in the central region.

The drift chambers operate in a high current avalanche mode. The single hit efficiency is above 96% when the particle flux along the gas mixture ($Ar(\sim 50\%) + iC_4H_{10}(\sim 50\%) + H_2O(0.5\%)$) is about 10 kHz/cm^2 . Tracking efficiency of the drift chamber system as a whole is about 99%, due to the requested number of hits per reconstructed track is less than the total number of sensitive planes crossed by a particle. A space-to-time relationship was extracted from the time spectrum and its integral distribution shown in Fig. 1.15, for a sample of clean events with a small amount of background hits. Study of the drift function parameters for different chamber planes at different beam intensities shows good stability of the above relation.

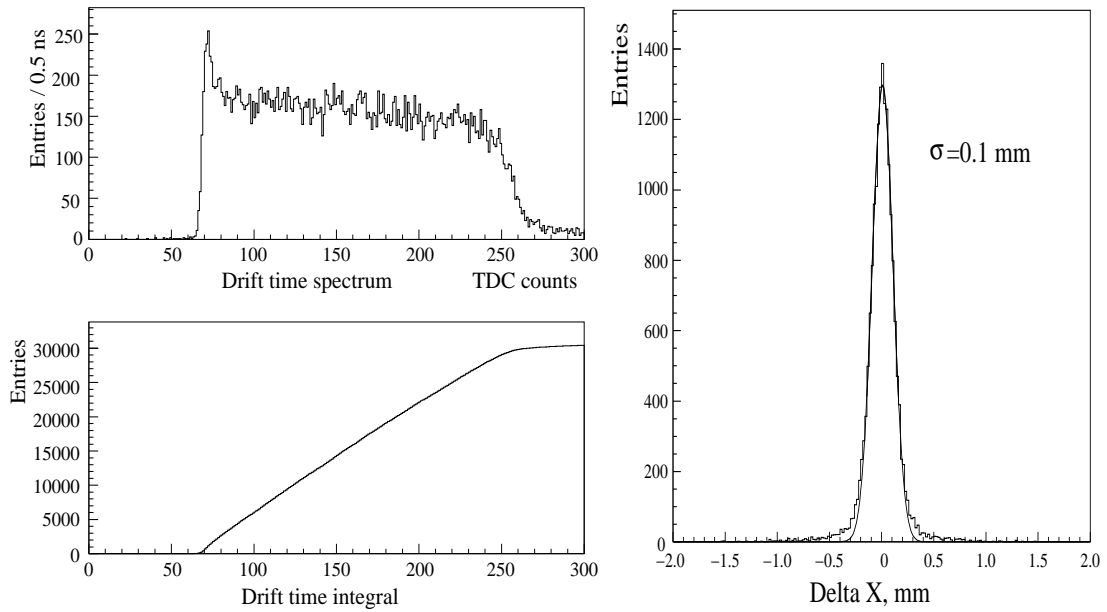


Figure 1.15: *Distribution of the drift time (left upper) and its integral spectrum (lower), horizontal scale is in TDC channels, bin width is 0.5 ns. On the right-hand side distribution of differences between the measured and predicted X-coordinate is displayed. Plots from X4 plane.*

Coordinate resolution of the DC system is illustrated too in Fig.1.15, where the distribution of differences between the predicted position and measured coordinates in one of the planes is shown (X4-plane right arm). The measured standard deviation, $\sigma = 100 \mu\text{m}$, is defined not only by the intrinsic chamber plane resolution, but also by the accuracy of the predicted track coordinates. Taking the latter into account the measured intrinsic space resolution of one plane is better than $90 \mu\text{m}$.

1.7.6 Time-of-Flight detector

A hodoscope system consisting of vertical and horizontal scintillation slabs has been placed downstream the drift chambers. It has the overall purpose of providing fast coincidence signals between both spectrometer arms, necessary

for the first level trigger and for events selection.

The vertical array of scintillation counters is used, in correlation with other detectors, in the definition of dedicated triggers for calibration purposes and of a higher level trigger for the selection of low Q events (see trigger section). A key function of this detector, which motivated a special design, is to provide a very accurate time definition of pion pairs originated from the same proton interaction (**prompt** pairs), in order to perform a clean separation (in off-line analysis) with respect to pairs in which the pions are produced at different times (**accidental** pairs). Used as a time-of-flight detector it allows to identify $p\pi^-$ pairs in prompt events, as they might constitute a significant source of background to the $\pi^+\pi^-$ signal.

The TOF detector (also called VH) consists of two identical telescopes matching the acceptance of the DC system. Each telescope contains an array of 18 vertical scintillation counters. The slab dimensions are 40 cm length, 7 cm width and 2.2 cm thickness. Scintillation light is collected at both ends by two 12-dynode Hamamatsu R1828-01 photomultipliers coupled to fish-tail light guides. The front-end electronics was designed to minimise the time jitter, providing a position independent time measurement.

The VH single-hit detection efficiency is 99.5% for the positive, and 98.8% for the negative hodoscope arms. In Fig.1.16 the distribution of the time difference between positive and negative pions in the spectrometer is shown. The observed ratio between prompt and accidental pairs in the 2σ cut region around the peak is about 16. The overall time resolution of the system has been measured with e^+e^- pairs to be 127 ps per counter [49], which corresponds to 174 ps accuracy for the time difference between positive and negative arms (time-of-flight resolution). The latter is shown in Fig.1.17. The dedicated e^+e^- calibration trigger selects e^+e^- pairs from γ conversions and Dalitz decays of π^0 which are almost synchronous in time, as the time of flight of e^+e^- pairs is momentum independent in the available setup range of momenta.

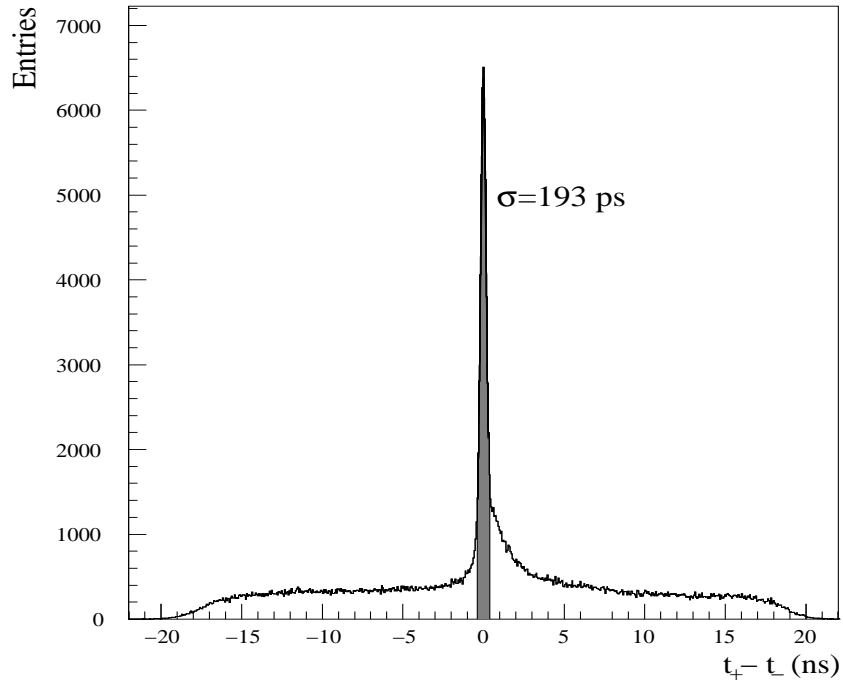


Figure 1.16: Time difference between charged positive and negative particles obtained from standard hadron trigger data. The central peak has a gaussian width of 193 ps, and the shaded area represents a 2σ cut used to select prompt $\pi\pi$ events. The flat background is originated from accidental pairs, not belonging to the same beam interaction. Note the shoulder on the right-hand side of the peak, due to π^-p prompt pairs.

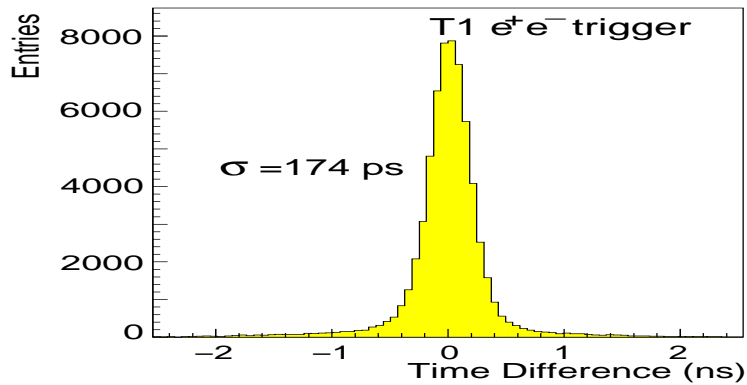


Figure 1.17: Time difference spectrum for e^+e^- pairs detected by the vertical hodoscopes, after path length correction. Data come from e^+e^- triggers.

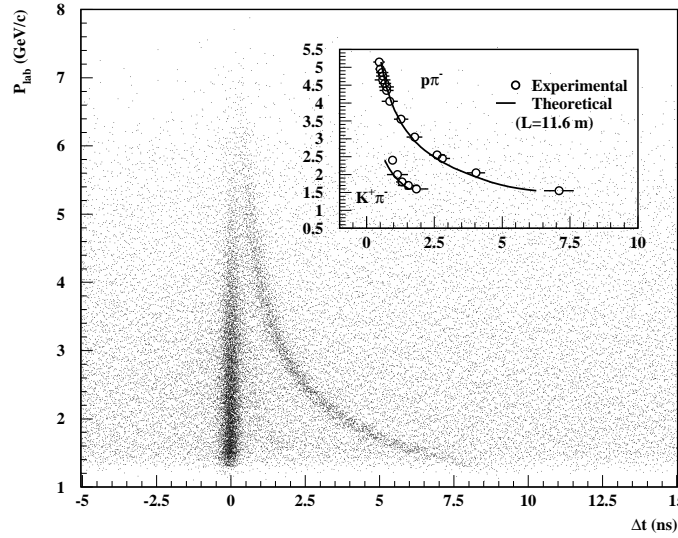


Figure 1.18: Correlation between the measured momentum of the positive particle and the VH time difference between the positive and negative spectrometer arm, taking into account the correction for the difference in path length. The accumulation bands correspond to $\pi^- \pi^+$ (vertical band) and $\pi^- p$ (curved band) pairs.

This timing capability allows to separate $\pi^+ \pi^-$ from $\pi^- p$ pairs in the momentum range from 1 to 5 GeV/c, and from $\pi^\mp K^\pm$ pairs in the range from 1 to 2.5 GeV/c, as illustrated in Fig.1.18.

1.7.7 The Horizontal Hodoscopes

The horizontal hodoscope system has a similar design and implication on the definition of the first level trigger as VH. Its response is used to apply a coplanarity criterion for triggering pairs hitting both detector arms. This trigger requirement selects oppositely charged particles with relative vertical displacement, Δy , less than 7.5 cm. Its response is used to select events with small relative angle in the Y direction, and to support the reconstruction with spatial track information.

It is also separated into two arms, each covering an area of $40 \times 130 \text{ cm}^2$. Each hodoscope consists of 16 horizontal extruded scintillating slabs of dimensions $130 \times 2.5 \text{ cm}^2$, with a thickness of 2.5 cm. Both ends of each slab are coupled to specially shaped light-guides.

Photomultipliers are equipped with a voltage divider allowing high counting rate capability. Front-end electronics system is the same as those for the vertical hodoscopes. The single hit detection efficiency of HH is greater than 96.6 % on both arms, and the time resolution is 320 ps.

1.7.8 The Cerenkov Counters

It provides the strong e/π separation capability needed by the experiment. This detector is essential for rejection of the main background of electron-positron pairs from photon conversion, Dalitz pairs, and to a minor extent from resonance decays. It is used in the first level $\pi^+\pi^-$ main trigger, in the calibration trigger to select e^+e^- pairs and its signals are available for offline analysis.

The Cerenkov radiation occurs when the velocity of charged particle exceeds the velocity of light in a dielectric medium, and it polarizes atoms resulting in emission of coherent radiation. DIRAC's Cerenkov detector is structured in two identical threshold Cerenkov counters [50], each covering one spectrometer arm (Fig.1.19). The gas radiator is enclosed in a volume with dimensions $143 \times 56 \text{ cm}^2$ and $336 \times 96 \text{ cm}^2$, respectively. The chosen radiator is N_2 at normal temperature and pressure ($\theta_c = 1.4^\circ$) and the counter length is 285 cm. Each counter is equipped with 20 mirrors and 10 photomultipliers on two rows. Cerenkov light reflected by pairs of adjacent mirrors is focused onto the same photomultiplier. The analog signals from PM are fed into two custom-made summing modules, discriminated and used for trigger purposes.

A single photoelectron peak is clearly observed in all channels and it is shown in Fig.1.20, where we can see the ADC spectra from pions(a) and from single electrons(b). The number of photoelectrons detected by one counter arm is shown in Fig.1.21, and from it we infer that both counters have an efficiency greater than 99.8 % when operated at a threshold slightly

less than 2 photoelectrons. The pion contamination above the detection threshold is estimated to be less than 1.5 %. Such contamination arises from pions with momenta above the cerenkov threshold and from accidental coincidences occurring within the trigger time-window.

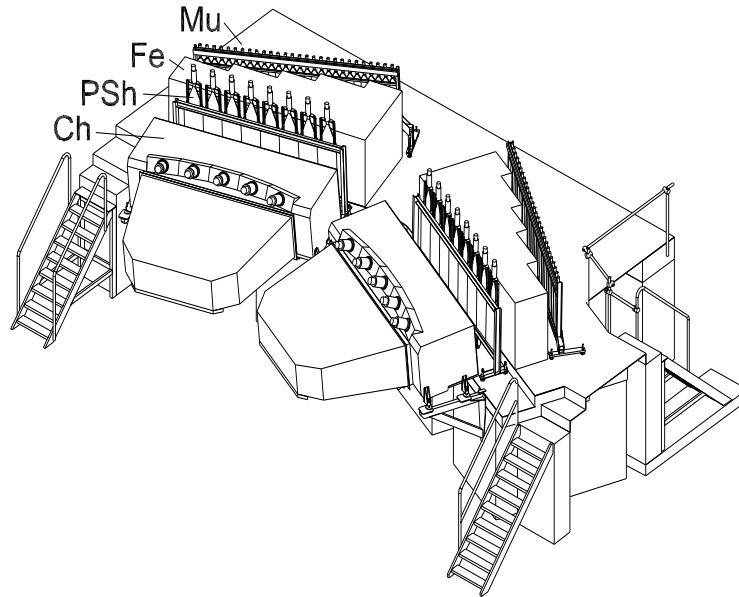


Figure 1.19: The far end part of the DIRAC setup, comprising threshold cerenkov counters (Ch), preshower detector (PSh), iron absorber (Fe) and muon counters (Mu).

1.7.9 The Preshower and Muon Detectors

The purpose of the Preshower detector is two-fold: it provides additional electron/pion separation power in the off-line analysis and it is used in the trigger generating logic as well (T1).

The PSH is based on an array of lead converters followed by scintillation detectors [51]. Electrons (positrons) initiate in the converters electromagnetic showers which are sampled in the scintillation counters while pions be-

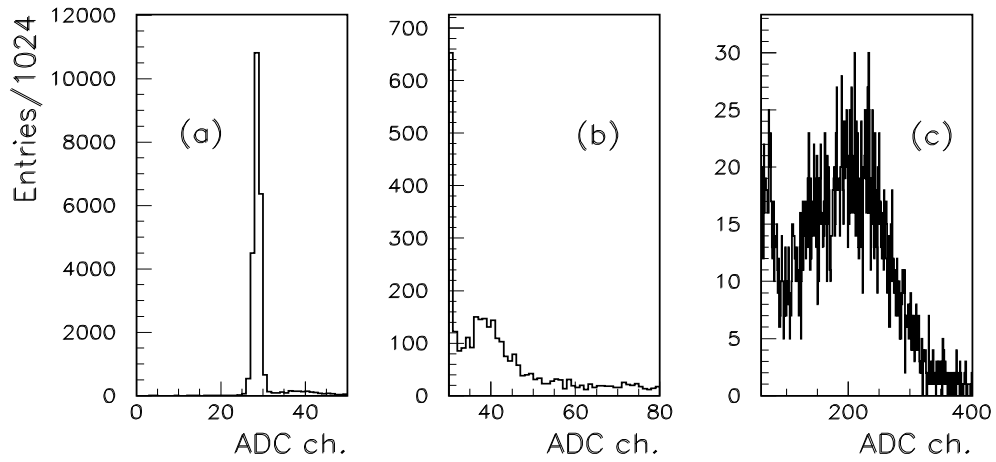


Figure 1.20: ADC spectrum from one cerenkov photomultiplier: (a) spectrum from pions (practically equal to the ADC pedestal distribution), (b) amplitude signal from single photoelectron, (c) spectrum from electrons.

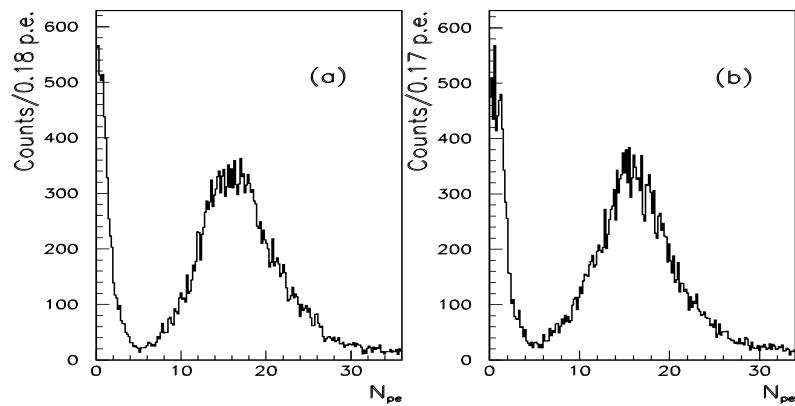


Figure 1.21: Distribution of the number of photoelectrons detected from the (a) positive and (b) negative cerenkov detector arms.

have mainly as minimum ionising particles. For trigger purposes, the signal has to be produced whether a pion or an electron cross a PSH counter.

The PSH consists of 16 detector elements placed symmetrically in two arms, as seen in Fig.1.19. Each element has a Pb converter and a scintillation counter. The converters of the two outermost elements of each arm (low momentum region) are 10 mm thick, whereas the rest are 25 mm thick (around 2 and 5 units of radiation length, respectively). The scintillator slab dimensions are $35 \times 75 \text{ cm}^2$ and 1 cm thickness. The detector signals are linearly split into two branches, one used for trigger purposes and another for ADC analysis. In the former, a leading edge discriminator is used with a threshold corresponding to efficient detection of minimum ionising particles.

The single arm detector efficiency is 99.5% for pions.

Admixture of decay muons in the $\pi\pi$ events can be a serious source of background. For this reason a muon detection system is implemented to provide efficient muon tagging in off-line analysis. Muons come almost entirely from pion decays with a small admixture from other decays and direct $\mu^+\mu^-$ pair production.

The muon detector consists of a double layer structure of scintillation counters (28 counters with equal scintillating slabs of $75 \times 12 \text{ cm}^2$ front area and 0.5 cm thickness per arm) placed behind a thick (from 60 to 140 cm, see Fig. 1.19) iron absorber which almost entirely absorbs hadrons and related hadronic showers. The thickness is larger in the region close to the spectrometer symmetry axis, in order to compensate for the harder pion momentum spectrum. This detector is placed at the downstream end of the DIRAC apparatus, few meters from the intense primary proton beam dump. As a result, the muon scintillation counters may undergo a high flux of background radiation from the beam dump area, which has required a special design of the counter arrays and electronics.

To reduce this background, data from muon detector are read out only if simultaneous signals from a pair of corresponding counters in the two layers are detected.

Off-line use of muon counters has been chosen to avoid suppression of useful pion events on-time with background signals in this detector. From experimental data we have inferred that the fraction of events containing at

least one muon is about 10% [52].

1.8 Trigger system

The trigger system was designed to provide a reduction of the event rate to a level acceptable to the data acquisition system which is around 700 events/spill. Pion pairs are produced in the target mainly in a free state with a wide distribution over their relative momentum Q , whereas atomic pairs from $A_{2\pi}$ disintegration have very low Q , typically below $3 \text{ MeV}/c$. The on-line data selection rejects events with pion pairs having approximately $Q_L > 30 \text{ MeV}/c$ or $Q_T > 10 \text{ MeV}/c$, keeping at the same time high efficiency for detection of pairs with Q components below these values.

A sophisticated multilevel trigger is used in DIRAC [53]. It comprises a very fast first level trigger and two higher level trigger processors.

Due to the requirements of the data analysis procedure, to the on-line selection of time correlated (prompt) pion pairs, is added a large number of uncorrelated, accidental, pion pairs. The statistical error of the $A_{2\pi}$ lifetime measurement depends on the number of both prompt and accidental detected pairs so events are collected inside a coincidence time window ($\pm 20 \text{ ns}$) between the times measured in the left (VH1) and right (VH2) vertical hodoscopes, centered around the peak of prompt events

A block diagram of the trigger architecture is presented in Fig.1.22. At first, pretrigger T0 starts DNA and the first level trigger T1 starts digitisation of the detector signals in the data acquisition (DAQ) modules (ADC, TDC, etc.). A positive response from T1 starts a powerful drift chamber trigger processor T4. At the next level the neural network trigger DNA/RNA rejects the events with high Q values, and a positive decision from it in coincidence with positive decision of T1 is used again in coincidence with T4 decision, which imposes additional constraints to the relative momentum and takes the final decision to accept or to reject the event, start the readout of all electronics or clear the buffer.

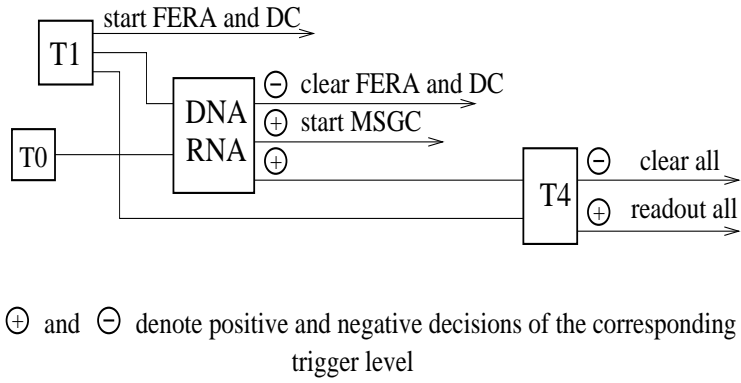


Figure 1.22: General block diagram of the DIRAC multilevel trigger.

In addition to the main trigger designed to detect pionic atoms, several calibration triggers are run in parallel.

1.8.1 First level trigger (T1)

The first level trigger (a detailed description is given in [54]) fulfils the following tasks:

- Selects events with signals in both detector arms.
- Classifies the particle in each arm as π^\pm or e^\pm depending on the presence of the cerenkov counter signal. Protons, kaons and muons are equally included in the “pion” class (the discrimination is done offline). For the pion signature $\pi^+\pi^-$ signature is needed a coincidence of a hit in VH, HH, no signal in Cerenkov counters and a signal coming from PSH in arm i :

$$(VH_i \cdot HH_i \cdot \overline{C}_i \cdot PSH_i)$$

Meanwhile for e^+e^- signal in Cerenkov is required:

$$(VH_i \cdot HH_i \cdot C_i \cdot PSH_i)$$

The signal from both arms are combined to produce the final decision

- Arranges the coincidences between the signals detected in the two arms with a $\pm 20\text{ns}$ time window in Vertical Hodoscopes.
- Applies a coplanarity (Copl) criterion to particle pairs: the difference between the hit slab numbers in the horizontal hodoscopes in the two arms (HH1 and HH2) should be ≤ 2 . This criterion forces a selection on the Q_y component of the relative momentum and provides a rate reduction by a factor of 2.
- Selects in parallel events from several physics processes needed for the setup calibration with desired rate: e^+e^- pairs, Λ decaying into a proton and a negative pion (see chapter 7), K^\pm decays to three charged pions.

The electronics of T1 gives a decision within 120ns. For Ni-2001 data physical pion trigger is set to $(T1 \cdot \pi^+ \pi^- \cdot \text{Copl})$.

1.8.2 Drift chamber processor (T4)

T4 is the final trigger stage and it requires DNA positive as input. T4 processor reconstructs straight tracks in the X-projection of the drift chambers which allows to select pairs with low relative momentum (the algorithm is described in [53]). The block diagram of the T4 operation is shown in Fig. 1.23. The drift chamber processor includes two stages: the track finder and the track analyser.

The **track finder** the hit wires information from all DC X-planes (drift time values are not used in the T4 logic). For each combination of hits in two edge base planes defines hit windows for the intermediate planes and number of hits inside it are counted and EXIGED bigger than 4. An identical processor is used for each arm.

If tracks are found in both arms, the **track analyser** continues the event evaluation. Track candidates are compared with the contents of a look-up memory table obtained with Monte Carlo methods containing all possible combinations of track identifiers for pion pairs with $Q_L < 30 \text{ MeV}/c$ and $Q_x < 3 \text{ MeV}/c$ and allows the start of data transfer to VME if a coincidence is found.

The T4 decision time depends on the complexity of the event and is around $3.5 \mu\text{s}$ on average, being forced a positive response if time exceeds a limit in order to reduce dead-time. The rejection factor of T4 is around 5 with respect to the T1 rate and around 2.5 with respect to DNA/RNA, and efficiency for $Q < 30 \text{ MeV}/c$ exceeds 99%.

The whole trigger system is fully computer controlled: no hardware intervention is needed in order to modify the trigger configuration. With all selection stages enabled the event rate at the typical experimental conditions is around 700 per spill, that is well below the limits of the DAQ rate capability, calibration triggers being 7%.

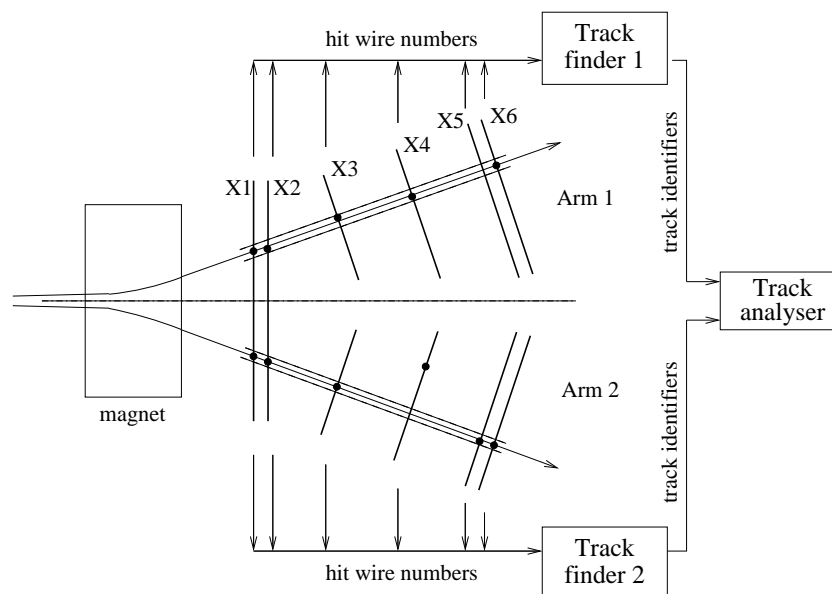


Figure 1.23: T4 operation block diagram. Only the drift chamber X-planes involved in T4 are shown.

1.8.3 Trigger performances

The performance of the trigger system as a whole in selecting low- Q events is illustrated in Fig 1.24, where the magnitude of relative momentum of pion pairs Q is shown (in their center-of-mass frame), after DNA/RNA and T4 trigger selection (see trigger section). Trigger efficiency as function of Q is flat in the low- Q region, as illustrated in Fig. 1.24. This is considered an important figure of merit of the spectrometer, for a precision study of the $\pi^+\pi^-$ Coulomb interaction.

Pions from ionisation of pionium entering the apparatus have momenta below 4 GeV/ c . The apparatus momentum acceptance for time-correlated pairs is flat for pions with momenta between 1.6 GeV/ c and 3 GeV/ c , and it decreases for higher momenta.

For the sake of completeness we also show the P and P_T distributions for a single π^- in Fig. 1.25, with superimposed a parameterisation of the inclusive yield based on the analytic representation [55], adapted to DIRAC center-of-mass energy ($\sqrt{s}=6.84$ GeV) [56].

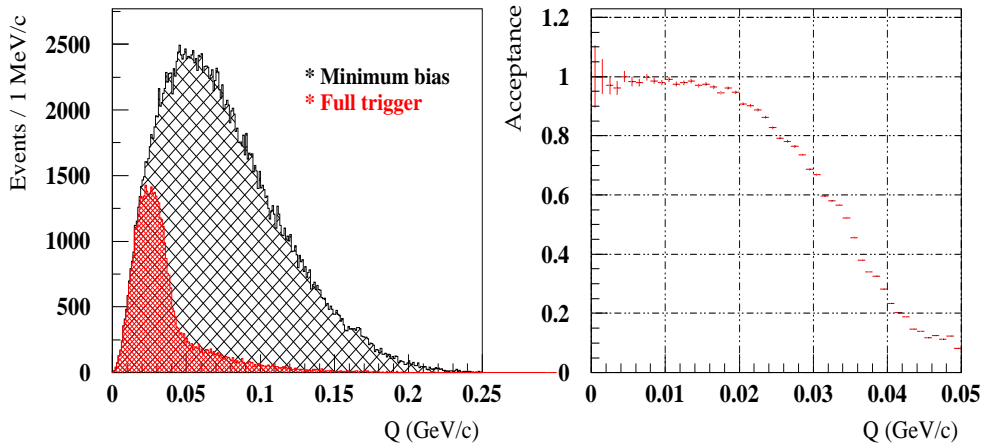


Figure 1.24: Left: Distribution of Q for accepted $\pi^+\pi^-$ pairs after the full DIRAC trigger system, and for minimum bias pairs. Right: trigger acceptance, determined as the ratio between the previous two distributions.

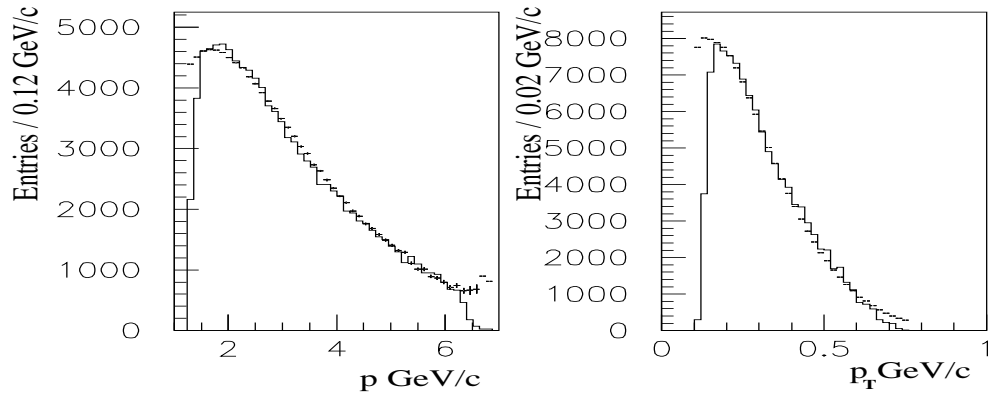


Figure 1.25: Experimental P and P_T distributions of π^- corrected for apparatus acceptance (histogram) with superimposed the results of the parameterisation [55][56].

1.9 Analysis method

1.9.1 Data selection

The analysis presented in this thesis has used the standard pre-selection procedure described in <http://dirac.web.cern.ch/DIRAC/pre-sel.html>, for 2002 and 2003 Ni target events. The cuts introduced in this filtering procedure do not produce any significant bias in the shape of two-pion Coulomb interaction spectrum, further than shrinking the Q_T distribution to an approximate cut of $Q_T < 6 \text{ MeV}/c$. In particular, they are sufficiently general not to introduce bias in upstream detector multiplicities.

The main use of this pre-selection stems from the strong data reduction, which facilitates data processing through multiple iterations. This is of course at the cost of having a slightly reduced span in the description of the Q_T spectrum of Coulomb interaction background. As we shall see, the Q_L spectrum will effectively provide a sufficient constraint, in a two-dimensional fit.

1.9.2 Reconstruction method

Pions are reconstructed according to the method described and evaluated in [6][57], which is a switchable option of the standard ARIANE program. This method has the distinct feature of having independent tracking in the upstream and downstream arms. This becomes possible when the full upstream spectrometer information is used, consisting (in 2002 and 2003) of 11 detector layers of MSGC/GEM (4), Scintillation Fibre Detector (SFD) (3), and Ionisation Hodoscope (IH) (4)[41]. In this region stray fields are negligible, so straightline fitting allows unambiguous reconstruction of pion pairs pointing to the beam intersection with the target. In a high radiation environment, this is important. The opening angle is then determined with very high precision, only limited in practice by multiple scattering inside the target foil, therefore Q_T resolution is excellent. Charge confusion is inevitable at very low opening angles (due to limited angle resolution in DC track extrapolation through the dipole magnet), but the sign of Q_T is not an objective of the experiment, since charge-conjugation symmetry is taken for granted in pion-pion interaction.

Upstream tracks make use of stereo angles of 4 MSGC/GEM detectors, in conjunction with TDC information from extrapolated X or Y SFD hits. As a consequence, they have a well defined time tag, which reduces the noise from out-of-time MSGC hits to a small amount.

As mentioned, upstream track pairs are matched with DC tracks in order to determine the correct charge assignment. Matching efficiency is uniform over detector acceptance, and it exceeds 95% everywhere [6] [57] [58]. Time information is used as part of the matching procedure. Pulse-height in IH is calibrated with single and double upstream tracks. Double ionisation signal is required in this detector to identify pion pairs, when only a single unresolved track can be matched to DC tracks.

In order to improve precision and minimize the effect of multiple scattering in the break-up probability measurement, only the signals from MSGC/GEM detector are used in the final track re-fit [58].

Standard cuts for muon background rejection using muon counters and pre-shower detector (PSH) are applied, and PSH pulses have been analysed

to cross-check and improve Cherenkov veto efficiency.

1.9.3 Monte Carlo simulation

In order to achieve the most accurate extrapolation of Coulomb interaction down to very small values of Q , we have chosen Monte Carlo simulation as the simplest analysis procedure. In addition, 50 % of the experiment DAQ was designed to collect accidental pairs, which were used in this analysis to perform trigger acceptance corrections to Q_L spectrum.

It should be understood that the use of Monte Carlo is entirely restricted to the description of experimental resolution, and by no means it implies specific model assumptions about proton-nucleus physics. In particular, Coulomb interaction is described by the Gamow enhancement of their Q -space wavefunctions. Even with the excellent time-of-flight resolution of the spectrometer, a non-Coulomb background remains in prompt-pair event selection. It consists of accidental pairs and other long-lifetime decays. Both are described by Monte Carlo, where pion pairs are simulated isotropically in their center-of-mass frame, and the Coulomb factor is removed [59].

The input lab-frame pion momentum spectrum p is actually taken from real spectrometer data. For this purpose, a de-convolution of the reconstructed prompt pair spectrum E as function of p and θ_b (angle with respect to the proton beam) is performed, according to the expression:

$$G_1(p, \theta_b) = \frac{E(p, \theta_b)}{\epsilon(p, \theta_b)} \frac{1}{A_C(Q)}$$

where $A_C(Q)$ is the Coulomb factor and the acceptance function ϵ is evaluated by Monte Carlo as follows :

$$\epsilon(p, \theta_b) = \frac{R(p, \theta_b)}{G_0(p, \theta_b)}$$

where R is the Monte Carlo reconstructed output for a given generator input G_0 . The procedure was iterated only once, and G_1 taken as final generator input. The acceptance function matrix $\epsilon(p, \theta_b)$ does not appear to depend significantly on G_0 . Two different G_1 functions were determined,

one for prompt events and another for accidental pairs. The latter (obtained with $A_C(Q) = 1$), is used for simulation of the accidental pair background in prompt events. Their corresponding spectra $E(p, \theta_b)$ do differ significantly, mainly due to the proton background which is present in accidental pairs. In fact, this point has been verified following the procedure outlined in reference [60] for 2001 data.

GEANT tracking is performed by the GEANT-DIRAC program [61] with standard geometry and detector files, but with modified average multiple scattering angle according to the chapter 4 in this thesis. GEANT detector digitisations were performed by ARIANE program [62]. The procedure for MSGC cluster patterning uses real data input to describe correlations between cluster total charge, micro-strip multiplicity and differential charge. Input data were selected to correspond to 2001 runs specifically.

Simulation of out-of-time noise hits in MSGC detectors is done by reproducing the experimentally observed characteristics of this background, namely:

- existence of significant hit multiplicity correlations from plane to plane (4 detectors), which are encoded by specific arrays determined from real data.
- absence of space correlations between different planes, once the two $\pi^+\pi^-$ triggering tracks are removed, thus indicating this background essentially originates from wide angle tracks with respect to the beam direction.

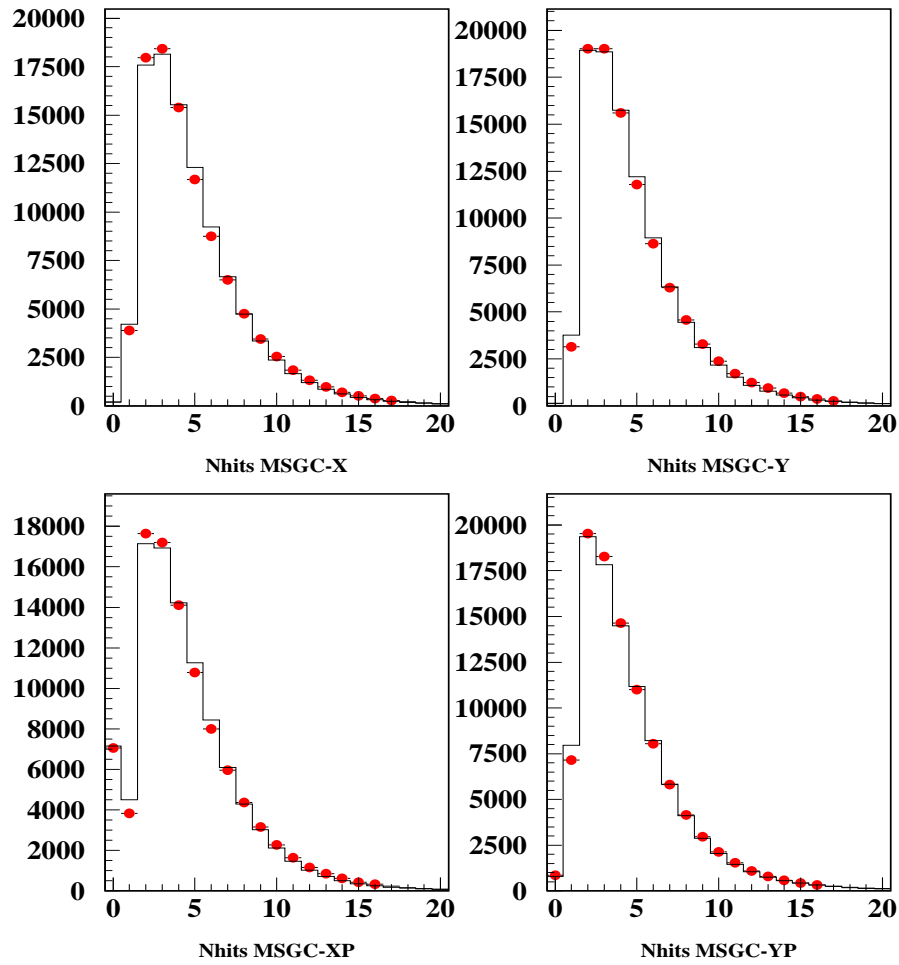


Figure 1.26: *Number of MSGC clusters found close to any of the drift chamber tracks, including the real signal pairs (dots), compared to Monte Carlo simulation (line). Detector ordering is X/Y (top left/right) and X' / Y' (bottom left/right). All data runs used in lifetime analysis were included.*

In figure 1.26 we compare the observed MSGC hit multiplicity distributions for each detector with Monte Carlo simulation. Only hits (real or

background) found within a momentum-dependent $\pm 3\sigma$ space window from a drift chamber track are retained. As it can be appreciated, MSGC background is perfectly well described.

A delicate challenge to the DIRAC reconstruction procedure arises from the response of Peak Sensing Circuit (PSC) electronics of the scintillation fibre detector, when two pulses arrive in strict time coincidence (prompt pairs) and within a given 8-channel group. In this case, suppression of one of the pulses occurs with a significant probability, at the level of 20-40% [41]. The distortion caused by this effect in close-pair efficiency at small distances (below 3 mm) is largely diminished when the previously described upstream tracking is used, where only one SFD hit (in X or Y projection) is required to perform time tagging, the track being actually measured by MSGC hits having stereo angles.

1.9.4 Analysis of Q-spectrum

A two-dimensional analysis of $\pi^+\pi^-$ spectrum in the center-of-mass frame has been carried out, choosing the transverse $Q_T = \sqrt{Q_X^2 + Q_Y^2}$ and longitudinal $Q_L = |Q_Z|$ components (with respect to the pair direction of flight Z) as independent variables. This analysis has been done independently at ten individual $600\text{MeV}/c$ bins of the laboratory-frame momentum p (magnitude of 3-vector sum of pion momenta p_1 and p_2), and also globally including all values of p in the same fit. The results will be presented in sections 6 and 7. Irrespective of the parameter variation strategy, or of the momentum definition followed in each case, the prompt two-pion spectrum in (Q_T, Q_L) plane has been χ^2 -analysed by comparison with the following input spectra:

- Monte Carlo describing the Coulomb final-state interaction by means of the Sakharov-Gamow-Sommerfeld factor (labelled CC), using single pion lab-frame momentum from de-convoluted prompt spectrometer data.
- Monte Carlo describing accidental coincidences taken by the spectrometer (labelled AC). It represents the uncorrelated non-Coulomb background in prompt events. Its laboratory momentum spectrum has

been generated according to that of true accidental pairs taken by the spectrometer, after de-convolution of detector acceptance. Its fraction has been determined from the time-of-flight (TOF) spectrum in each momentum bin, and the values obtained are represented in figure 1.27

- Monte Carlo describing Coulomb non-interacting $\pi^+\pi^-$ (labelled NC). It simulates accidental pairs as well as any additional fraction of non-Coulomb events where one of the pions originates from decay of long-lifetime resonances (up to ns scale). Such events are still detected as time-correlated by the precision coincidence of the spectrometer. We assume they have a strictly isotropical distribution in their center-of-mass frame. Their lab-frame momentum spectrum (entirely decoupled from Q-space) is also taken from spectrometer data.
- Pionium atom Monte Carlo model [59], which is used to cross-check and fit the observed deviation with respect to the continuum Coulomb background spectrum constructed from the previous input (it is labelled AA)

The total number of events used from the above samples are denoted by N_{CC}, N_{AC}, N_{NC} and N_{AA} respectively, whereas N_p represents the total number of prompt events in the analysis, under the reference cuts $Q_T < 5MeV/c$ and $Q_L < 20MeV/c$. Index k runs over all (i, j) bins of the (Q_T, Q_L) histograms, and we denote by N_{CC}^k the number of Coulomb events observed in each particular bin (i, j) . Similarly for the other input spectra, namely N_{AC}^k, N_{NC}^k and N_{AA}^k . The χ^2 analysis is based upon the expression:

$$\chi^2 = \sum_k \frac{\left(N_p^k - \beta(\alpha_1[\epsilon \frac{N_{KK}^k}{N_{KK}} + (1 - \epsilon) \frac{N_{CC}^k}{N_{CC}}] - \alpha_2 \frac{N_{AC}^k}{N_{AC}} - \alpha_3 \frac{N_{NC}^k}{N_{NC}} - \gamma \frac{N_{AA}^k}{N_{AA}}) \right)^2}{N_p^k + \beta^2(\alpha_1^2[(1 - \epsilon)^2 \frac{N_{CC}^k}{N_{CC}^2} + \epsilon^2 \frac{N_{KK}^k}{N_{KK}^2}] + \alpha_2^2 \frac{N_{AC}^k}{N_{AC}^2} + \alpha_3^2 \frac{N_{NC}^k}{N_{NC}^2} + \gamma^2 \frac{N_{AA}^k}{N_{AA}^2})} \quad (1.20)$$

where α_i and γ are the respective Monte Carlo type fractions (according to $\alpha_1 + \alpha_2 + \alpha_3 + \gamma = 1$), and *epsilon* is the fraction of K^+K^- contamination. We call $Q_L < 2MeV/c$ the extrapolation region. A control region is defined by the domain under the cut $Q_L > 2MeV/c$, where we do not expect

deviations with respect to the continuum Coulomb interaction background. We call $Q_L < 2MeV/c$ the extrapolation region.

Subtraction of accidental pairs is performed by blocking the α_2 parameter to the experimentally observed values. Minimisation of the above χ^2 over the entire (Q_T, Q_L) plane determines the non-Coulomb fraction α_3 , and the atom fraction γ as free parameters. The β parameter, which represents the overall Monte Carlo normalisation, is actually determined by the number of prompt events in the domain under fit, and it does not need to be varied.

Once the previous fit has converged, we define the atom signal in each (i, j) bin as the difference between the prompt spectrum (after subtraction of accidentals) and the Monte Carlo with the pionium component (AA) removed. This 2D signal, which reveals the excess with respect to the calculated Coulomb interaction enhancement, is analysed in detail in sections 6 and 7, where it is compared with the Monte Carlo prediction for atom production. Further χ^2 tests are performed both in the $Q_L > 2MeV/c$ (control region, where pionium Monte Carlo does not contribute) and in the $Q_L < 2MeV/c$ (extrapolation region) separately.

1.9.5 Accidental pairs

The fraction of accidental pairs (α_2 in the fit) inside the prompt coincidence has been experimentally determined, from analysis of the precision TOF spectrum. It was determined as function of the pair momentum, and separately for 2002 and 2003 data, and the results are given in table also the 2001 data are given. Nevertheless, it should be noted that the sum $\alpha_1 + \alpha_2$ (non-Coulomb fraction) is left as a free parameter in the fit (table 1.2). For the sake of reference, also the 2001 data are given.

The Vertical Hodoscope resolution remained approximately constant for the experiment's lifetime, however amount of background increased in 2002 and 2003, probably due to the effect of increased average beam intensity.

Table 1.1: Numerical values of K^{th} as defined in the text. Each row corresponds to a given rectangular cut in (Q_T, Q_L) plane, with $Q_T^c = 5\text{MeV}/c$ and $Q_L^c = 20\text{MeV}/c$ being the reference cut values. K^{th} values are obtained by integration of (1.21) in cylindrical coordinates.

$Q_L^{cut}(\text{MeV}/c)$	K^{theo}
0.5	0.4372
1.0	0.2389
1.5	0.1669
2.0	0.1300
$Q_T^{cut}(\text{MeV}/c)$	K^{theo}
0.5	3.2457
1.0	1.2382
1.5	0.6995
2.0	0.4674
2.5	0.3426
3.0	0.2660
3.5	0.2147
4.0	0.1781
4.5	0.1509
5.0	0.1300

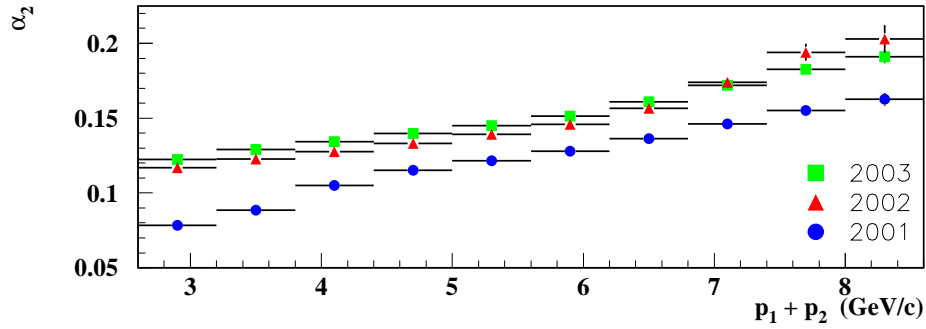


Figure 1.27: *Accidental pair fractions in table 1.2 as function of pair momentum.*

Table 1.2: *Accidental pair contamination inside the prompt coincidence , as determined from analysis of the TOF spectrum. Data are given for each datataking year.*

	p (GeV/c)	% 2001	% 2002	% 2003
p_1	2.6 - 3.2	0.0783 ± 0.0007	0.1225 ± 0.0006	0.1169 ± 0.0011
p_2	3.2 - 3.8	0.0886 ± 0.0007	0.1289 ± 0.0007	0.1228 ± 0.0013
p_3	3.8 - 4.4	0.1051 ± 0.0007	0.1343 ± 0.0006	0.1276 ± 0.0010
p_4	4.4 - 5.0	0.1152 ± 0.0008	0.1397 ± 0.0006	0.1332 ± 0.0012
p_5	5.0 - 5.6	0.1216 ± 0.0009	0.1451 ± 0.0008	0.1391 ± 0.0015
p_6	5.6 - 6.2	0.1281 ± 0.0010	0.1513 ± 0.0009	0.1460 ± 0.0018
p_7	6.2 - 6.8	0.1362 ± 0.0014	0.1609 ± 0.0013	0.1565 ± 0.0024
p_8	6.8 - 7.4	0.1462 ± 0.0019	0.1720 ± 0.0018	0.1738 ± 0.0036
p_9	7.4 - 8.0	0.15525 ± 0.0027	0.1826 ± 0.0026	0.1940 ± 0.0057
p_{10}	8.0 - 8.6	0.1625 ± 0.0041	0.1909 ± 0.0042	0.2030 ± 0.0093

1.9.6 K-factors and break-up probability

The conversion from integrated atom production signal to break-up probability is done by means of the so-called K-factors, which are defined as follows.

Let us call $S_B(\Omega)$ the measured ratio between the number of atoms N_A and the number of Coulomb pairs N_C , both observed in the same kinematical region Ω of the (Q_T, Q_L) plane. This quantity can be converted into a measurement of the atom break-up probability P_{Br} , because the number of atoms n_A produced in a given phase-space volume can be calculated analytically in quantum mechanics [63] according to :

$$K^{th} = \frac{n_A}{N_C} = 8\pi^2 Q_0^2 \frac{\sum_1^\infty \frac{1}{n^3}}{\int A_C(Q) d^3Q} \quad (1.21)$$

where the integral in the denominator extends over the desired Q-space volume. $Q_0 = \alpha M_\pi$ is two times the atom Bohr momentum p_B , and n its principal quantum number. For the sphere of radius $Q < Q_c$ the following expression is obtained:

$$K^{th}(Q_c) = \frac{n_A}{N_C} = \frac{\sum_1^\infty \frac{1}{n^3}}{\int_0^{Q_c/2p_B} \frac{kdk}{1-\exp(-2\pi/k)}}$$

For a rectangular domain Ω in the (Q_T, Q_L) plane, integration of (1.21) in cylindrical coordinates provides the values given in table 1.1.

However, the actual K-factor which must be taken into account in the measurement (K^{exp}) differs from K^{th} due to experimental resolution [64] [65] , which is a function of the domain Ω . The break-up probability is then determined as:

$$P_{Br} = \frac{S_B(\Omega)}{K^{exp}(\Omega)}$$

with the experimental K-factor defined in the following way:

$$K^{exp}(\Omega) = K^{th}(\Omega) \frac{\epsilon_A(\Omega)}{\epsilon_C(\Omega)}$$

where:

$$\epsilon_A(\Omega) = \frac{n_A^{rec}(\Omega)}{n_A^{gen}(\Omega)} \quad \text{and} \quad \epsilon_C(\Omega) = \frac{n_C^{rec}(\Omega)}{n_C^{gen}(\Omega)}$$

define the acceptance of the experimental apparatus as a whole for atoms and Coulomb pairs, respectively, in a given kinematical region Ω . The factors ϵ_A and ϵ_C are determined with high precision using separate Monte Carlo inputs, after processing the full simulation/digitisation/reconstruction chain. They are ratios between reconstructed output and generated input.

For a given momentum interval, the measured values of P_{Br} should not depend on the actual domain Ω which is chosen to perform the measurement, and this particular point will be studied in the following sections.

The K-factor values do however exhibit a momentum dependence, which we have analysed in detail, and it is indicated in table 1.3. These values have been taken into account in the determination of break-up probability in chapters 6 and 7.

Table 1.3: *K-factors determined in 10 intervals of laboratory-frame momentum.*

p interval (GeV/c)	K - factor
2.6-3.2	0.1140 ± 0.0005
3.2-3.8	0.1196 ± 0.0004
3.8-4.4	0.1267 ± 0.0005
4.4-5.	0.1316 ± 0.0005
5.-5.6	0.1368 ± 0.0007
5.6-6.2	0.1407 ± 0.0008
6.2-6.8	0.1431 ± 0.0011
6.8-7.4	0.1474 ± 0.0015
7.4-8.	0.1451 ± 0.0021
8.-8.6	0.1490 ± 0.0043

1.9.7 K^+K^- background

Since the publication of our measurement of ponium lifetime [66], we have investigated experimentally the possible presence of missidentified K^+K^- pairs in the $\pi^+\pi^-$ sample. Although the level of such contamination was expected to be very small [1], its importance stems from the fact that the Coulomb interaction is much stronger for K^+K^- than it is for $\pi^+\pi^-$, at the same value of Q . This is a consequence of the different Bohr radius in the Sommerfeld wave function (factor $A_C(Q)$). Our investigation proceeded in two steps. First, we determined the contamination fraction $r_K = K^+K^-/\pi^+\pi^-$ at low pair momentum ($p = 2.8 \text{ GeV}/c$) to be $r_K = (2.38 \pm 0.35) \times 10^{-3}$, by means of the TDC information of upstream detectors [67], using standard physics triggers. Secondly, we performed a new measurement at higher momentum using Λ triggers and high precision time-of-flight measurements from the Vertical Hodoscopes [68], which allowed us to determine the momentum derivative of r_K . In order to reach a better understanding of the momentum dependence of the K^+K^- signal, we examined in detail both the production of $K^\pm\pi^\mp$ and the semi-inclusive K^+K^- [68], which we compared with a specific Monte Carlo model, the UrQMD [69]. Very good agreement was found between our DIRAC data and UrQMD, particularly concerning the momentum dependence, as a result of our study. Certainly the result is much more constraining in the former case ($K^\pm\pi^\mp$), where we have very high statistics. It seems that the prediction of the momentum derivative is an easier task for Monte Carlo models than it is the strangeness (s, \bar{s}) yield itself. Therefore the extrapolation from $p = 2.9 \text{ GeV}/c$ to $p = 6.0 \text{ GeV}/c$ seems to be precise and reliable, when UrQMD Monte Carlo is used. In addition, of course, we have our experimental measurement at $p = 4.8 \text{ GeV}/c$ which comes to confirm that prediction.

Our basic approach has been to fully simulate the K^+K^- background as function of pair momentum, and include the simulated (Q_T, Q_L) spectrum in our standard χ^2 -analysis, as a modification of the Coulomb $\pi^+\pi^-$ spectrum. The term $\alpha_1 n_{CC}$ in expression (1) of reference [66] is replaced by the term $\alpha_1(\epsilon n_{KK} + (1 - \epsilon)n_{CC})$ where n_{KK} are the normalized spectra for K^+K^- . The fractions $\epsilon(p)$ are determined from our experimental mea-

surements, which follow the parametrization indicated in Fig. 1.28, which is taken from reference [68].

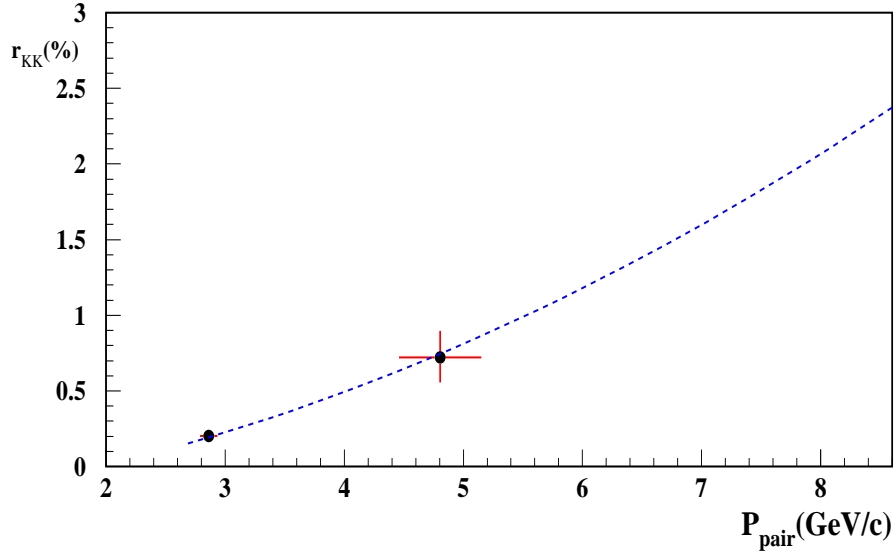


Figure 1.28: *Experimental measurements by DIRAC of the $K^+K^-/\pi^+\pi^-$ ratio r_{KK} at two different values of the average pair momentum, namely 2.9 GeV/c and 4.8 GeV/c. The UrQMD Monte Carlo prediction is shown as the dotted line, multiplied by a factor 0.37.*

Generation of K^+K^- pairs is achieved, in the center-of-mass frame, by means of the standard DIRAC atom pair generator [59] [70] after modification of the Bohr radius in the Coulomb factor. Pairs are then boosted into the DIRAC laboratory frame.

It should be noted that the experimental values of Q determined by the spectrometer (from the ARIANE program) are of course calculated under the $\pi^+\pi^-$ hypothesis, and are subject to the standard kinematical cuts implied by the trigger system. As a consequence, the Q range for the center-of-mass generator must actually be enlarged by nearly a factor 4, with respect

to the standard trigger cuts, in order to cover completely the spectrometer acceptance. This relativistic consideration enhances, in practical terms, the level of the contamination by nearly that factor.

As we will see in section 3 and 4, the χ^2 -analysis shows a significant improvement after the K^+K^- correction.

1.9.8 Q_L acceptance correction

Accidental pairs have been used to calibrate the spectrometer acceptance as function of Q_L , due to non-uniform trigger efficiency. The ratio R between Monte Carlo simulated non-Coulomb Q_L spectrum and that obtained from accidental pairs has been observed to be slightly non uniform. Since accidental triggers have undergone the same electronics readout chain as the prompt data, this ratio has been used as a correction factor to the Monte Carlo, in the analysis of Q_L spectrum. As it will be seen below, this is supported by the fact that the corrected results are in very good agreement with the analytical prediction based on the Sakharov factor for Coulomb pairs. This ratio R has been determined not only globally but also in each individual momentum interval. The correction has been smoothed by making linear or polynomial fits in the region $|Q_L| > 10MeV/c$, with results indicated in figure 1.29.

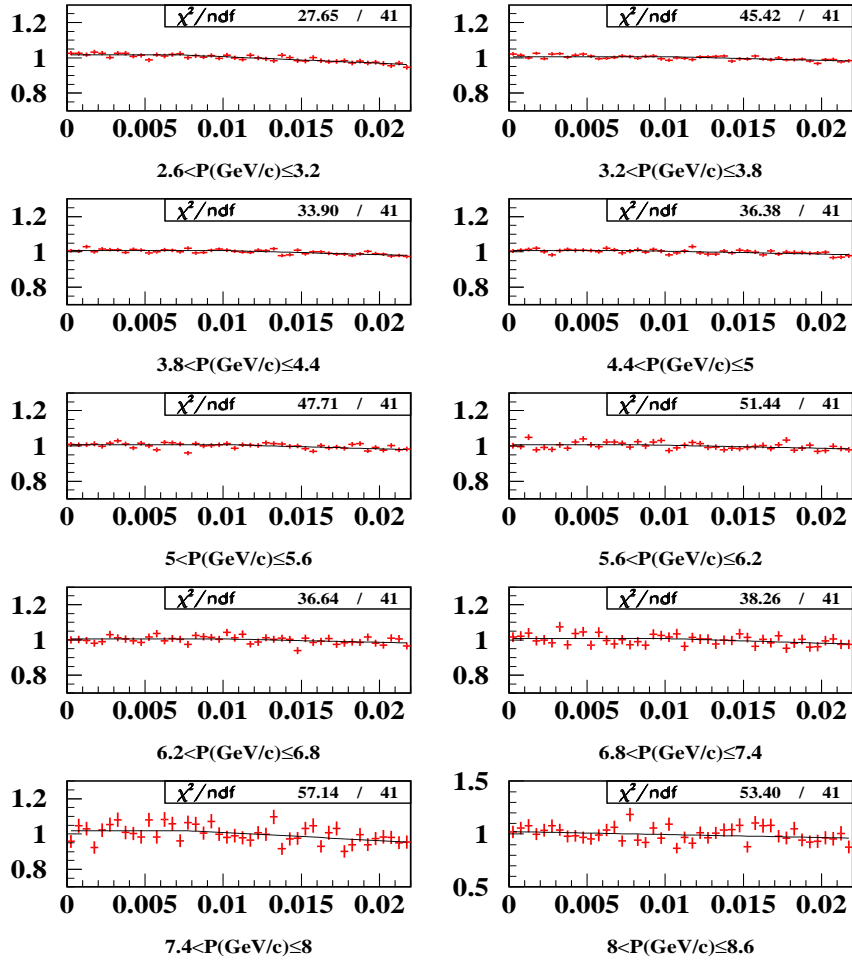


Figure 1.29: Ratio between non-Coulomb Monte Carlo and observed accidental Q_L spectrum in 10 different intervals of lab-frame momentum p

1.9.9 Target impurity correction

We analysed the existing data from the collaboration concerning measurements, as well as calculations, of the effect on the breakup probability of the

small impurity of the Ni target foil, from elements of lower Z values [71]. This work was used as the basis to perform a small (positive) correction to the lifetime, which had not been done before in our analysis.

For the sake of easy comparison, we present our correction by quoting the breakup probabilities (P_{Br}) that would have been obtained in a pure Ni target. An identical result for the pionium lifetime would be obtained, of course, if we retained our unambiguous measurement of P_{Br} and used the pionium propagation code in a contaminated target.

In order to check a possible dependence of the P_{Br} correction on the pair momentum p , a simulation was done using the propagation code [59] having Al as target foil material. The ratio between the two was plotted as function of p , and the observed slope was $0.05/GeV$. Given such small value, we consider a sufficiently good approximation to apply the same correction factor (1.014) in all momentum bins. When the experimental function $P_{Br}(p)$ is re-fitted to the Monte Carlo prediction, a lifetime increase $\Delta\tau = +0.10 fs$ is generically observed, very weakly dependent on the status of other corrections.

Chapter 2

Upstream Detectors Alignment

The method used in DIRAC to get the $|a_0 - a_2|$ measurement requires high accuracy in the relative pion momentum components in the center of mass system, and this only can be achieved after upstream detectors (MSGC and SFD) alignment is done.

The DIRAC reconstruction code, called ARIANE [62], was used to read the DIRAC files collected during 2002 and 2003 years. Two tracks per event, associated to the two pions, are reconstructed and some requirements to these tracks need to be done to improve the alignment:

- Prompt events (events in time coincidence in the Vertical Hodoscopes).
- Tracks with hits in all MSGC layers and also in SFD-X and SFD-Y.

The alignment method used is an iterative method where each layer is moved independently to center the residual (defined below) distributions.

The following parameters have been determined as output of the calibration procedure:

- 7 Euler rotations of each plane about the Z-axis (precise tuning of the θ_i angles).

- 7 offsets of individual detector planes in the direction perpendicular to the corresponding strips or fibres (position of the first strip).
- mean position in X and Y of the beam center.

In order to evaluate the upstream detectors parameters (offsets and Euler angles) we base on the non-correlated residuals of each MSGC and SFD plane. Residuals are calculated as the difference between track extrapolation to the desired plane and the coordinate of closest registered hit. Although in data selection and track recognition all available information is used, a non-correlated residual distribution is determined by dropping individual detector hits from the track fitting, avoiding biases from the studied detector information. The SFD-U hit also is dropped in the fit.

2.1 Angle alignment.

The width and shape of the residuals depends on the spatial orientation of the detector. In the figure 2.1 we show the dependence of the width of residual with the variation of the angle in 3 *mrاد* steps for the MSGC-X. A clear minimum is observed and this is selected to be the correct orientation of the layer. In the figure 2.2 the residual distributions for the nine angle variation of the figure 2.1 are shown. It can be observed like the width and also the shape change for different orientations of the layer.

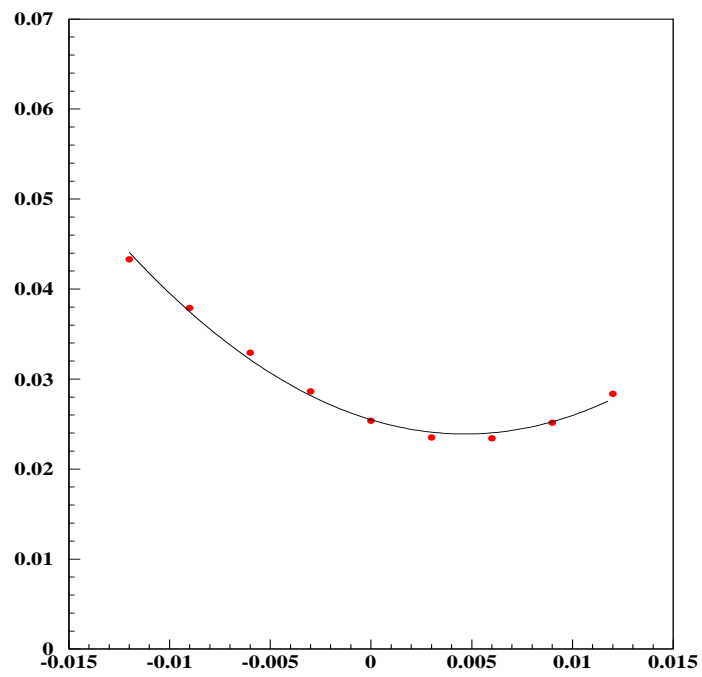


Figure 2.1: *Dependence of the residual width (in cm) on the angle for the MSGC-X layer.*

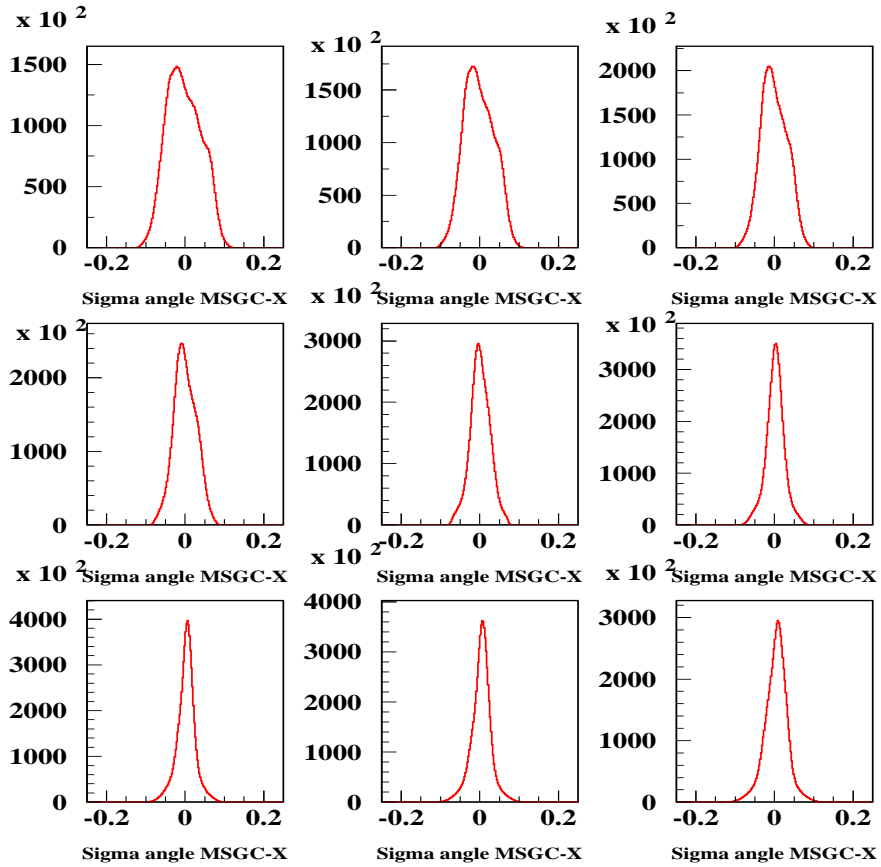


Figure 2.2: Residuals distribution for nine orientations of the MSGC-X layer.

2.2 Position alignment

Residuals distributions calculated with the described method for MSGC and SFD are fitted with a gaussian distribution, and mean value is used as estimator of the offset position for the detector with respect to the upstream block.

After alignment jobs, typically residual distributions are displayed in Fig.2.4, meanwhile offsets are plotted in Fig.2.3 again for comparison purpose.

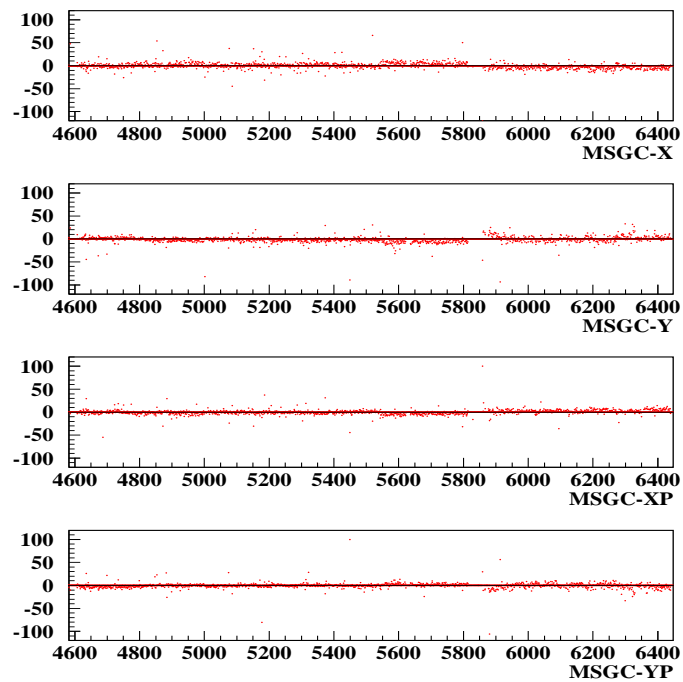


Figure 2.3: Residuals (in μm) for the four MSGC planes in function of the run number.

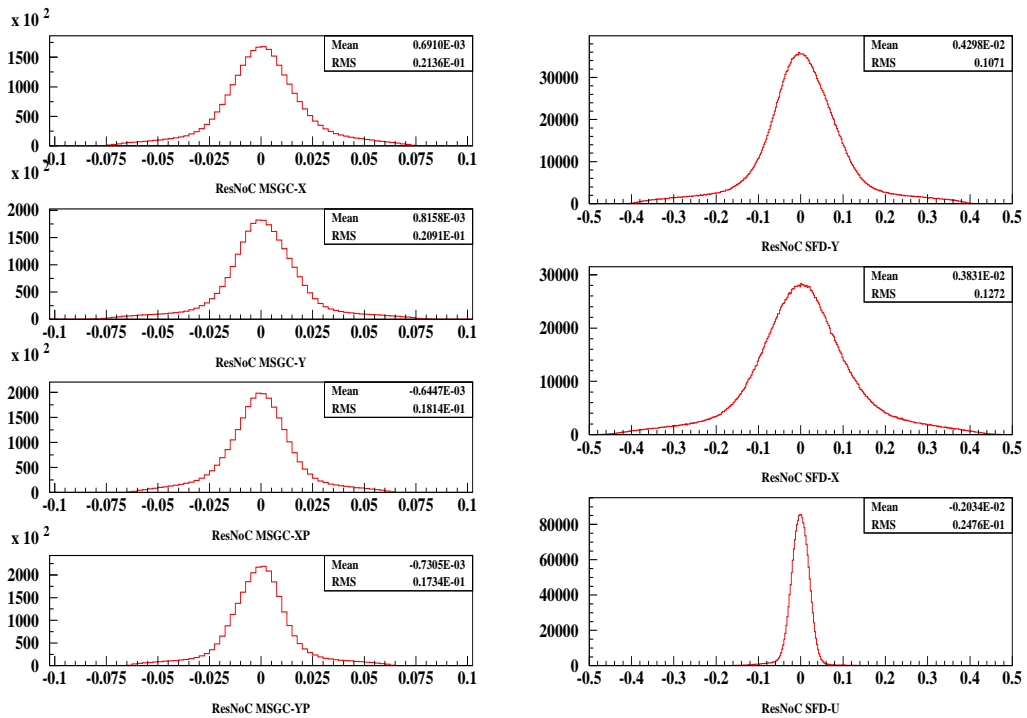


Figure 2.4: Residuals (in μm) for the seven upstream planes. MSGC (SFD) detectors are displayed at left (right) side.

2.3 Beam position

Coordinates of proton beam intersection with the target plane, plays an important role in the hit identification for tracks during the pattern recognition procedure and to get a good description of lab-frame momenta of particles.

The beam spot coordinates are obtained for each run by making a gaussian fit to the unconstrained intersection of fitted tracks with the target plane.

In figure 2.5 the X and Y coordinates of this intersection are displayed. They are showed in function of the run number. For comparison also is shown the beam position stimulated used only the information of the Drift Chambers

hits.

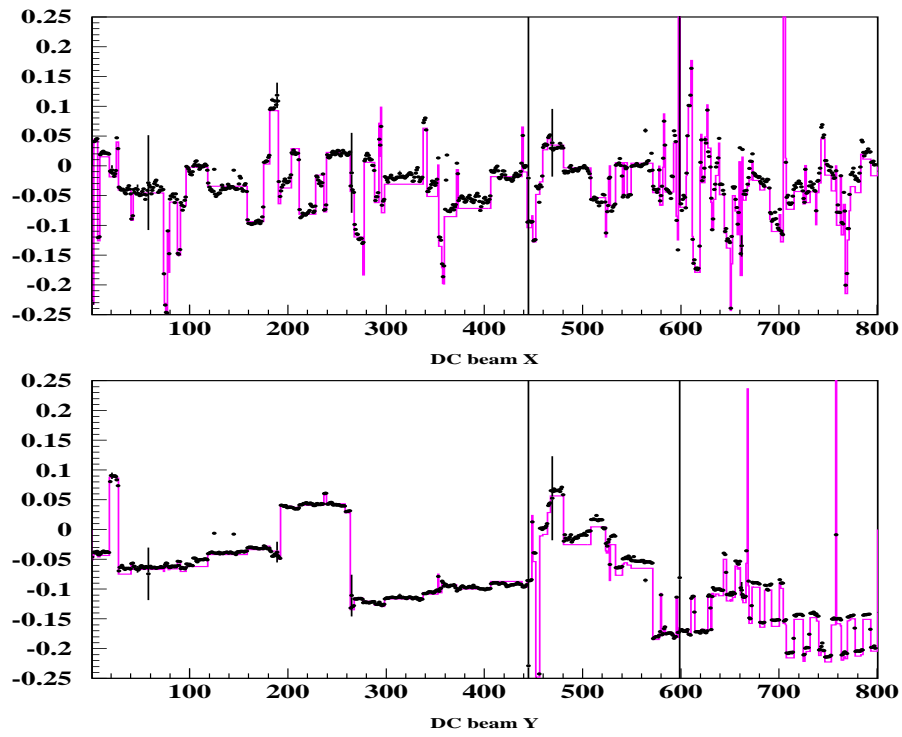


Figure 2.5: Beam intersection with target plane (in X coordinate) determined with upstream detectors (black) as function of the run number. In pink a beam position estimation using only information from the drift chambers.

Chapter 3

SFD Efficiency Using MSGC-GEM for 2001 Data

The DIRAC upstream arm consists of three detectors, using totally different technologies, namely the Microstrip Gas Chambers and GEM (MSGC), the Scintillation Fibre (SFD), and the Ionisation Hodoscope (IH). The first two (MSGC+SFD) provide a tracker to measure accurately the pion pair separation, whereas the IH scintillator measures the double pulse-height expected when the close-angle pair cannot be resolved by the tracker.

The amount of background noise in all three detectors is very high, as we shall see, and this is posing a serious problem for the determination of transverse momentum of the pairs, as well as for the recognition of the true particles coming from the target foil. Of course, this problem translates itself into uncertainty in the determination of ponium lifetime.

The ultimate origin of this strong background is surely the high intensity of the proton beam. However the readout systems of these three detectors have a totally different response in each case [41]. For SFD and IH, the inevitable use of photomultipliers and light-guides so close to the beam aggravates the noise conditions, despite the effective use of TDC's. Discrimination of SFD signals is achieved by Peak Sensing Circuit (PSC). A drawback of this (otherwise very effective) device is that when two pulses arise from adjacent fibre columns, one of them is suppressed with probability in the range 30-40% [41], thus degrading the double-track resolution of SFD.

In the case of MSGC, the limited bandwidth in the pipelined readout (built in 1997) originates an affective time gate of approximately 250 ns, which increases significantly the hit multiplicity. The latter agrees perfectly well with the expected performance of this detector when it was designed [72], [73].

It is therefore clear that a precise tracking in the DIRAC experiment cannot be achieved without fully exploiting the redundancy of the upstream detectors in a systematic way. Cross-checking between these detectors is essential, and every attempt to by-pass a real tracking procedure risks leading to doubtful, or even erroneous, results. In any case, both the statistical and systematic errors in the lifetime measurement will clearly reflect the tracking procedure used.

What I present in this chapter is how the MSGC detectors can be used to perform an unbiased assesment of SFD detector response, in terms of two-particle and single-particle efficiency, as well as cross-talk. A conceptually similar study to the one we present here was done by V. Yazkov [74] using data runs from 2002 on, making use of the U-plane at 45° of SFD. However such study could never be made with the 2001 data, due to the fact that U-plane was not installed in DIRAC at that time. The results here can certainly be compared with those of reference [75], obtained by means of IH detector and drift chambers only. The agreement is reasonable, despite the intrinsic difficulty of the latter analysis.

3.1 Tracking procedure and results

In order to evaluate the SFD-X detector all of its detector hits were removed from the 2001 data sample, and the measurement of X-coordinate was done using only MSGC detectors, together with the Y-coordinate provided by SFD-Y. An identical procedure can of course be applied for SFD-Y (X), reciprocally.

5-hit tracks are selected by requiring signal in MSGC X,Y,X',Y' plus SFD-Y, and extrapolate them to the SFD-X plane. The full upstream tracking procedure is used, taking into account multiple scattering detector correla-

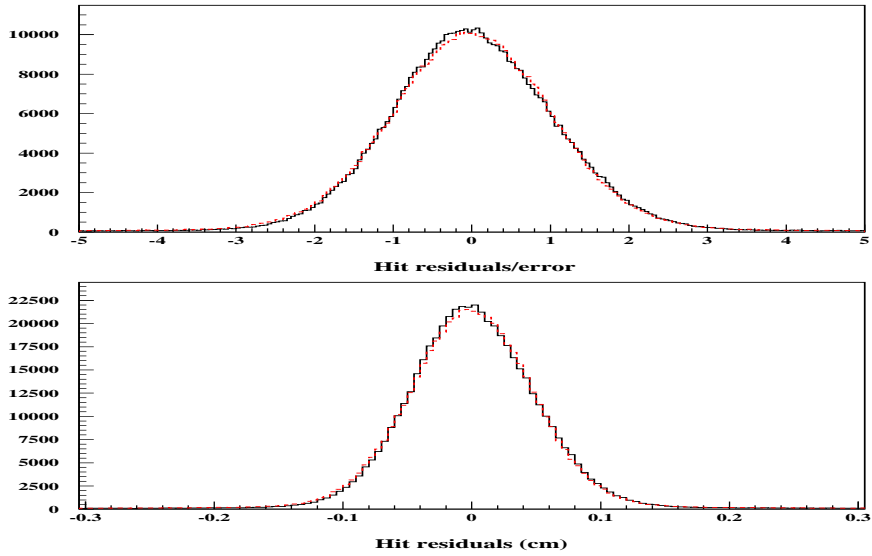


Figure 3.1: *Distribution of SFD-X residuals(bottom) and residuals divided by error(top), obtained from extrapolation of 5-hit tracks, fitted with vertex constraint.*

tions and vertex constraint [57]. Track pairs are matched with downstream spectrometer tracks, using the standard procedure for full-tracking (F) in ARIANE. Track pairs are furthermore required to be prompt (strict time coincidence with vertical hodoscope), to have momentum $p > 2$ GeV/c and probability larger than 2%. The distribution of the residuals of the closest SFD-X hit found, is given in figure 3.1. Track pairs then are divided into three categories, namely:

- a) those for which both the positive and the negative tracks contain a SFD-X hit within $\pm 3\sigma$ of track extrapolation. It may be the same hit, when the pion pair is not resolved by SFD-X detector.
- b) those for which one of the two tracks contains a hit within $\pm 3\sigma$ window and the other does not.

- c) those for which none of the two tracks contains a hit within $\pm 3\sigma$ window.

In figure 3.2 the ratio between the number of events in each category divided by the total is shown, as function of the distance between the two hits measured by the MSGC's. I call them probability densities $P(2)$, $P(1)$ and $P(0)$, respectively.

The interpretation of $P(2)$ and $P(1)$ is that they map the double-track efficiency and single-track inefficiency of SFD-X, respectively. This is so because of the mismatch between the space resolution of MSGC and SFD ($200\mu\text{m}$ pitch improved by center-of-gravity determination for the first, digital readout and $430\mu\text{m}$ pitch for the latter), together with the fact that the stereo angles of X' and Y' ($\pm 5^\circ$) enable smooth zero-crossing in X , due to track opening in vertical plane.

In order to derive quantitative results about SFD performance, the experimental data in figure 3.2 can be compared with a Monte Carlo simulation in which the SFD is made 100% efficient, and the PSC malfunction suppressed. This prediction is also shown in figure 3.2 as a dotted line. The enhancement of $P(1)$ around zero distance indicates the ideal double-track resolution of SFD, essentially determined by fibre pitch, whereas the difference between real data and ideal SFD Monte Carlo in the plateau regions (left and right) shows constant SFD single-hit inefficiency. I define this difference to be $2(1 - \epsilon)$, where ϵ is SFD efficiency (likewise, the difference in $P(2)$ is 2ϵ). The non-zero values of $P(1)$ in the plateau region for the ideal SFD Monte Carlo are determined by background noise in MSGC detector and to a lesser extent by far-away hits in SFD that scape the 3σ cut due to tails of multiple scattering. The result for a Monte Carlo with null MSGC background and ideal SFD is also shown in figure 3.2. Details about this background simulation are given in the next section.

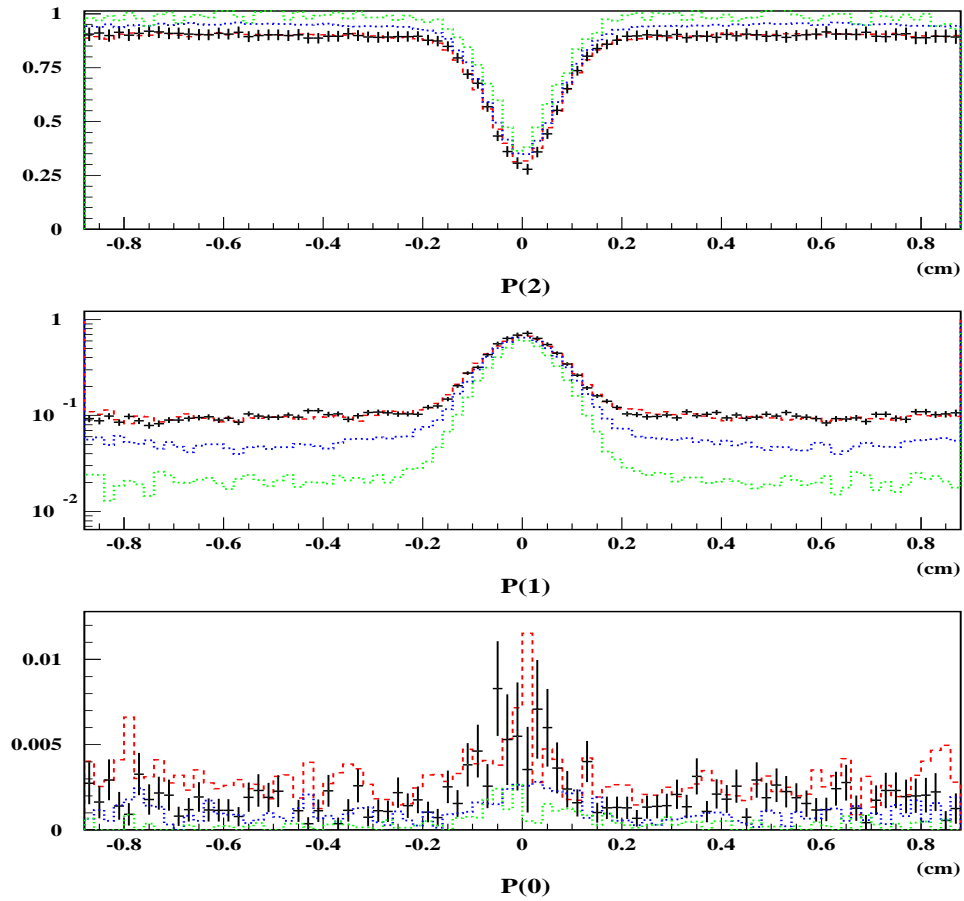


Figure 3.2: *Distribution of two-particle ratios $P(2)$ (top), $P(1)$ (central) , and $P(0)$ (bottom), according to the definition given in the text, for SFD-X detector. Prompt data from 2001 are shown by black crosses. Blue dotted line is Monte Carlo with ideal SFD and red dashed line is Monte Carlo with full simulation and optimised PSC threshold. Green dotted line (lowest in $P(1)$) shows Monte Carlo prediction with null MSGC background and ideal SFD.*

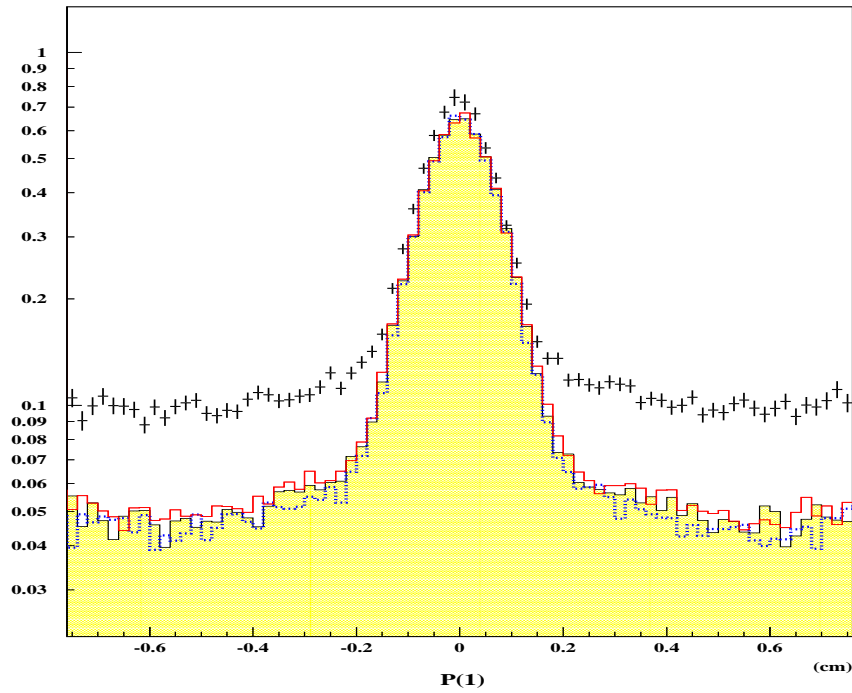


Figure 3.3: *Distribution of two-particle ratio $P(1)$ according to the definition provided in the text. The black crosses corresponds to 2001 real data, the filled grey line to ideal SFD Monte Carlo, and the red and blue lines correspond to $\pm 5\%$ variation of MSGC background.*

According to the definition, we determine $\epsilon = 97.4 \pm 0.2\%$ to be the average efficiency of SFD-X. All 2001 Ni 24 GeV/c data runs were used for this analysis. Similarly we determine $\epsilon = 97.5 \pm 0.2\%$ for SFD-Y. The main contribution to the error is believed to be systematic, and it is attributed to the precision in the description of MSGC background noise. A conservative $\pm 5\%$ variation of average hit multiplicity has been considered for this purpose, and further enlarged by a factor 2. The corresponding variation of $P(1)$ is illustrated in figure 3.3.

Now the PSC threshold parameter has been changed in SFD simulation

(see FFREAD datacards in ARIANE 304-36) in order to achieve best agreement between Monte Carlo and real data. In fact, the results of figure 3.2 show that good agreement can be found (with parameter value 1.5) for $P(2)$ and $P(1)$. Variations in the level and shape of SFD cross-talk do not make a visible change in previous figures, neither moderate variations in SFD background noise, although $P(0)$ is more sensitive to the latter. Note that the central enhancement observed in $P(0)$ distribution with real data appears to be described by Monte Carlo. In this respect our results seem to differ slightly from those of reference [74]. Figure 3.4 shows the corresponding result for SFD-Y.

3.2 Monte Carlo simulation of MSGC background noise

As we have seen MSGC background is, for this particular study, quantitatively at the same level as SFD inefficiency. Therefore, like in the pionium lifetime measurement, it is important to have control on the accuracy of the simulation procedure, which we describe next.

The source of MSGC background is real particles that cross the detector outside the trigger gating time. Pipeline delay was adjusted at installation time so that maximum pulse-height is obtained within the experiment trigger gate, and it decreases by approximately a factor two at the borders of the $250ns$ time acceptance.

Clusters (or hits) are defined as a continuous set of strips above threshold. Monte Carlo simulation takes into account the following aspects:

- 1) cluster strip-multiplicity and pulse-height pattern within a cluster
- 2) clusterisation code
- 3) detector-correlated hit multiplicity
- 4) space correlations within the same detector (pair production, showers)

- 5) absence of space correlations between different detectors (when trigger particles are removed)

In all cases mentioned, an average of all Ni data spectrometer runs from 2001 has been used as input for the simulation code. For the first item, all information is encoded from real data under the form of dedicated input histograms initialised by ARIANE. For the second, the same clusterisation routine is used as in ARIANE reconstruction. Concerning the third item, hit multiplicities are also input from experimental data, but under the form of 4-fold correlation matrices, so that 4 multiplicities for X,Y,X',Y' detectors are generated jointly.

As far as item 4 is concerned, it is observed that a fraction of close-hit pairs are produced near the detector frames, outside the acceptance of the drift chambers. Therefore we focus our simulation for those MSGC hits that actually lie on the path of the extrapolated drift chamber tracks. So we define a hit multiplicity N_h as the sum of all hits found within a 3σ cut around the extrapolated coordinates of positive and negative tracks to all MSGC detectors. The same momentum-dependent σ is used here as for the matching procedure in ARIANE reconstruction [57].

The observation mentioned in item 5 was demonstrated by showing that events with one-sided activity in X-coordinate did not have corresponding activity in X' (likewise for Y and Y'), when hits from real trigger tracks were removed. Therefore simulation of space correlations appeared to be unnecessary.

We should mention that, because of the non-linear response of the clusterisation routine, which combines near-by particles together at large particle densities, the simulation procedure generally requires several iterations to converge. The final results for simulated MSGC hit multiplicities are illustrated in figure 3.5.

3.3 Conclusions

We have determined the single-hit average efficiency of SFD-X and SFD-Y detectors for Ni 2001 data runs, and also evaluated the double-track reso-

lution of these detectors, using MSGC planes X,Y,X', and Y'. The results obtained demonstrate that, despite the strong noise conditions in DIRAC upstream arm (IH, SFD and MSGC), pion pairs can be unambiguously measured provided full tracking information is used.

The following points have been demonstrated:

- DIRAC spectrometer double-track resolution is basically determined by MSGC detector
- PSC malfunction is totally circumvented by the use of MSGC's
- ARIANE F-tracking performs well both at long and short distances
- GEANT-DIRAC Monte Carlo simulation performs rather accurately for all critical functions, such as MSGC background, PSC simulation, as well as SFD and MSGC digitisations

It is shown in particular that the problem originated by SFD single-hit inefficiency at large angles (fake close pairs) can be effectively reduced by use of MSGC's. Overall tracking resolution for critical kinematic variables for lifetime measurement will be reviewed elsewhere.

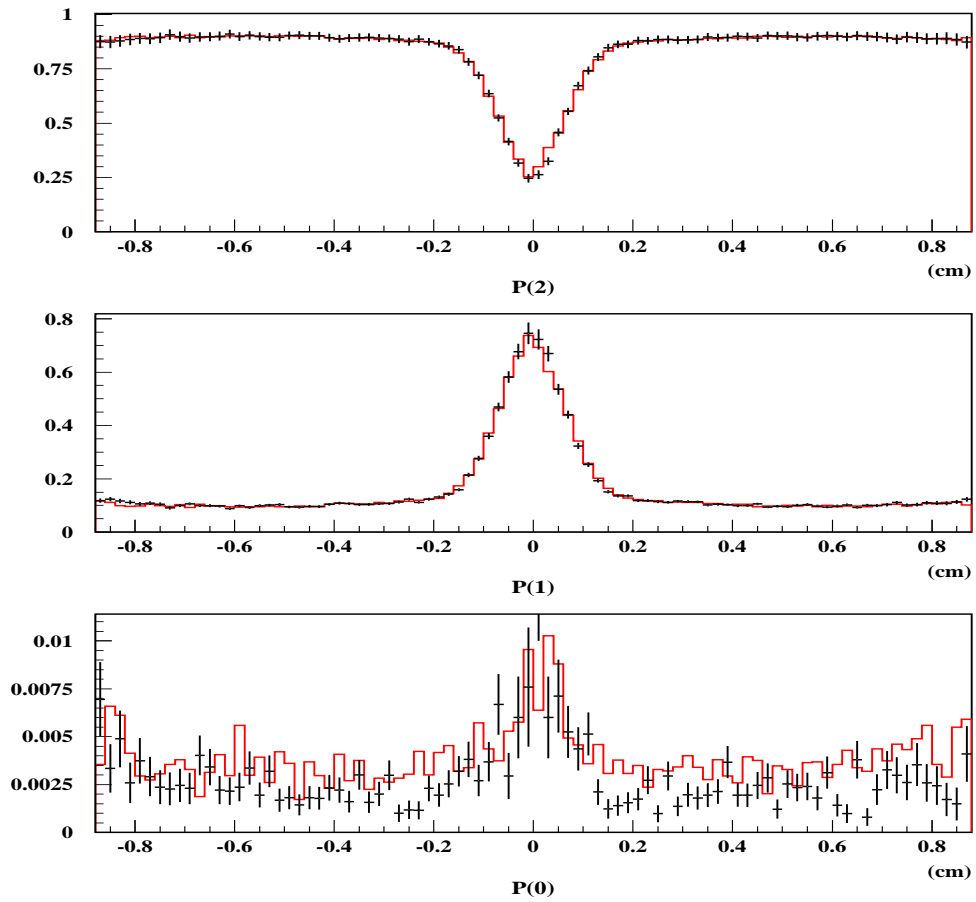


Figure 3.4: Distribution of two-particle ratios $P(2)$ (top), $P(1)$ (central), and $P(0)$ (bottom), according to the definition provided in the text, for SFD-Y detector. Prompt data from 2001 are shown in black continuous line, whereas red dotted line indicates full Monte Carlo simulation, as in figure 3.2.

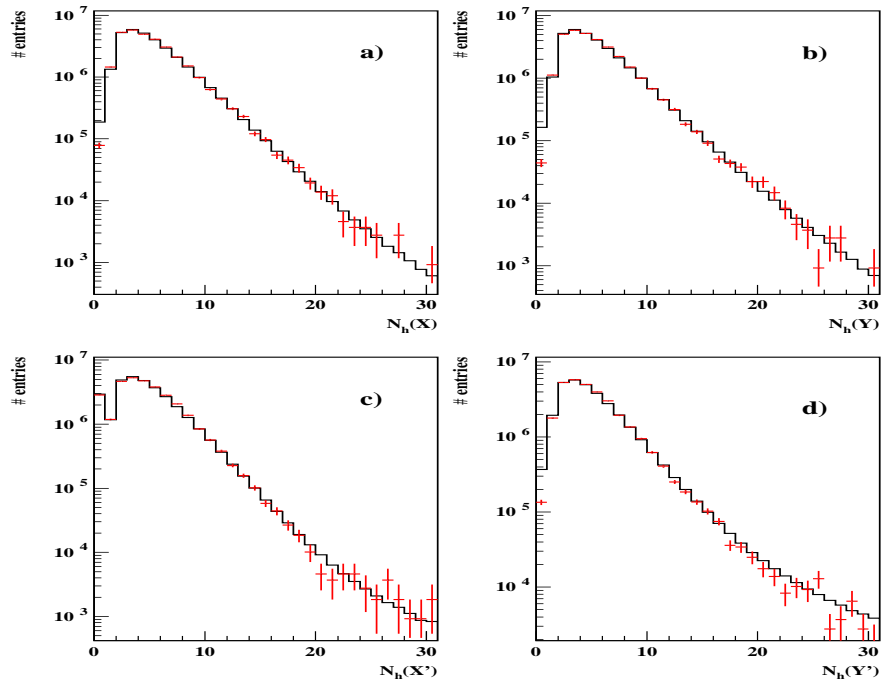


Figure 3.5: Continuous lines represent observed hit multiplicity in MSGC X (a), Y (b), X' (c) and Y' (d) detectors for 2001 data runs, as described in the text. Coloured crosses are the Monte Carlo simulations described in the text, for each detector.

Chapter 4

Multiple Scattering in Upstream Detectors

Knowledge of multiple scattering in DIRAC experiment is important because it determines Q resolution when Monte Carlo is used to extract the narrow signal from atom pairs. The upstream radiation length fraction is specially critical for Q_T resolution.

Chemical specifications, precise thicknesses and difficulty of very detailed geometry of components of SFD and MSGC detectors do not allow an "a priori" knowledge of the material contribution better than roughly 10%. Therefore measurements must be made with real data, in order to attain the percent accuracy level.

The four MSGC high resolution detectors placed at 2.5 m from the target foil, together with the GEANT [76] tracking capability using Molière theory, provide a clean determination of multiple scattering fluctuations to this accuracy. Using tracking detectors to evaluate their own multiple scattering is the natural and standard way to do this job. The tracking tools were implemented in reference [57].

The obvious idea is to exploit the fact that real $\pi^+\pi^-$ prompt interactions come from a single mathematical space point (of nuclear size dimensions), and to use beam unconstrained track fitting to study the error.

4.1 Vertex resolution analysis

A vertex position has been defined inside the target plane by coordinates $(x_1 - x_2, y_1 - y_2)$ where $x_{1,2}$ are extrapolated X-coordinates for positive and negative tracks (likewise for $y_{1,2}$) that pass the standard ARIANE reconstruction procedure, with full tracking. By taking the differences, the measurement becomes insensitive to fluctuations of track origin within the beam profile. Such fluctuations become uncorrelated only in the case of accidental pairs, where each track originates from an independent interaction.

In this analysis, prompt pairs (by time-of-flight cut) were selected, in order to make sure that multiple scattering and, to a much lesser extent, detector resolution, are really the dominant contributions to the vertex error.

A gaussian fit was done to the vertex distributions in X and Y projections in seven bins of track momentum, in the range from 1.5 GeV/c to 3.5 GeV/c. It is worth noting at this point that, as a standard part of the track fitting procedure, far-away hits with respect to the track are removed by a 3σ cut. Only 6-hit track were retained for this analysis.

In order to make a meaningful comparison with the Monte Carlo with prompt pion production, a 10% fraction of the vertex distribution observed with accidental pairs has been subtrated at each momentum bin. This point will be discussed in more detail in section 3.5 below.

The gaussian fit to the vertex distribution appears to be good in the central region, while small tails are observed at fixed momentum. These are a consequence of Coulomb large-angle scatters, as well as possible reminders from accidentals and decays. The fits were consistently performed in the region $\pm 2\sigma$, in order to minimise the impact of the tails. For illustration, we show in figure 4.1 the vertex distributions in X and Y projections for the maximum and minimum momentum bins.

Please note that pattern recognition of individual tracks (which takes place prior to track fitting) requires the presence of MSGC and SFD hits within a pointing geometry with respect to the beam intersection with the target foil. Space windows used are explained in some detail in reference [57], and they are sized (analytically) in order to catch the interaction signal within approximately 2.5σ from the predicted value, while removing at the same time

decays and other background sources outside spotted region. This cut has been tightened for this study, for the reasons mentioned above.

We have calibrated the mean vertex position for different run periods in 2001, and found that its time dependence is strongly correlated with that observed from direct drift chamber alignment with respect to the beam. Although this is irrelevant for the difference $x_1 - x_2$, this calibration was indeed taken into account for track pattern recognition.

The evolution of fitted σ values with momentum, after subtraction of accidentals, is plotted in figures 4.2 and 4.3. These are called in the following vertex resolutions. Empirically, we have parametrised the momentum dependence of vertex resolution by the function $\sigma = a + b/p$, which provides an excellent description of the data.

Now the results obtained with the full 2001 24 GeV/c data sample (94 μ m Ni target) were compared with the GEANT-DIRAC Monte Carlo using standard geometry files, 94 μ m Ni target thickness, and specific material contributions for MSGC and SFD detectors as indicated in tables 4.1 and 4.2. The values of A, Z, density ρ and thickness for each simulated material layer, which are the real input for GEANT-DIRAC, are given in the first four columns of this table.

It is important to recall here that the default version of GEANT program [76], (which is the one used by GEANT-DIRAC [61]), makes use of the Molière theory of multiple scattering, which operates at every step during the tracking, subject to the condition that the parameter Ω_0 is greater than 20. Ω_0 represents the number of scatters that take place in a given step length t , according to the expression:

$$\Omega_0 = b_c \frac{t}{\beta^2}$$

where

$$b_c = 6702.33 \rho Z'_s e^{(Z'_E - Z'_X / Z'_s)}$$

with

$$Z'_s = \sum_i \frac{p_i}{A_i} Z_i (Z_i + 1)$$

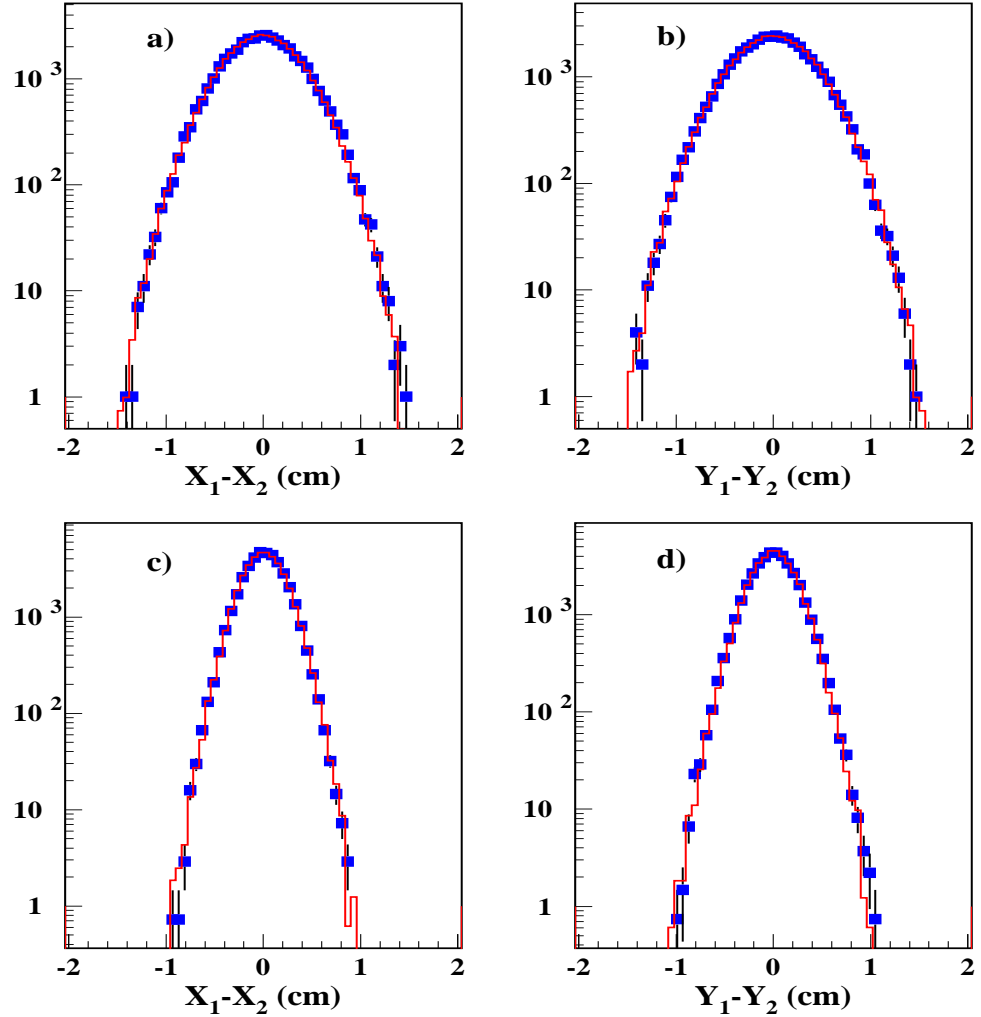


Figure 4.1: Vertex distributions in X and Y projections. Only the minimum ($p < 1.60 \text{ GeV}/c$, top), and maximum ($p > 3.25 \text{ GeV}/c$, bottom) momentum bins of figure 4.2 are shown. GEANT Monte Carlo is superimposed for the optimum $\bar{\theta}_0$ found.

$$Z'_E = \sum_i \frac{p_i}{A_i} Z_i (Z_i + 1) \log Z_i^{-2/3}$$

$$Z'_X = \sum_i \frac{p_i}{A_i} Z_i (Z_i + 1) \log \left[1 + 3.34 \left(\frac{\alpha Z_i}{\beta} \right)^2 \right]$$

where p_i are the proportions by weight of atom type i with atom number Z_i and mass number A_i , within a compound made of $i = 1, N$ different elements. β is the particle velocity and α the fine structure constant.

In the setup of DIRAC upstream detectors, the condition $\Omega_0 > 20$ is only violated (in a significant number of steps) in air gaps and MSGC DME gas, where GEANT is forced by the volume size to take a too small step size, in proportion with $1/\rho$. In those cases, a precise parametrisation is performed by GEANT, called plural scattering [76]. I do not enter here into a more detailed discussion of this part, because the impact of those cases in the overall scattering angle is, in any case, negligible.

More important is that the concept of radiation length X_0 [77], usually related to the multiple scattering angle θ_0 by formula [78]:

$$\theta_0 = \frac{13.6 \text{ MeV}}{\beta p} \sqrt{\frac{t}{X_0}} \left[1 + 0.038 \log \left(\frac{t}{X_0} \right) \right] \quad (4.1)$$

is not actually used by the Monte Carlo realisation of the Molière theory in GEANT (as it is very well explained in [76]) due to the fact that the scattering angles through consecutive small steps do not add up in quadrature in this theory. Instead, GEANT Monte Carlo calculates the scattering angle θ_0 through a given material step t according to detailed parametrisations of the exact Molière theory, corrected for finite angle scattering as described by Bethe. These parametrisations depend only on the quantities specified in the first four columns in tables 4.1 and 4.2, apart from pion energy and velocity.

For the sake of comparison with other approaches, one may however wish to make the approximation of obtaining an equivalent radiation length X_0 from the effective A , Z and ρ input values given to GEANT-DIRAC in tables 4.1 and 4.2. In order to do so, we may use for example the formula due to Dahl [78]:

$$X_0 = \frac{716.4 \text{ gcm}^{-2} A}{Z(Z+1) \log(287/\sqrt{Z}) \rho} \quad (4.2)$$

and the result of this exercise is indicated in the last two columns of tables 4.1 and 4.2, where the values of X_0 and X_0 % fraction (corresponding to real thickness) are given for each tracking medium. Following this approximation, a total radiation length can be obtained by adding the contributions of individual layers in each MSGC and SFD detector, which is also presented in the last row ¹.

The vertex resolution falls short with these parameters with respect to the one observed with real data, as illustrated in figures 4.2 and 4.3. The difference is very appreciable.

The most obvious interpretation for this difference is that the average radiation length fraction for upstream detectors is underestimated by the Monte Carlo. In fact, the data were provided by detector builder groups, and most of the materials are composites for which chemical composition is uncertain with accuracy better than 10-20%. In addition, the list of small components in GEANT is never complete, and approximations have been made to simplify the geometry. On the other hand, both purity and thickness of the 94 μm target foil were subject to specific controls, so I did not assume that they should be changed. In any case, our analysis was restricted to the 94 μm data sample (in correspondance with the Monte Carlo input), leaving aside the 98 μm data. I do not include the Ionisation Detector (IH) in this particular definition of upstream detectors, since obviously it cannot be responsible for the discrepancy, being located past the SFD.

In order to check whether this hypothesis is correct, the average multiple scattering angle was increased, which I call $\bar{\theta}_0$, in all upstream detectors (excluding the target foil, which is well measured) by 12%, 13.5%, 15%, 16.5%, 18% 19.5% and 21%, and re-processed all GEANT-DIRAC tracking. The output for every dataset (40 buffer files of 50000 events each) is avail-

¹these one-detector values (55.45×10^{-4} for MSGC and 83.79×10^{-4} for SFD-X) can be compared with those obtained in reference [79], namely 53.86×10^{-4} for MSGC and 83.36×10^{-4} for SFD-X, with a specific definition of equivalent X_0 , outside the GEANT framework. Comments about this result will follow in section 6.

able for use by ARIANE, so that detector digitisations and/or reconstruction procedures may be easily changed afterwards.

A good description of the data is in fact achieved by the Monte Carlo with 15% increase in $\bar{\theta}_0$, both in normalisation and in momentum derivative, as it is illustrated in figures 4.2 and 4.3. In fact, in order to measure the agreement between each Monte Carlo hypothesis of $\bar{\theta}_0$ and the prompt data, a χ^2 has been defined as:

$$\chi^2 = \sum_i \frac{(\sigma_p^i - \sigma_{MC}^i)^2}{(\Delta\sigma_p^i)^2 + (\Delta\sigma_{MC}^i)^2} \quad (4.3)$$

where i runs over seven bins of track momentum in each projection (X or Y). The evolution of χ^2 as function of $\Delta\bar{\theta}_0/\bar{\theta}_0$ is shown in figure 4.4 for X and Y projections separately. Note that $\Delta\bar{\theta}_0/\bar{\theta}_0$ indicates the relative change in the mean multiple scattering angle $\bar{\theta}_0$ with respect to the nominal (0%) values indicated in tables 4.1 and 4.2.

A minimum χ^2 (after parabolic interpolation) is found in X projection at approximately +16.5% and +14.5% in Y. A systematic error is estimated in $\pm 1.5\%$ from the figures, and from the relative consistency between both projections. This point will be confirmed by the studies made in the following section. It applies to a mean observed deviation of +15%.

The vertex distributions for the best Monte Carlo fit are also compared in figure 4.1 with real prompt data, and excellent agreement is found. Although maximum and minimum momentum bins were chosen for illustration, agreement is equally good in all momentum bins.

Let me clearly point out that this Monte Carlo corresponds to the standard $\pi^+\pi^-$ Coulomb-correlated generator input, as it is used for the lifetime analysis, where a good description of Q_T and Q_L is essential.

4.2 Checks on systematic effects

Let us now review other aspects of the GEANT-DIRAC Monte Carlo simulation and reconstruction, apart from the upstream radiation length fraction,

that might be unrealistic and could perhaps explain the observed deficit in vertex resolution.

4.2.1 Track fitting procedure

The vertex resolution deficit observed with the standard GEANT-DIRAC Monte Carlo does not depend on the particular choice of track fitting procedure that it is adopted. In fact, there are two (ARIANE selectable) mathematical procedures that have been used:

- A) simple straight-line fit
- B) multiple scattering correlated fit

Both of them perform a least-squared method to minimize the track χ^2 , and are described in detail in reference [57]. In method A, the detector covariance matrix consists of only diagonal terms, namely the inverse of the squared intrinsic resolutions of the seven upstream detectors (6 in 2001 configuration). In method B, momentum-dependent non-diagonal terms are added in order to describe multiple scattering correlations between detector elements, as well as diagonal terms describing particle propagation through multiple thin layers. In both of them, detector resolutions are input to the program, and need to be known "a priori". As we shall see, the fitted track parameters depend on those only at second order.

The fit results are (in both cases) insensitive to an overall covariance matrix normalization factor. As a consequence, in method A a global scale factor on the MSGC and SFD resolution hypothesis is irrelevant. Only the ratio between the two is significant, which is approximately given by a factor 2, according to their respective pitch distances. In method B, the radiation length fractions of individual detector elements are given as input for the correlation matrix (values indicated in reference [41] were used for this purpose), as well as particle momenta determined by ARIANE event by event.

Figures 4.5 and 4.6 show a comparison between vertex resolution obtained with methods A and B, for the same hypothesis of detector resolution, in X and Y projections respectively. One can see that the differences

between the two methods are small, due to the fact that in a given projection there are only 3 effective detectors subject to correlation (for example, $X, X', SFD - X$), which is the minimum in order for the formalism to be effective. Method B simply provides a slightly better resolution at low momentum, better appreciated in X .

Now figure 4.7 shows the effect of changing the ratio $\sigma_{sfd}/\sigma_{msgc}$ from 1 to 4 in method A, and figure 4.8 the effect of changing the average radiation length in all detector layers by $\pm 50\%$, in method B (leaving detector resolutions unchanged). Both changes are very extreme (by far inconsistent with our knowledge of those parameters), but nevertheless their impact on vertex resolution is minor.

In summary, it has been shown that differences due to the tracking procedure are themselves smaller than the observed resolution deficit, therefore it is excluded that they could explain it. Although we reported here (for brevity) the results obtained with real spectrometer data, we observe exactly the same trend with Monte Carlo data.

After consideration of the previous results, we have adopted method A as the baseline for our analysis, consistently throughout this note. Clearly the issue is not having the best resolution, but rather being more sensitive to multiple scattering and insensitive to tracking details, particularly when the amount of matter is itself subject to evaluation.

4.2.2 MSGC clusterisation

The second aspect of Monte Carlo simulation that we have analysed in detail is whether MSGC ARIANE digitisations (i.e. cluster strip multiplicities and charges) might be wrongly simulated. In other words, whether the description of detector resolution parameters of MSGC might influence the results. Of course, it is quite clear that with a single-hit resolution of $50\mu\text{m}$ [41] this influence is bound to be small as compared to multiple scattering, given the detector geometry. In any case, here again the Monte Carlo is severely constrained by the real data which are used as input.

For illustration, we show in figure 4.9 the prediction for vertex resolution under the assumption that all cluster sizes were equal to one microstrip and that all were equal to two microstrips. The microstrip multiplicity distribution

is indicated in figure 4.10. It is clear that both assumptions are extreme, in relation with the precision of the digitisation code. However, the changes induced are very small.

The conclusion of this study is that strong variations in the intrinsic resolution of MSGC cannot explain the observed discrepancy in vertex resolution, and hardly change the Monte Carlo prediction.

4.2.3 MSGC background

Noise level is quite strong in both MSGC and SFD detectors. Because the vertex resolution relies mostly on the MSGC, we have studied the influence of changing the MSGC background conditions on the previous results.

The general characteristics of MSGC background are described in reference [80], together with the simulation tools used. It is important to note that this simulation is totally constrained by the observed hit multiplicities. We show in figure 4.11 (bottom part) the number of MSGC hits found within a 3σ road around drift chamber tracks, for each detector plane, together with Monte Carlo simulation. The full 2001 data sample is included, in order to account for possible run-to-run variations. As it can be appreciated, the simulation quality is excellent. Not only average values are described, but also multiplicity shape is correctly reproduced.

We show in figure 3.5 the vertex resolution obtained after $\pm 10\%$ variation of average hit multiplicity, as compared with the observed average values. For reference, we also show the prediction for null MSGC background. It is clear that significant changes on noise conditions hardly change the result. The extreme hypothesis of null background clearly illustrates the effect of noise. At low momentum (where search windows are larger for multiple scattering), the probability for noise hits to enter the track is higher, given the fact that pattern recognition uses the calibrated beam spot center. Therefore, the vertex resolution becomes artificially improved.

We conclude that a wrong simulation of MSGC background does not significantly change the observed deficit in vertex resolution.

4.2.4 SFD background

In figure 4.12 we show the vertex resolution obtained with SFD background removed, as compared with the one with nominal parameters. Although the background level (under control of ARIANE via flux and cross-talk parameters) is high, its influence on vertex resolution is negligible (both in X and Y). This is understood, since noise SFD hits will not be followed by MSGC hits in front, and the track will not be reconstructed (let us recall that 6-hit tracks were selected in this analysis).

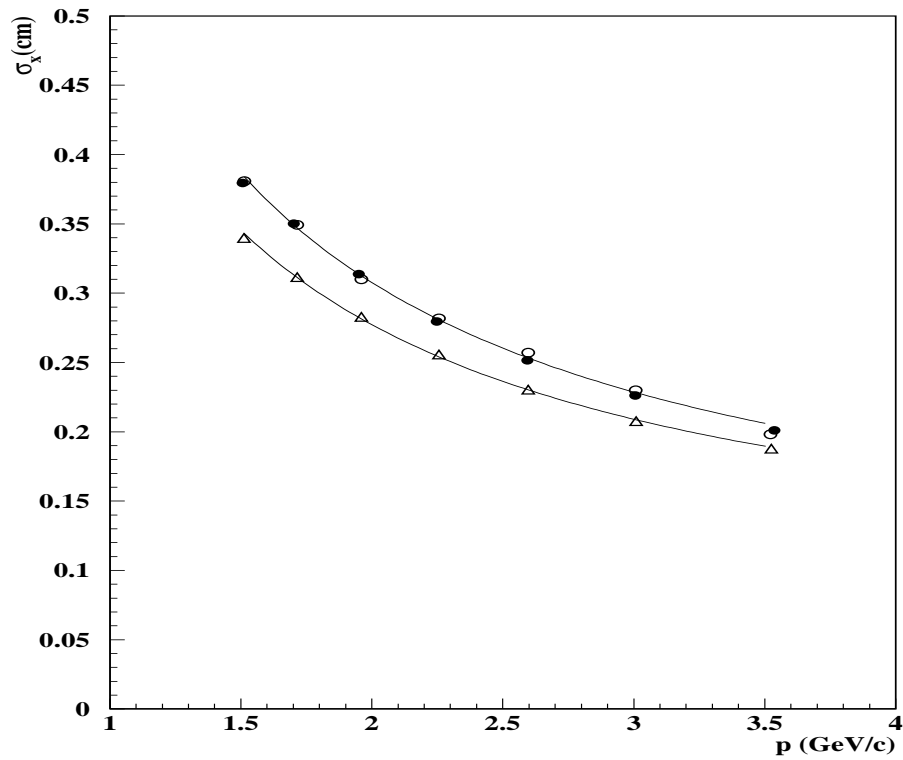


Figure 4.2: Vertex resolution in X -projection, as function of track momentum. Full circles are real prompt pairs (accidentals subtracted), and open circles the best Monte Carlo option illustrated in figure 4.4. Open triangles show the prediction from the standard GEANT-DIRAC, with material definition as in tables 4.1 and 4.2.

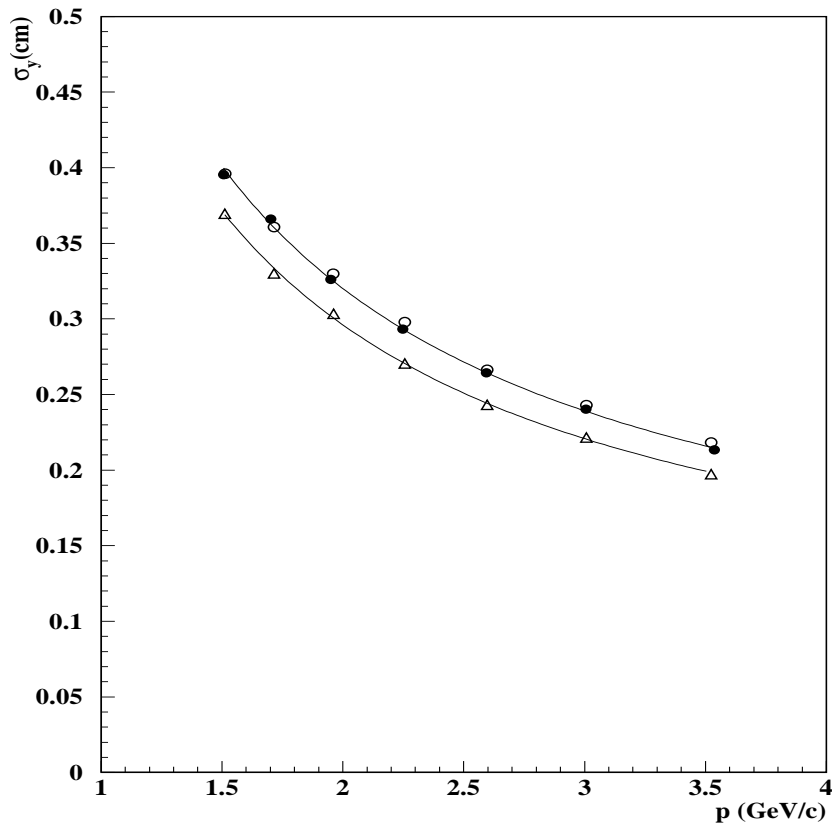


Figure 4.3: Vertex resolution in Y-projection, as function of track momentum. Full circles are real prompt pairs (accidentals subtracted), and open circles the best Monte Carlo option illustrated in figure 4.4. Open triangles show the prediction from the standard GEANT-DIRAC, with material definition as in tables 4.1 and 4.2.

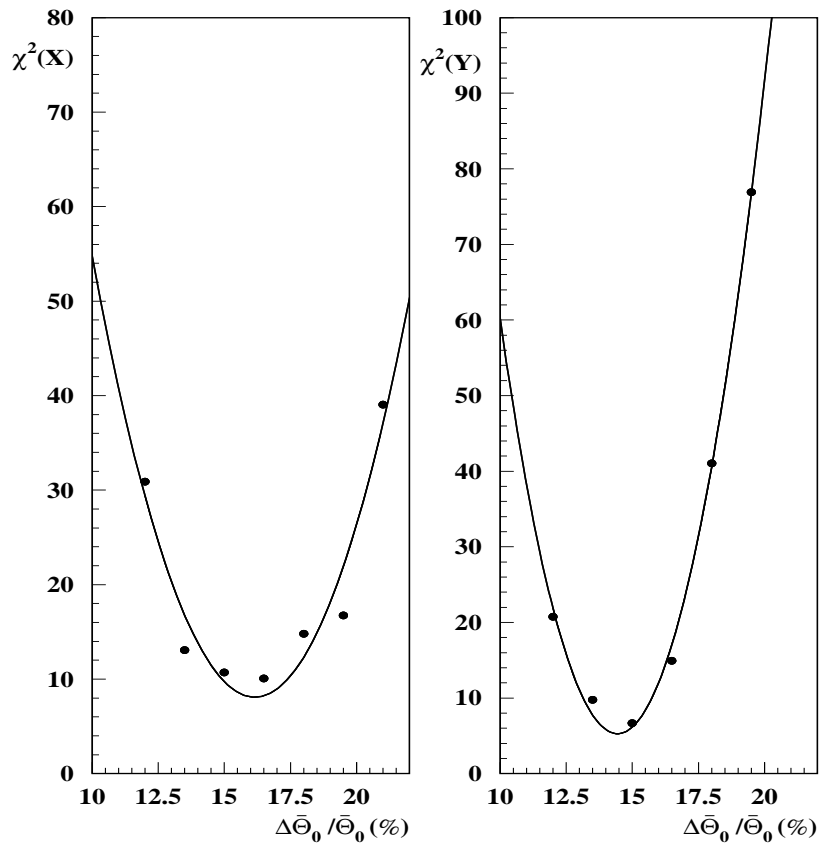


Figure 4.4: χ^2 between real data and Monte Carlo (as defined in the text) as function of increased average multiple scattering angle in upstream detectors, for X (left) and Y (right) projections. Only points near the minimum are shown.

Table 4.1: *Tracking medium data used by standard GEANT-DIRAC for one generic MSGC detector. There are four identical planes.*

<i>Material</i>	<i>A</i>	<i>Z</i>	$\rho(g/cm^3)$
DME	25.95	12.02	1.85×10^{-3}
DESAG($\times 2$)	25.75	12.52	2.51
Copper($\times 2$)	63.54	29.00	8.96
Kapton($\times 2$)	12.70	6.36	1.42
<i>Material</i>	<i>t = Δz</i>	<i>X₀(cm)</i>	<i>t/X₀($\times 10^{-4}$)</i>
DME	25.95	0.200	14540.
DESAG($\times 2$)	0.0231	9.877	23.39
Copper($\times 2$)	0.00050	1.469	3.404
Kapton($\times 2$)	0.00250	28.91	0.8647
Total			$55.45 \times 4 = 221.8$

Table 4.2: *Tracking medium data used by GEANT-DIRAC for one SFD detector. There are two identical planes, X and Y (in 2001).*

<i>Material</i>	<i>A</i>	<i>Z</i>	$\rho(g/cm^3)$
Polystyrene	11.16	5.61	1.032
Paint($\times 2$)	18.08	8.77	1.26
Cobex($\times 2$)	13.94	6.90	1.35
<i>Material</i>	<i>t = Δz</i>	<i>X₀(cm)</i>	<i>t/X₀($\times 10^{-4}$)</i>
Polystyrene	0.250	43.55	57.40
Paint($\times 2$)	0.01465	26.23	5.585
Cobex($\times 2$)	0.022	28.91	7.609
Total			$83.79 \times 2 = 167.6$

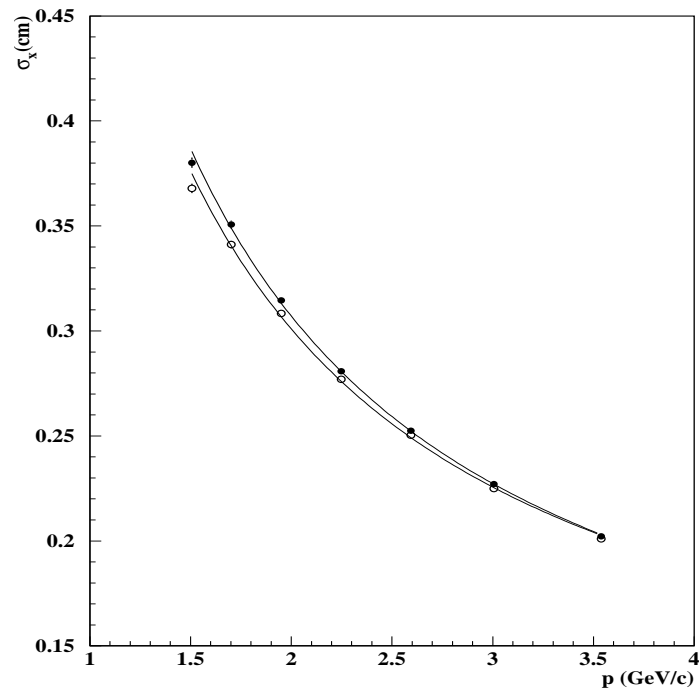


Figure 4.5: Comparison between the vertex resolution in X projection obtained from fitting methods A (full circles) and B (open circles) described in the text. Detector resolutions were $260 \mu\text{m}$ for SFD and $116 \mu\text{m}$ for MSGC.

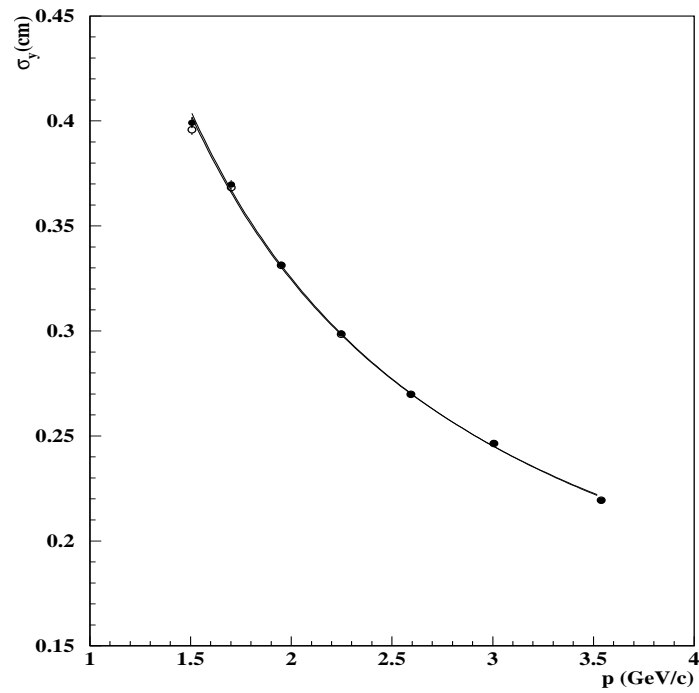


Figure 4.6: Comparison between the vertex resolution in Y projection obtained from fitting methods A (full circles) and B (open circles) described in the text. Same conditions as in figure 4.5.

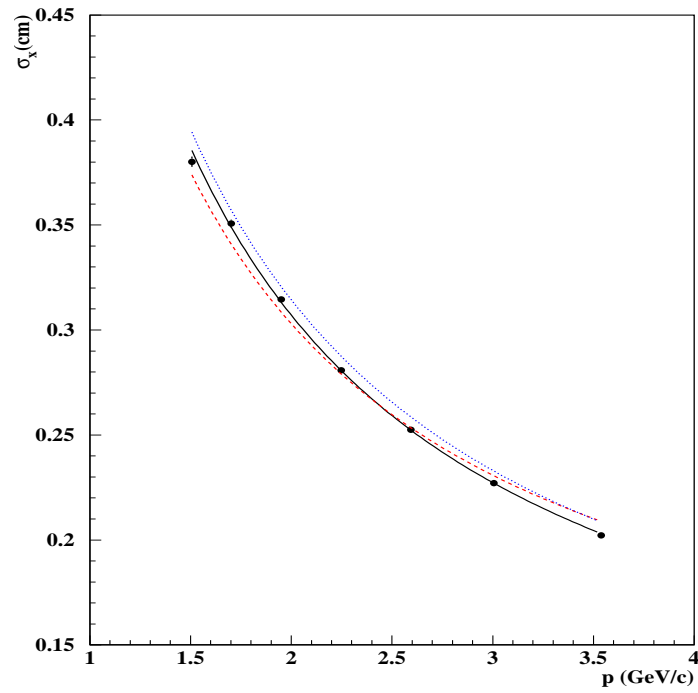


Figure 4.7: Comparison between vertex resolution obtained (in method A) from different hypothesis for the ratio of detector resolutions $\sigma_{sfd}/\sigma_{msgc}$ namely 2 (line), 4 (dashed) and 1 (dotted).

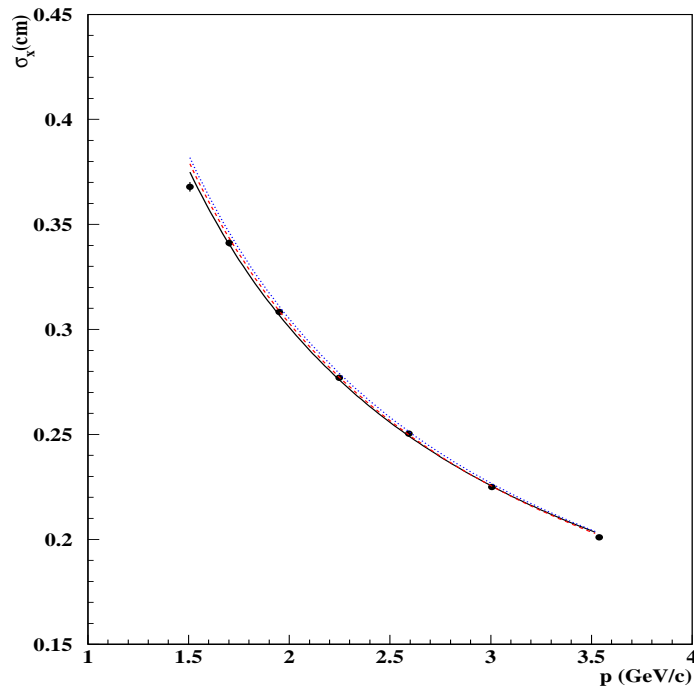


Figure 4.8: Comparison between vertex resolution (X -projection) obtained in method B from different scale factors on overall radiation length detector fractions in covariance matrix. Continuous line and full circles corresponds to the standard setting, dotted line to scale factor 1.5 and dashed line to scale factor 0.5 (note scattering angle scales with the square).

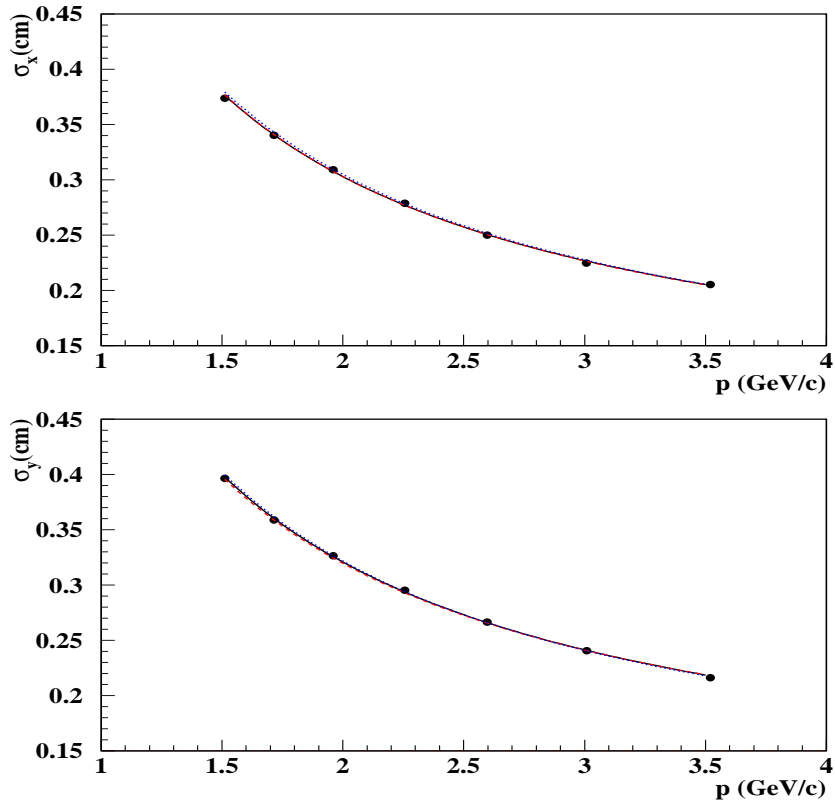


Figure 4.9: Comparison between vertex resolution obtained after variation of the MSGC cluster size shown in figure 4.10. The full circles and line correspond to the standard digitisation, where real multiplicity is simulated. Dotted/dashed lines are obtained with all clusters having one/two microstrips only.

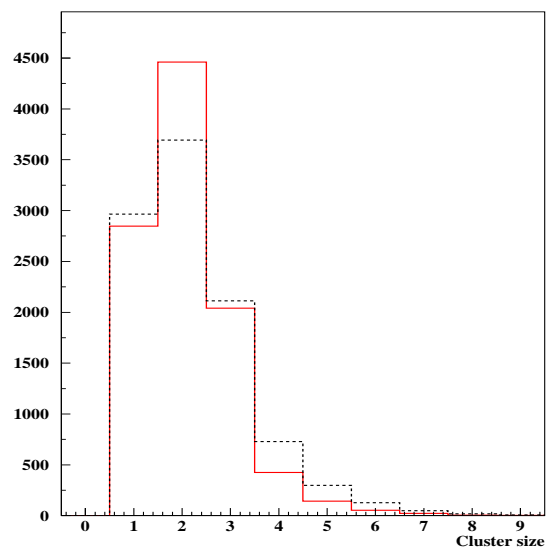


Figure 4.10: *Distribution of microstrip multiplicity (cluster size) of MSGC hits in real 2001 data. Black dashed line includes background hits, whereas red line only those that belong to tracks.*

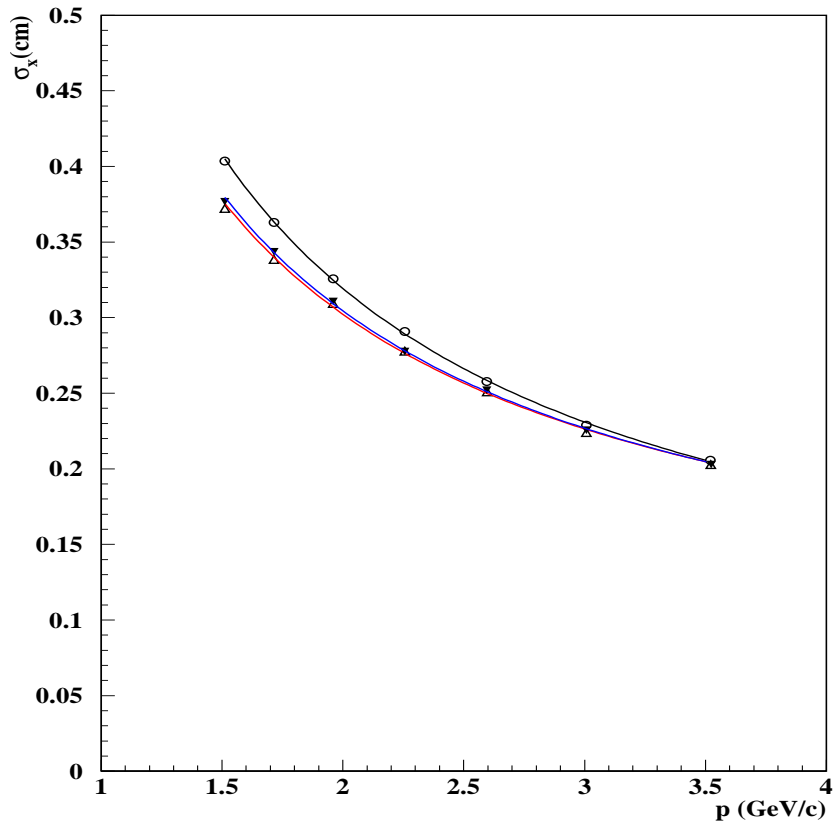


Figure 4.11: Comparison between vertex resolution (X -projection) obtained after variation of MSGC background level. Open/full triangles indicate $\pm 10\%$ variation of MSGC average hit multiplicity, with respect to the observed (standard) values in figure ???. Open circles show the case where MSGC background is totally removed (lines are also shown in all cases, following a fit to $a + b/p$ parametrisation).

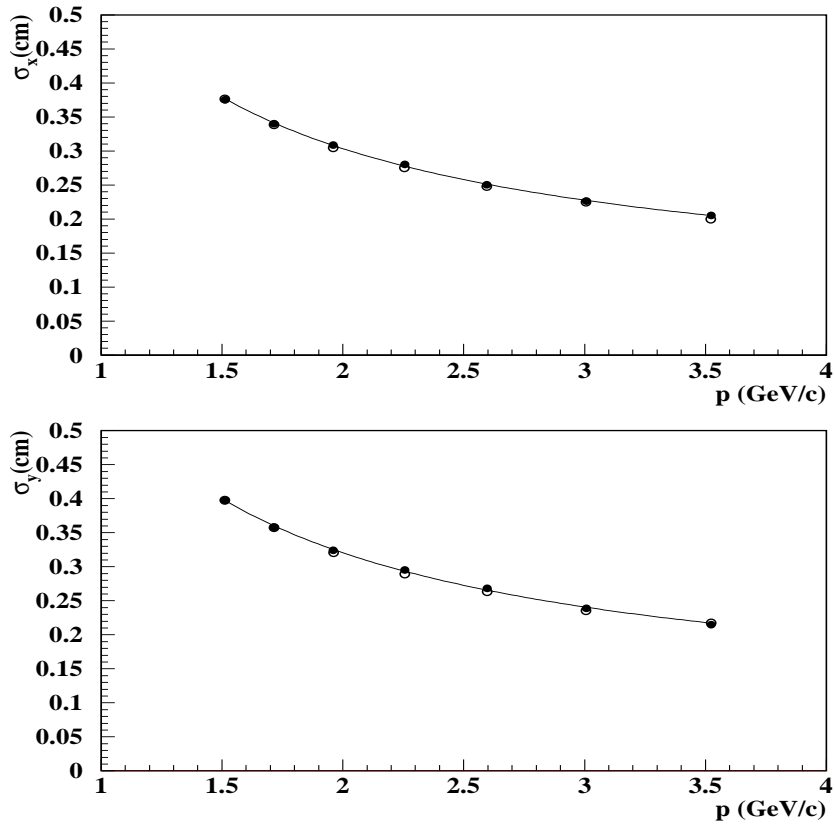


Figure 4.12: Comparison between vertex resolution in X (top) and Y (bottom) obtained from standard simulation (full circles) and simulation with SFD background removed.

4.2.5 Beam spotsize and accidental pairs

In order to make an accurate comparison between spectrometer data and $\pi^+\pi^-$ Monte Carlo, we have corrected the prompt experimental data to account for the approximately 10% background of accidental pairs which can be determined from observation of the precision time-of-flight spectrum. In fact, vertex resolution (determined by the MSGC's) is sensitive to the presence of fluctuations of track origin within the beam dimensions, as they are expected to happen with accidental pairs. This is illustrated in figure 4.13, where prompt pairs are compared with accidentals. The difference is more significant in the vertical projection, where the beam dispersion is significantly larger.

In the results presented so far, a 10% fraction of the observed vertex distribution for accidental pairs was subtracted bin-by-bin from the prompt distribution, before the Gaussian fit is done, at every momentum interval. The actual effect of this subtraction is quite small, even in vertical projection. It should be recalled that only the central part of the vertex distribution is fitted to a Gaussian (see figure 4.2). We have cross-checked that the observed behaviour with real data is indeed well understood by a specific Monte Carlo made for accidental pairs, where the beam dimensions can be changed.

The beam spotsize can be determined using only experimental data, by fitting the points in figure 4.13 to the expression $\sigma_{x,y} = \sqrt{A_{x,y}^2 + B_{x,y}^2/p^2}$, where the $A_{x,y}$ parameter represents momentum-independent fluctuations (detector resolution and beam size), and the $B_{x,y}$ parameter those from multiple scattering. By taking the differences $\sqrt{A_{acc}^2 - A_{prompt}^2}$ we can estimate the beam dimensions, and the results are indicated in table 4.3. They are in reasonable agreement with those of reference [81]. It is remarkable that, despite the strong variation from A_x to A_y for accidental pairs (due to beam width), the values of B_x and B_y are hardly different, as expected. Note the data cover the full 2001 data period with Ni 24 GeV/c beam.

Table 4.3: *Fitted values for A and B from prompt and accidental pairs, and beam spot sizes σ_x and σ_y determined from A parameters. Note that only statistical errors are quoted here.*

	$A_x(\text{cm})$	$B_x(\text{cm}\cdot\text{GeV}/c)$	$A_y(\text{cm})$	$B_y(\text{cm}\cdot\text{GeV}/c)$
Prompt	0.133 ± 0.002	0.552 ± 0.003	0.154 ± 0.002	0.570 ± 0.003
Accidentals	0.150 ± 0.002	0.552 ± 0.003	0.252 ± 0.001	0.547 ± 0.003
	$\sigma_x(\text{cm})$	$\sigma_y(\text{cm})$		
	0.069 ± 0.005	0.204 ± 0.002		

4.2.6 Long lifetime particles

The strong time coincidence, achieved with precision time-of-flight counters for prompt pairs, may still correlate pion pairs from the same proton interaction, where one of them is actually the decay product of another particle, with delay shorter than 0.9 ns . It is in principle possible that those long-lifetime decays (no larger than 10% , as determined by the pionium analysis program) gave a wider transverse vertex distribution, and that this effect might be the explanation of the resolution shortfall.

We have made a simple check, by selecting only pairs where one of them has a muon tag, determined by the coincidence of muon counters and pre-shower detector signals. The vertex resolution from those events (100% muon tagged) is compared with the standard one from prompt pairs (where muon tagged events were vetoed) and it is shown in figure 4.14. The observed muon fraction (rejected by standard ARIANE reconstruction) is about 10%, in agreement with expectation, and the lab momentum spectra are compared in figure 4.14, showing a softer muon spectrum, probably due to neutrino emission. Despite the fact that pion lifetime is larger than any other possible long-lifetime resonance contribution, the vertex distribution is

hardly distorted in the transverse direction. Note should be taken that the $Q_T < 4\text{MeV}/c$ cut avoids large-angle tracks by construction, no matter how large the resonance mass can be. So it is clear that a possible explanation of resolution deficit by long-lifetime decays can be safely excluded.

4.3 Conclusions

The following conclusions can be derived from the analysis presented in this note:

- 1) The average multiple scattering angle in upstream detectors is underestimated by standard GEANT-DIRAC Monte Carlo by $15 \pm 1.5\%$. Wrong values were therefore used as the baseline analysis for DIRAC lifetime publication [5], which needs to be revised, both for real values and for systematic error analysis. The results agree with our presentation to the collaboration made on February 19. We find no other possible interpretation of the vertex resolution data analysed here.
- 2) Measurements of multiple scattering angle from a dedicated setup using drift chambers have been reported [79]. We did not find in this publication a direct comparison with GEANT-DIRAC Monte Carlo for the detectors under test, but rather a determination of an equivalent radiation length based upon a three-Gaussian fit². Since this is far from being the approach followed by GEANT, we see no way to derive conclusions from the approximate equality of the equivalent radiation lengths found in [79] for MSGC and SFD-X and those quoted in tables 4.1 and 4.2. Apart from the fact that the usual radiation length fraction concept, as illustrated for example in formula (4.1), is not used in any of the two approaches, the definition of *equivalent* is different: in one case, it arises from the three-Gaussian fit, and in the other

²it is interesting to remark that this equivalent radiation length of pure elements like Ni and Al are larger than those reported by the Particle Data Group [78] by factors 1.15 and 1.20, respectively.

from utilisation of Dahl's formula (4.2), actually outside the GEANT tracking framework.

- 3) We find no sign of poor performance of GEANT-DIRAC tracking, using Molière-Bethe theory, after having rescaled the average multiple scattering angle in upstream detectors. On the contrary, after this rescaling (which is mathematically equivalent to a redefinition of average A, Z and/or small thickness or geometry changes), the performance is really good in all critical distributions such as momentum and opening-angle dependence of vertex resolution. This is the simplest and most effective solution, since what the DIRAC experiment needs is an accurate description of Q_T resolution in $\pi^+\pi^-$ phase space, and this goal is fully achieved, as it has been demonstrated.

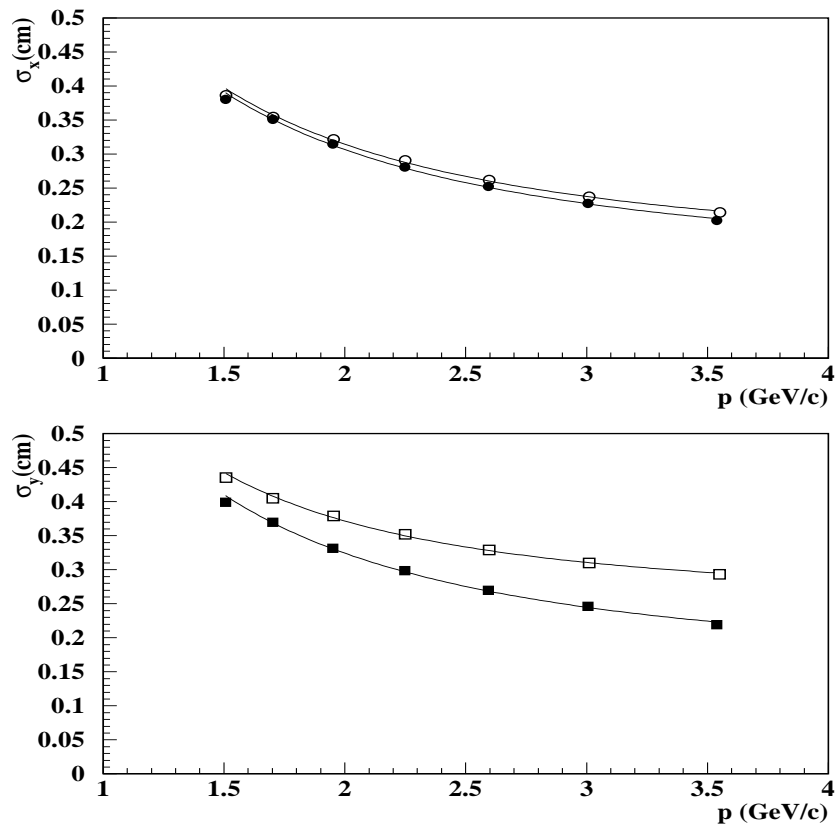


Figure 4.13: Comparison between vertex resolution observed for prompt pairs (black) and accidental pairs (open) of 2001 data period. Top figure refers to X-projection and bottom figure to Y-projection.

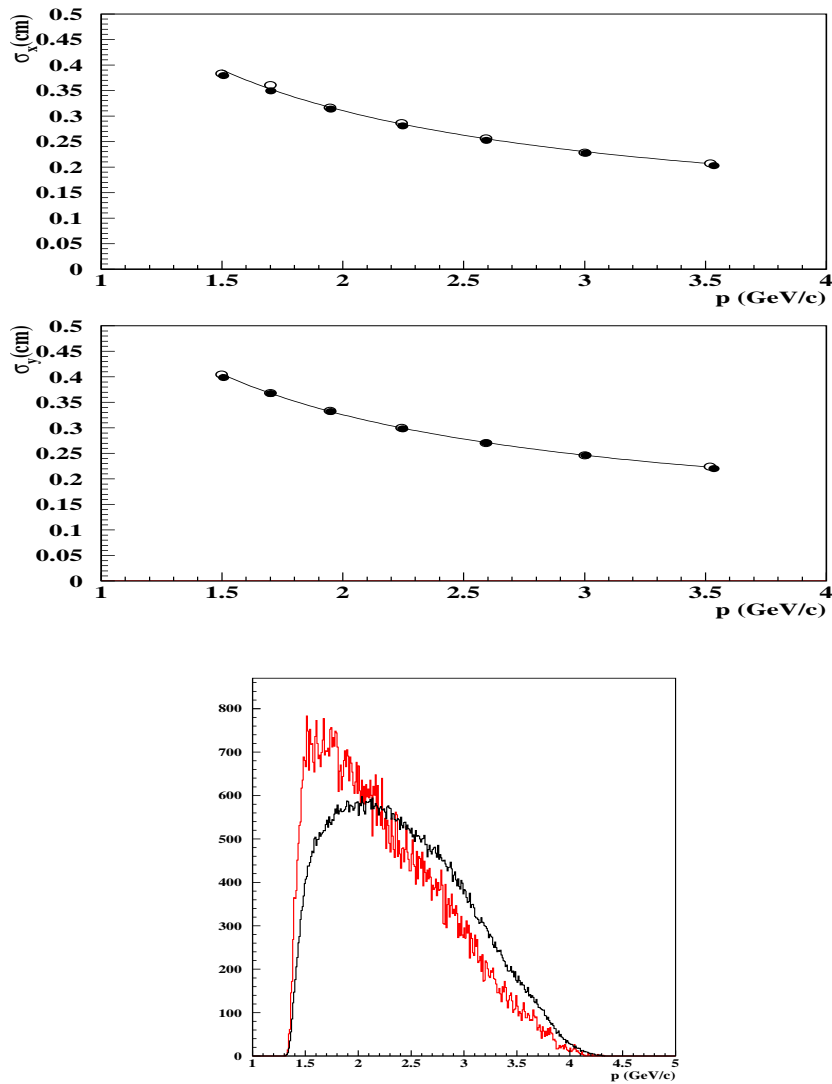


Figure 4.14: Comparison between vertex resolution observed with prompt pairs having muon tags removed (full circles) and pairs with only muon tags (open circles). X and Y projections are shown separately. The bottom figure shows the momentum spectra for the corresponding prompt (black) and muon-tagged (red) pairs, with equal normalisation.

Chapter 5

Study of Kaon Contamination in DIRAC

5.1 Determination of the $K^\pm\pi^\mp/\pi^+\pi^-$ ratio

In order to understand the physics of strangeness production in proton-Ni collisions in DIRAC (at $24 \text{ GeV}/c$ proton momentum), particularly in 2001 data runs, we have determined the momentum dependence of the observed $K^+\pi^-$ and $K^-\pi^+$ signals, normalized to the semi-inclusive $\pi^+\pi^-$ production. The results obtained were compared with the UrQMD Monte Carlo [69], with special emphasis in checking whether the momentum derivative is correctly described by this relativistic model. In the following, we shall denote these by ratios $r_K^+ = K^+\pi^-/\pi^+\pi^-$ and $r_K^- = K^-\pi^+/\pi^+\pi^-$.

The TOF detector (Vertical Hodoscopes) is sufficiently precise to provide a clear K^\pm signal from the time difference $\Delta t = t_- - t_+$ between the two hodoscopes [82], once the pion mass hypothesis is made in the (\mp) arm, opposite to the charged kaon under search. The best K^+ signal analysis is provided by the invariant mass squared, according to the expression:

$$M_+^2 = p_+^2 \left[\left(\frac{L_-}{L_+} \sqrt{1 + \frac{M_\pi^2}{p_-^2}} - \frac{c\Delta t}{L_+} \right)^2 - 1 \right] \quad (5.1)$$

and similarly M_-^2 for K^- , after overall sign flipping in the above expres-

sion. L_{\pm} and p_{\pm} are the respective pathlengths and momenta, in each arm. Invariant mass resolution degrades with increasing momentum of the analyzed particle p_{\pm} , which is equivalent to increasing momentum of the sum $p = p_{+} + p_{-}$, given the fact that the trigger structure makes positive and negative momenta nearly equal. We have analyzed both the positive and negative kaon mass spectra in 11 $200\text{MeV}/c$ bins of the pair momentum p , as it is shown in Figs. 5.1 to 5.11. It can be appreciated that mass resolution is still good enough up to pair momenta of $5.0\text{ GeV}/c$. Guided by the observed spectra, we have parametrized the signals by a two-gaussian fit added to a polynomial background, for each momentum bin. The $\pi^{+}\pi^{-}$ signal (which is observed at M_{π}^2), was also analysed in this way, using the same two-gaussian parametrization as for the $K^{\pm}\pi^{\mp}$ signal, as expected from the approximately equal resolution. The ratio r_K^{\pm} found after background subtraction at each momentum bin, is displayed in Fig. 5.12 as function of pair momentum p . The analysis shown in the previous figures includes the full Ni 2001 data sample, with normal physics runs, as it was used for pionium lifetime analysis [66]. In the 3 lowest momentum bins the statistical errors were slightly increased (by factors 2.5, 2.3 and 1.8 for K^{-} and 2.0, 1.9 and 1.2 for K^{+}), in order to cope with a small systematic discrepancy with respect to the parametrization at the left side of both the $K^{+}\pi^{-}$ and $K^{-}\pi^{+}$ signals, nearly invisible in the figures. Such increase was not needed in the other bins, the χ^2 values being excellent in all cases.

Fig. 5.12 shows a clear rise of both r_K^{+} and r_K^{-} ratios as function of momentum. In addition, the K^{+} signal is very significantly larger than the K^{-} , by a factor 2.75 on average. We have studied whether this behaviour can be understood by the strangeness production model in the UrQMD Monte Carlo, and for that purpose we evaluated both the physics output of the model, as well as the DIRAC spectrometer efficiency, particularly important because of the K^{\pm} longer lifetime as compared to $\pi^{+}\pi^{-}$.

This was done in two steps:

a) 2049 million $p\text{Ni}$ events were generated at proton momentum $24\text{ GeV}/c$ (using UrQMD version 1.3) and all $K^{+}\pi^{-}$, $K^{-}\pi^{+}$ and $\pi^{+}\pi^{-}$ pair combinations were selected in the final state, after requiring $4.5^{\circ} < \theta < 7.0^{\circ}$ where θ is the angle between the vector sum of the particle momenta and the in-

coming proton direction. The ratios $K^+\pi^-/\pi^+\pi^-$ and $K^-\pi^+/\pi^+\pi^-$ are plotted as function of pair momentum p in Fig. 5.12. A cut $Q < 30\text{MeV}/c$ was applied to the center-of-mass momentum Q , calculated in the $\pi^+\pi^-$ hypothesis irrespective of particle masses. An additional momentum cut $1.3\text{ GeV}/c < p_{+-} < 5.0\text{ GeV}/c$ was applied for each track.

The UrQMD time parameter [69], which governs the hadron physics, was fixed to $t = 20\text{fm}/c$. In order to take into account the contribution of weak decays into both K^\pm and π^\pm , we have implemented an interface with the PHYTIA/JETSET program by which mesons and baryons are weakly decayed. The correction with respect to the undecayed spectra is small (approximately 5%).

b) in order to evaluate the spectrometer efficiency, we generated π^+K^- events using the standard DIRAC generator for Coulomb pairs (including the correct Coulomb factor with $K\pi$ Bohr momentum) and processed them first through the GEANT-DIRAC interface with the correct particle assignment (lifetime in particular), and later reconstructed them with the same version of the ARIANE program as it was used for the experimental data, under the cuts $Q_L < 22\text{MeV}/c$ (of course calculated in $\pi^+\pi^-$ hypothesis) and $Q_T < 5\text{MeV}/c$. The momentum spectrum of reconstructed $K^\pm\pi^\mp$ events was determined, and divided by that of the generated events, in order to determine the spectrometer acceptance efficiency function. The same operation was done for $\pi^+\pi^-$ pairs, using this time the standard Monte Carlo production chain. It was noted that in the central momentum region (unaffected by edge effects) the $K^+\pi^-$ spectrometer acceptance had a steeper momentum dependence than it had for $\pi^+\pi^-$, as expected from the longer K^+ lifetime. What we are interested in is the ratio between $K^\pm\pi^\mp$ and $\pi^+\pi^-$ efficiency functions. This function is actually the same, for both K^\pm charge modes.

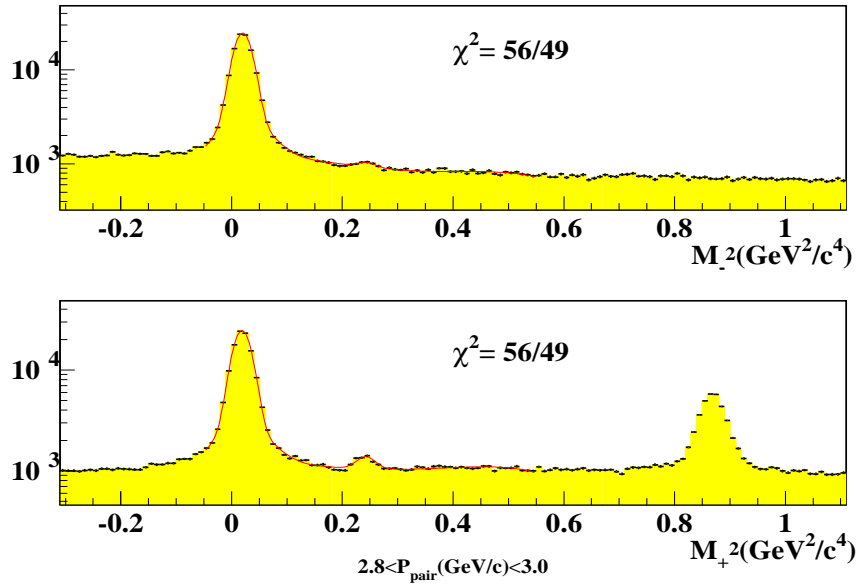


Figure 5.1: Spectrum of squared invariant mass of negative particle M_-^2 when pion mass is assumed in the opposite arm (top). The positive mass M_+^2 is also shown, with the corresponding hypothesis (bottom). Pair momentum interval as indicated. χ^2/ndf values are given for the fit described in the text.

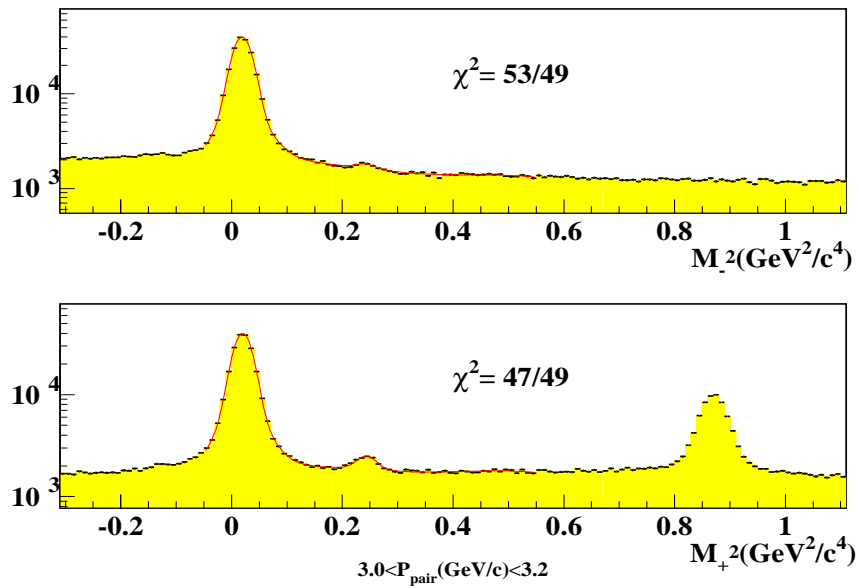


Figure 5.2: Spectrum of squared invariant mass of negative particle M_-^2 when pion mass is assumed in the opposite arm (top). The positive mass M_+^2 is also shown, with the corresponding hypothesis (bottom). Pair momentum interval as indicated.

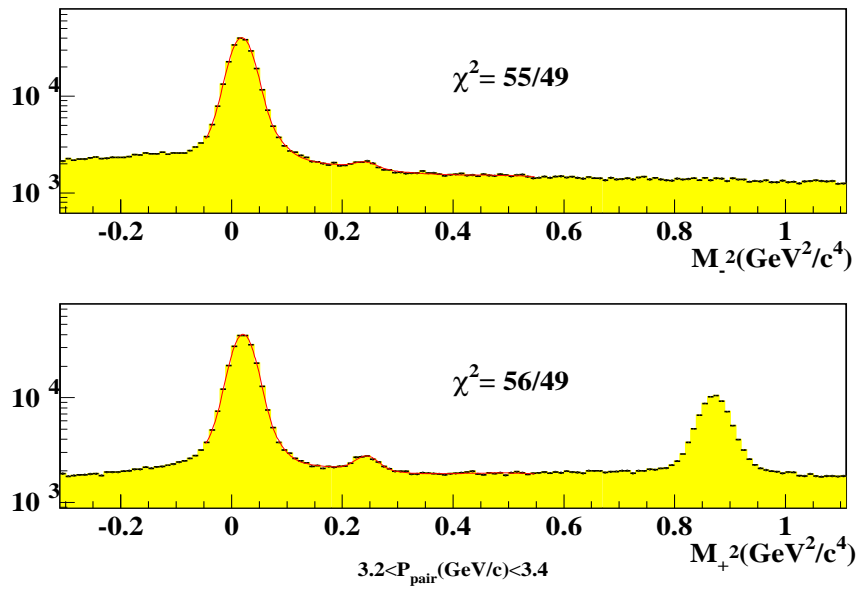


Figure 5.3: Spectrum of squared invariant mass of negative particle M_-^2 when pion mass is assumed in the opposite arm (top). The positive mass M_+^2 is also shown, with the corresponding hypothesis (bottom). Pair momentum interval as indicated.

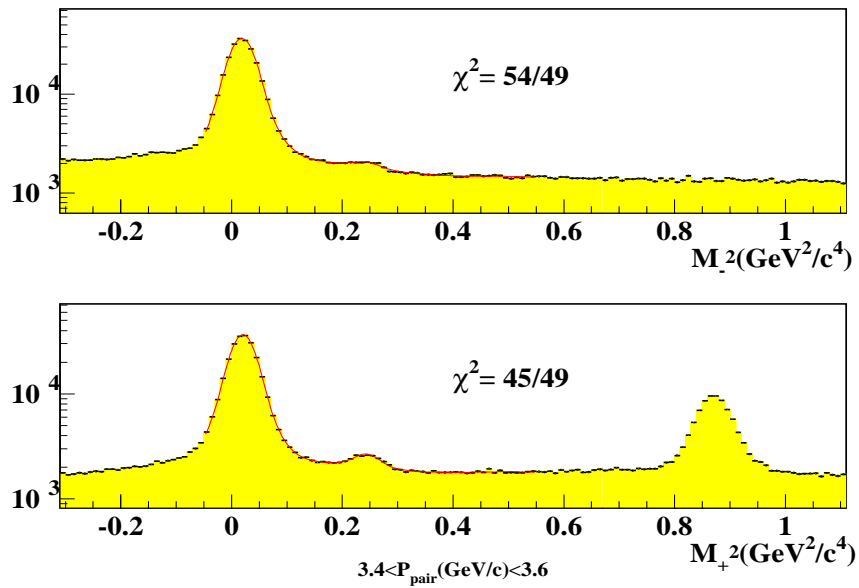


Figure 5.4: Spectrum of squared invariant mass of negative particle M_-^2 when pion mass is assumed in the opposite arm (top). The positive mass M_+^2 is also shown, with the corresponding hypothesis (bottom). Pair momentum interval as indicated.

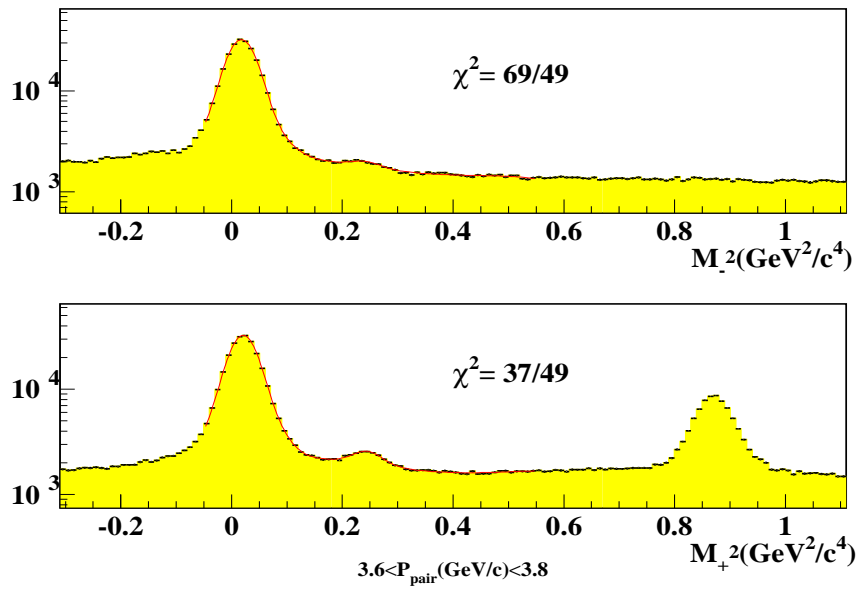


Figure 5.5: Spectrum of squared invariant mass of negative particle M_-^2 when pion mass is assumed in the opposite arm (top). The positive mass M_+^2 is also shown, with the corresponding hypothesis (bottom). Pair momentum interval as indicated.

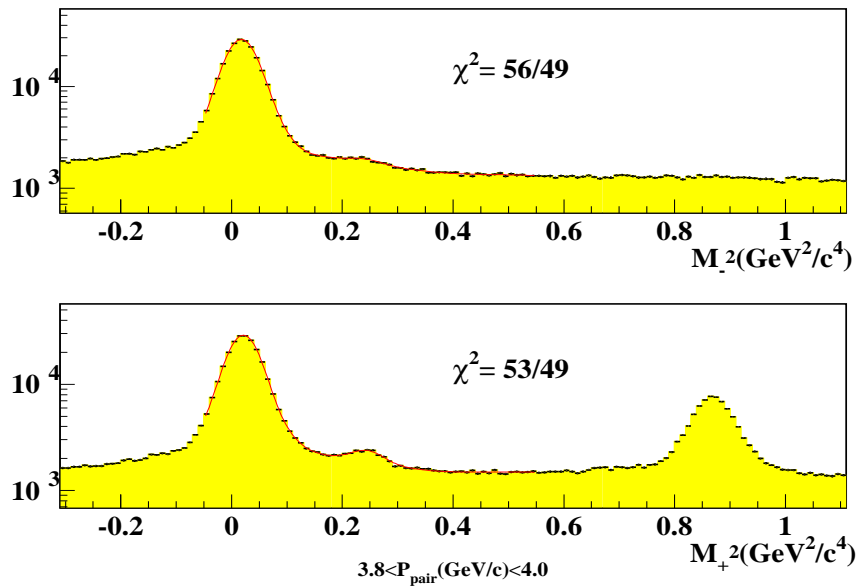


Figure 5.6: Spectrum of squared invariant mass of negative particle M_-^2 when pion mass is assumed in the opposite arm (top). The positive mass M_+^2 is also shown, with the corresponding hypothesis (bottom). Pair momentum interval as indicated.

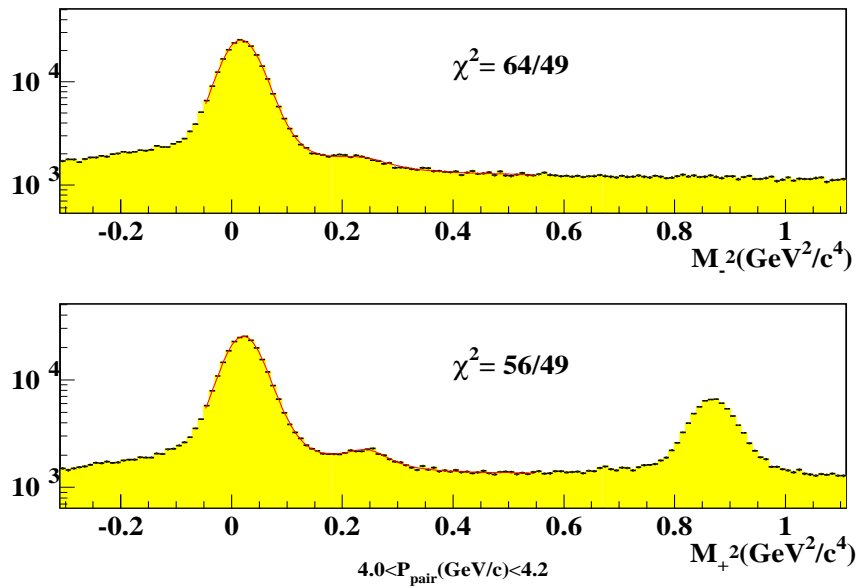


Figure 5.7: Spectrum of squared invariant mass of negative particle M_-^2 when pion mass is assumed in the opposite arm (top). The positive mass M_+^2 is also shown, with the corresponding hypothesis (bottom). Pair momentum interval as indicated.

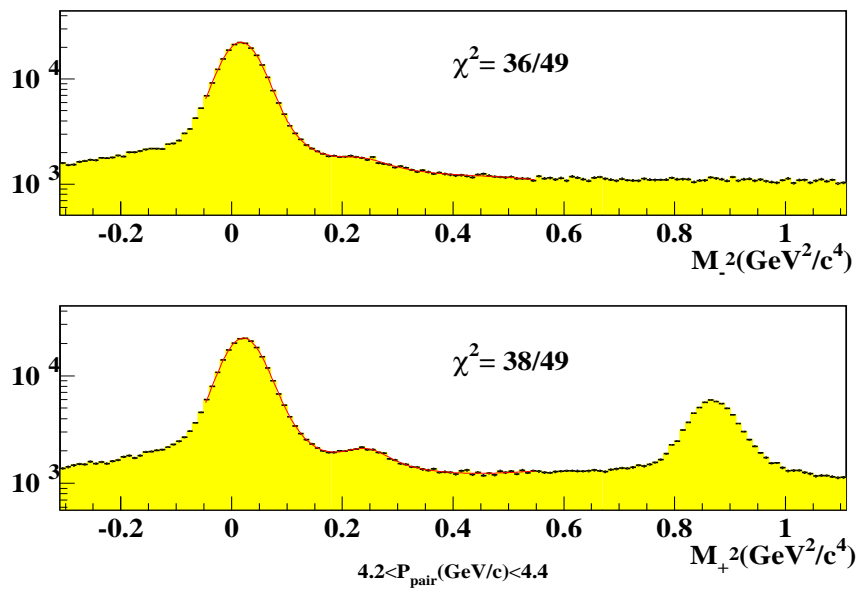


Figure 5.8: Spectrum of squared invariant mass of negative particle M_-^2 when pion mass is assumed in the opposite arm (top). The positive mass M_+^2 is also shown, with the corresponding hypothesis (bottom). Pair momentum interval as indicated.

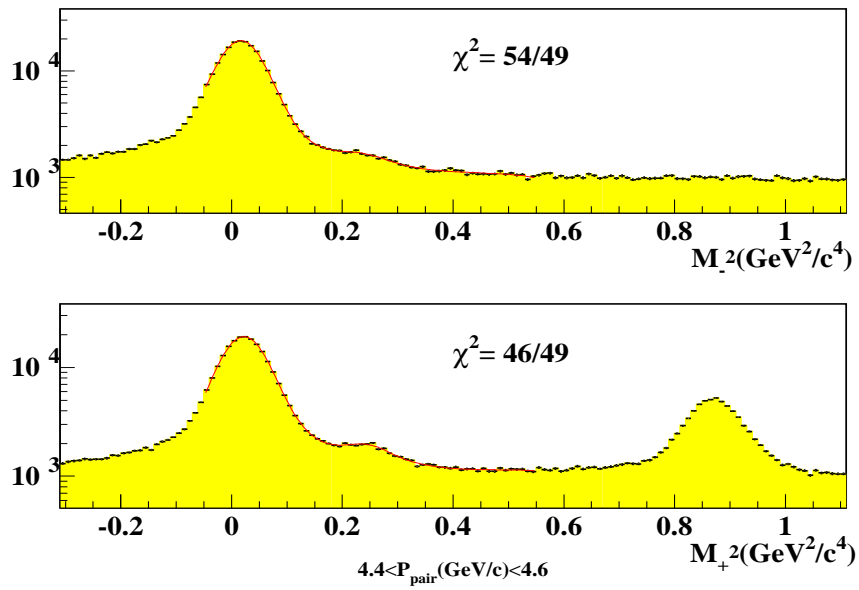


Figure 5.9: Spectrum of squared invariant mass of negative particle M_-^2 when pion mass is assumed in the opposite arm (top). The positive mass M_+^2 is also shown, with the corresponding hypothesis (bottom). Pair momentum interval as indicated.

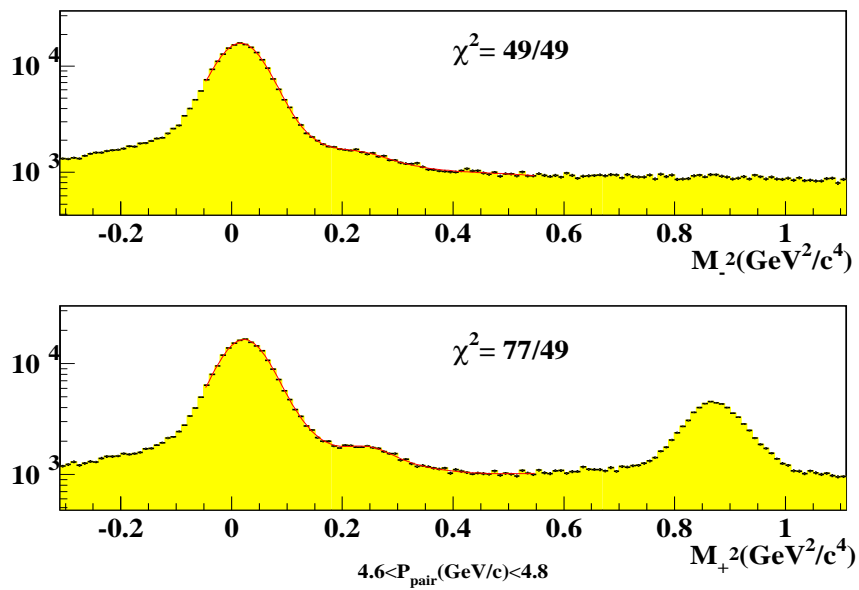


Figure 5.10: Spectrum of squared invariant mass of negative particle M_-^2 when pion mass is assumed in the opposite arm (top). The positive mass M_+^2 is also shown, with the corresponding hypothesis (bottom). Pair momentum interval as indicated.

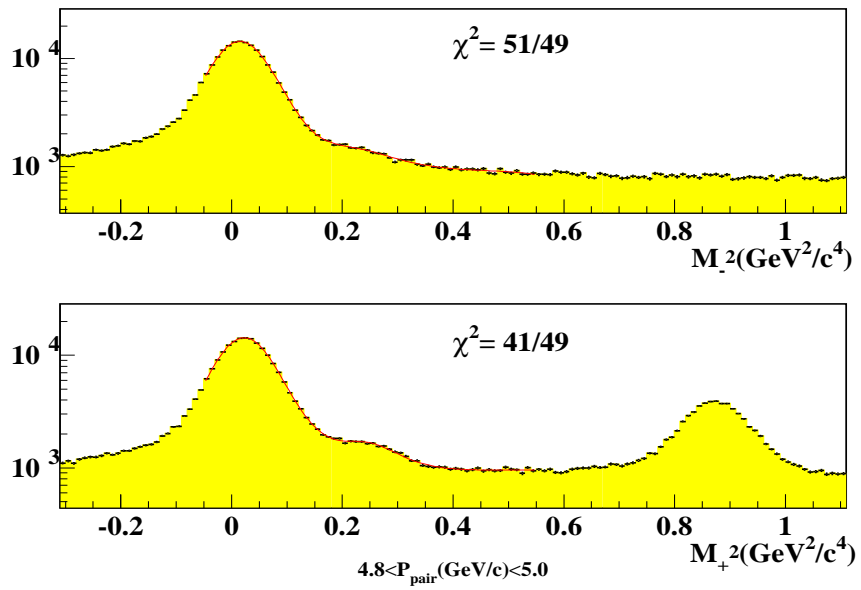


Figure 5.11: Spectrum of squared invariant mass of negative particle M_-^2 when pion mass is assumed in the opposite arm (top). The positive mass M_+^2 is also shown, with the corresponding hypothesis (bottom). Pair momentum interval as indicated.

The r_K^{\pm} spectra given by the UrQMD Monte Carlo physics at the generator level were multiplied by the efficiency function defined above, and the corrected function was compared with the experimental data in Fig. 5.12. It can be appreciated that the momentum derivative of the $K^\pm\pi^\mp/\pi^+\pi^-$ ratio is perfectly well described by UrQMD, for both charge signs in the analysed momentum range. However, the values of r_K^+ and r_K^- ratios do not appear to be correctly described, since the Monte Carlo predictions had to be multiplied by factors 0.60 and 0.31, respectively, in order to find agreement with the experimental data. It seems that, whereas the strangeness momentum spectra are well described, the integrated production rates are not. In any case, the Monte Carlo predicts correctly a smaller $K^-\pi^+$ rate, as compared to $K^+\pi^-$.

5.2 Measurement of K^+K^- at 2.9 GeV/c

When the positive and negative particles accepted by the spectrometer have equal mass, the previous method does not allow mass discrimination, despite the excellent resolution of Time-of-Flight (TOF) hodoscopes. This is because of the narrow Q_L acceptance for normal physics triggers, which makes both particles reach the hodoscopes at practically the same time.

However, upstream tracks contain time information from SFD and Ionization Hodoscope (IH) TDCs. We have up to 6 independent TDC measurements (SFD-X, SFD-Y, IH- X_A , IH- X_B , IH- Y_A , IH- Y_B) for each charged track, so that the time of flight Δt between upstream detectors and vertical hodoscopes can be measured with improved statistical precision. A similar method was used to analyze the $p\pi^-$ background in accidental pairs [60].

For equal-mass pairs, charge ambiguity in the matching procedure does not impede a clear determination of Δt . This is particularly important for the IH, where the probability that both particles hit the same 6 mm slab is high. In this case, only one TDC will be retained, which is perfectly adequate for the measurement.

The time delay Δt can in general be defined as $\Delta t = t_{VH} - t_{up}$, where the upstream time can be constructed by averaging N measurements among

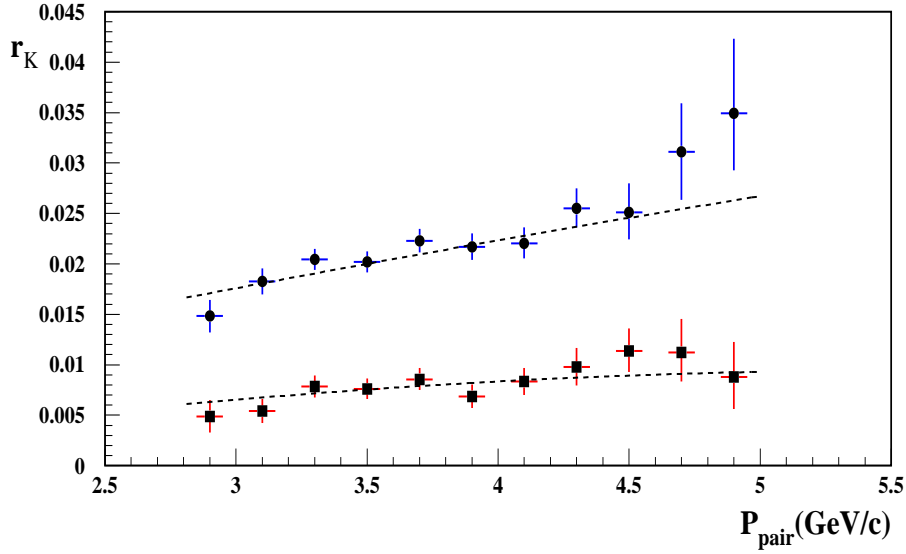


Figure 5.12: Momentum dependence of the measured ratios r_K^+ (circles) and r_K^- (squares). The corresponding dotted lines indicate the acceptance corrected UrQMD Monte Carlo predictions, multiplied by factors 0.5 and 0.25 respectively.

the 6 available detectors $t_{up} = (1/N) \sum_i t_i$.

It is however more convenient to measure squared invariant masses M_i^2 of individual time measurements $\Delta t_i = t_{VH} - t_i$ associated by the upstream tracking to a given charged particle in one arm, with momentum p and path length L :

$$M_i^2 = p^2 \left(\frac{c^2 \Delta t_i^2}{L^2} - 1 \right) \quad (5.2)$$

The particle M^2 is then obtained by averaging the appropriate N individual measurements $M^2 = (1/N) \sum_i M_i^2$.

All IH detector TDC signals associated to upstream tracks are time-

aligned with respect to each other, taking into account propagation time between different layers, as a necessary first step. Despite the excellent detector calibration work available [83], we have noticed that the IH- X_B detector has a wider TDC distribution and slightly different properties than the others. As a consequence, no attempt has been made to include this detector in subsequent analysis, in order to avoid any doubts.

Searching for a K^+K^- signal implies to suppress a huge background from $\pi^+\pi^-$. The most general way to achieve this goal is to use a certain number of detectors to veto the pion signal and a different detector set to perform the mass measurement. According to this, we have developed two extreme methods. The first (method A) is use the three IH detectors to veto and the two SFD's to perform the measurement. The second (method B) is to perform an unbiased measurement (no pion veto) and concentrate all detector measurements to improve mass resolution at the distribution tail.

In both cases, particle velocity has been reduced by a momentum cut $1.4 < p < 1.5$ GeV/c applied for every charged track.

5.2.1 Results from method A

Pairs were selected by requiring that $M_L^2 < M_i^2 < M_H^2$ for all IH hits i associated to tracks by upstream tracking (6 measurements), for different choices of the lower cut M_L^2 , and the squared mass distributions were analysed using SFD X and Y (4 measurements).

A clear signal is observed at the kaon squared-mass, of about the same size as that observed for the pion. As expected, lowering the cut M_L^2 results in increasing pion background, and the opposite effect is observed by setting higher values of M_L^2 , as shown in figure 5.13. The K^+K^- signal is however not unaffected by the M_L^2 values either, due to the acceptance variations implied by the pion veto, which will be studied below.

In order to measure this signal we have first determined the pion squared-mass resolution function $R(x)$, which is a continuous curve (normalized to one) peaked at $x = 0$, with $x = M^2 - M_\pi^2$ and M_π^2 the observed pion mass¹. We determine this curve with high statistical precision by going to lower

¹the analytical expression and parameter values of this function will be reported in the

values of M_L^2 , and apply the same resolution function for the kaon, since all instrumental effects are identical in both cases ².

A maximum likelihood fit is then performed to the entire mass spectra for 8 different choices of M_L^2 , having a generic number of events N in the fit. The probability density for an event with mass M_i^2 is given by :

$$L_i = (1 - \alpha)R(M_i^2 - M_\pi^2) + \alpha R(M_i^2 - M_K^2) \quad (5.3)$$

where the M_π^2 value is left free to allow for small biases as function of pion veto. The kaon mass M_K^2 is however a fixed parameter, with its value being calibrated by the observed pion mass M_π^2 without pion veto, after adding the difference $M_K^2 - M_\pi^2$ given by PDG values.

Maximization of $\prod_{i=1}^N L_i$ as function of α , under the constraint $\int_{-C}^C R(x)dx = 1$ with $C = 0.4GeV^2/c^4$, provides the number of K^+K^- pairs as $N(K^+K^-) = \alpha N$.

Because of the fact that the kaon resolution function is not entirely contained within the bias interval (M_L^2, M_H^2) , the K^+K^- signal efficiency will be a calculable function of the lower limit M_L^2 . Note that the relevant resolution function $R(x)$ here involves the measurement with a single generic IH detector ³, and it can be easily determined with pions. Its parametrization is given in table 5.2 (see next subsection). If we call $\epsilon = \int_{M_L^2}^{\infty} R(x)dx$ then the K^+K^- acceptance probability is given by :

$$A(M_L^2) = \epsilon^{6-3s(1-s)^2-2[3s^2(1-s)]-3s^3} \quad (5.4)$$

where s is the average probability that both particles intersect the same IH slab. The last three terms in the exponent are related to the probability of single, double and triple same-slab coincidences among the three active counters, respectively. They can easily be determined from real data by using the upstream track extrapolations. The above expression takes into account

next subsection.

²a partial derivative analysis of expression (5.2) reveals that a resolution factor $\sigma(M_\pi^2)/\sigma(M_K^2) = \sqrt{M_\pi^2 + p^2}/\sqrt{M_K^2 + p^2}$ is expected from the slightly different mass scale. This accounts for a 5% effect only, and its effect is negligible.

³the average is taken between the three active detectors, which differ very little among themselves

the fact that rather than having 6 independent detector measurements, there are actually a reduced number of them, due to same-slab intersections. The effective exponent is accurately determined from the real data to be 5.14, which corresponds to $s = 0.30$.

In figure 5.16 we show that the function $A(M_L^2)$ provides a good description of the K^+K^- signal data found from the 8 maximum likelihood fits. Errors in α are given by MINOS variation with account taken of the correlation with M_π^2 . These are converted into $N(K^+K^-) = \alpha N$ errors, where the observed number of events N is also subject to error. A line for a 0.5% contamination hypothesis is also shown in figure 5.16 for reference.

The plateau value indicates 61 ± 10 K^+K^- events, where the 1σ error can be determined from any of the M_L^2 choices without significant variation ($0.15 \text{ GeV}^2/c^4$ is chosen for reference). It should be noted that this plateau is rather insensitive to small variations of the exponent, compatible with the data. As a matter of fact, a change of ± 0.2 (contradicting measured values) produces only ± 1 events in the plateau, still having a good description of the data in figure 5.16.

It is clear that the observed K^+K^- signal is genuine and it can by no means be explained as a consequence of the applied bias. This point has been checked by applying an opposite bias according to the mirror-symmetric cut $2M_\pi^2 - M_L^2 < M_i^2 < 2M_\pi^2 - M_H^2$ for all active IH detectors i . The result are shown in figures 5.17 and 5.18 for 6 different values of M_L^2 . In fact, the K^+K^- signal is totally removed, and in addition no significant signal is generated in the bias region, which shows that correlation between IH and SFD measurements is actually quite small. A significant correlation could only be induced by the presence of background tracks crossing all upstream detectors, which is strongly suppressed by the timing requirements ($5.5ns$) of upstream tracking.

When the total number of $\pi^+\pi^-$ pairs is taken into account, the previous result can be converted into a measurement of the ratio $\epsilon_K = N(K^+K^-)/N(\pi^+\pi^-) = 0.238 \pm 0.035 \%$.

5.2.2 Results from method B

A second analysis method comes from making a direct fit to the mass spectrum in which all (IH+SFD) detectors are used for the measurement, without any attempt to perform a $\pi^+\pi^-$ veto. The K^+K^- signal is then observed at the distribution tail. A good description of the pion resolution function for the mass measurements M_i^2 is provided by the parametrization:

$$R(x) = Ae^{-(a_1|x|^2+a_2|x|^3+a_3|x|^4)} \quad (5.5)$$

for $x \geq 0$ and $R(x) = Ae^{-(b_1|x|^2+b_2|x|^3+b_3|x|^4)}$ for $x \leq 0$, with $x = M_i^2 - M_\pi^2$, where M_π^2 defines the peak value, which is allowed to differ slightly from the true pion squared-mass from PDG, due a systematic error. Since there is no reason to expect left/right symmetry about the peak value, $a_i \neq b_i$ are allowed by the fit. Proper normalization is ensured by the A parameter, according to $1/A = \int_{M_\pi^2-C}^{M_\pi^2+C} R(x)dx$ with $C=0.4 \text{ GeV}^2/c^4$ (which is infinity in practical terms).

The K^+K^- signal is parametrized by the same function $R(x)$ used for the pion, with peak value shifted by $M_K^2 - M_\pi^2$ according to PDG values. As in the case described above for method A, a maximum likelihood fit is made to the hypothesis expressed by equation (5.3) in the mass interval $I_C = (M_\pi^2 - C, M_\pi^2 + C)$, as shown in figure 5.19, in order to determine the fraction α , and the corresponding number of K^+K^- pairs.

The fit has been done in two steps: first determine the 7 parameters of the resolution function (a_i, b_i and M_π^2) for $M^2 \leq M_0^2$ ($M_0^2 = 0.135 \text{ GeV}^2/c^4$ has been chosen), and then extend the fit to the full region I_C , keeping the $R(x)$ parametrization fixed. Results can be appreciated in figure 5.19 and in table 5.1. The fitted number of K^+K^- pairs is 65 ± 10 .

For the sake of simplicity, we have referred throughout this note to a generic pion resolution function $R(x)$, due to the fact that all parametrizations of it do have the same functional form. However, the parameter values are different in each case, depending upon which (and how many) detectors are used for the measurement. We give in table 5.2 the fitted parameters when SFD X and Y detectors are used in method A, and also those corresponding to a single (generic) IH detector, as it was used for the acceptance

Table 5.1: Parameter values for parametrization (5.5) obtained for mass measurement using all (IH+SFD) upstream detectors (left), and fit results for method B described in the text (right). The variation of the likelihood is also indicated for two hypothesis: 0.5 % K^+K^- signal, and no signal at all.

M_π	$0.0188 \pm 0.0014 \text{ GeV}^2/c^4$
a_1	201 ± 18
a_2	-462 ± 181
a_3	511 ± 508
b_1	199 ± 8
b_2	-137 ± 46
b_3	-650 ± 92
α	0.9975 ± 0.0004
N_k	65 ± 10
$\epsilon_k(\%)$	0.253 ± 0.038
χ^2/ndf	$69.57 / 55$
$\Delta L(\text{no signal})$	38
$\Delta L(\text{signal } 0.5\%)$	17

ϵ calculation.

Table 5.2: *Parameter values for the pion squared-mass resolution function according to expression (5.5), from minimum- χ^2 fits for measurements using SFD X and Y without pion veto (left), and using a single generic IH detector (right). For the latter, the average between the three active detectors has been taken, as described in the text.*

	SFD	IH
$M_\pi(\text{GeV}^2/c^4)$	0.0114 ± 0.0004	0.0378 ± 0.0007
a_1	103 ± 8	66.8 ± 3.4
a_2	-216 ± 12	$105. \pm 13$
a_3	258 ± 24	47.5 ± 12.6
b_1	131 ± 10	43.0 ± 5.4
b_2	39.7 ± 33.3	5.79 ± 29.97
b_3	-713 ± 29	-85.4 ± 44.5
χ^2/ndf	$9.3 / 11$	$23.3/25$

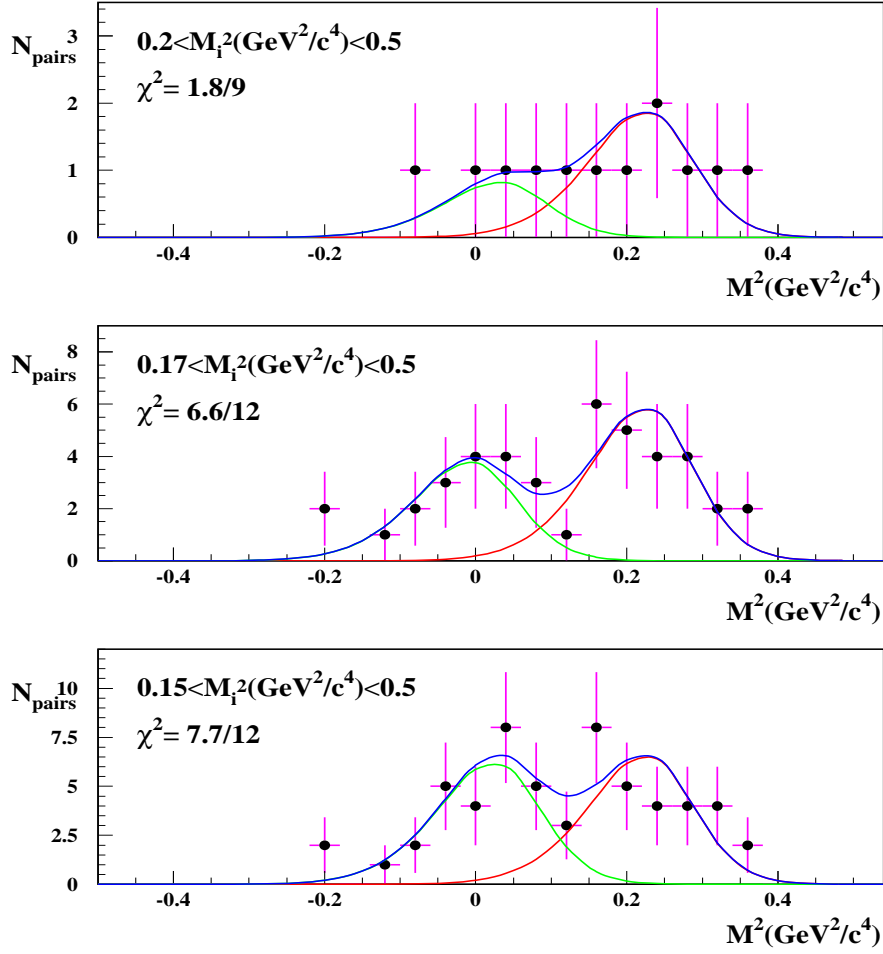


Figure 5.13: Average squared invariant mass of particle pairs measured from TDCs of SFD X-Y according to expression (5.2). All individual hit measurements M_i^2 associated to any of the two upstream tracks in IH detectors have been restricted to the indicated limits $M_L^2 < M_i^2 < M_H^2$. The results of the maximum likelihood fit are shown in each case, indicating the progression of the $\pi^+\pi^-$ (green), K^+K^- (red) signals, and of the sum (blue), with decreasing lower limit M_L^2 . χ^2 values are indicated only for reference.

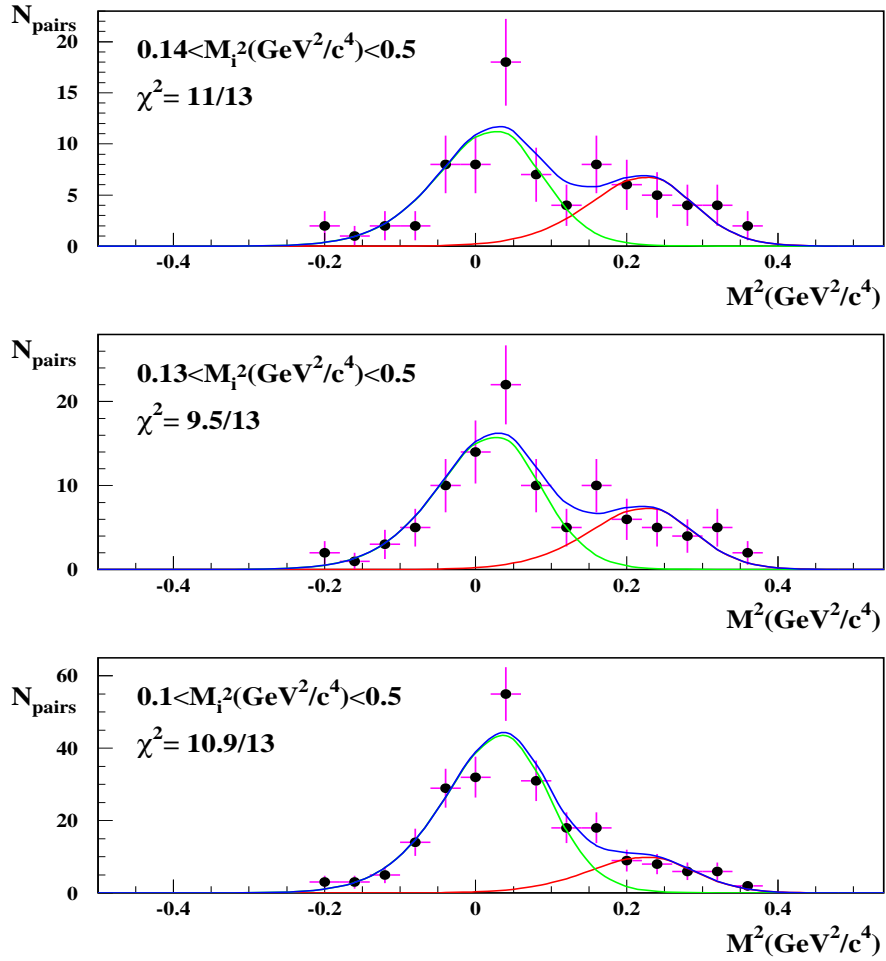


Figure 5.14: Contents are the same as in figure 5.13, the progression continues from $M_L^2 = 0.14 \text{ GeV}^2/c^4$ (top) to $M_L^2 = 0.10 \text{ GeV}^2/c^4$ (bottom)

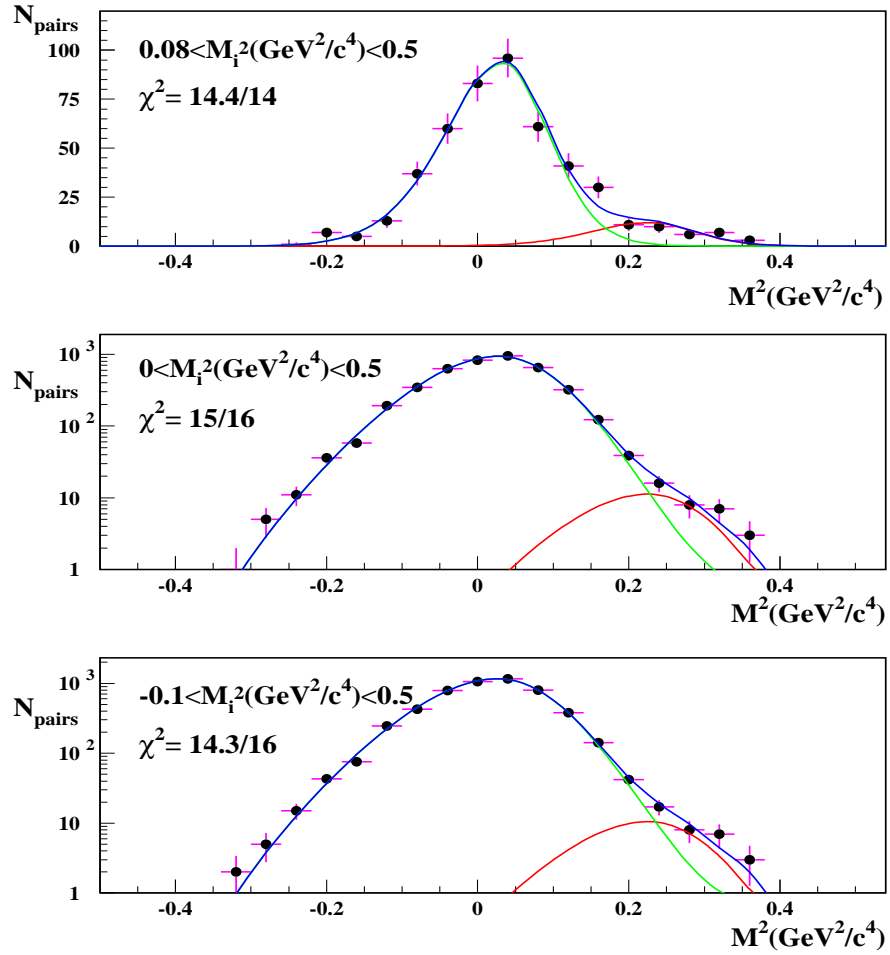


Figure 5.15: Contents are the same as in figure 5.13, the progression continues from $M_L^2 = 0.08 \text{ GeV}^2/c^4$ (top) to $M_L^2 = -0.10 \text{ GeV}^2/c^4$ (bottom)

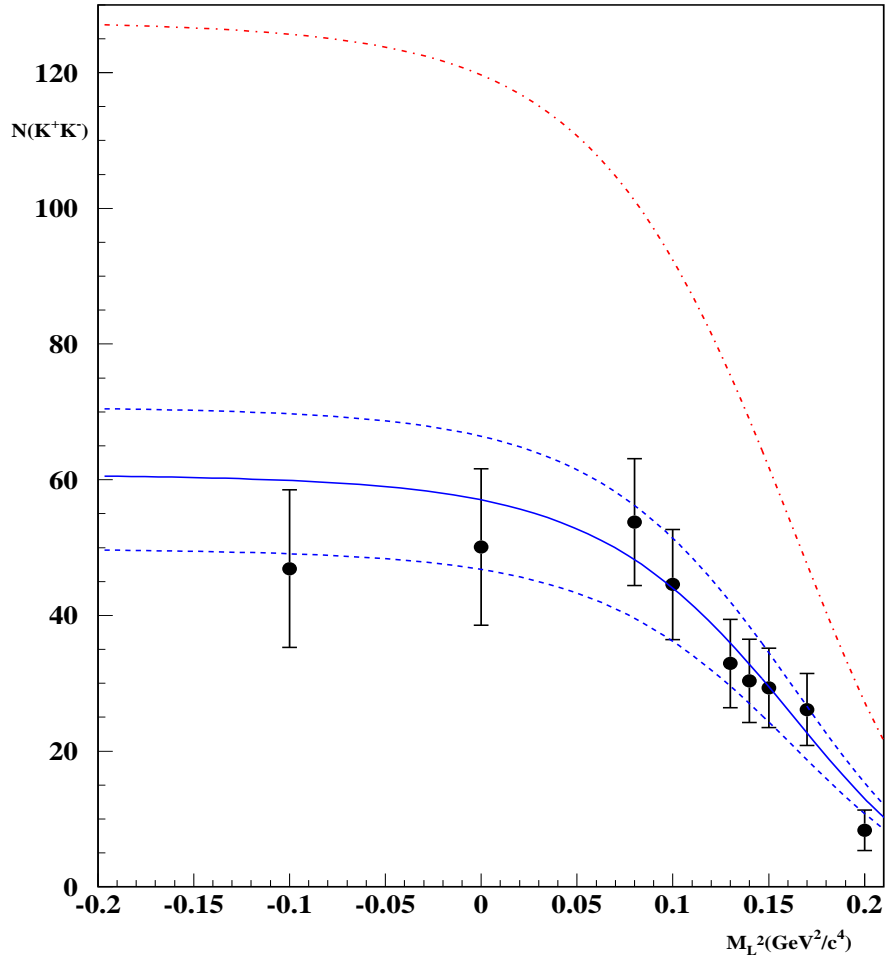


Figure 5.16: Number of K^+K^- pairs determined from the maximum likelihood fit shown in figures 2 to 4. The continuous line shows the function $A(M_L^2)$ (5.4) multiplied by $N(K^+K^-)=61$ events.

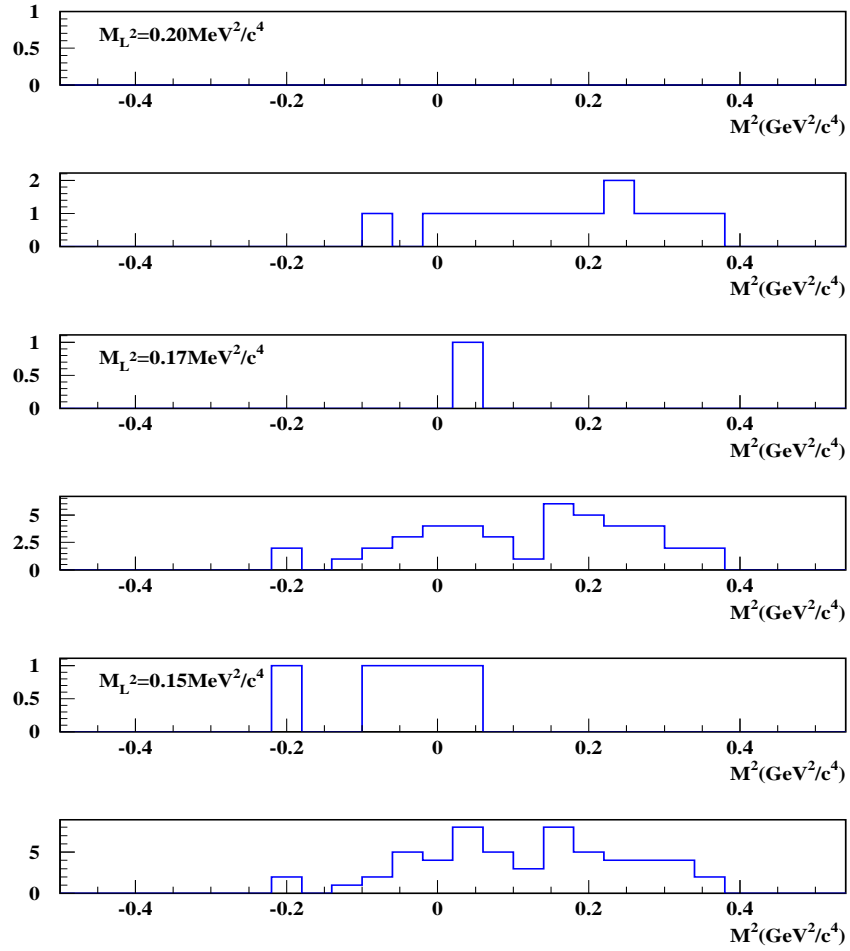


Figure 5.17: Comparison between some of the squared-mass distributions in figures 2 to 4 (bottom) and the ones obtained with the mirror-symmetric cuts $2M_\pi^2 - M_L^2 < M_i^2 < 2M_\pi^2 - M_H^2$ (top), with values of M_L^2 as indicated, and $M_H^2 = 0.50 \text{ GeV}^2/c^4$. Disappearance of K^+K^- signal is clearly appreciated in all cases.

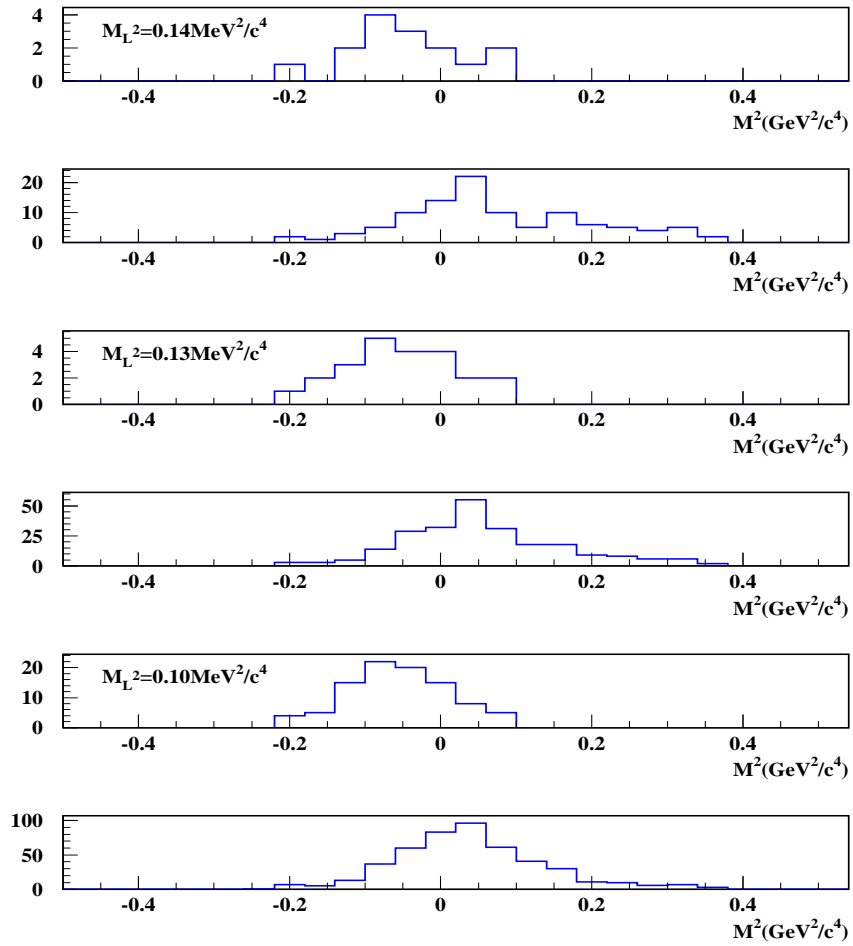


Figure 5.18: Contents the same as figure 5.17, with higher values of M_L^2 .

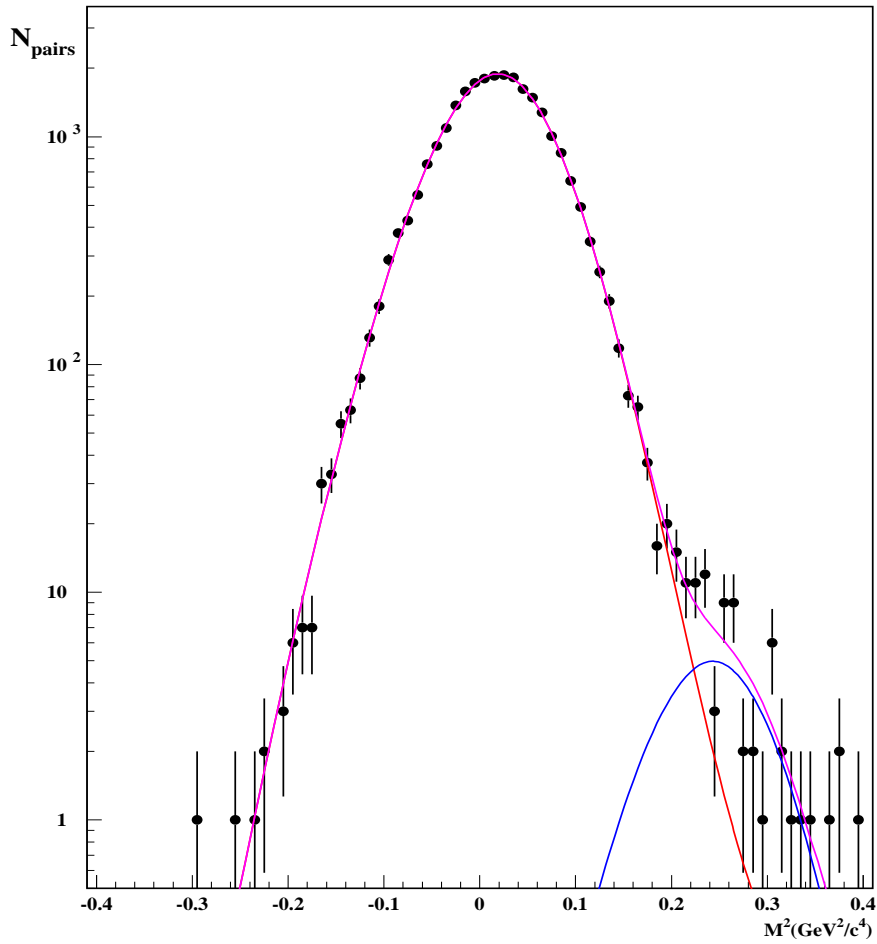


Figure 5.19: Squared invariant mass for particle pairs, measured from the average of all detectors hits associated with (positive and negative) upstream tracks in IH and SFD. No attempt has been made to reduce the $\pi^+\pi^-$ background (red), which is described by the parametrization (5.5). Fit results, indicated in table 5.1, are shown for the K^+K^- signal (blue) and for the sum (purple).

5.3 Analysis of $K^+K^-/\pi^+\pi^-$ at high momentum

In a previous note [67] we have determined the $K^+K^-/\pi^+\pi^-$ ratio at $p = 2.9 \text{ GeV}/c$, using the full Ni 2001 data sample with the standard physics triggers used in pionium analysis. Because of the low-Q (symmetric) trigger structure, the precision time-difference between vertical hodoscopes becomes useless for equal-mass pairs, and only the upstream time-of-flight measurements could be used successfully in that analysis. As a consequence, pair momentum was bound to be extremely low, thus providing no information on the momentum derivative.

The precise measurement of pionium lifetime [66] will require a small correction that takes into account the missidentified K^+K^- pairs in the $\pi^+\pi^-$ sample, and we need to know the yield and momentum dependence of this contamination, in order to evaluate the correction.

If we want to search for a K^+K^- signal at higher values of momentum, we need to go to asymmetric (unequal velocity) triggers. In this way, the precision time-difference between the two arms will become useful for mass discrimination. Fortunately the Lambda triggers are very well suited for the purpose [84],[85]. The only problem is statistics, since these triggers only occupy a small fraction of the normal DAQ runs. In order to cope with this, we have consistently integrated in our analysis all p-Ni data from 2001, 2002 and 2003 data taking periods.

As best discriminator to obtain the K^+K^- signal we define the *upstream mass squared*, associated to a given upstream detector i , for positive (negative) particle as:

$$m^2_{+(-)} = p^2_{+(-)} \left[\left(\frac{\Delta t^i_{+(-)} c}{L^i_{+(-)}} \right)^2 - 1 \right] \quad (5.6)$$

where c is light velocity, $p_{+(-)}$ is the positive (negative) particle momentum, $\Delta t^i_{+(-)}$ is the delay between upstream detector i and VH for positive (negative) particle and $L^i_{+(-)}$ are the path lengths between detector i and VH. The upstream detectors are designated by $i = 1, \dots, 4$ for IH [83] and

$i = 5, 6$ for SFD (X and Y).

In addition we define, only for the positive particle, the *average* upstream mass squared:

$$m^2_+ = \frac{\sum m^{2i}_+}{N} \quad (5.7)$$

where the sum runs over the N upstream detectors involved. Only events whose negative track has hits in all upstream detectors are actually retained in the subsequent analysis.

We select events in the range $1.2 \text{ GeV}/c < p_- < 1.6 \text{ GeV}/c$ and $2.8 \text{ GeV}/c < p_+ < 4.0 \text{ GeV}/c$. Note that the positive particle average momentum is significantly higher than the negative one, due to the Lambda trigger structure (see [85] for more details).

The 6 experimental distributions obtained with $\pi^+\pi^-$ pairs for m^{2i}_- as well as that for m^2_+ are very well described by the generic (asymmetric) parametrization:

$$R(x) = Ae^{-(a_1|x|^2+a_2|x|^3+a_3|x|^4)} \quad (5.8)$$

for $x \geq 0$ and $R(x) = Ae^{-(b_1|x|^2+b_2|x|^3+b_3|x|^4)}$ for $x \leq 0$, with $x = m^2 - m_0^2$, where m^2 is any of the upstream masses defined above and m_0^2 is an arbitrary parameter to locate the peak value. This parameter is set to the pion mass $m_0^2 = m_\pi^2$, but it can be changed to other values, because m^2 resolution is weakly dependent on the mass scale. The a_i and b_i parameter values were determined independently in each case, and the fitted curves are shown in Fig. 5.20 for m^2_+ and Fig. 5.21 for m^{2i}_- . They represent the experimental resolution functions for each quantity. Note for example that the negative invariant mass resolution is better than the positive one, as it can be clearly appreciated from a comparison between the previous figures, as a consequence of the difference in momentum spectrum mentioned earlier.

Protons are removed by the cut $-0.2 < m^2_+(\text{GeV}^2/c^4) < 0.5$, whereas K^- identification is provided by requiring $0.015 < m^{2i}_-(\text{GeV}^2/c^4) < 0.44$ for all upstream detectors $i = 1, 6$ ⁴. These cuts play the role of a very strong

⁴except for $IH - B$ where the upper limit was $0.7 \text{ GeV}^2/c^4$ (see Fig. 5.21).

pion veto, based upon the upstream time-of-flight measurements only. Their effect is illustrated in Figs. 5.20 and 5.21 by showing as shaded area the event fractions retained in each case.

Table 5.3: *Efficiency implied by upstream positive mass cuts.*

Particle	Efficiency(%)
π^+	65
K^+	63
<i>proton</i>	10

Table 5.4: *Implied efficiency values for each upstream detector mass cuts.*

Detector	Efficiency(%)
IHXA	91
IHXB	92
IHYA	92
IHYB	90
SFDY	87
SFDX	86
Total	54

After the background suppression provided by the above cuts, we are now in position to analyze the fine structure of the spectrum of the negative mass M_-^2 , defined from the precision time-difference in the Vertical Hodoscopes, which is given by:

$$M_-^2 = p_-^2 \left[\left(\frac{L_+}{L_-} \sqrt{1 + \frac{M_K^2}{p_+^2}} - \frac{c\Delta t}{L_-} \right)^2 - 1 \right] \quad (5.9)$$

following the same notation as previously used for expression (5.1), with the remark that the K^+ hypothesis in the opposite arm has now been chosen. The spectrum with full statistics is shown in figure 5.22, where four enhancements can be observed, which we attribute in principle to $\pi^+\pi^-$, K^-p , K^+K^- , and π^+K^- production. Please note that only the K^+K^- signal is seen at the correct mass hypothesis ($M_-^2 = M_K^2$), the others being shifted according to predictable deviations due to the positive particle time slewing. A more detailed analysis of this particular spectrum shows that the second peak is actually dominated by a background originated from a reflection of the negative upstream mass cuts, as we will see below, and that this is the reason for its broader structure.

The signal yield is analyzed by maximization of the following likelihood function:

$$L(x) = \sum_{\alpha=1}^3 A_{\alpha} G_{\alpha}(x - x_{0\alpha}, \sigma_{\alpha}) + A_b G_b(x - x_{0b}, \sigma_b) + B P_4(x) \quad (5.10)$$

where $x = M_-^2$ and $G_{\alpha}(x)$ represent normalized gaussian functions with peak value at $x = x_{0\alpha}$ and width σ_{α} describing the $\pi^+\pi^-$, K^+K^- and π^+K^- signals for $\alpha = 1, 2, 3$, respectively. Similarly $G_b(x)$ is a gaussian describing the background broad structure in the neighbourhood of the K^-p signal. An additional smooth background is described by the normalized fourth order polynomial $P_4(x) = (1 + \sum_{i=1}^4 c_i x^i) / I_4$ where $I_4 = \int_{x_1}^{x_2} (1 + \sum_{i=1}^4 c_i x^i) dx$ is the normalization integral. The signal event rates are then provided by the coefficients A_{α} .

The parameters $x_{0\alpha}, \sigma_2$ and σ_3 were determined independently, and remained fixed in the fit procedure. The rest ($\sigma_1, \sigma_b, A_{\alpha}, A_b, B, c_i$) were left free. The location of the $x_{0\alpha}$ peaks was determined by selecting signal events under the peak with the correct mass hypothesis and projecting them into the uncorrect hypothesis, in order to evaluate the mass shift.

Table 5.1 and Figure 5.22 show the fit results.

The number of K^+K^- pairs found by the fit are $N_{KK}^{obs} = 70_{-16}^{+17}$, and the total number of $\pi^+\pi^-$ pairs found when removing the m_-^{2i} cuts is $N_{\pi\pi}^{obs} = 22942$. Both numbers need to be corrected for acceptance. The positive

Table 5.5: *Parameter setting in maximum likelihood fit to M_-^2 spectrum.*

<i>Parameter</i>	Value	<i>Parameter</i>	Value
$x_{\pi\pi}^0$	0.07	$\sigma_{\pi\pi}$	0.025
x_{KK}^0	0.24	σ_b	0.029
$x_{\pi K}^0$	0.29	$A_{\pi\pi}$	1327.2
x_b^0	0.16	A_{KK}	79.9
σ_{KK}	0.02	$A_{\pi K}$	101.8
$\sigma_{\pi K}$	0.02	A_b	311.8

<i>Parameter</i>	Value
B	1449.2
$c0$	0.5978
$c1$	0.3687
$c2$	-3.9717
$c3$	4.3075
$c4$	-1.3526

mass cut efficiency (see Fig. 5.20 top) is involved in the $\pi\pi$ case:

$$N_{\pi\pi} = N_{\pi\pi}^{obs} \times \frac{1}{Eff(\pi^+)} = 22942 \times \frac{1}{0.6514} = 35219 \quad (5.11)$$

whereas for N_{KK} both the positive (see Fig. 5.20 center) and negative mass cuts are subject to independent efficiency corrections. In the latter case a 6-fold product of efficiency factors was taken into account (see Fig. 5.21 and Table 5.4). The final numbers are:

$$N_{KK} = N_{KK}^{obs} \times \frac{1}{Eff(K^+)} \times \frac{1}{Eff(K^-)} = 70 \times \frac{1}{0.6303} \times \frac{1}{0.5409} = 205 \quad (5.12)$$

so the measured contamination fraction at $4.8 \text{ GeV}/c$ is:

$$r_{KK} = \frac{N_{KK}}{N_{\pi\pi}} = \frac{205}{35219} = 5.8 \times 10^{-3} \quad (5.13)$$

5.3.1 Comparison with UrQMD Monte Carlo

The r_{KK} ratio we have obtained at the average momentum $p = 4.8 \text{ GeV}/c$ can be compared with our measurement at $p = 2.9 \text{ GeV}/c$ using normal physics runs with 2001 data [67] and see whether the evolution of K^+K^- cross-section is well described by the UrQMD Monte Carlo.

In fact, this is the main purpose of this note, because if the experimental data follow this model, it means we can rely on it to perform an accurate correction to ponium lifetime measurement.

In order to make the comparison as accurate as we can, we need to take into consideration the Coulomb interaction. First of all, we notice that UrQMD does not contain this effect, only relevant at very small values of Q .

Concerning the experimental data, it should be noted that because of the different trigger structure and cuts in the analysis at $p = 2.9 \text{ GeV}/c$ and that at $p = 4.8 \text{ GeV}/c$, the Coulomb interaction has a different magnitude in each case, which is true for both K^+K^- and $\pi^+\pi^-$ pairs. Moreover, in the standard analysis of ponium lifetime, the cuts are again different from the ones above.

For a given kinematical configuration Ω , we define the average value of the Coulomb enhancement for $a = \pi\pi, KK$ pair production cross-section as :

$$C_a = \frac{\int_{\Omega} A_C(Q) \left(\frac{d\sigma_a}{d^3Q} \right) d^3Q}{\int_{\Omega} \left(\frac{d\sigma_a}{d^3Q} \right) d^3Q} = \langle A_C(Q) \rangle$$

where $A_C(Q)$ is the corresponding Sakharov factor. Concerning the kinematical domain Ω , we have defined three different cases of interest, namely:

- A) $1.31 < p_{+-} (\text{GeV}/c) < 1.50$
- B) $Q_T < 5 \text{ MeV}/c$ and $Q_L < 22 \text{ MeV}/c$
- C) $Q_T < 5 \text{ MeV}/c$ and $Q_L < 16 \text{ MeV}/c$

The first (A) corresponds to the analysis at $p = 2.9 \text{ GeV}/c$ [67], whereas (B) and (C) correspond to two typical versions of the standard pionium lifetime analysis [66].

The correction factors obtained for the previous cuts are indicated in table 5.6, having in mind the following remarks:

a) the cuts indicated above are allways applied to Q-values evaluated in the $\pi\pi$ hypothesis, which is the one implied by ARIANE reconstruction.

b) in the case of asymmetric triggers, the average Q-values are so large ($\langle Q \rangle = 130 \text{ MeV}/c$ and $\langle Q \rangle = 400 \text{ MeV}/c$ in the $\pi^+\pi^-$ and K^+K^- mass hypothesis respectively) that the Coulomb correction factor is negligible for both $\pi\pi$ and KK .

With the help of table 5.6, we have plotted the evolution of the ratio r_K as function of the lab-frame momentum p of the pair, taking into account Coulomb corrections. For the sake of reference, we have chosen the configuration that corresponds to the standard pionium lifetime analysis (cuts C above), and used the correction factors $R_C/R_A = 0.88$ at $2.9 \text{ GeV}/c$ and $R_C = 1.29$ at $4.8 \text{ GeV}/c$.

Table 5.6: *Coulomb correction factors for the kinematical cuts A, B and C defined in the text for K^+K^- and $\pi^+\pi^-$ production. Last column shows the ratios $R = C_{KK}/C_{\pi\pi}$.*

<i>cuts</i>	C_{KK}	$C_{\pi\pi}$	R
<i>A</i>	2.38	1.63	1.46
<i>B</i>	1.79	1.45	1.24
<i>C</i>	2.00	1.56	1.29

The prediction of UrQMD Monte Carlo was evaluated by running 2049 million p-Ni events from the generator and selecting K^+K^- and $\pi^+\pi^-$ pairs with the cuts: $4.5^\circ < \theta < 7.0^\circ$, $1.3 \text{ GeV}/c < p_{+-} < 5.0 \text{ GeV}/c$ and $Q < 30 \text{ MeV}/c$ in the $\pi\pi$ hypothesis, where θ is the angle between the vector sum of the particle momenta and the incoming proton direction and p_{+-} is

the momentum of positive or negative particle. The uncorrected curve was multiplied by an acceptance efficiency function determined separately after GEANT-DIRAC processing of K^+K^- pairs, in order to take into account the K^\pm lifetime effect in spectrometer acceptance.

The UrQMD Monte Carlo prediction can be appreciated in Figure 5.23 as a dotted line. At $2.9 \text{ GeV}/c$ the r_{KK} ratio comes out 0.56 (after Coulomb correction), which is larger than the experimental value by a factor 2.7. We have however normalized the Monte Carlo to the experimental value at $2.9 \text{ GeV}/c$. We then see that very good agreement is found with respect to the data measured at $4.8 \text{ GeV}/c$.

Similarly to the case studied for $K^\pm\pi^\mp$ in the previous section, it seems that UrQMD describes correctly the cross-section dependence on the lab-frame momentum, although the magnitude of the strangeness ratio r_K is not reproduced correctly.

In conclusion, we find that the contamination fractions relevant for pionium analysis are:

$$\frac{N_{KK}}{N_{\pi\pi}} = 5.8 \times 10^{-3} \times 1.23 = 7.2 \times 10^{-3} \quad (5.14)$$

at $4.8 \text{ GeV}/c$ based upon the UrQMD Monte Carlo extrapolation, in agreement with the experimental data, and

$$\frac{N_{KK}}{N_{\pi\pi}} = 2.38 \times 10^{-3} \times 0.845 = 2.0 \times 10^{-3} \quad (5.15)$$

at $2.9 \text{ GeV}/c$, according to the Coulomb-corrected experimental measurement.

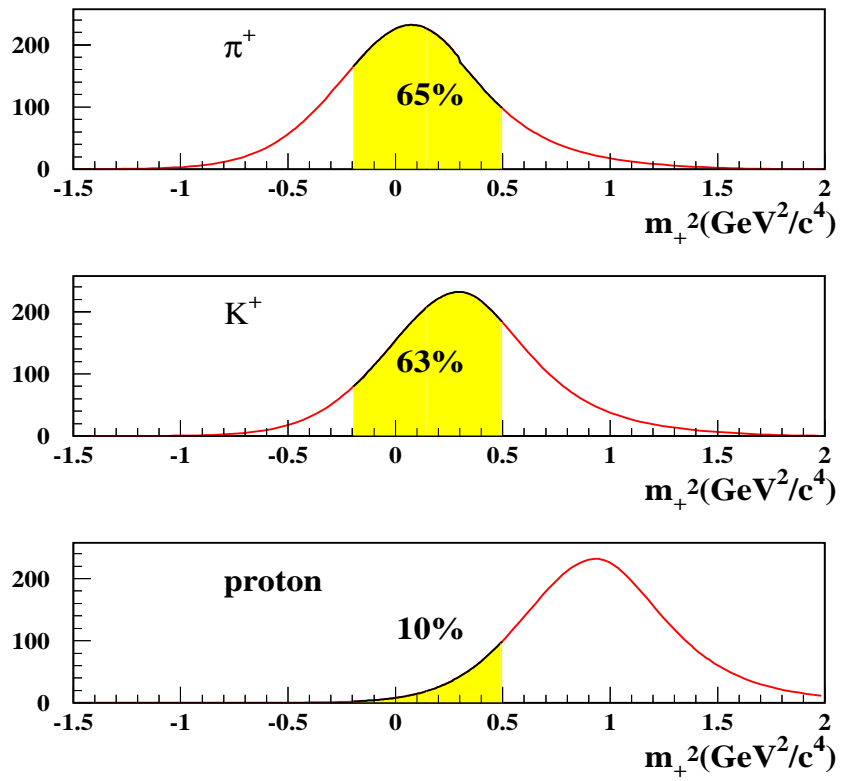


Figure 5.20: Resolution function for the positive upstream squared mass m_+^2 , obtained from a parametrization fitted to the experimental $\pi^+\pi^-$ data. The peak value has been displaced to three different mass hypothesis, in order to appreciate the effect of the cuts described in the text.

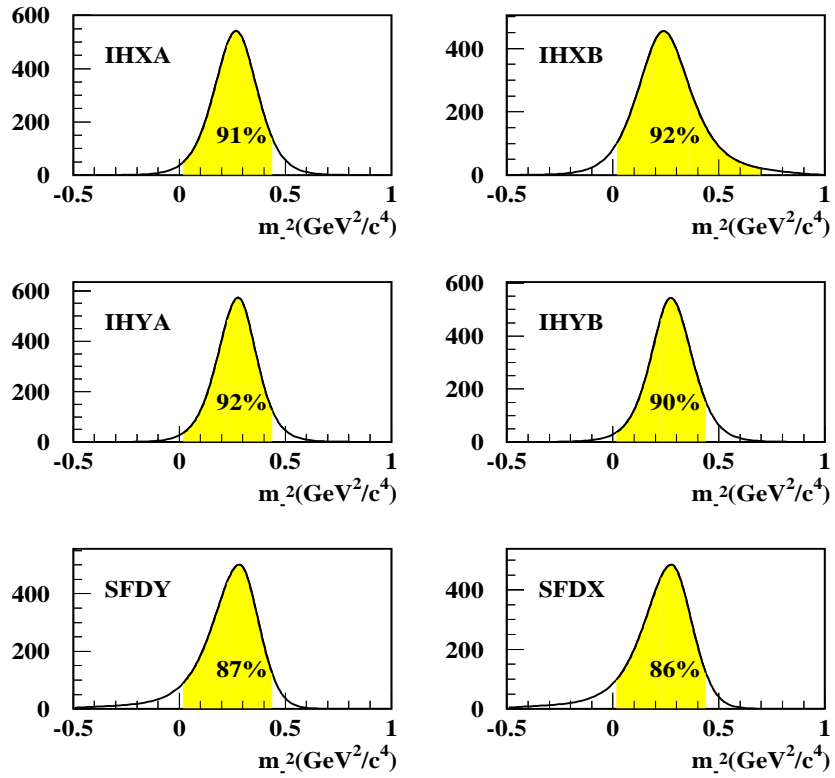


Figure 5.21: Negative upstream mass resolution functions, obtained for each of the 6 Ionization Hodoscope (IH) detectors, obtained from parametrizations fitted to the experimental $\pi^+\pi^-$ data. The peak values were centered at $M_{K^-}^2$, in order to illustrate the effect of the cuts given in the text for K^- selection.

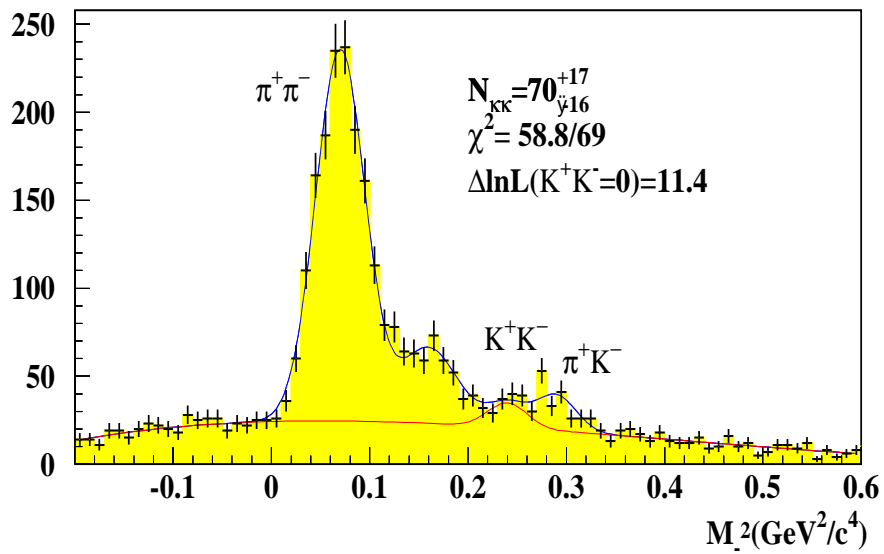


Figure 5.22: Spectrum of squared negative mass M_-^2 measured with Vertical Hodoscopes under K^+ mass hypothesis, for the complete 2001,2002 and 2003 $p - Ni$ data sample with Lambda triggers. The maximum likelihood fit is explained in the text. The significance of the K^+K^- signal at average pair momentum $p = 4.8\text{GeV}/c$ is indicated.

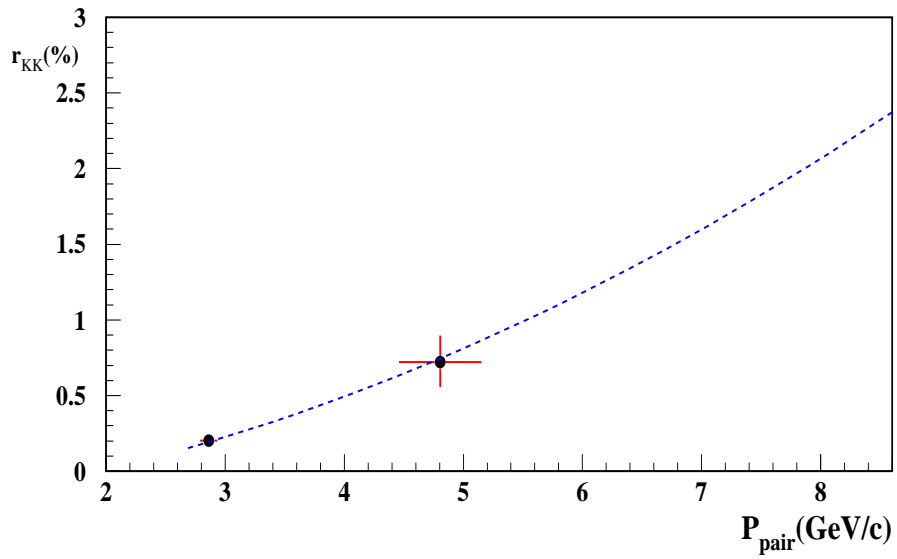


Figure 5.23: *Experimental measurements by DIRAC of the $K^+K^-/\pi^+\pi^-$ ratio r_{KK} at two different values of the average pair momentum, namely 2.9 GeV/c and 4.8 GeV/c. The UrQMD Monte Carlo prediction is shown as the dotted line, multiplied by a factor 0.37.*

5.3.2 The K^-p signal

The presence of a K^-p signal in the M_-^2 spectrum of Fig. 5.22 can only be unambiguously established when the analysis is made with the correct proton hypothesis for the positive track, rather than the K^+ hypothesis. When this is done, for the particular cuts applied in Fig. 5.22, no significant signal appears at $M_-^2 = M_K^2$. But indeed these cuts are not appropriate to search for K^-p , since a proton veto has been applied by means of the requirement $-0.2 < m_+^2 < 0.5 \text{ GeV}^2/c^4$. When this cut is turned into $m_+^2 > 0.7 \text{ GeV}^2/c^4$, in order to enhance the proton yield, a clear K^-p signal shows up, as it can be seen in Fig. 5.24. Having demonstrated the signal ⁵, we did not proceed further to a precise determination of the acceptance, since our main interest in this note is the K^+K^- .

It is worth to note that, as a consequence of the combined effect of negative and positive upstream mass cuts, a bias is produced in the M_-^2 distribution which causes an enhancement in the region $M_-^2 \approx 0.125 \text{ GeV}^2/c^4$, well appreciated in Fig. 5.24. We have verified that such characteristic enhancement is actually the origin of the broad structure seen in Fig. 5.22 at $M_-^2 \approx 0.160 \text{ GeV}^2/c^4$, after taking into account the difference in mass hypothesis and upstream mass cuts. This background actually overwhelms the genuine K^-p signal in Fig. 5.22 which would otherwise be located at the same M_-^2 value.

For the sake of completeness, we also show in Fig. 5.25 the M_-^2 spectrum with the π^+ hypothesis, showing the π^+K^- and $\pi^+\pi^-$ signals with improved resolution. The cut $m_+^2 < 0.0 \text{ GeV}^2/c^4$ was used in this case, in order to suppress both the K^+ and proton yields (according to Fig. 5.20).

⁵the complete statistics of 2001, 2002 and 2003 p-Ni data from Lambda triggers was used

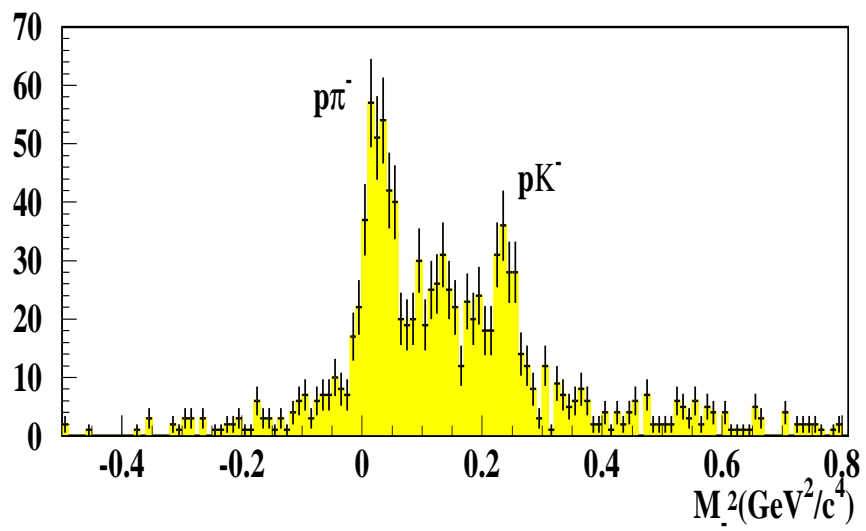


Figure 5.24: Spectrum of squared negative mass M_-^2 measured with Vertical Hodoscopes under proton mass hypothesis. The same data as in Fig. 5.22, other than the cut $m_+^2 > 0.7 \text{ GeV}^2/c^4$.

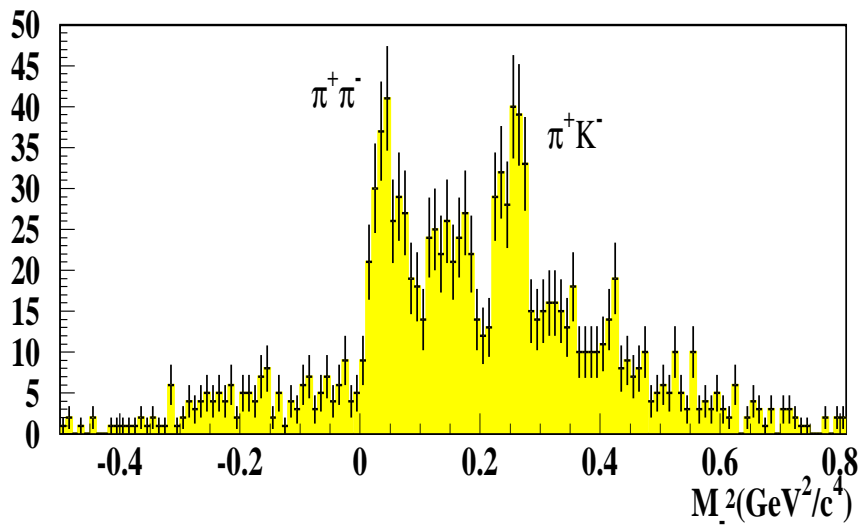


Figure 5.25: Spectrum of squared negative mass M_-^2 measured with Vertical Hodoscopes under π^+ mass hypothesis. The same data as in Fig. 5.22, other than the cut $m_+^2 < 0.0\text{GeV}^2/c^4$.

5.4 Summary and conclusions

A detailed analysis has been done of the pair momentum dependence of the ratios $K^\pm\pi^\mp/\pi^+\pi^-$ and $K^+K^-/\pi^+\pi^-$ in DIRAC. As far as the momentum derivative is concerned, very good agreement is found with the UrQMD Monte Carlo in both cases. The integrated yields are however at variance with UrQMD, and the corresponding factors have been given. These results provide a good ground for using this Monte Carlo to extrapolate the measured K^+K^- contamination at $p = 2.9 \text{ GeV}/c$ to higher values of momentum, in order to perform an accurate correction for the measurement of pionium lifetime.

Chapter 6

Pionium Lifetime using 2002 and 2003 Data

6.1 Global fit analysis

For completeness, we provide in table 6.1 the K-factors for the p-integrated case (global fit) and in table 6.2 the p-dependent ones, for the standard cuts $Q_T < 5MeV/c$ and $Q_L < 2MeV/c$. Both are entirely consistent with those calculated for 2001 data.

The global fit consists in minimizing the χ^2 defined in (1.20) in $2D$ with respect to α_3 (non-Coulomb fraction) and γ parameters, using the momentum-integrated sample. The α_2 and ϵ parameters remain fixed in this fit, and α_2 is determined by the direct measurement of the accidental pairs fraction from the analysis

Table 6.1: Numerical values of K^{th} and K^{exp} as defined in reference [66], obtained for our improved Monte Carlo simulation. Each row corresponds to a given rectangular cut in (Q_T, Q_L) plane, with $Q_T^c = 5MeV/c$ and $Q_L^c = 2MeV/c$ being the reference cut values. No practical change is observed with respect to earlier values.

$Q_L^{cut}(MeV/c)$	K^{theo}	K^{exp}
0.5	0.4372	0.2937 ± 0.0009
1.0	0.2389	0.2135 ± 0.0005
1.5	0.1669	0.1581 ± 0.0003
2.0	0.1300	0.1246 ± 0.0002
$Q_T^{cut}(MeV/c)$	K^{theo}	K^{exp}
0.5	3.2457	0.9319 ± 0.0089
1.0	1.2382	0.6963 ± 0.0037
1.5	0.6995	0.5224 ± 0.0020
2.0	0.4674	0.3965 ± 0.0012
2.5	0.3426	0.3089 ± 0.0008
3.0	0.2660	0.2465 ± 0.0006
3.5	0.2147	0.2017 ± 0.0004
4.0	0.1781	0.1687 ± 0.0004
4.5	0.1509	0.1438 ± 0.0003
5.0	0.1300	0.1246 ± 0.0002

of the precision time-of-flight spectrum. ϵ is fixed to the K^+K^- fraction experimentally determined and used in [86]. β can either be left as a free parameter, or be fixed to the total number of prompt pairs in the fir region (N_p), or to the ratio $\beta = N_p^c/f_c$ where N_p^c is the number of prompt events with $Q_L > 2MeV/c$ (control region) and f_c is the ratio between the number of Monte Carlo pairs in the control region and the total number of Monte Carlo events. These choices are small variations with respect to N_p and produce slight changes in the fit results, as indicated in table 6.5.

We have chosen to perform the fit in $0.25 \times 0.25 (MeV/c)^2$ bins in the

(Q_T, Q_L) plane, for the global fit. Variations with respect to this choice will be reported in table 6.5.

Once the fit has converged, we define the atom signal in each (i, j) bin as the difference between the prompt spectrum (with accidentals subtracted as explained before) and the Monte Carlo with the ponium component (AA) removed. This 2D signal, which reveals the excess with respect to the calculated Coulomb interaction enhancement background, is what we call the ponium spectrum. The atom breakup probability P_{br} is then determined [66] by means of the K-factors.

Just as we did with the 2001 data [86], we present the fit results in several steps. The correction sequence is defined in a cumulative way, namely:

- a) use improved statistics Monte Carlo.
- b) include K^+K^- correction.
- c) perform the target impurity correction.
- d) remove the $\omega - \eta'$ finite-size correction, according to reference [35].

In table 6.3 we present the χ^2 values (separately in control and extrapolation regions), the number of atoms N_A , the number of Coulomb pairs in the complete fit range N_{CC} , the β parameter and the P_{br} for each option.

Please note that whereas the introduction of the K^+K^- contamination decreases the total χ^2 by 5.1 units, the removal of the $\omega - \eta'$ finite-size correction decreases it by 12.7 units. The combined effect of both actions decreased the total χ^2 by 17.8 units. We remark that, in agreement with our earlier findings, the $\omega - \eta'$ finite-size correction is not wanted by the data. The statistical significance will be further enhanced when we report the momentum-dependent fit in subsection 6.2.

In addition, we illustrate here again an effect that was already pointed out with 2001 data [86], namely that the K^+K^- correction introduces a significantly better stability of the measured P_{Br} values with respect to the Q_T cut, and also a better agreement between the Q_T and Q_L series of cuts to define the atom signal, at the limit of very low Q_T and Q_L values, as it can be clearly appreciated in the figure 6.9.

As far as the K^+K^- correction is concerned, we have made the exercise of letting the ϵ parameter free in the fit. When this is done, we obtain $\epsilon = 0.0138 \pm 0.0053$ which is entirely compatible with the value $\epsilon = 0.0072$ used in the fit, determined from our measurement [67].

The ponium $2D$ signal is shown in the form of lego plots in figures 6.7 and 6.8.

Our standard fit domain is the region $Q_L < 20\text{MeV}/c$ and $Q_T < 5\text{MeV}/c$, and the dependence of the P_{Br} with respect to the Q_L upper limit (Q_L^{up}) is analysed in table 6.6. We see how the P_{Br} fluctuates in a random way, with no appreciable systematics, and that the value at $Q_L^{up} = 20\text{MeV}/c$ is close to the average.

Table 6.2: *K*-factors determined in 10 intervals of laboratory-frame momentum, re-evaluated for the new Monte Carlo simulation.

<i>p</i> interval (GeV/c)	<i>K</i> – factor
2.6-3.2	0.1105 ± 0.0005
3.2-3.8	0.1173 ± 0.0004
3.8-4.4	0.1237 ± 0.0005
4.4-5.0	0.1294 ± 0.0006
5.-5.6	0.1334 ± 0.0007
5.6-6.2	0.1373 ± 0.0008
6.2-6.8	0.1396 ± 0.0011
6.8-7.4	0.1457 ± 0.0015
7.4-8.0	0.1459 ± 0.0022
8.-8.6	0.1453 ± 0.0032

Table 6.3: Fit results for the correction options a), b), c), d)) indicated in the text. χ^2 's in the full domain, and its restriction to the control and extrapolation regions separately, are given. Also the total number of atoms N_A and coulomb pairs N_{CC} , the β parameter and the break-up probabilities are indicated.

	a)	a+b)
χ^2_{tot}/ndf	1675.4/1600	1670.3/1600
χ^2_{ext}/ndf	171.5/160	168.0/160
χ^2_{cont}/ndf	1503.9/1440	1502.3/1440
N_A	10826 ± 307	10406 ± 295
N_{CC}	1290416 ± 7305	1270596 ± 7177
β	1601905	1601931
P_{Br}	0.421 ± 0.013	0.411 ± 0.013
	a)+b)+c)	a)+b)+c)+d)
χ^2_{tot}/ndf	1670.3/1600	1657.6/1600.0
χ^2_{ext}/ndf	168.0/160	167.1/160
χ^2_{cont}/ndf	1502.3/1440	1490.5/1440
N_A	10406 ± 295	10557 ± 298
N_{CC}	1270596 ± 7177	1255217 ± 7111
β	1601930	1601954
P_{Br}	0.417 ± 0.013	0.427 ± 0.013

Table 6.4: Comparison of global fit results for three different choices of the β parameter definition.

	β	P_{Br}	χ^2/ndf
β all range	1603179	0.419 ± 0.013	1658.3/1600
β ($Q_L > 2\text{MeV}/c$)	1602820	0.424 ± 0.013	1658.0/1600
β free	1601954	0.427 ± 0.013	1657.6/1600

Table 6.5: Comparison of global fit results using two different (Q_T, Q_L) binsizes.

	β	P_{Br}	χ^2/ndf
0.25×0.25	1601954	0.427 ± 0.013	1657.6/1600
0.5×0.5	1602913	0.426 ± 0.013	358.7/400

Table 6.6: Values of break-up probability P_{Br} obtained from different choices of the upper limit (Q_L^{cut}) used to define the control region in Q_L projection.

$Q_L^{cut} (MeV/c)$	P_{Br}
22	0.424 ± 0.013
21	0.428 ± 0.013
20	0.427 ± 0.013
19	0.424 ± 0.013
18	0.418 ± 0.013
17	0.420 ± 0.013
16	0.420 ± 0.014
15	0.422 ± 0.014
14	0.425 ± 0.014
13	0.419 ± 0.014

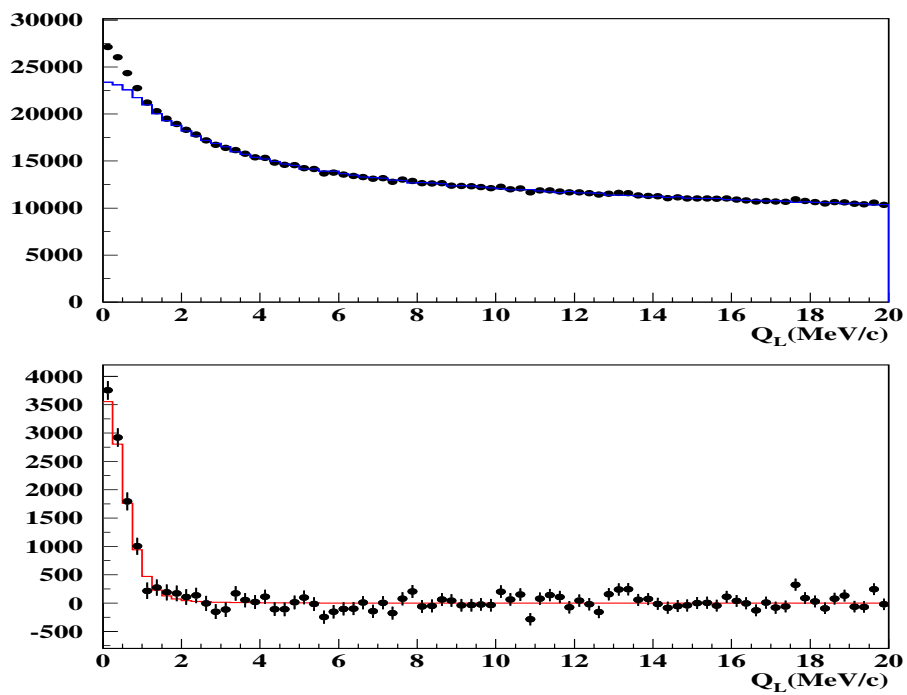


Figure 6.1: Two-dimensional global fit projection onto Q_L . The standard $Q_T < 4 \text{ MeV}/c$ cut has been applied. The difference between prompt data (dots) and Monte Carlo (blue line), which corresponds to pionium signal, is plotted at the bottom, where the signal is compared with the pionium atom Monte Carlo (red line).

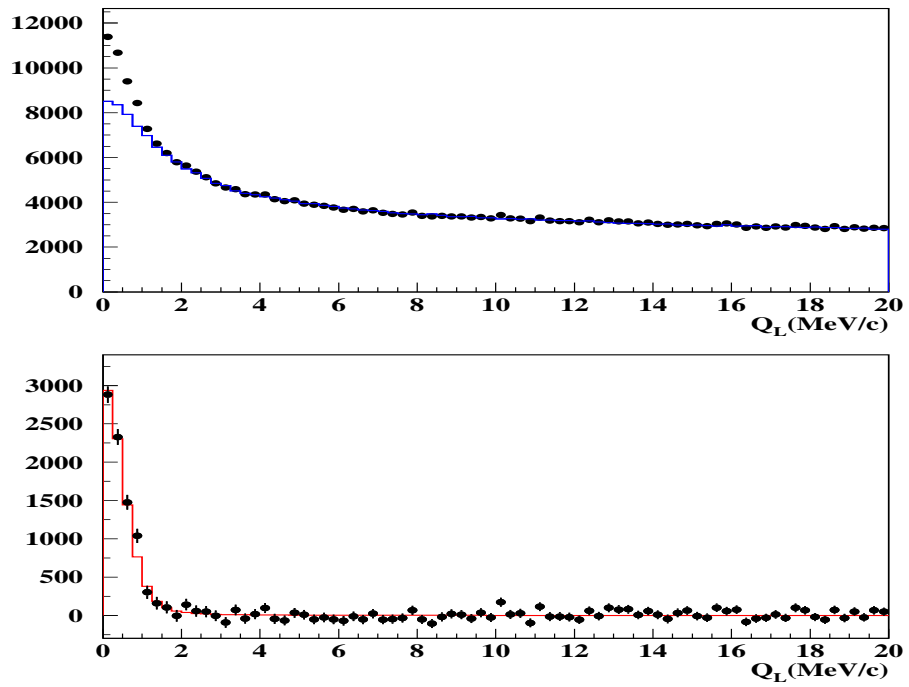


Figure 6.2: Two-dimensional global fit projection onto Q_L . A more restrictive $Q_T < 2$ MeV/c cut has been applied to enhance the signal. The difference between prompt data (dots) and Monte Carlo (blue line), which corresponds to pionium signal, is plotted at the bottom, where the signal is compared with the pionium atom Monte Carlo (red line).

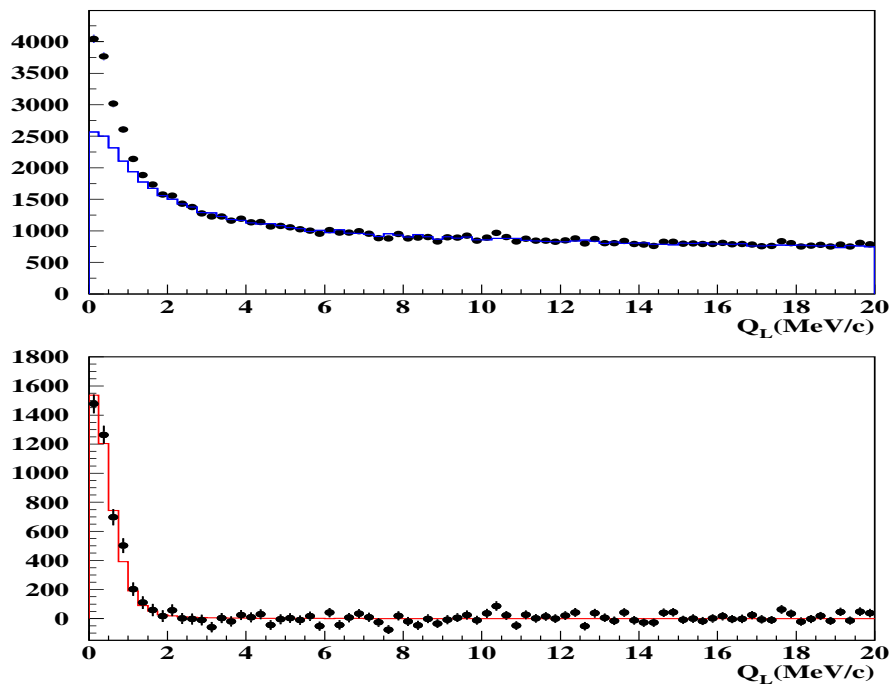


Figure 6.3: Two-dimensional global fit projection onto Q_L . A more restrictive $Q_T < 1$ MeV/c cut has been applied to enhance the signal. The difference between prompt data (dots) and Monte Carlo (blue line), which corresponds to pionium signal, is plotted at the bottom, where the signal is compared with the pionium atom Monte Carlo (red line).

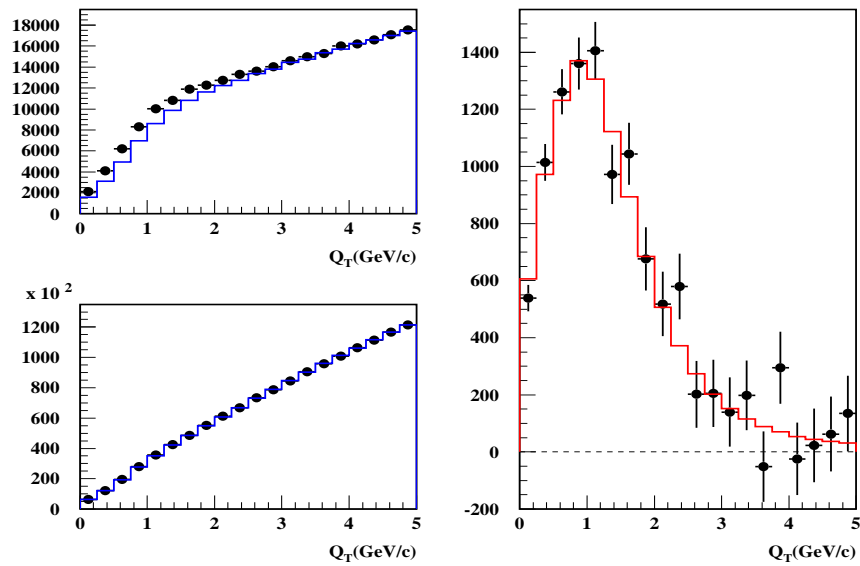


Figure 6.4: Two-dimensional global fit projection onto Q_T . The data are shown separately for $Q_L < 2\text{MeV}/c$ (left top) and $Q_L > 2\text{MeV}/c$ (left bottom). The difference between prompt data (dots) and Monte Carlo (blue line), which corresponds to transverse pionium signal, is plotted (right) and compared with the pionium atom Monte Carlo (red line).

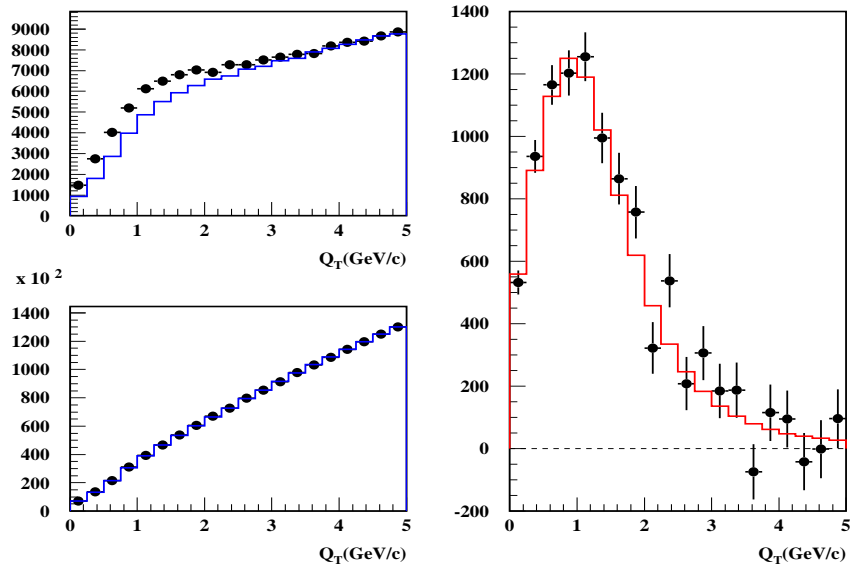


Figure 6.5: Two-dimensional global fit projection onto Q_T . The data are shown separately for $Q_L < 1\text{MeV}/c$ (left top) and $Q_L > 1\text{MeV}/c$ (left bottom). The difference between prompt data (dots) and Monte Carlo (blue line), which corresponds to transverse pionium signal, is plotted (right) and compared with the pionium atom Monte Carlo (red line).

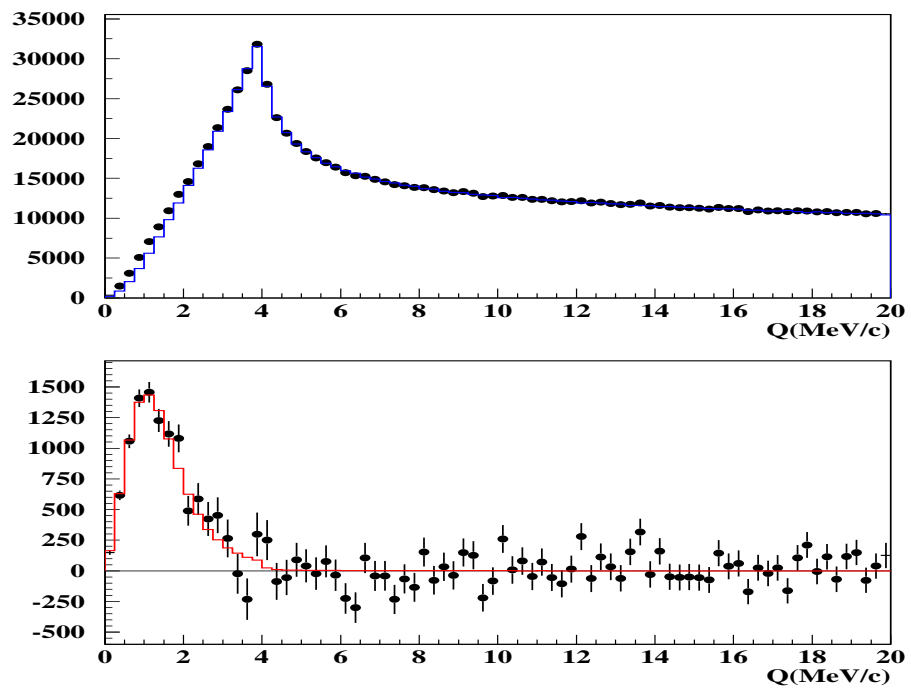


Figure 6.6: *Two-dimensional global fit projection onto Q . The standard $Q_T < 4 \text{ MeV}/c$ cut was applied. The difference between prompt data (dots) and Monte Carlo (blue line), which corresponds to pionium signal, is plotted at the bottom. The signal is compared with the pionium atom Monte Carlo (red line).*

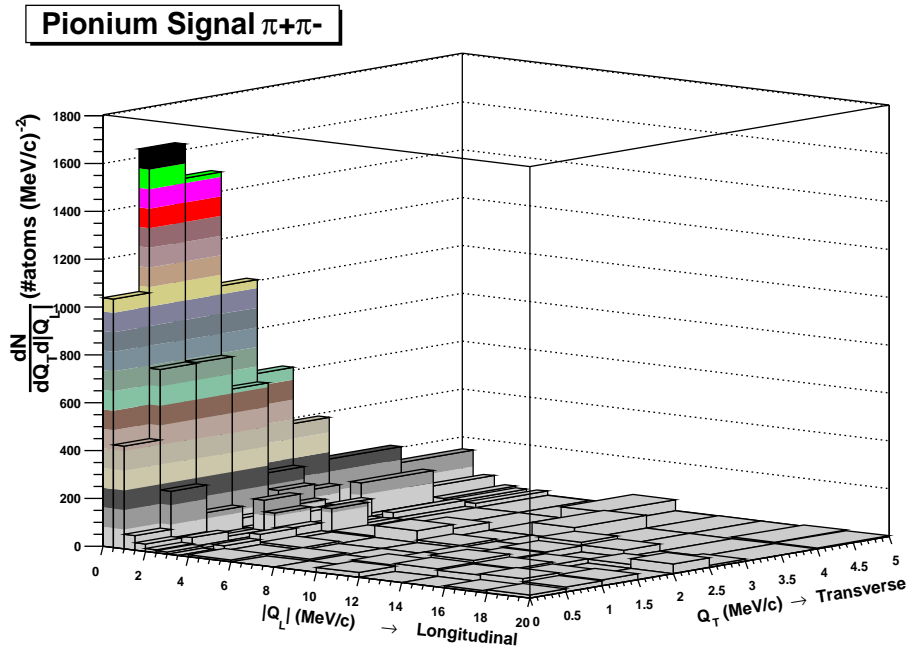


Figure 6.7: Lego plot showing the pionium break-up spectrum in Ni in the $(Q_T, Q_L = |Q_Z|)$ plane, after subtraction of the Coulomb background.

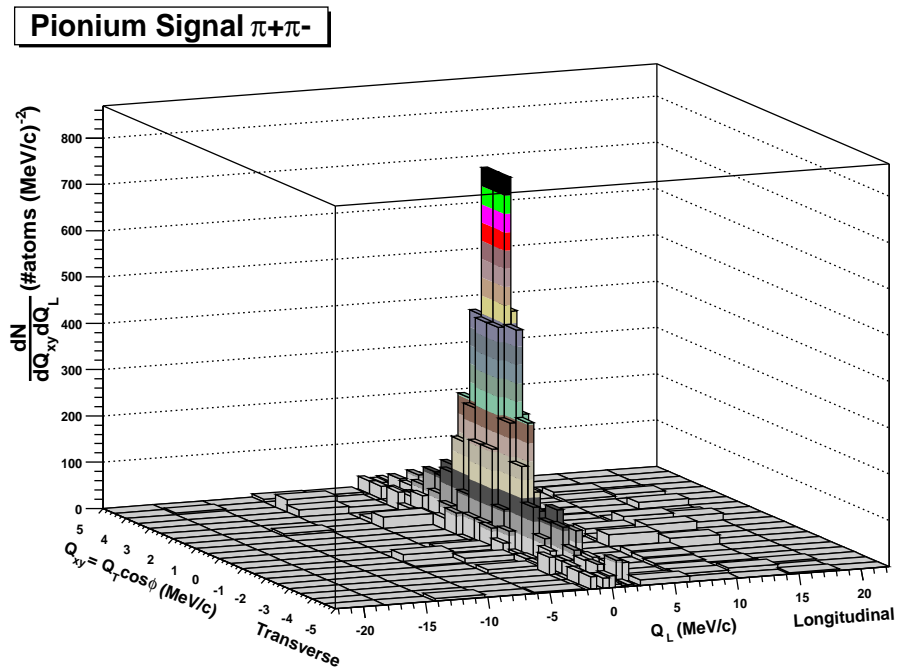


Figure 6.8: Lego plot showing the pionium break-up spectrum in Ni in the (Q_{xy}, Q_L) plane, after subtraction of Coulomb background. The transverse component $Q_{xy} = Q_T \cos\phi$ is defined as the product of the measured Q_T value times the cosine of a random azimuth.

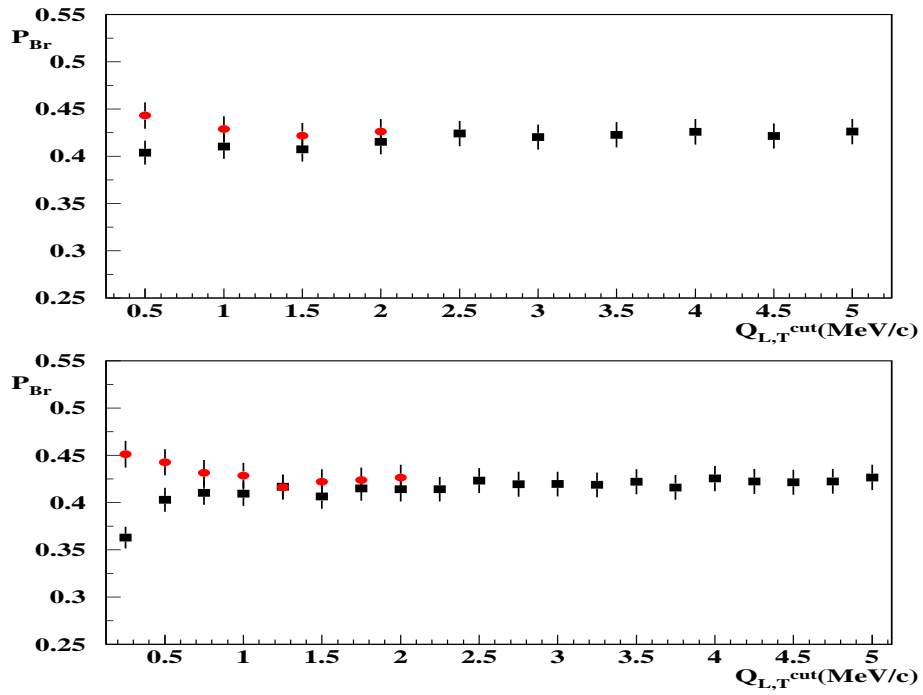


Figure 6.9: Pionium break-up probabilities determined from different choices of the upper limits ($Q_{T,L}^u$) in the rectangular integration domain to define the atom signal. Top plot shows the 2002+2003 results after the introduction of K^+K^- correction, in $0.5\text{MeV}/c$ steps of Q_L^u (red dots) and Q_T^u (black squares). Bottom plot shows the same in $0.25\text{MeV}/c$ steps.

6.2 Momentum-dependent analysis

Following the approach of our earlier work [66], in this section we split the pair momentum spectrum in ten 600 MeV/c bins and perform independent fits at each momentum interval. The corrections applied are the same as for the global fit. The only change with respect to the latter is the choice of $0.5 \times 0.5(\text{MeV}/c)^2$ binsize, which is now obliged due to the strong statistics reduction at individual 2D bins. We use the same definition of β as in section 6.2.1.

6.2.1 Fit results

As we did with 2001 data, we now present the final results after the introduction of all corrections, in order to avoid proliferation of figures. However, we keep record of the individual changes at each step, by giving the p-dependent and global fit results in the form of tables, distributed as follows:

- a) Table 6.8: The new Monte Carlo is used.
- b) Table 6.9: K^+K^- contamination is introduced, after the parametrization given in [86].
- c) Table 6.10: New Monte Carlo, K^+K^- contamination and target impurity correction.
- d) Table 6.11: In addition to the above, the $\omega - \eta'$ finite-size correction is dropped.

Figures from 6.10 to 6.19 show the result of the 10 independent fits in the form of atom spectra (Q_L and Q_T) and break-up probabilities as function of Q_L and Q_T cuts.

The Pionium line-shape shows good agreement between the prompt data signal and the Monte Carlo.

In table 6.7 a new global χ^2 has been defined as the sum of the individual ones at each momentum bin, and a combined P_{Br} value and error have been

Table 6.7: *Combined momentum dependent fit, for progressive fit conditions as defined in the text.*

	A	A+B	A+B+C	A+B+C+D
χ^2	3207.5/3157	3200.1/3157	3200.1/3157	3175.2/3157
P_{Br}	0.418 ± 0.014	0.414 ± 0.014	0.420 ± 0.014	0.427 ± 0.014
N_A	10741 ± 320	10465 ± 313	10465 ± 313	10553 ± 315
N_C	869436 ± 5515	857043 ± 5427	857043 ± 5427	847754 ± 5383

calculated after proper account of the independent statistical errors. The number of atoms (N_A) and Coulomb pairs (N_C) are also indicated.

From table 6.7 we draw the same conclusions as from the global analysis. The introduction of K^+K^- simulation improves the χ^2 by 10.7 units, and when the $\omega - \eta'$ finite-size correction is removed, the χ^2 improves by 32.5 additional units. We consider this a clear indication that the latter should be done. Adding this two changes, the χ^2 is reduced by 46.2 units.

Table 6.8: Results of the momentum-dependent fit, using correction a) only (see text). Break-up probability values P_{Br} , number of atom pairs N_A , α_1 and χ^2 over the entire fit region are indicated in this table, for every 600 MeV/c momentum interval p_i as defined in table 6.2.

	P_{Br}	N_A	α_1	χ^2 /ndf	χ_e^2 / ndf
p_1	0.375 ± 0.035	1289 ± 107	0.788 ± 0.013	301.4/288	27.3/32
p_2	0.467 ± 0.031	2533 ± 149	0.791 ± 0.010	289.9/288	33.1/32
p_3	0.377 ± 0.028	1887 ± 127	0.822 ± 0.011	274.2/288	26.0/32
p_4	0.407 ± 0.032	1596 ± 112	0.812 ± 0.013	282.8/288	21.5/32
p_5	0.425 ± 0.044	1291 ± 120	0.842 ± 0.015	267.7/288	25.9/32
p_6	0.462 ± 0.049	945 ± 87	0.807 ± 0.019	341.8/288	29.6/32
p_7	0.486 ± 0.073	598 ± 78	0.811 ± 0.025	316.0/288	44.5/32
p_8	0.525 ± 0.161	354 ± 98	0.804 ± 0.036	312.6/288	45.3/32
p_9	0.495 ± 0.143	160 ± 41	0.764 ± 0.046	284.9/282	23.4/32
p_{10}	0.787 ± 0.247	89 ± 21	0.612 ± 0.070	234.9/251	24.7/32

Table 6.9: Results of the momentum-dependent fit, using corrections $a+b$ (see text). Break-up probability values P_{Br} , number of atom pairs N_A , α_1 and χ^2 over the entire fit region are indicated in this table, for every 600 MeV/c momentum interval p_i as defined in table 6.2.

	P_{Br}	N_A	α_1	χ^2 /ndf	χ_e^2 / ndf
p_1	0.373 ± 0.035	1275 ± 106	0.786 ± 0.013	301.9/288	27.2/32
p_2	0.465 ± 0.031	2504 ± 148	0.788 ± 0.010	289.4/288	33.4/32
p_3	0.373 ± 0.028	1847 ± 125	0.817 ± 0.011	274.3/288	26.5/32
p_4	0.401 ± 0.032	1548 ± 110	0.806 ± 0.013	282.7/288	21.9/32
p_5	0.416 ± 0.044	1239 ± 117	0.835 ± 0.015	266.0/288	25.1/32
p_6	0.452 ± 0.049	902 ± 84	0.797 ± 0.019	341.2/288	28.7/32
p_7	0.482 ± 0.073	575 ± 76	0.798 ± 0.024	315.6/288	43.1/32
p_8	0.519 ± 0.160	337 ± 94	0.790 ± 0.035	312.2/288	43.8/32
p_9	0.481 ± 0.140	150 ± 38	0.750 ± 0.046	285.1/282	22.4/32
p_{10}	0.816 ± 0.257	87 ± 21	0.595 ± 0.068	235.3/251	24.5/32

Table 6.10: Fit results of the momentum-dependent fit, using corrections $a+b+c$ (see text). Break-up probability values P_{Br} , number of atom pairs N_A , α_1 and χ^2 over the entire fit region are indicated in this table, for every 600 MeV/c momentum interval p_i as defined in table 6.2.

	P_{Br}	N_A	α_1	χ^2 /ndf	χ_e^2 / ndf
p_1	0.378 ± 0.035	1275 ± 106	0.786 ± 0.013	301.9/288	27.2/32
p_2	0.472 ± 0.031	2504 ± 148	0.788 ± 0.010	289.4/288	33.4/32
p_3	0.378 ± 0.029	1847 ± 125	0.817 ± 0.011	274.3/288	26.5/32
p_4	0.406 ± 0.032	1548 ± 110	0.806 ± 0.013	282.7/288	21.9/32
p_5	0.422 ± 0.044	1239 ± 117	0.835 ± 0.015	266.0/288	25.1/32
p_6	0.458 ± 0.049	902 ± 84	0.797 ± 0.019	341.2/288	28.7/32
p_7	0.489 ± 0.074	575 ± 76	0.798 ± 0.024	315.6/288	43.1/32
p_8	0.526 ± 0.162	337 ± 94	0.790 ± 0.035	312.2/288	43.8/32
p_9	0.488 ± 0.142	150 ± 38	0.750 ± 0.046	285.1/282	22.4/32
p_{10}	0.827 ± 0.261	87 ± 21	0.595 ± 0.068	235.3/251	24.5/32

Table 6.11: Final fit results of the momentum-dependent fit, using all corrections $a+b+c+d$ (see text). Break-up probability values P_{Br} , number of atom pairs N_A , α_1 and χ^2 over the entire fit region are indicated in this table, for every 600 MeV/c momentum interval p_i as defined in table 6.2.

	P_{Br}	N_A	α_1	χ^2 /ndf	χ_e^2 / ndf
p_1	0.386 ± 0.036	1291 ± 107	0.777 ± 0.013	299.7/288	27.1/32
p_2	0.481 ± 0.032	2534 ± 149	0.779 ± 0.010	286.5/288	33.2/32
p_3	0.386 ± 0.029	1873 ± 126	0.807 ± 0.011	272.2/288	26.0/32
p_4	0.413 ± 0.033	1564 ± 110	0.797 ± 0.013	280.7/288	21.8/32
p_5	0.429 ± 0.045	1250 ± 117	0.826 ± 0.015	264.0/288	25.0/32
p_6	0.463 ± 0.050	906 ± 85	0.789 ± 0.018	338.1/288	28.6/32
p_7	0.492 ± 0.074	576 ± 76	0.790 ± 0.024	313.6/288	42.7/32
p_8	0.520 ± 0.162	332 ± 94	0.784 ± 0.035	309.4/288	43.1/32
p_9	0.469 ± 0.139	144 ± 37	0.748 ± 0.045	282.9/282	22.3/32
p_{10}	0.778 ± 0.248	83 ± 20	0.599 ± 0.068	233.9/251	24.5/32

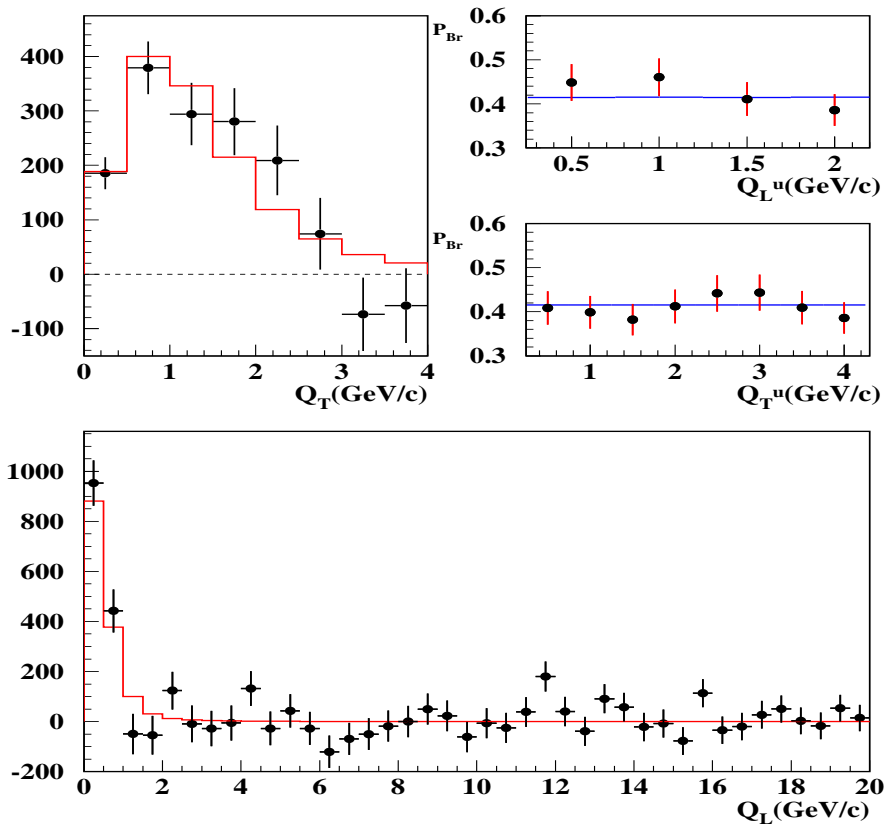


Figure 6.10: Fit results for the $\pi^+\pi^-$ momentum bin $2.6 < p < 3.2$ GeV/c in lab-frame. Q_T (top left) and Q_L (bottom) projections of the atom signal found in the extrapolation region ($Q_L < 2$ MeV/c) after subtraction of the Monte Carlo prediction with Pionium component removed. Values of breakup probability determined for different integration upper limits Q_T^u and Q_L^u to define the atom signal (top right). Note the different Q_L^u values are all defined for $Q_T^u = 5$ MeV/c and Q_T^u values are defined for $Q_L^u = 2$ MeV/c. The blue line indicates the P_{Br} determined from atom counting using the Monte Carlo.

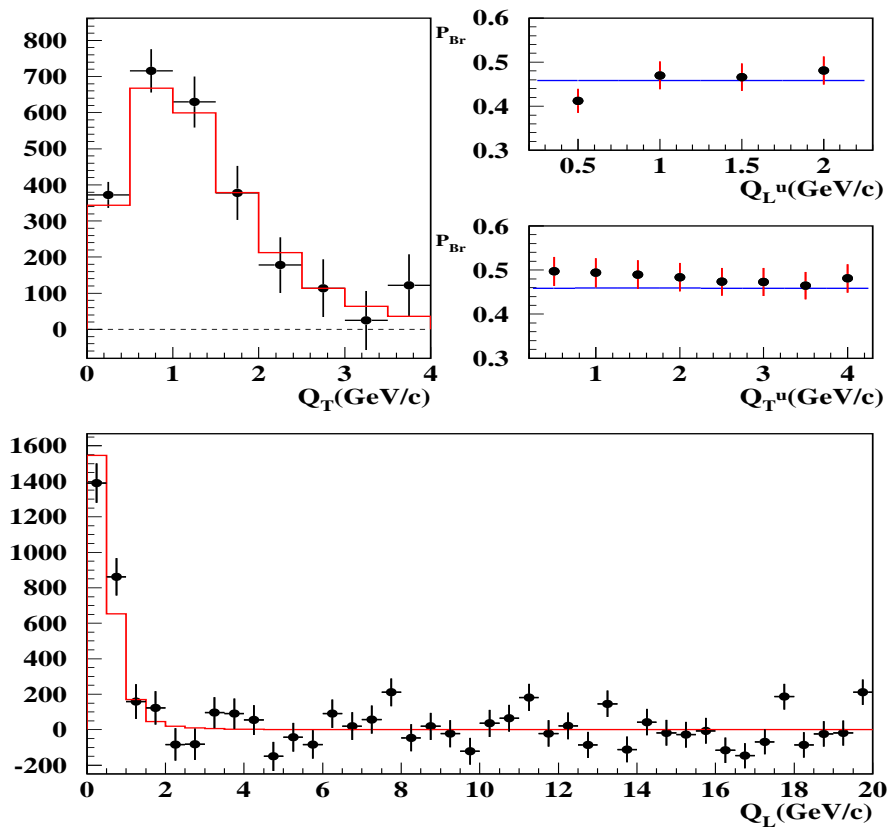


Figure 6.11: Fit results for the $\pi^+\pi^-$ momentum interval $3.2 < p < 3.8$ GeV/c in lab-frame. Caption is identical to figure 6.10 for the rest.

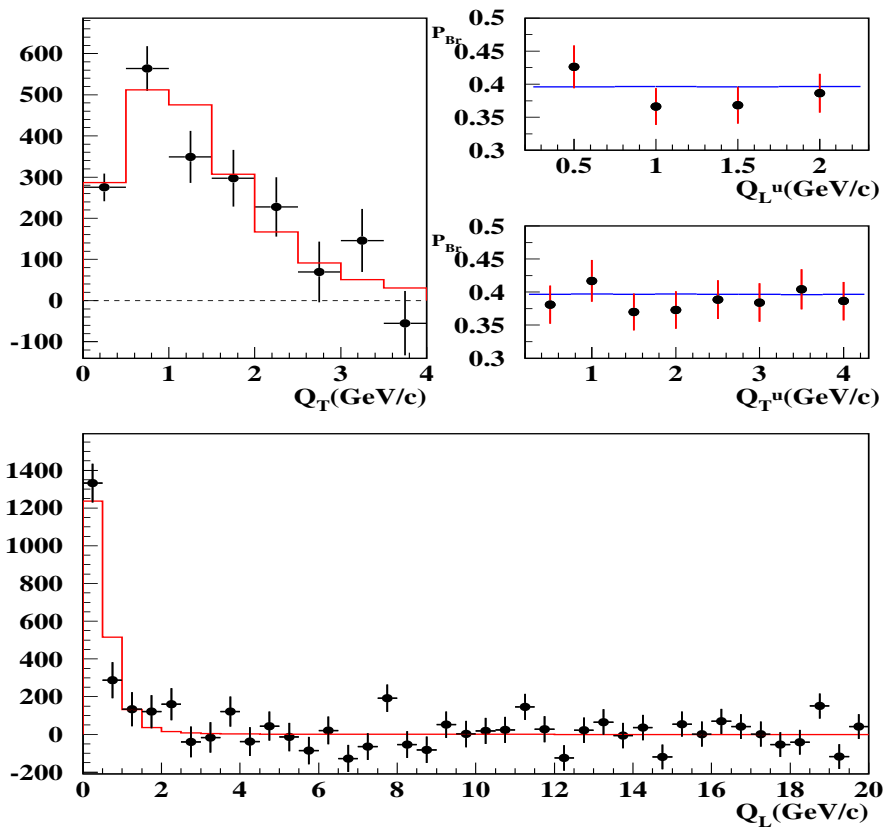


Figure 6.12: Fit results for the $\pi^+\pi^-$ momentum interval $3.8 < p < 4.4$ GeV/c in lab-frame. Caption is identical to figure 6.10 for the rest.

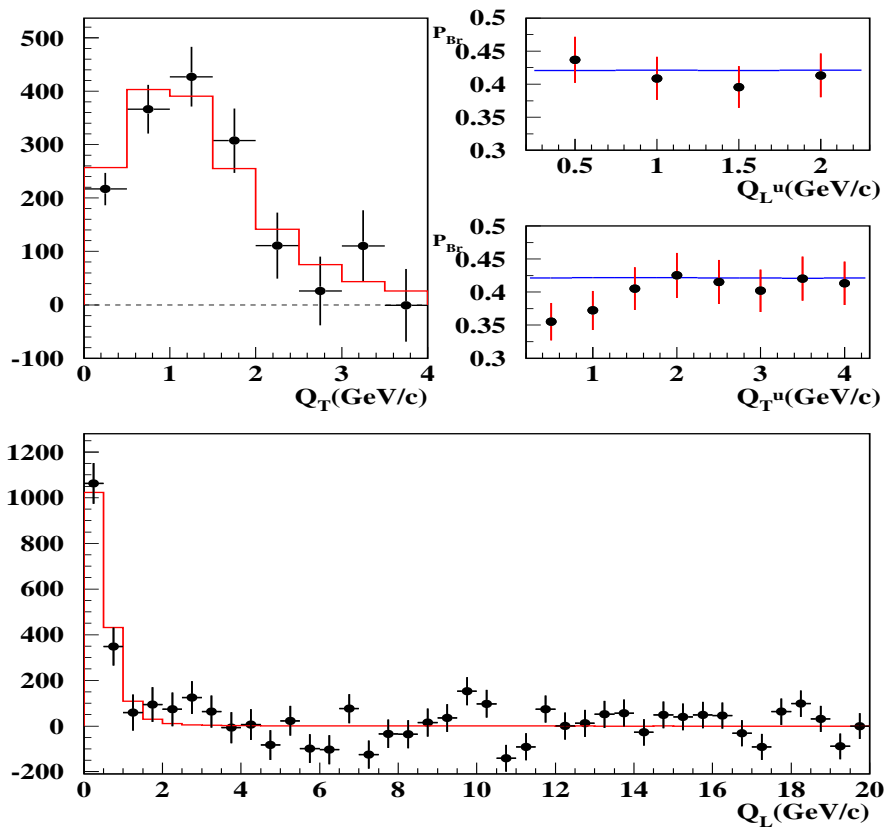


Figure 6.13: Fit results for the $\pi^+\pi^-$ momentum interval $4.4 < p < 5.0$ GeV/c in lab-frame. Caption is identical to figure 6.10 for the rest.

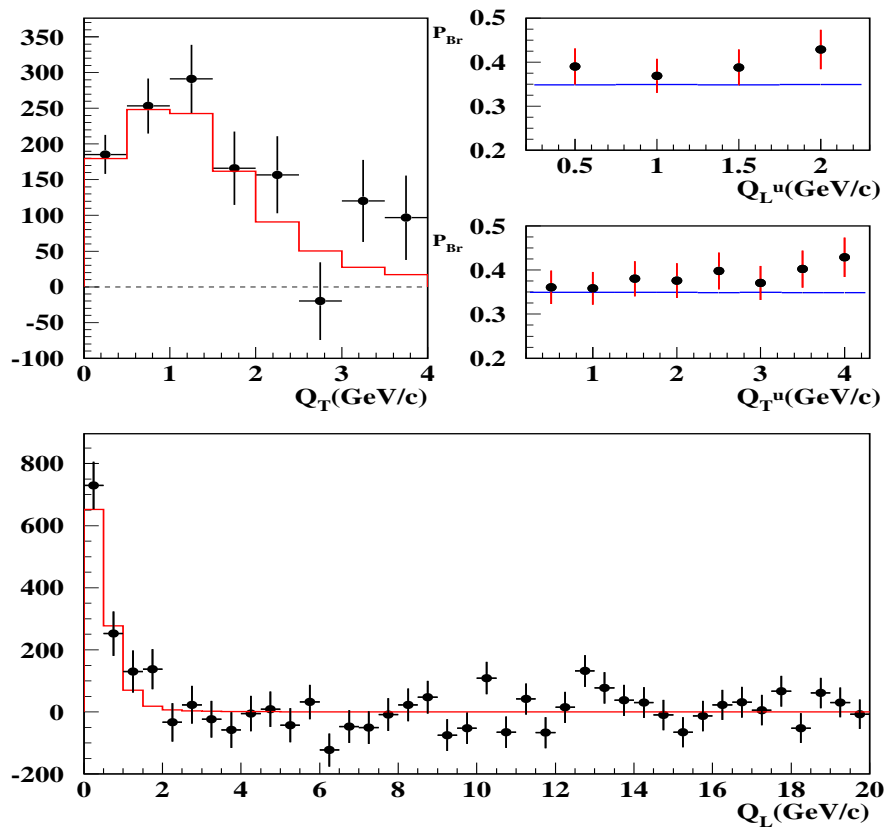


Figure 6.14: Fit results for the $\pi^+\pi^-$ momentum interval $5. < p < 5.6$ GeV/c in lab-frame. Caption is identical to figure 6.10 for the rest.

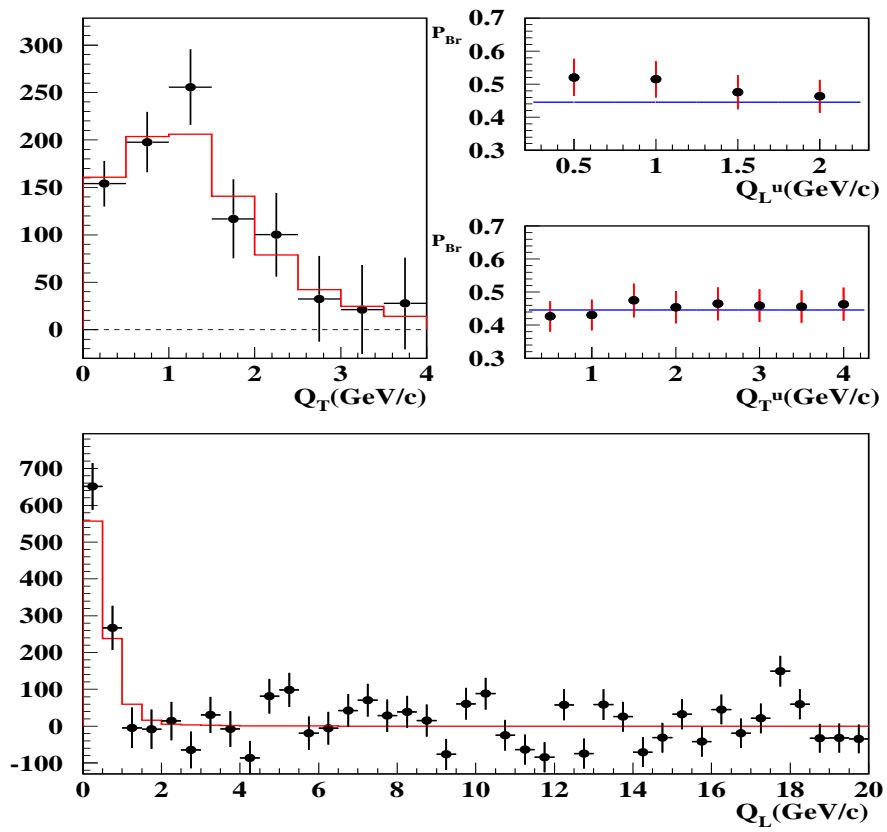


Figure 6.15: *Fit results for the $\pi^+\pi^-$ momentum interval $5.6 < p < 6.2$ GeV/c in lab-frame. Caption is identical to figure 6.10 for the rest.*

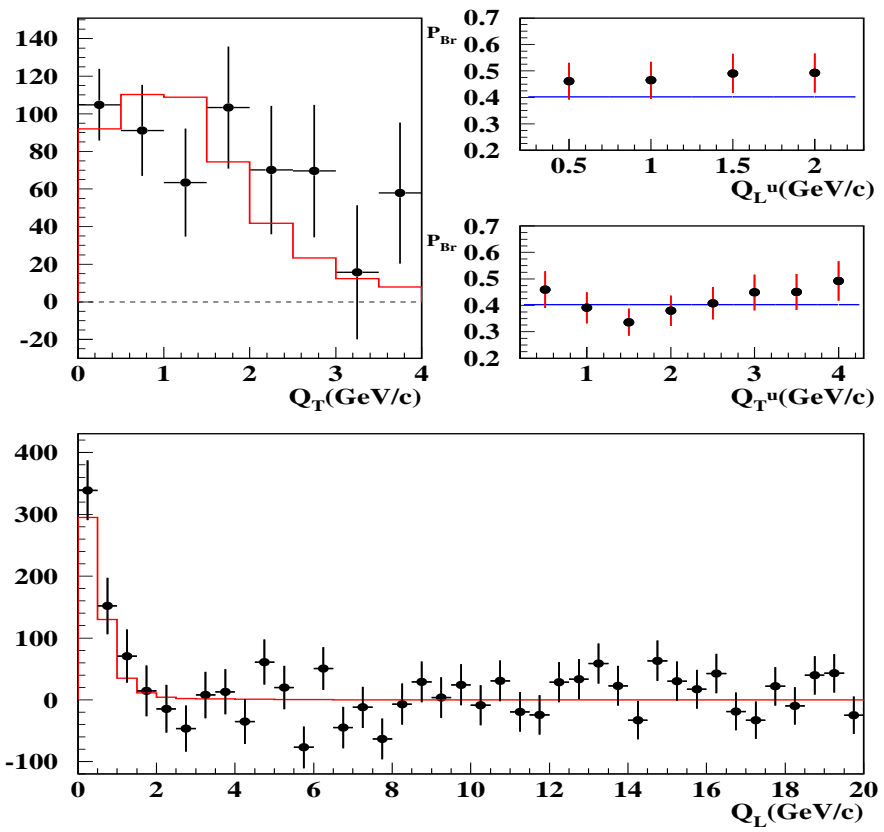


Figure 6.16: Fit results for the $\pi^+\pi^-$ momentum interval $6.2 < p < 6.8$ GeV/c in lab-frame. Caption is identical to figure 6.10 for the rest.

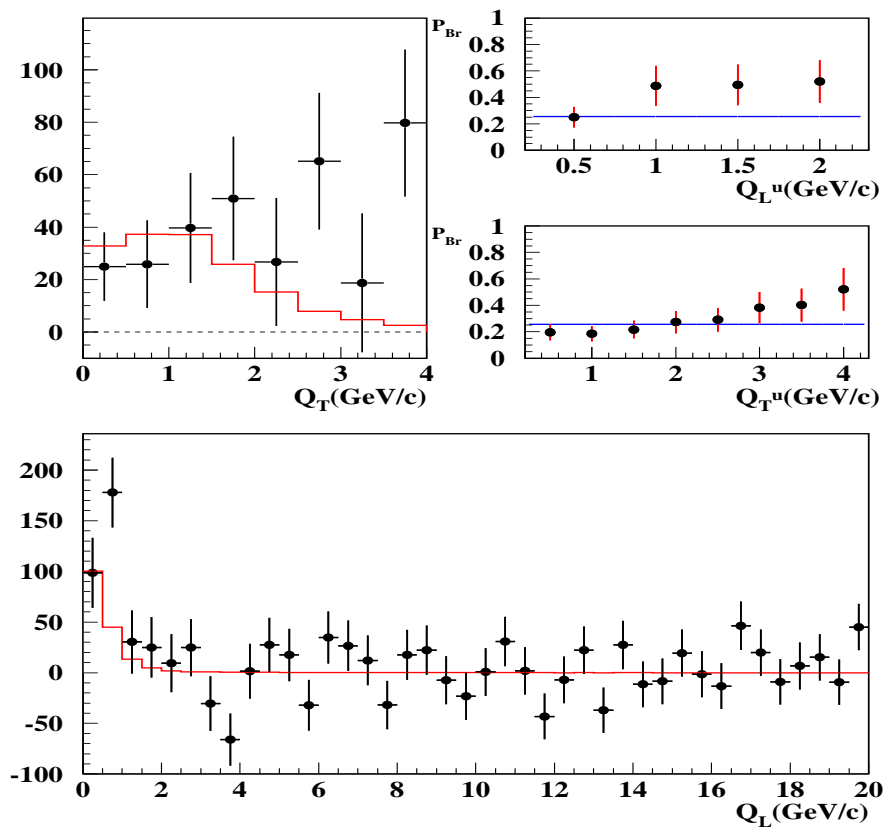


Figure 6.17: Fit results for the $\pi^+\pi^-$ momentum interval $6.8 < p < 7.4$ GeV/c in lab-frame. Caption is identical to figure 6.10 for the rest.

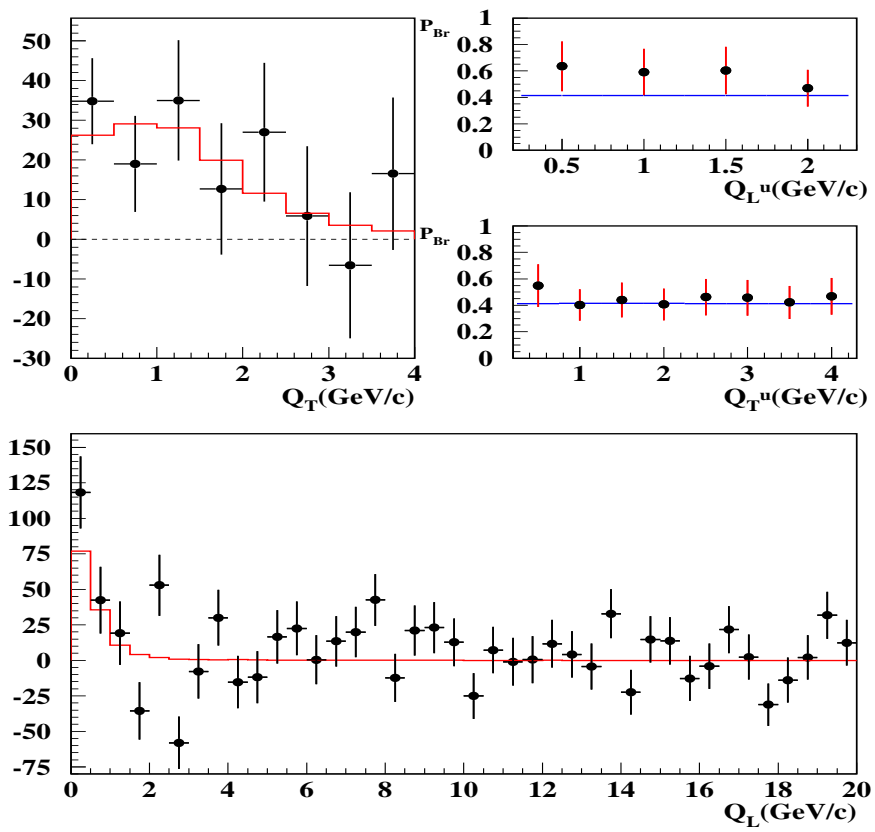


Figure 6.18: Fit results for the $\pi^+\pi^-$ momentum interval $7.4 < p < 8.0$ GeV/c in lab-frame. Caption is identical to figure 6.10 for the rest.

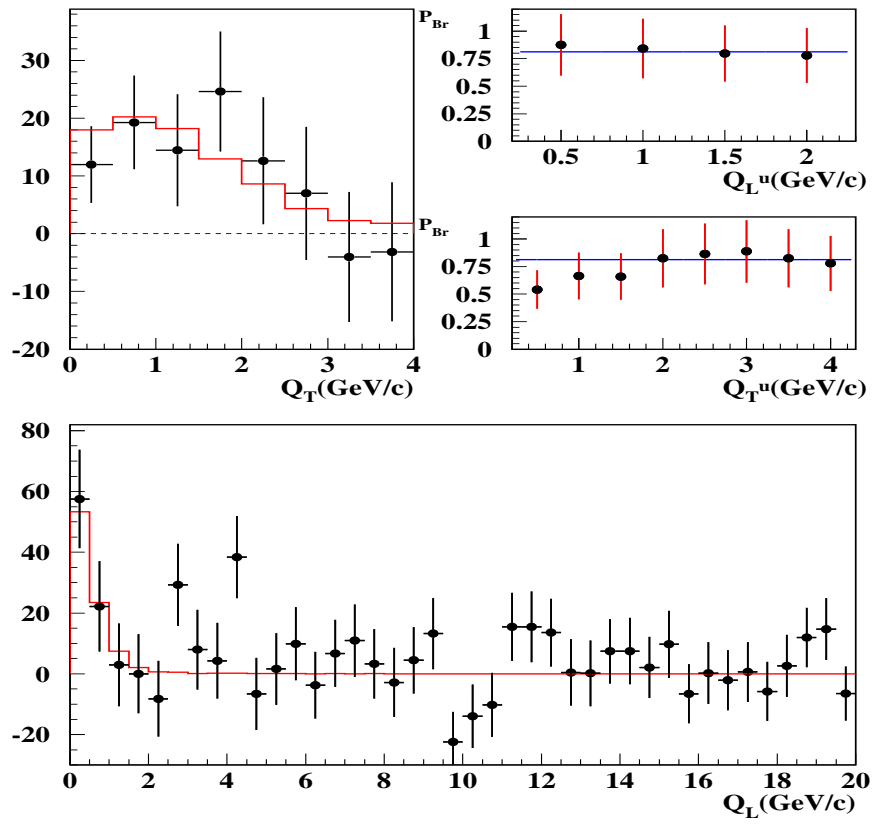


Figure 6.19: Fit results for the $\pi^+\pi^-$ momentum interval $8.0 < p < 8.6$ GeV/c in lab-frame. Caption is identical to figure 6.10 for the rest.

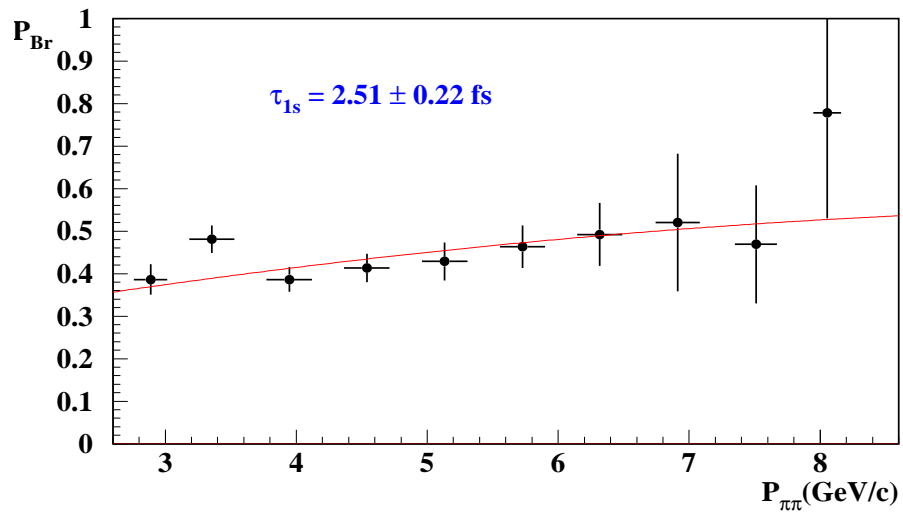


Figure 6.20: Pionium break-up probability P_{Br} as function of atom momentum, as compared to best fit Monte Carlo prediction with average *Ni* foil thickness. The fit χ^2 is 11.2 for 9 degrees of freedom. Pionium $1s$ lifetime value and error are indicated, for 2002+2003 data.

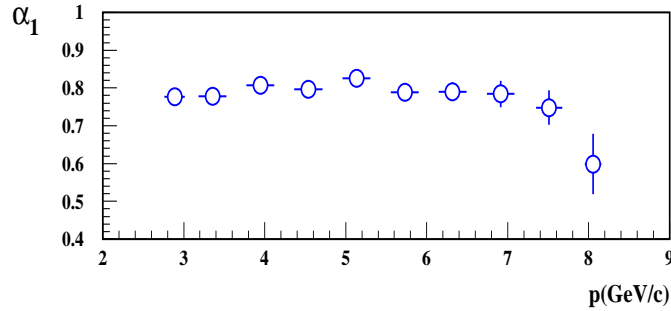


Figure 6.21: Fitted values of α_1 parameter as function of $\pi^+\pi^-$ momentum.

The number of atom pairs N_A determined as function of p is plotted in figure 6.22 along with the number of Coulomb pairs given by the fit in each bin. Errors in N_A are given by MINOS variation of γ parameter. It is seen that atom production follows rather closely the spectrum of semi-inclusive $\pi^+\pi^-$ differential cross-section, as expected from bound state production. Please note that both of these spectra are uncorrected for spectrometer acceptance.

Pionium break-up probabilities can now be determined by using the momentum-dependent K-factors calculated in table 6.2, and they are shown in figure 6.20. Errors were propagated from those provided by the fit for N_A and N_C . P_{Br} values are compatible with a smooth increase with increasing atom momentum, as predicted by Monte Carlo tracking inside the target foil [59] [70]. We generate a continuous set of $P_{Br}(p)$ curves with varying values of the $1s$ pionium lifetime (τ_{1s}). χ^2 minimization with respect to this set provides a measurement of τ_{1s} with an error.

The fitted values of α_1 parameter (fraction of Coulomb pairs) are also shown in figure 6.21 as function of p . They show a smooth behaviour.

In figure 6.23 we plot the number of non-Coulomb pairs determined by the fit as function of p , after subtraction of accidentals (see [66]), and we

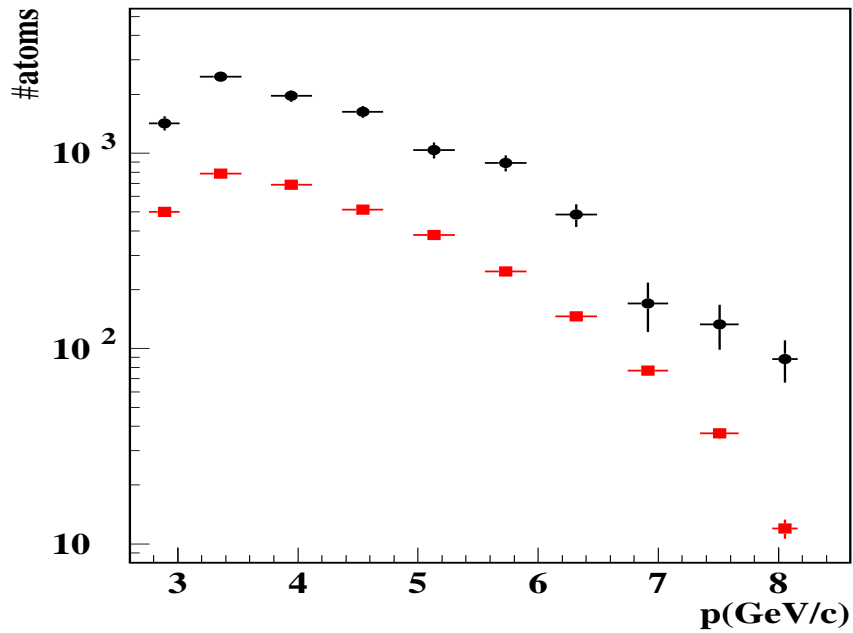


Figure 6.22: Fitted number of atom pairs as function of their lab-frame momentum (black circles), as compared to the fitted number of Coulomb pairs for $Q_L > 2\text{MeV}/c$ (coloured rectangles). The latter were normalized to half the area, to avoid the very large difference in actual scale.

compare the spectrum with that previously determined for Coulomb pairs (see figure 6.22). The non-Coulomb spectrum is significantly softer than the Coulomb spectrum, probably due to parent multibody decays of the accompanying long-lifetime particle.

6.3 Break-up probability measurement

Pionium break-up probability P_{Br} in the Ni foil has been determined in two different ways. One is making a global (momentum-integrated) fit, which

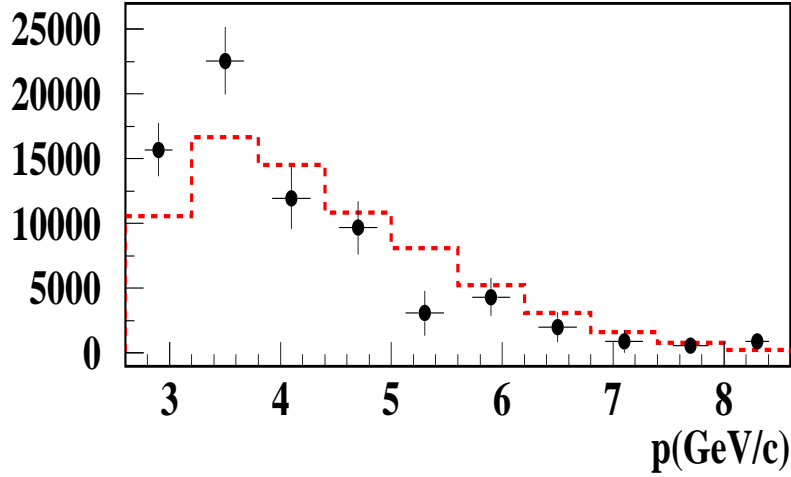


Figure 6.23: Fitted number of long-lifetime pairs (circles), determined from α_3 parameter, as function of $\pi^+\pi^-$ momentum. It is compared with the number of Coulomb pairs in figure 6.22 (dotted line), normalized to the same area.

provides a single measurement for the average P_{Br} , and another is making 10 independent experiments to measure this quantity in $600\text{MeV}/c$ wide intervals of pionium momentum. The results are in very good agreement with each other when the average P_{Br} values are compared, and have equal statistical errors. Both of them provide a high fit quality with respect to the Monte Carlo hypothesis, in terms of χ^2 probability.

Taking into account the systematic error estimated in section 7.4, we have the break-up probability measurement:

$$P_{Br} = 0.427 \pm 0.013 \text{ (stat)} \pm 0.006 \text{ (syst)}$$

or having both error sources in quadrature:

$$P_{Br} = 0.427 \pm 0.015$$

Using the relationship between P_{Br} and lifetime obtained from the pionium propagation code [59] [70], we determine the pionium $1s$ lifetime from 2002+2003 data alone:

$$\tau_{1s} = 2.51^{+0.24}_{-0.22} \text{ fs}$$

Chapter 7

Pionium Lifetime and $|a_0 - a_2|$

7.1 Summary of corrections

At this point it is necessary to remember small corrections applied, that they were pointed in the chapter 1.

These corrections are: Q_L trigger acceptance correction, based upon the observed behavior of the full sample of accidental pairs [86, 87]. A K^+K^- correction, applied using Monte Carlo and real data (chapter 5), as explained in chapter 1. Also a target impurity correction is done according to reference [71] and, finally, it is very important to point that $\omega - \eta'$ finite-size correction appears to be unnecessary [86], as it will be seen in tables 7.1, 7.8 and 7.9.

7.2 Combined global fit analysis

The global fit consists in minimizing the χ^2 defined in (1.20) in $2D$ with respect to α_3 (non-Coulomb fraction) and γ parameters, using the momentum-integrated sample. The α_2 and ϵ parameters remain fixed in this fit, and α_2 is determined by the direct measurement of the accidental pairs fraction from the analysis of the precision time-of-flight spectrum, as it can be seen in table 1.2. ϵ is fixed to the experimentally determined K^+K^- fraction previously used in chapter 5 and reference [86]. β can either be left as a free parameter, or be fixed to the total number of prompt pairs in the fit region

(N_p), or to the ratio $\beta = N_p^c/f_c$ where N_p^c is the number of prompt events with $Q_L > 2MeV/c$ (control region) and f_c is the ratio between the number of Monte Carlo pairs in the control region and the total number of Monte Carlo events. These options mean small variations with respect to N_p and produce slight changes in the fit results, as indicated in table 7.3.

We have chosen to perform the fit in $0.25 \times 0.25 (MeV/c)^2$ bins in the (Q_T, Q_L) plane, for the global fit. Variations with respect to this choice are reported in table 7.3.

Once the fit has converged, we define the atom signal in each (i, j) bin as the difference between the prompt spectrum (with accidentals subtracted) and the Monte Carlo with the pionium component (AA) removed. This 2D signal, which reveals the excess with respect to the calculated Coulomb interaction enhancement β background, is what we call the pionium spectrum. The atom breakup probability P_{br} is then determined [66] by means of the K-factors.

This analysis has already been carried out separately for 2001 Ni data [86] and 2002+2003 Ni data [87], and what we are going to present in the following are the combined results for the full DIRAC Ni data sample. As we did for the partial samples, we will illustrate the various corrections by flashing the results at each correction step.

The correction sequence is defined in a cumulative way, namely:

- a) use improved statistics Monte Carlo.
- b) include K^+K^- correction.
- c) perform the target impurity correction.
- d) remove the $\omega - \eta'$ finite-size correction, according to reference [35].

Given the fact that the Monte Carlo simulations are slightly different for each period, we will present the combined χ^2 -fit results as those of a single fit with χ^2 values and number of degrees of freedom added independently.

In table 7.1 we present the χ^2 values (separately in control and extrapolation regions), the number of atoms N_A , the number of Coulomb pairs in the complete fit range N_{CC} , the β parameter and the P_{br} for each option.

Table 7.1: Fit results for the correction options a), b), c), d) indicated in the text. χ^2 's in the full domain, and its restriction to the control and extrapolation regions separately, are given. Also the total number of atoms N_A and coulomb pairs N_{CC} , the β parameter and the break-up probabilities are indicated.

	a)	a+b)
χ^2_{tot}/ndf	3222.6/3200	3215.2/3200
χ^2_{ext}/ndf	326.1/320	322.3/320
χ^2_{cont}/ndf	2896.5/2880	2892.9/2880
N_A	17250 ± 374	16562 ± 360
N_{CC}	2028303 ± 8702	1996876 ± 8552
β	2484578	2484842
P_{Br}	0.422 ± 0.010	0.411 ± 0.010

χ^2_{tot}/ndf	3215.2/3200	3198.0/3200
χ^2_{ext}/ndf	322.3/320	321.3/320
χ^2_{cont}/ndf	2892.9/2880	2876.7/2880
N_A	16562 ± 360	16814 ± 363
N_{CC}	1996876 ± 8552	1972693 ± 8468
β	2484842	2484812
P_{Br}	0.417 ± 0.010	0.427 ± 0.010

We recover, now enhanced, the effects that we already discussed separately. Whereas the introduction of the K^+K^- contamination [67].[68] decreases the total χ^2 by 7.4 units, the removal of the $\omega - \eta'$ finite-size correction decreases it by 17.2 units. The combined effect of both actions decreased the total χ^2 by 24.6 units. We remark that, in agreement with our earlier findings, the $\omega - \eta'$ finite-size correction is not wanted by the data. The statistical significance will be further enhanced when we report the momentum-dependent fit in subsection 7.3.

The K^+K^- correction introduces a better stability of the measured P_{Br} values with respect to the Q_T cut, and also a better agreement between the Q_T and Q_L series of cuts to define the atom signal, at very low Q_T and Q_L values, as it can be clearly appreciated in figure 7.10.

The pionium $2D$ signal is shown in the form of lego plots in figures 7.8 and 7.9.

Table 7.2: Comparison of global fit results for three different choices of the β parameter definition.

	β	P_{Br}	χ^2/ndf
β all range	2486202	0.419 ± 0.010	3199.0/3200
β ($Q_L > 2\text{MeV}/c$)	2485678	0.426 ± 0.010	3198.4/3200
β free	2483534	0.430 ± 0.010	3196.1/3200

Table 7.3: Comparison of global fit results using two different (Q_T, Q_L) binsizes.

	β	P_{Br}	χ^2/ndf	N_A
0.25×0.25	2483534	0.430 ± 0.010	3196.1/3200	16915 ± 366
0.5×0.5	2485567	0.427 ± 0.010	751.9/800	16803 ± 366

7.2.1 Dependence on the Q_L upper limit

Our standard fit domain is the region $Q_L < 20\text{MeV}/c$ and $Q_T < 5\text{MeV}/c$, and the dependence of the P_{Br} with respect to the Q_L upper limit (Q_L^{up}) is

Table 7.4: Values of break-up probability P_{Br} obtained from different choices of the upper limit (Q_L^{cut}) used to define the control region in Q_L projection.

$Q_L^{cut}(MeV/c)$	P_{Br}
22	0.426 ± 0.010
21	0.430 ± 0.010
20	0.430 ± 0.010
19	0.429 ± 0.010
18	0.426 ± 0.010
17	0.426 ± 0.010
16	0.428 ± 0.011
15	0.429 ± 0.011
14	0.429 ± 0.011
13	0.424 ± 0.011

analysed in table 7.4 and figure 7.1. No appreciable systematics is observed and the value at $Q_L^{up} = 20MeV/c$ is close to the average.

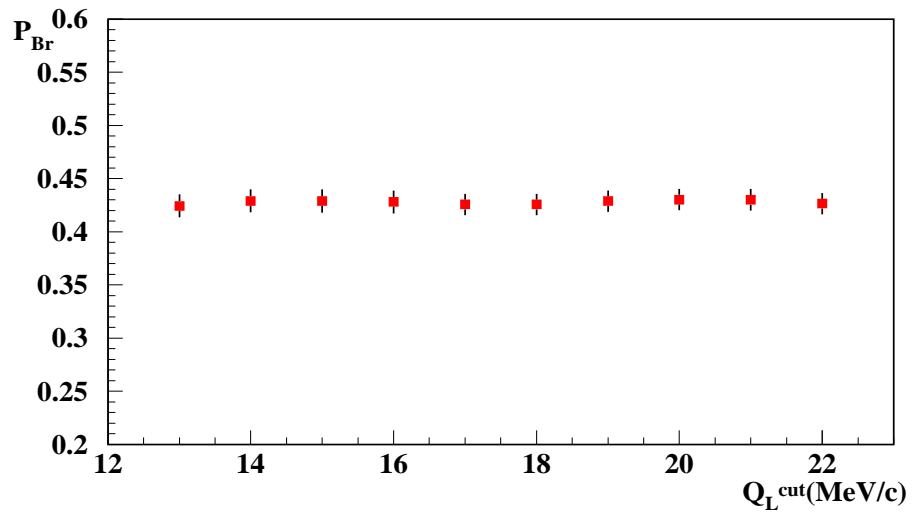


Figure 7.1: *Dependence of the break-up probability on the Q_L upper cut.*

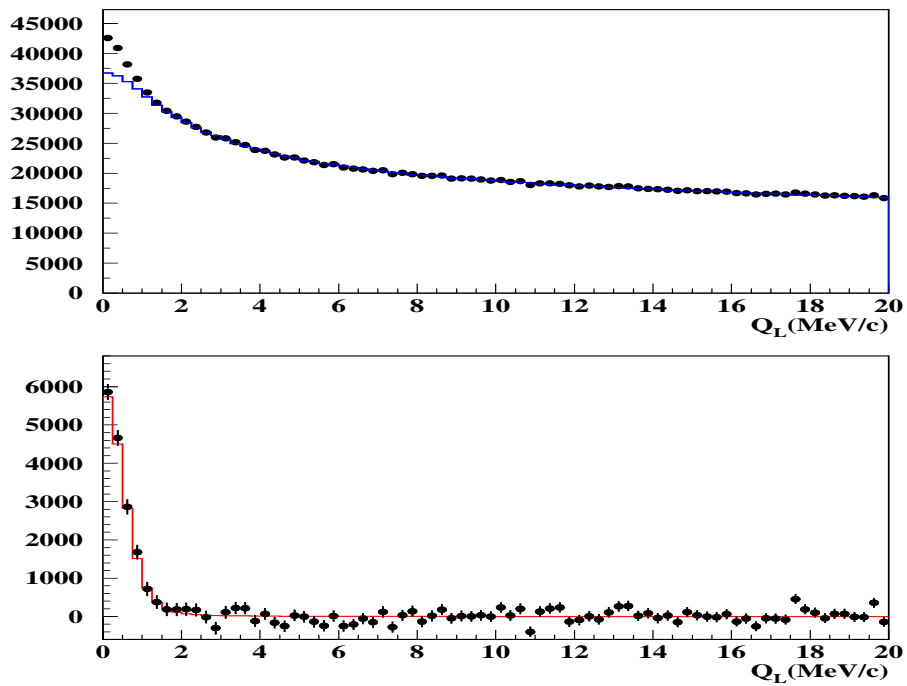


Figure 7.2: Two-dimensional global fit projection onto Q_L . The standard $Q_T < 4$ MeV/c cut has been applied. The difference between prompt data (dots) and Monte Carlo (blue line), which corresponds to pionium signal, is plotted at the bottom, where the signal is compared with the pionium atom Monte Carlo (red line).

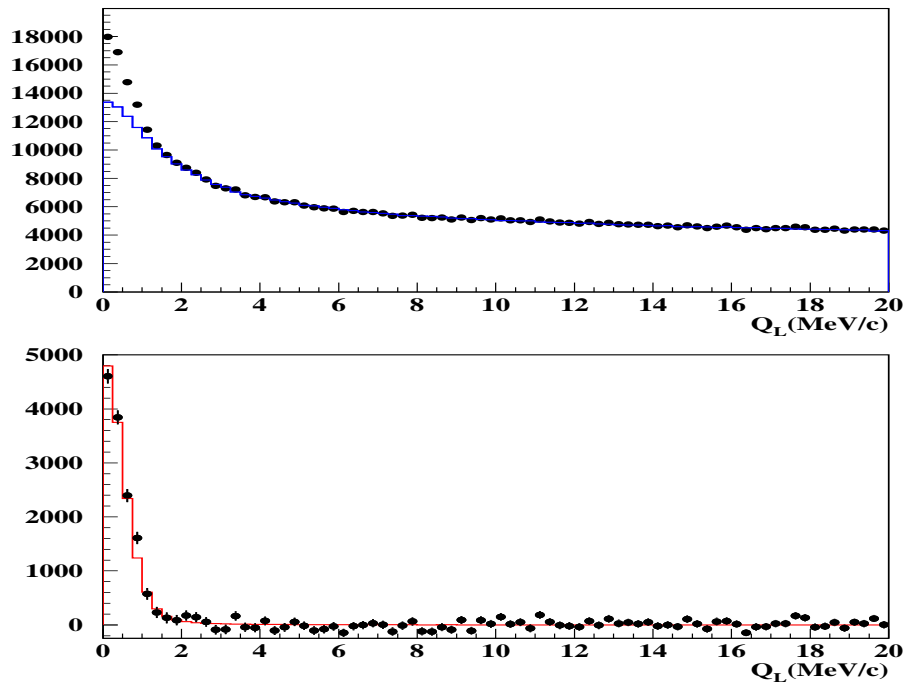


Figure 7.3: Two-dimensional global fit projection onto Q_L . A more restrictive $Q_T < 2 \text{ MeV}/c$ cut has been applied to enhance the signal. The difference between prompt data (dots) and Monte Carlo (blue line), which corresponds to pionium signal, is plotted at the bottom, where the signal is compared with the pionium atom Monte Carlo (red line).

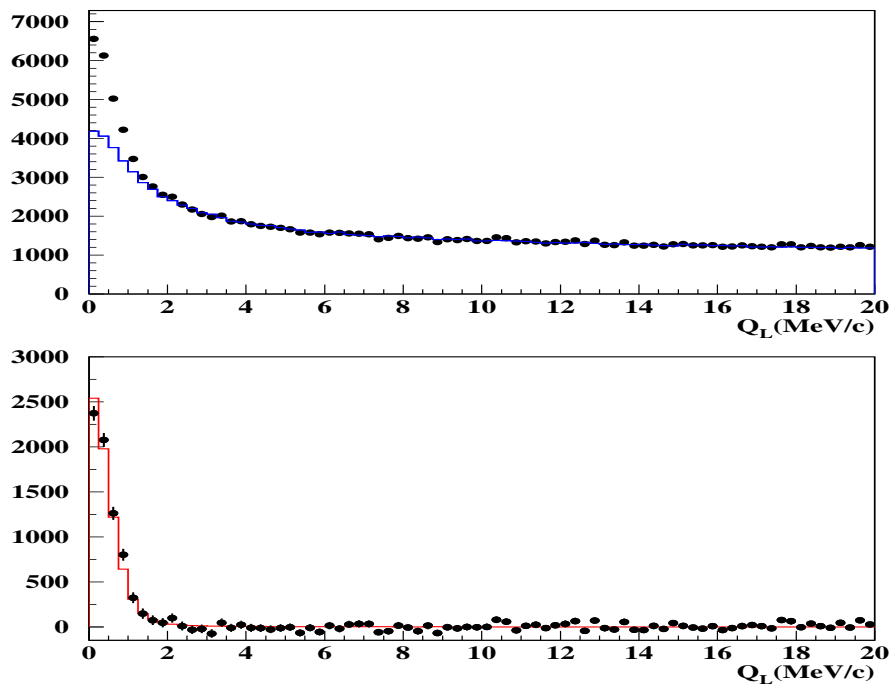


Figure 7.4: Two-dimensional global fit projection onto Q_L . A more restrictive $Q_T < 1$ MeV/c cut has been applied to enhance the signal. The difference between prompt data (dots) and Monte Carlo (blue line), which corresponds to pionium signal, is plotted at the bottom, where the signal is compared with the pionium atom Monte Carlo (red line).

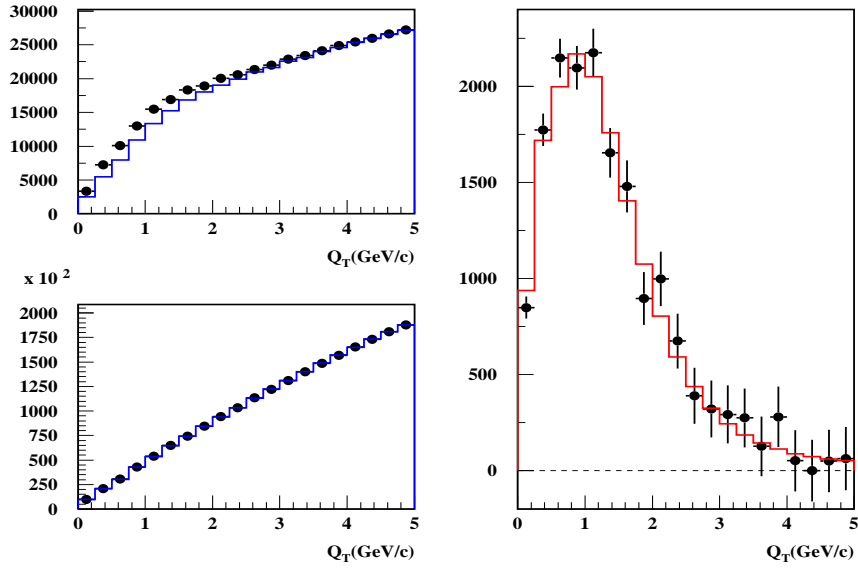


Figure 7.5: Two-dimensional global fit projection onto Q_T . The data are shown separately for $Q_L < 2\text{MeV}/c$ (left top) and $Q_L > 2\text{MeV}/c$ (left bottom). The difference between prompt data (dots) and Monte Carlo (blue line), which corresponds to transverse pionium signal, is plotted (right) and compared with the pionium atom Monte Carlo (red line).

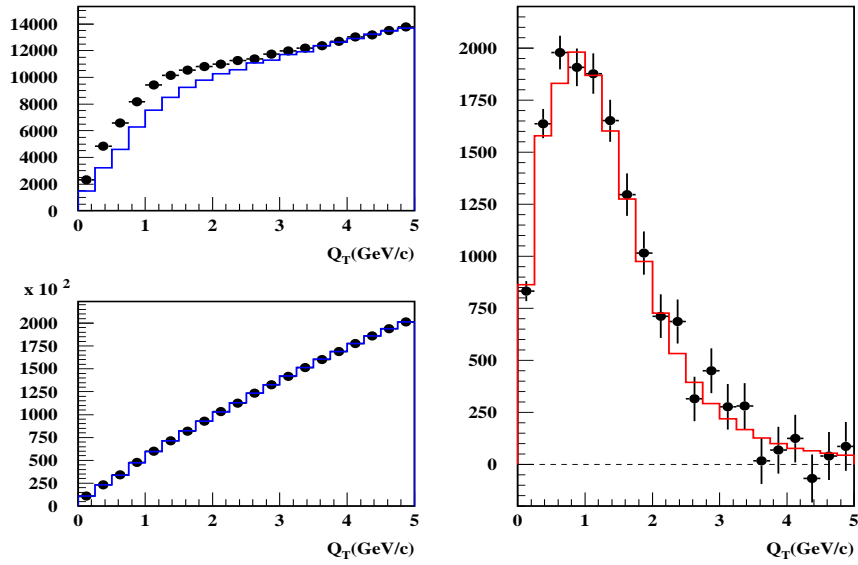


Figure 7.6: Two-dimensional global fit projection onto Q_T . The data are shown separately for $Q_L < 1\text{MeV}/c$ (left top) and $Q_L > 1\text{MeV}/c$ (left bottom). The difference between prompt data (dots) and Monte Carlo (blue line), which corresponds to transverse pionium signal, is plotted (right) and compared with the pionium atom Monte Carlo (red line).

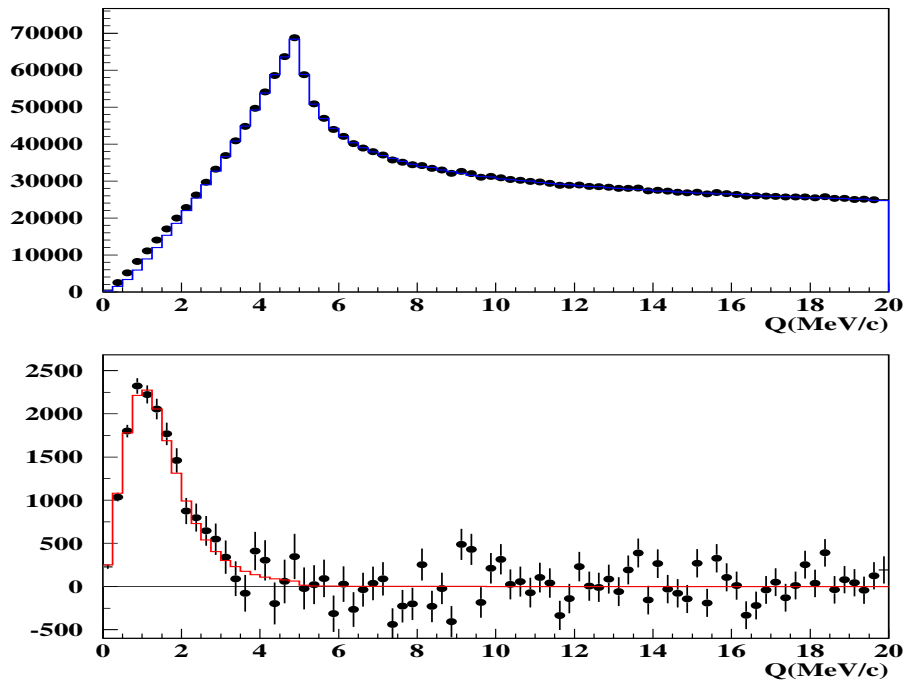


Figure 7.7: *Two-dimensional global fit projection onto Q . The standard $Q_T < 4 \text{ MeV}/c$ cut was applied. The difference between prompt data (dots) and Monte Carlo (blue line), which corresponds to ponium signal, is plotted at the bottom. The signal is compared with the ponium atom Monte Carlo (red line).*

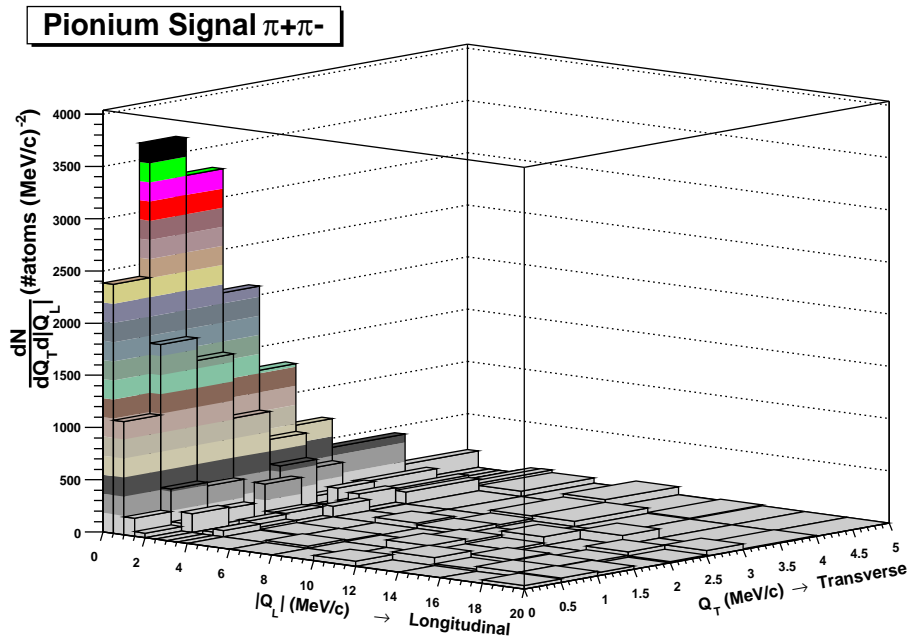


Figure 7.8: Lego plot showing the pionium break-up spectrum in Ni in the $(Q_T, Q_L = |Q_Z|)$ plane, after subtraction of the Coulomb background.

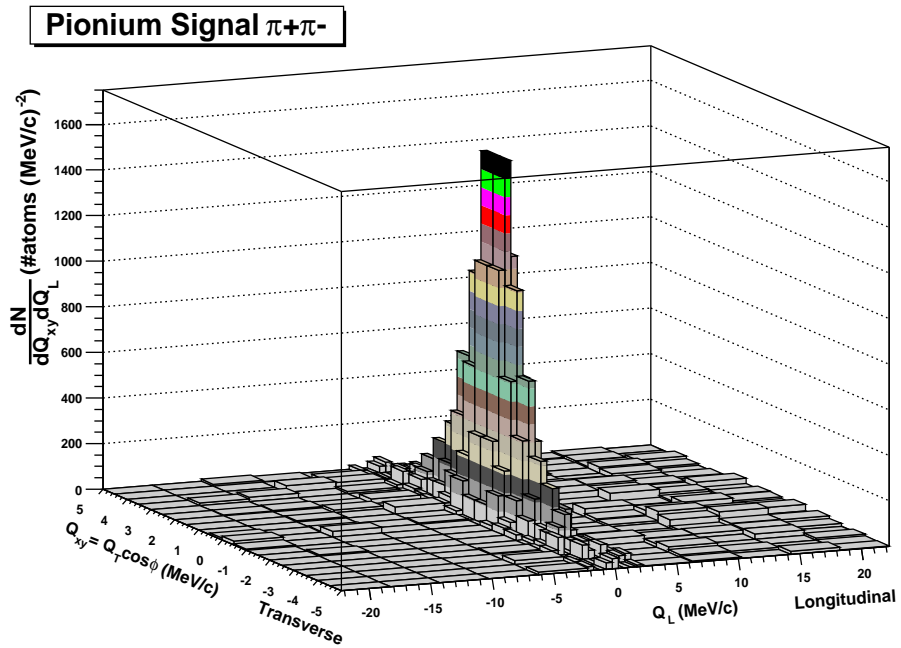


Figure 7.9: Lego plot showing the pionium break-up spectrum in Ni in the (Q_{xy}, Q_L) plane, after subtraction of Coulomb background. The transverse component $Q_{xy} = Q_T \cos\phi$ is defined as the product of the measured Q_T value times the cosine of a random azimuth.

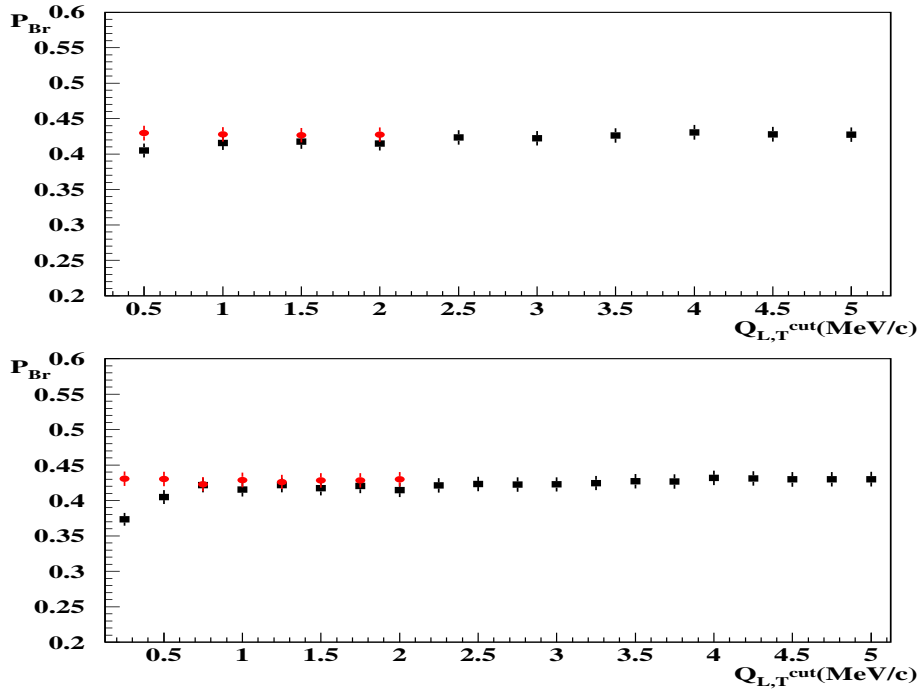


Figure 7.10: Pionium break-up probabilities determined from different choices of the upper limits ($Q_{T,L}^u$) in the rectangular integration domain to define the atom signal. Top plot shows the 2001+2002+2003 results after the introduction of K^+K^- correction, in $0.5\text{MeV}/c$ steps of Q_L^u (red dots) and Q_T^u (black squares). Bottom plot shows the same in $0.25\text{MeV}/c$ steps.

7.3 Momentum-dependent analysis

Following the approach of our earlier work [66], in this section we split the pair momentum spectrum in ten 600 MeV/c bins and perform independent fits at each momentum interval. The corrections applied are the same as for the global fit. The only change with respect to the latter is the choice of $0.5 \times 0.5(\text{MeV}/c)^2$ binsize, which is now obliged due to the strong statistics reduction at individual 2D bins.

We shall keep track of the results at each correction step as follows:

- a) Table 7.6: The standard Monte Carlo is used.
- b) Table 7.7: K^+K^- contamination is introduced, after the parametrization given in [86].
- c) Table 7.8: Standard Monte Carlo, K^+K^- contamination and target impurity correction.
- d) Table 7.9: In addition to the above, the $\omega - \eta'$ finite-size correction is dropped. This is the final result.

Figures from 7.11 to 7.20 show the result of the 10 independent fits in the form of atom spectra (Q_L and Q_T) and break-up probabilities as function of Q_L and Q_T cuts.

The signal line-shape shows good agreement with the pionium Monte Carlo simulation [59],[70].

In table 7.5 a new global χ^2 has been defined as the sum of the individual ones at each momentum bin, and a combined P_{Br} value and error have been calculated after proper account of the independent statistical errors. The sum has been further extended to include the independent 2001 and 2002+2003 data samples. The number of atoms (N_A) and Coulomb pairs (N_C) are also indicated.

From table 7.5 we draw the same conclusions as from the global analysis. The introduction of K^+K^- simulation improves the χ^2 by 12.6 units, and when the $\omega - \eta'$ finite-size correction is removed, the χ^2 improves by 36.0 additional units. We consider this a clear indication that the latter should be done. Adding this two changes, the χ^2 is reduced by 48.6 units.

Table 7.5: Combined momentum dependent fit, for progressive fit conditions as defined in the text.

	A	A+B	A+B+C	A+B+C+D
χ^2	6926.0/7047	6913.4/7047	6913.4/7047	6877.4/7047
P_{Br}	0.424 \pm 0.011	0.417 \pm 0.010	0.423 \pm 0.010	0.432 \pm 0.010
N_A	17401 \pm 394	16835 \pm 384	16835 \pm 384	17005 \pm 386
N_C	1601446 \pm 7252	1578030 \pm 7154	1578030 \pm 7154	1560276 \pm 7092

Table 7.6: Results of the momentum-dependent fit, using correction a) only (see text). Break-up probability values P_{Br} , number of atom pairs N_A , α_1 and χ^2 over the entire fit region are indicated in this table, for every 600 MeV/c momentum interval p_i .

	P_{Br}	N_A	α_1	χ^2 /ndf	χ_e^2 / ndf
p_1	0.392 \pm 0.027	2094 \pm 130	0.789 \pm 0.013	614.2/648	71.8/72
p_2	0.433 \pm 0.023	3798 \pm 177	0.804 \pm 0.007	638.9/648	81.1/72
p_3	0.400 \pm 0.022	3158 \pm 160	0.816 \pm 0.008	634.3/648	55.2/72
p_4	0.436 \pm 0.026	2779 \pm 147	0.831 \pm 0.009	601.8/648	72.2/72
p_5	0.424 \pm 0.031	2080 \pm 141	0.848 \pm 0.011	613.2/648	52.1/72
p_6	0.445 \pm 0.037	1491 \pm 108	0.816 \pm 0.013	692.5/648	64.9/72
p_7	0.462 \pm 0.055	944 \pm 996	0.824 \pm 0.018	670.9/648	77.0/72
p_8	0.621 \pm 0.108	623 \pm 110	0.777 \pm 0.025	631.9/642	112.6/72
p_9	0.571 \pm 0.105	303 \pm 53	0.838 \pm 0.018	617.9/615	71.5/72
p_{10}	0.764 \pm 0.228	154 \pm 64	0.742 \pm 0.046	480.7/534	71.2/72

Table 7.7: Results of the momentum-dependent fit, using corrections $a+b$ (see text). Break-up probability values P_{Br} , number of atom pairs N_A , α_1 and χ^2 over the entire fit region are indicated in this table, for every 600 MeV/c momentum interval p_i .

	P_{Br}	N_A	α_1	χ^2 / ndf	χ_e^2 / ndf
p_1	0.390 ± 0.027	2070 ± 128	0.786 ± 0.013	614.8/648	72.0/72
p_2	0.429 ± 0.022	3741 ± 175	0.800 ± 0.007	638.4/648	81.9/72
p_3	0.395 ± 0.022	3080 ± 156	0.811 ± 0.008	634.3/648	56.4/72
p_4	0.428 ± 0.026	2684 ± 143	0.824 ± 0.009	601.8/648	71.9/72
p_5	0.411 ± 0.031	1983 ± 137	0.840 ± 0.011	611.2/648	50.0/72
p_6	0.430 ± 0.036	1411 ± 103	0.804 ± 0.013	691.8/648	63.0/72
p_7	0.458 ± 0.055	907 ± 96	0.810 ± 0.017	670.6/648	74.8/72
p_8	0.607 ± 0.107	588 ± 105	0.763 ± 0.024	630.5/642	110.0/72
p_9	0.522 ± 0.100	269 ± 48	0.821 ± 0.025	618.2/615	70.8/72
p_{10}	0.774 ± 0.238	140 ± 66	0.665 ± 0.058	480.3/534	70.9/72

Table 7.8: *Fit results of the momentum-dependent fit, using corrections $a+b+c$ (see text). Break-up probability values P_{Br} , number of atom pairs N_A , α_1 and χ^2 over the entire fit region are indicated in this table, for every 600 MeV/c momentum interval p_i .*

	P_{Br}	N_A	α_1	χ^2 / ndf	χ_e^2 / ndf
p_1	0.395 ± 0.027	2070 ± 128	0.786 ± 0.013	614.8/648	72.0/72
p_2	0.436 ± 0.022	3741 ± 175	0.800 ± 0.007	638.4/648	81.9/72
p_3	0.402 ± 0.023	3080 ± 156	0.811 ± 0.008	634.3/648	56.4/72
p_4	0.433 ± 0.026	2684 ± 143	0.824 ± 0.009	601.8/648	71.9/72
p_5	0.417 ± 0.031	1983 ± 137	0.840 ± 0.011	611.2/648	50.0/72
p_6	0.437 ± 0.036	1411 ± 103	0.804 ± 0.013	691.8/648	63.0/72
p_7	0.465 ± 0.055	907 ± 96	0.810 ± 0.017	670.6/648	74.8/72
p_8	0.615 ± 0.108	588 ± 105	0.763 ± 0.024	630.5/642	110.0/72
p_9	0.530 ± 0.102	269 ± 48	0.822 ± 0.025	618.2/615	70.8/72
p_{10}	0.785 ± 0.242	140 ± 66	0.841 ± 0.109	480.3/534	70.9/72

Table 7.9: Final fit results of the momentum-dependent fit, using all corrections $a+b+c+d$ (see text). Break-up probability values P_{Br} , number of atom pairs N_A , α_1 and χ^2 over the entire fit region are indicated in this table, for every 600 MeV/c momentum interval p_i .

	P_{Br}	N_A	α_1	χ^2 / ndf	χ_e^2 / ndf
p_1	0.404 ± 0.028	2098 ± 129	0.777 ± 0.013	611.5/648	71.7/72
p_2	0.445 ± 0.023	3794 ± 176	0.790 ± 0.007	634.8/648	81.8/72
p_3	0.410 ± 0.023	3125 ± 158	0.801 ± 0.008	631.5/648	55.8/72
p_4	0.442 ± 0.026	2715 ± 144	0.816 ± 0.010	598.8/648	71.8/72
p_5	0.425 ± 0.031	2005 ± 137	0.831 ± 0.011	608.2/648	49.8/72
p_6	0.443 ± 0.037	1422 ± 104	0.796 ± 0.013	688.0/648	62.9/72
p_7	0.470 ± 0.056	910 ± 96	0.802 ± 0.017	667.4/648	74.3/72
p_8	0.615 ± 0.108	583 ± 105	0.756 ± 0.024	626.9/642	109.1/72
p_9	0.504 ± 0.099	257 ± 47	0.811 ± 0.029	614.4/615	70.6/72
p_{10}	0.742 ± 0.231	133 ± 67	0.840 ± 0.111	477.6/534	70.7/72

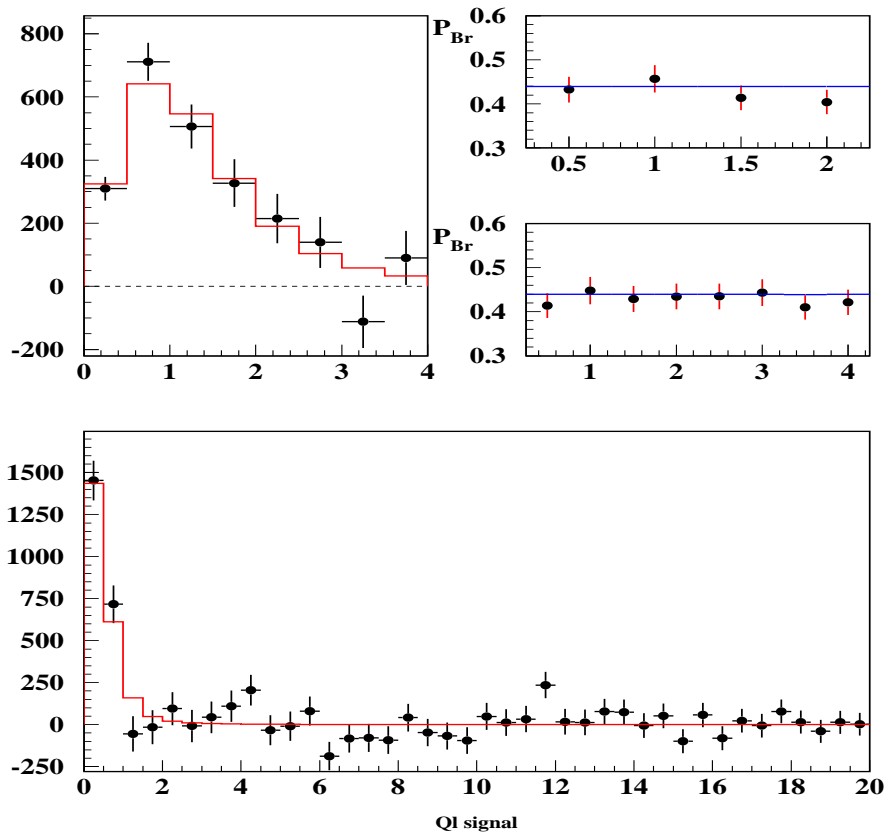


Figure 7.11: Fit results for the $\pi^+\pi^-$ momentum bin $2.6 < p < 3.2 \text{ GeV}/c$ in lab-frame. Q_T (top left) and Q_L (bottom) projections of the atom signal found in the extrapolation region ($Q_L < 2 \text{ MeV}/c$) after subtraction of the Monte Carlo prediction with Pionium component removed. Values of breakup probability determined for different integration upper limits Q_T^u and Q_L^u to define the atom signal (top right). Note the different Q_L^u values are all defined for $Q_T^u = 5 \text{ MeV}/c$ and Q_T^u values are defined for $Q_L^u = 2 \text{ MeV}/c$. The blue line indicates the P_{Br} determined from atom counting using the Monte Carlo.

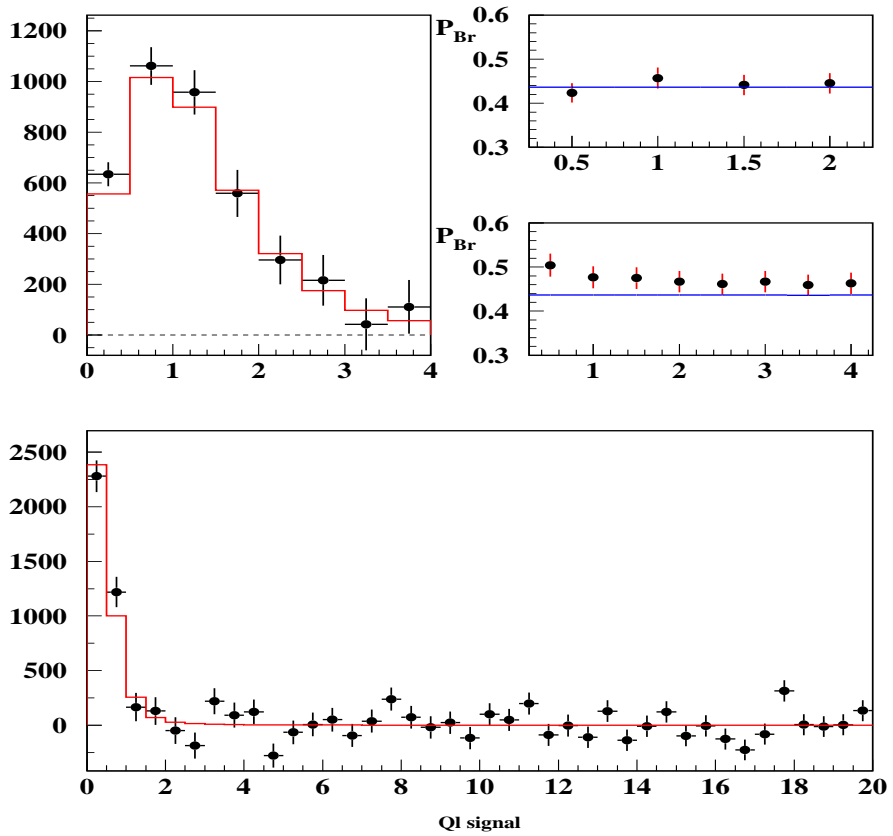


Figure 7.12: Fit results for the $\pi^+\pi^-$ momentum interval $3.2 < p < 3.8$ GeV/c in lab-frame. Caption is identical to figure 7.11 for the rest.

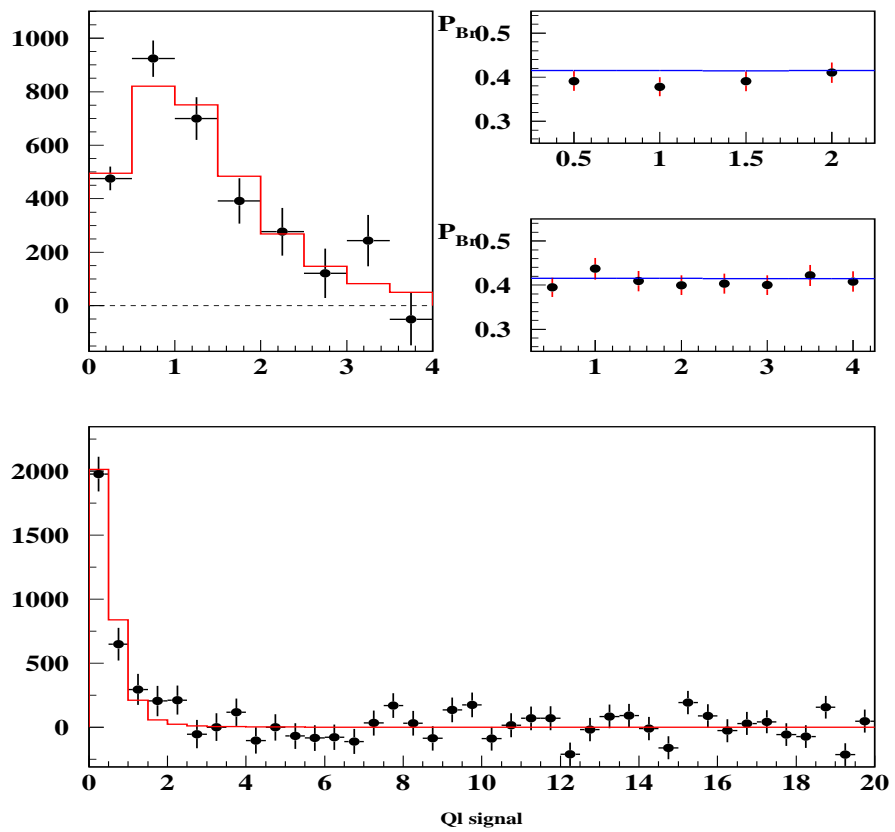


Figure 7.13: Fit results for the $\pi^+\pi^-$ momentum interval $3.8 < p < 4.4$ GeV/c in lab-frame. Caption is identical to figure 7.11 for the rest.

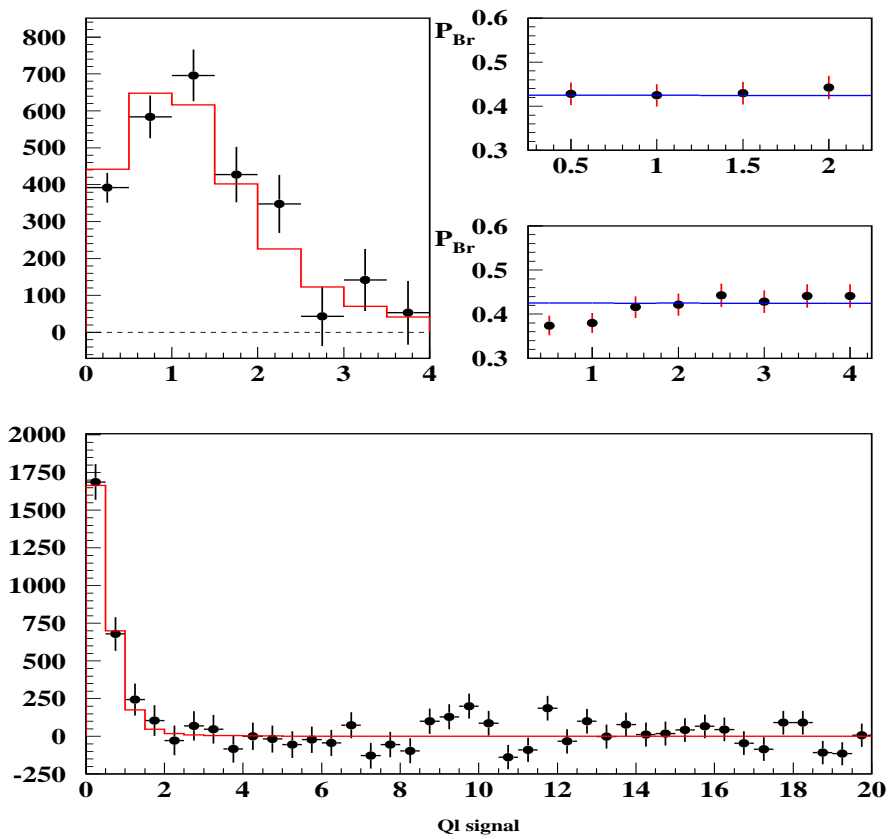


Figure 7.14: Fit results for the $\pi^+\pi^-$ momentum interval $4.4 < p < 5.0$ GeV/c in lab-frame. Caption is identical to figure 7.11 for the rest.

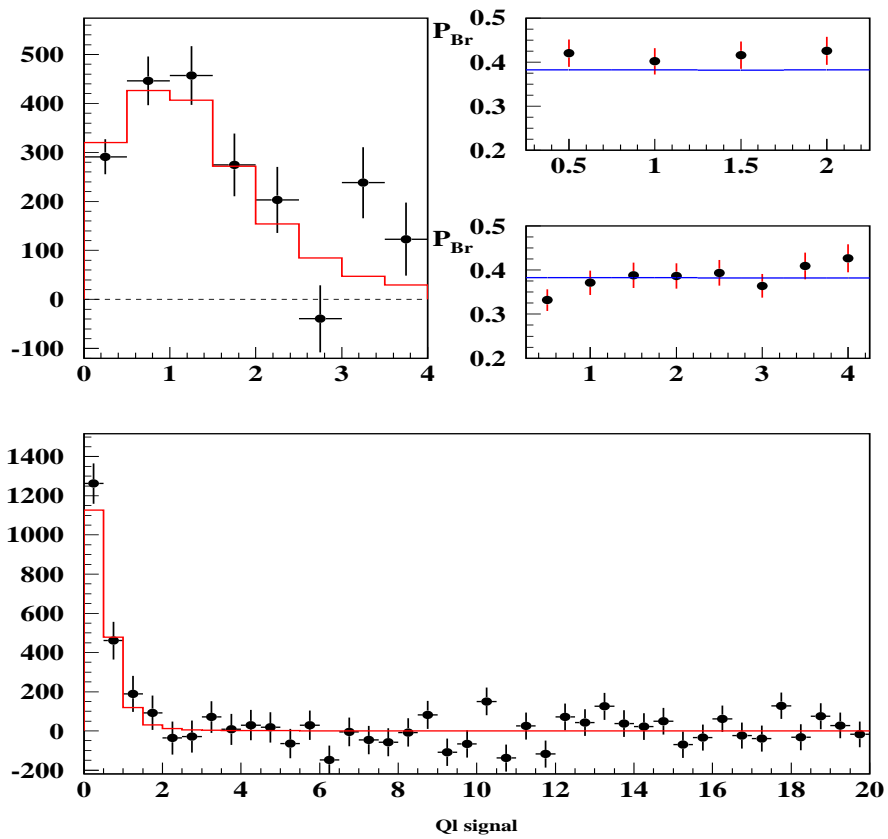


Figure 7.15: Fit results for the $\pi^+\pi^-$ momentum interval $5. < p < 5.6$ GeV/c in lab-frame. Caption is identical to figure 7.11 for the rest.

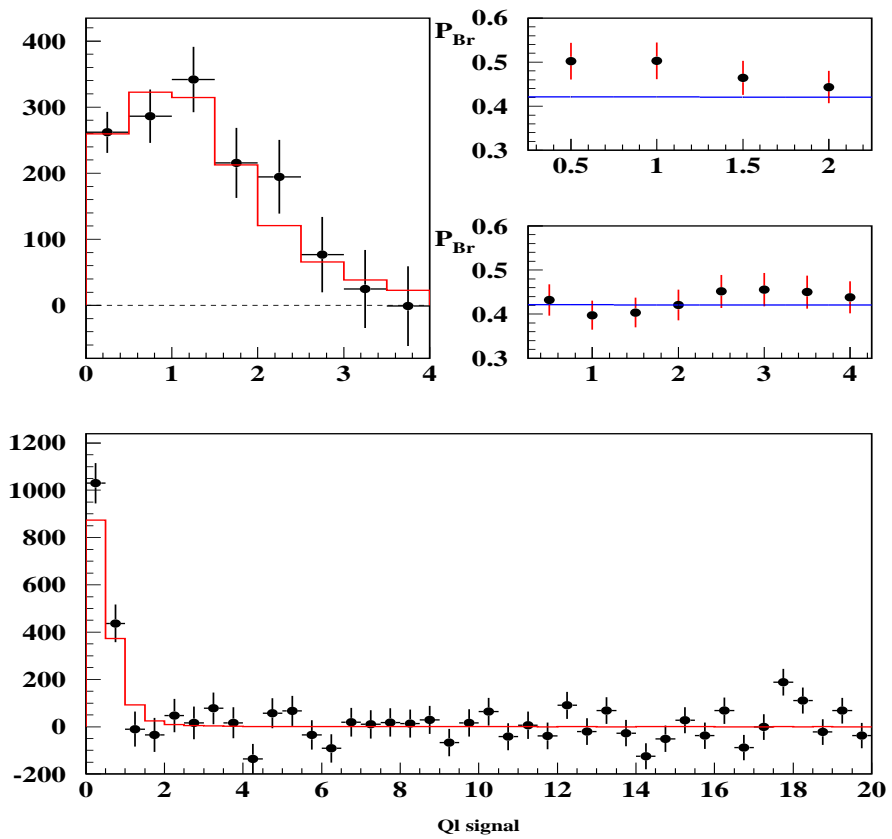


Figure 7.16: Fit results for the $\pi^+\pi^-$ momentum interval $5.6 < p < 6.2$ GeV/c in lab-frame. Caption is identical to figure 7.11 for the rest.

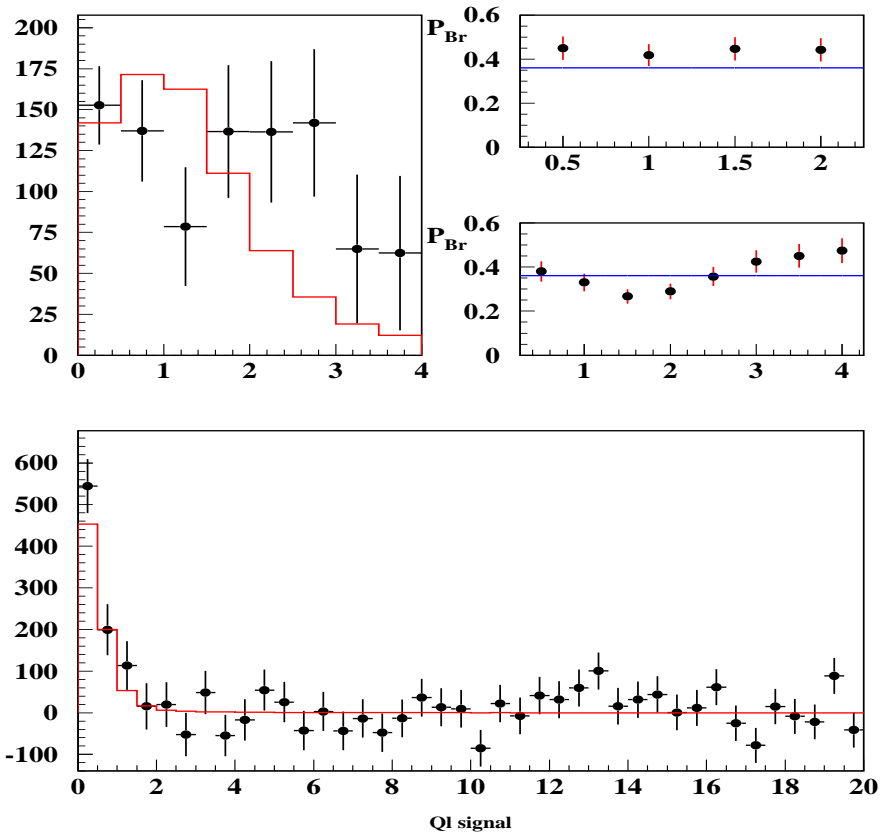


Figure 7.17: Fit results for the $\pi^+\pi^-$ momentum interval $6.2 < p < 6.8$ GeV/c in lab-frame. Caption is identical to figure 7.11 for the rest.

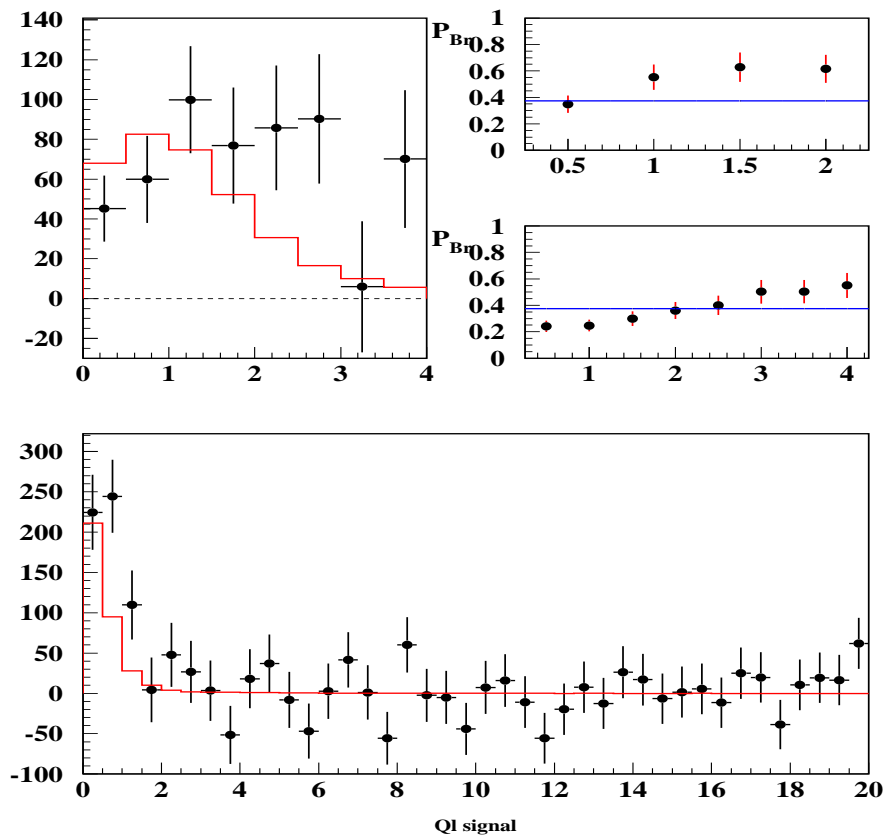


Figure 7.18: Fit results for the $\pi^+\pi^-$ momentum interval $6.8 < p < 7.4$ GeV/c in lab-frame. Caption is identical to figure 7.11 for the rest.

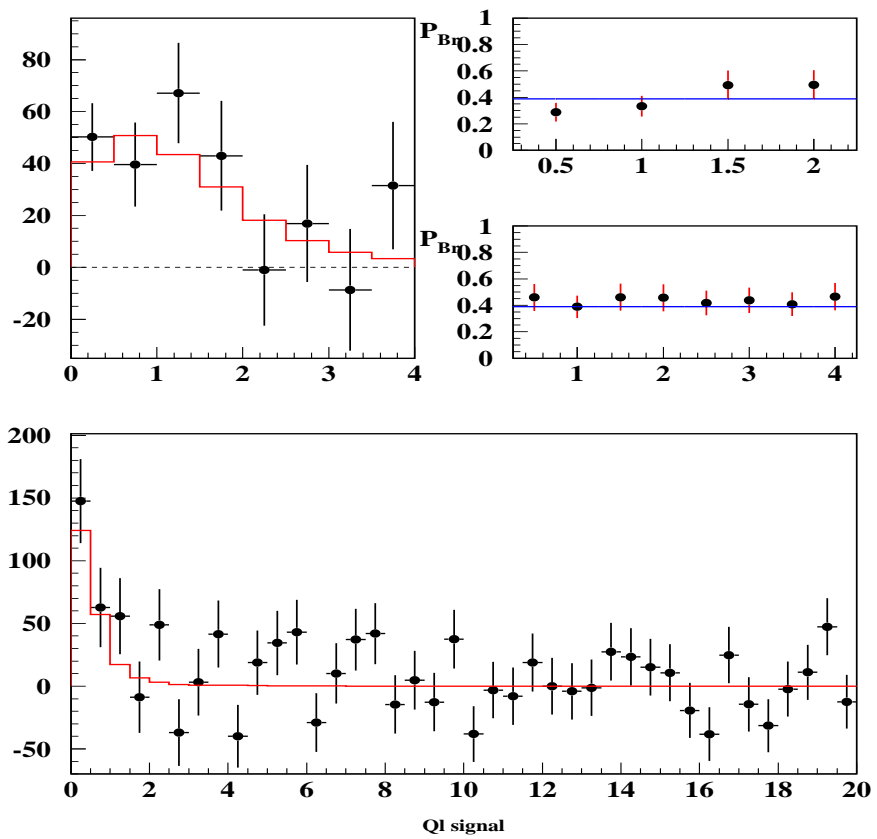


Figure 7.19: Fit results for the $\pi^+\pi^-$ momentum interval $7.4 < p < 8.0$ GeV/c in lab-frame. Caption is identical to figure 7.11 for the rest.

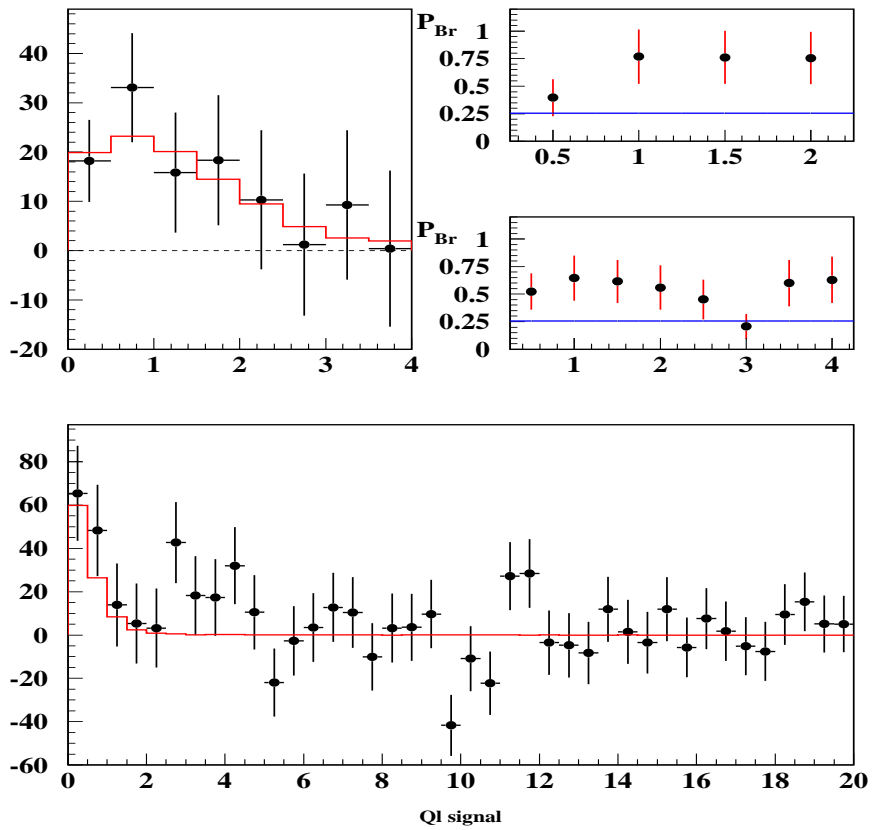


Figure 7.20: Fit results for the $\pi^+\pi^-$ momentum interval $8.0 < p < 8.6$ GeV/c in lab-frame. Caption is identical to figure 7.11 for the rest.

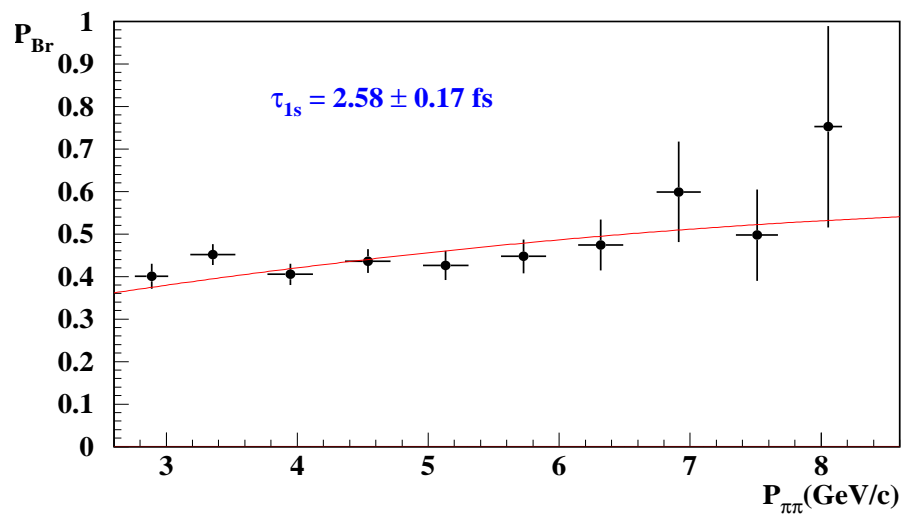


Figure 7.21: Pionium break-up probability P_{Br} as function of atom momentum, as compared to best fit Monte Carlo prediction. The fit χ^2 is 9.6 for 9 degrees of freedom. Pionium $1s$ lifetime value and error are indicated, for 2001+2002+2003 data.

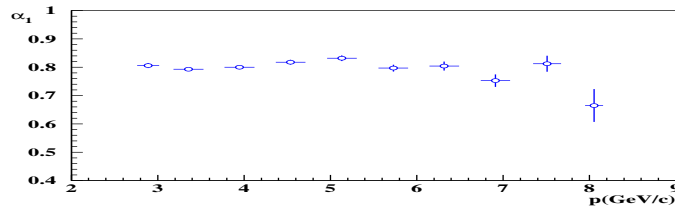


Figure 7.22: Fitted values of α_1 parameter as function of $\pi^+\pi^-$ momentum.

The number of atom pairs N_A determined as function of p is plotted in figure 7.23 along with the number of Coulomb pairs given by the fit in each bin. It is seen that atom production follows rather closely the spectrum of semi-inclusive $\pi^+\pi^-$ differential cross-section, as expected from bound state production. Note that both of these spectra are uncorrected for spectrometer acceptance.

Pionium break-up probabilities can now be determined using the momentum-dependent K-factors and they are shown in figure 7.21. Errors were propagated from those provided by the fit for N_A and N_C . P_{Br} values are compatible with a smooth increase with increasing atom momentum, as predicted by Monte Carlo tracking inside the target foil [59] [70]. We generate a continuous set of $P_{Br}(p)$ curves with varying values of the $1s$ pionium lifetime (τ_{1s}). χ^2 minimization with respect to this set provides a measurement of τ_{1s} and an error.

The fitted values of α_1 parameter (fraction of Coulomb pairs) are also indicated in figure 7.22 as function of p . They show a smooth behaviour.

In figure 7.24 we plot the number of non-Coulomb pairs determined by the fit as function of p , after subtraction of accidentals (as in [66],[86]), and we compare the spectrum with that previously determined for Coulomb pairs (in figure 7.23). The non-Coulomb spectrum is significantly softer than the Coulomb spectrum, probably due to parent multibody decays of the accompanying long-lifetime particle.

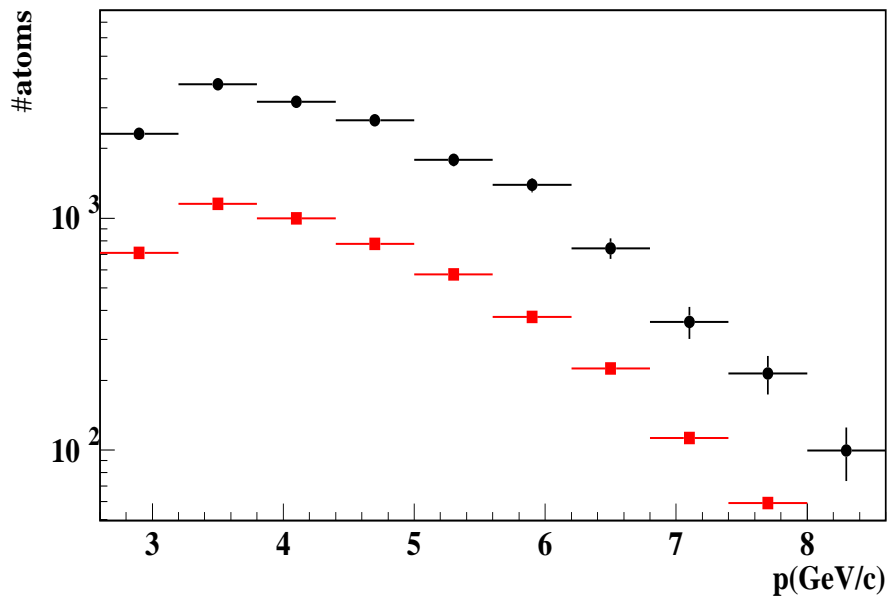


Figure 7.23: Fitted number of atom pairs as function of their lab-frame momentum (black circles) , as compared to the fitted number of Coulomb pairs for $Q_L > 2MeV/c$ (coloured rectangles). The latter were normalized to half the area, to avoid the very large difference in actual scale.

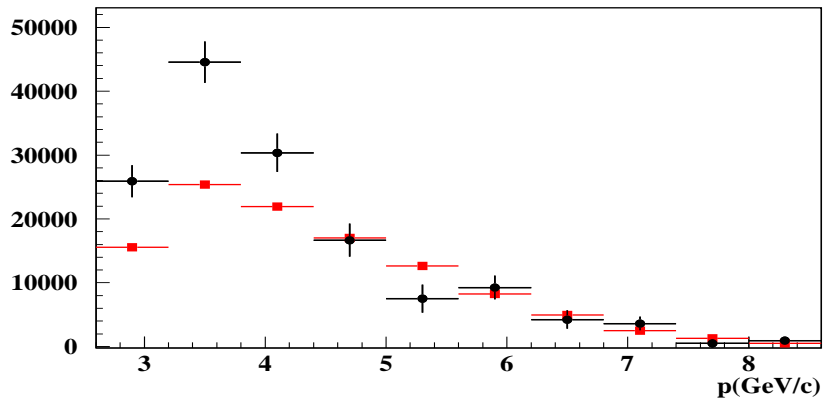


Figure 7.24: Fitted number of long-lifetime pairs (circles), determined from α_3 parameter, as function of $\pi^+\pi^-$ momentum. It is compared with the number of Coulomb pairs in figure 7.23 (dotted line), normalized to the same area.

7.4 Systematic error

We shall address here what we think are the most significant sources of systematic error in the P_{Br} measurement, which we have summarized in table 7.10.

The precise criterium adopted to produce this table is to quote, for each entry, the maximum accepted variation of the measured values with respect to the true values, according to our studies. From this point of view, deviations beyond the quoted values are assigned to have a null probability, whereas deviations within range are assumed to have a constant probability density. Since the precise origin of the systematic errors is by definition unknown, the previous hypothesis is at least as good as any other. If we were to adopt, for instance, a gaussian probability density for the systematic deviations, then the entries of table 7.10 should be replaced by standard deviations, rather than maximum allowed values. In this case, they should be multiplied by $1/\sqrt{3}$.

Concerning the multiple scattering uncertainty, we think that the error from this particular source can be neglected. To illustrate this, in figure 7.25 we compare the reconstructed Pionium spectrum using our GEANT-DIRAC Monte Carlo with 15% increase of upstream radiation length (which corresponds to our 1.5% measurement [88]), to the Monte Carlo used in GEANT-DIRAC version 2.63, which is based upon a different radiation length hypothesis. The difference in both Q_L and Q_T appears to be insignificant, in terms of atom counting. Not only the multiple scattering in upstream detectors is known with 1.5% precision, but in addition the use of only the first planes of MSGC/GEM detectors in the final track fit [58] strongly decreases the multiple scattering uncertainty.

Other source of systematic error is the Q_L trigger acceptance. We show the parametrization found using accidentals in the figure 1.29 and in the table 7.4.

Simulation of the detector backgrounds, resolution and double ionization cuts (IH) are all known with high precision (see [66]), which is reflected in the small estimated systematic errors indicated in table 7.10.

The uncertainty of K^+K^- background is small, as a result of the re-

sults shown in chapter 5. Moreover, the data show some sensitivity to this correction, in quantitative terms, as reported in section 7.3 .

Target impurity correction is not 100% known, because what we have are basically upper limits of contamination values. However, we believe an error of 30% of the correction is conservative. Only a chemical analysis of the bulk of the target foil would reduce this error to zero.

Assuming uncorrelated sources, we simulated random numbers with flat probability distributions within \pm the extreme values indicated in table 7.10, each being added to the contribution of the previous one, and repeated this experiment many times. The output values show a fairly gaussian distribution with $\sigma = 0.006$, which can be used as a 1σ -equivalent estimator of the systematic error.

Translation of ΔP_{Br} into $\Delta\tau_{1s}$ is done by means of the curve in figure 1.4.

Table 7.10: *Estimated contributions to systematic error in average break-up probability measurement. Last row indicates total systematic error equivalent to 1σ , under the assumption of uncorrelated effects.*

Simulation error	ΔP_{Br} extreme values
Trigger acceptance	± 0.004
MSGC+SFD backgrounds	± 0.006
Double-track resolution	± 0.003
Double ionization cut	± 0.003
Target impurity	± 0.003
K^+K^- contamination	± 0.003
Total 1σ equivalent	± 0.006

7.5 Lifetime and $|a_0 - a_2|$ measurement

Pionium break-up probability P_{Br} in the Ni foil has been determined in two different ways. One is making a global (momentum-integrated) fit, which provides a single measurement for the average P_{Br} , and another is making 10 independent experiments to measure this quantity in $600MeV/c$ wide intervals of pionium momentum. The results (see tables 7.2 and 7.5) are in very good agreement with each other when the average P_{Br} values are compared, and have equal statistical errors. Both of them provide a high quality fit with respect to the Monte Carlo hypothesis, in terms of χ^2 probability. From each of them we can determine the pionium $1s$ lifetime, using the standard pionium propagation code inside the foil.

From the p -dependent fit in table 7.5, with the systematic error estimated in section 7.4, we have :

$$P_{Br} = 0.432 \pm 0.010 (stat) \pm 0.006 (syst)$$

or having both error sources in quadrature:

$$P_{Br} = 0.432 \pm 0.0117$$

Using the relationship between P_{Br} and lifetime obtained from the pionium propagation code [59] [70], we determine the pionium $1s$ lifetime from the full DIRAC data sample :

$$\tau_{1s} = 2.58^{+0.19}_{-0.18} fs$$

where the error includes both statistic and systematic sources. It can be converted into a measurement of the difference of s-wave scattering lengths:

$$|a_2 - a_0| = 0.279 \pm 0.010 M_\pi^{-1}$$

by means of the expression [2]:

$$\Gamma_{1s} = \frac{1}{\tau_{1s}} = \frac{2}{9} \alpha^3 p |a_2 - a_0|^2 (1 + \delta) M_\pi^2$$

where $\delta = (5.8 \pm 1.2) \times 10^{-2}$ and $p = \sqrt{M_{\pi^+}^2 - M_{\pi^0}^2 - (1/4)\alpha^2 M_{\pi^+}^2}$.

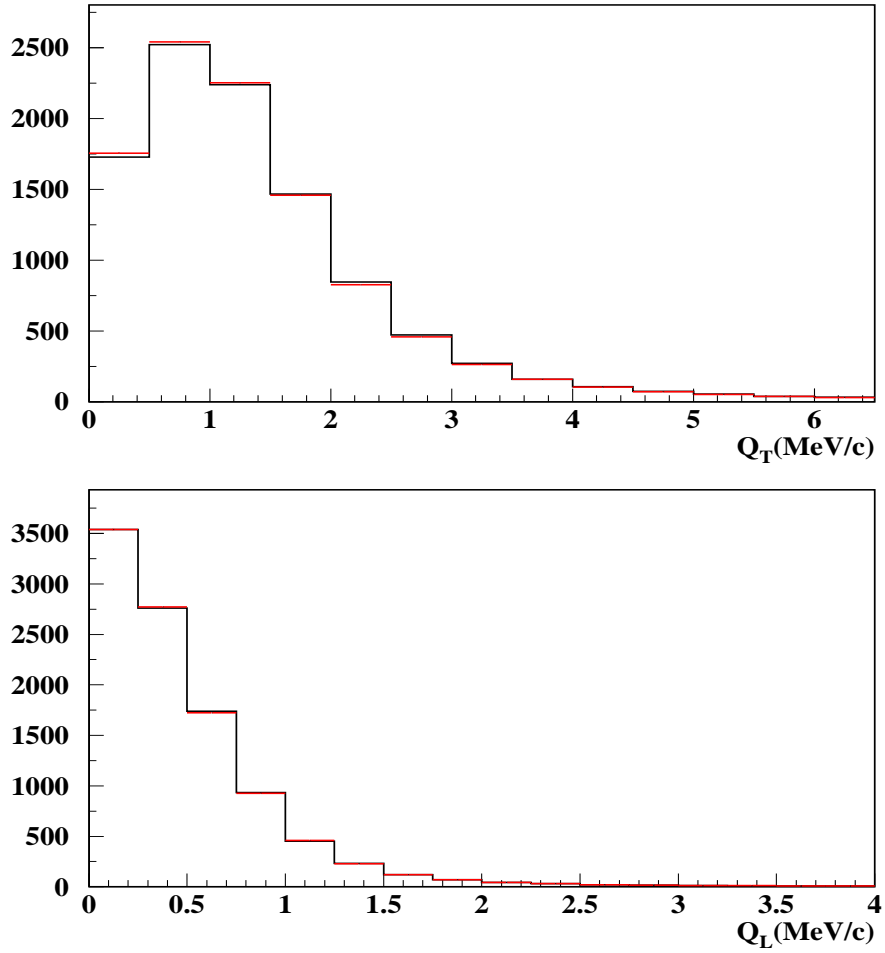


Figure 7.25: Comparison between the reconstructed Pionium Monte Carlo spectra using our GEANT-DIRAC version with increased 15% radiation length (black) and the GEANT-DIRAC version 2.63 (red).

Chapter 8

Summary of results and conclusions

The work presented in this thesis is effectively the final outcome of a long-standing effort made by the group of the university of Santiago de Compostela and by the DIRAC collaboration at CERN, for a period of 13 years, starting with the first proposal of the experiment in December 1994. My work is based upon a vast amount of essential contributions, personal and institutional, which have made possible the achievement of the experiment's goal, and which I am proud and fortunate to have brought to a successful conclusion here.

Among the contributions realized in this thesis, let me pick up those which I consider the most significant:

- 1) the measurement of multiple scattering in upstream detectors with 1.5% precision, with the essential help of the GEM-MSGC detector. This is a key contribution to the final lifetime measurement, given the fact that in 2005 multiple scattering was regarded as the main component the systematic error [5]. Moreover, the results presented here [88] sharply contradicted hasty measurements done with scattered pions [79] which were argued to cast doubts on our work. A new study made within the collaboration came to recognize the validity of our original claim that radiation length was underestimated in the Monte

Carlo by 15% using a different method [89], albeit with lower precision.

- 2) the measurement of K^+K^- background at low pair momentum (2.9 GeV/c) was a second important achievement towards reducing another component of the systematic error, so far considered rather serious [5]. In the absence of experimental semi-inclusive pNi data at beam momenta close to $p=24$ GeV/c , using Monte Carlo models in such a complex physics region in QCD appeared to be uncertain. Fortunately, the existence of a powerful TDC electronics deployment in upstream detectors (both SFD and IH) came to help us, and rendered possible a previously unthinkable measurement, namely the discrimination of equal-mass pairs, where the time-difference (+/-) with precision hodoscopes becomes useless. The K^+K^- contamination was experimentally determined and fully simulated, thus producing a new key component in the complete set of small corrections to the lifetime measurement.
- 3) another ingredient, which actually represents the main effort in this thesis, is the development of a tracking method to perform pattern-recognition of the $\pi^+\pi^-$ pairs in upstream detectors, in the presence of strong backgrounds and multiple scattering. The GEM-MSGC detectors were of course instrumental to achieve this goal, but the necessity to combine the space information with the time taggers from the SFD really complicated the tracking algorithms. Fortunately, the existence of a powerful simulation (GEANT-DIRAC), and the availability of a very strong computing resources from CESGA, rendered this task not only viable, but exceedingly performing. Thanks to this work the transverse momentum Q_T of the $\pi^+\pi^-$ pairs could be unambiguously determined.
- 4) the last and fundamental step in the development of this work was to extend our previous measurement using only 2001 Ni data [6] to the full DIRAC data sample (2001+2002+2003). The improved spectrometer performance in the last two years facilitated this task, and provided an important increase in the statistics of pionium pairs.

As a consequence of the results summarized above, and others also discussed in the thesis, our conclusions can be established as follows:

- 1) a new final state, never accessed before in particle physics, the ponium or $\pi^+\pi^-$ bound states, has been copiously produced in the laboratory (17050 atom pairs), and its ionization spectrum has been fully mapped in both the longitudinal and transverse projections, in its center-of-mass frame.
- 2) based upon the extrapolation method with the observed Coulomb $\pi^+\pi^-$ interaction, and making no assumptions on the physics of pNi collisions, we have determined the ponium lifetime (in 1s state) to be $\tau_{1s} = 2.58^{+0.19}_{-0.18} \text{ fs}$, using the full DIRAC experiment data sample.
- 3) given the existence of a rigorous next-to-leading order calculation in QCD and QED [2] the ponium lifetime determination has been converted into a 3.5% measurement of the s-wave isospin $\pi\pi$ scattering length difference $|a_0 - a_2|$ in the process $\pi^+\pi^- \rightarrow \pi^0\pi^0$ at threshold, with the result: $|a_0 - a_2| = 0.279 \pm 0.010 m_\pi^{-1}$.

Bibliography

- [1] B. Adeva, et al., DIRAC proposal, CERN/SPSLC 95-1, SPSLC/P 284 (1994).
- [2] J. Gasser, V. E. Lyubovitskij, A. Rusetsky and A. Gall, Phys. Rev. D 64, 016008 (2001).
- [3] G. Colangelo, J. Gasser and H. Leutwyler, Nucl. Phys. B603, 125 (2001).
- [4] J. Stern, H. Sazdjian and N.H. Fuchs, Phys. Rev. D47 (1993) 3814. ; M. Knecht, B. Moussalham, J. Stern, and N.H. Fuchs, Nucl. Phys. B457 (1995) 513. ; M. Knecht, B. Moussalham, J. Stern, and N.H. Fuchs, Nucl. Phys. B471 (1996) 445.
- [5] B. Adeva et al., "First Measurement of the $\pi^+\pi^-$ lifetime, Phys. Letters B 619, 50-60.
- [6] Otón Vázquez Doce, PhD Thesis, Study of ponium lifetime in pNi collisions at $p=24$ GeV/c. University of Santiago de Compostela.
- [7] B. Adeva, A. Romero Vidal and O. Vázquez Doce, Eur. Phys. Journal A, 10, 50-57 (2007), 29 September 2006 .
- [8] S. Weinberg, Physica A 96, 327 (1979).
- [9] J. Gasser and H. Leutwyler, Ann. Phys. (N.Y.) 158 , 142 (1984)
- [10] J. Gasser and H. Leutwyler, Nucl. Phys. B250, 465 (1985).

- [11] A. Pich, Chiral Perturbation Theory, hep-ph /9502366, February 1995.
- [12] S. Scherer, Introduction to Chiral Perturbation Theory, hep-ph/0210398, October 2002.
- [13] H. Leutwyler, proceedings of the workshop *Chiral Dynamics, Theory and Experiment*, Durham/Chapel Hill, NC, USA. hep-ph/0612112v1, 11 Dec. 2006.
- [14] S. Weinberg, Phys. Rev. Lett. 17 (1966) 616.
- [15] J. Gasser and H. Leutwyler, Phys. Lett. B 125 (1983) 325. ; Annals Phys. 158 (1984) 142.
- [16] J. Bijnens, G. Colangelo, G. Ecker, J. Gasser and M.E. Sainio, Phys. Lett. B374 (1996) ; Nucl. Phys. B 508 (1997) 263.; ibid. B 517 (1998) 639 (E).
- [17] S. Pislak et al. [BNL-E865 Collaboration], Phys. Rev. Lett. 87 (2001) 221801; Phys. Rev. D 67 (2003) 072004.
- [18] J. R. Pelaez and F. J. Yndurain, Phys. Rev. D 71 (2005) 074016.
- [19] S. Descotes-Genon, N. H. Fuchs, L. Girlanda and J. Stern, Eur. Phys. J. C24 (2002) 469.
- [20] N. Cabibbo, Phys. Rev. Lett. 93 (2004) 121801.
- [21] N. Cabibbo and G. Isidori, JHEP 0503 (2005) 021.
- [22] G. Colangelo, J. Gasser, B. Kubis and A. Rusetsky, Phys. Lett. B 638. (2006) 187.
- [23] E. Gamiz, J. Prades and I. Scimemi, hep-ph/0602023.
- [24] L. Masetti, Proc. ICHEP06, hep-ex/0610071.
- [25] J. Gasser, V. E. Lyubovitskij and A. Rusetsky , arXiv:0711.3522v1 [hep-ph] 22 Nov 2007.

- [26] W. E. Caswell, *Physics Letters B* 167 (1986) 437-442.
- [27] A. Gall, J. Gasser, V. E. Lyubovitskij and A. Rusetsky , *Physics Letters B* 462 (1999) 335-340.
- [28] J. Gasser, V. E. Lyubovitskij and A. Rusetsky , *Physics Letters B* 471 (1999) 244-250.
- [29] J. Gasser, V. E. Lyubovitskij, A. Rusetsky and A. Gall , *Physical Review D* 64, 016008.
- [30] M. Knetcht, B. Moussallam, J. Stern, and N.H. Fuchs, *Nucl. Phys.* B457, 513 (1995); B471, 455 (1996)
- [31] H. W. Hammer and J. N. Ng, *Eur. Phys. J. A* 6 (1999) 115. (hep-ph/9902284)
- [32] J. Schweizer, *Phys. Lett. B* 587 (2004) 33. (hep-ph/0401048). J. Schweizer, *Eur. Phys. J. C* 36 (2004) 483. (hep-ph/0405034).
- [33] L. Nemenov, *Sov. J. Nucl. Phys.* 41, 629 (1985). *Yad. Fiz.* 41, 2015 (1985).
- [34] A.D.Sakharov, *Z.Eksp.Teor.Fiz.* 18 (1948) 631.
- [35] DIRAC note 04-06. "Finite-size effects on two-particle production in continuous and discrete spectrum", R. Lednicky.
- [36] L. G. Afanasyev and A. V. tarasov, *Yad. Fiz.* 59, 2212 (1996). *Phys. At. Nucl.* 61, 1517 (1998).
- [37] C. Santamarina, M. Schumann, L. G. Afanasyev, T. Heim, *J. Phys. B* 36, 4273 (2003).
- [38] K. G. Denisenko and S. Mrówczyński, *Phys. Rev. D* 36, 1529 (1987).
- [39] A. V. Tarasov and I. U. Khristova, *JINR-P2-91-10* (1991).

- [40] T. Heim, et al., J. Phys. B 34, 3763 (2001).
- [41] B. Adeva et al., Nucl. Inst. and Meth. A515 (2003) 467-496.

- [42] K. Brown, D. Carey, C. Iselin, F. Rothacker. , CERN-80-04 (1980).
- [43] DIRAC note 96-07 (1996), "Preliminary calculations of neutron background in the DIRAC experiment, I.A. Kurochkin (IHEP), (http://dirac.web.cern.ch/DIRAC/i_notes.html).
- [44] V. Agoritsas et al., Nucl. Instr. and Meth., A411, 17-30 (1998).
- [45] A. Gorin et al., Nucl. Instr. and Meth., A452, 280-288 (2000).
- [46] DIRAC NOTE 02-09 : "New ionization hodoscope: design and characteristics", V. Brekhovskikh M. Jabitski, A. Kuptsov, V. Lapshin, V. Rykalin, L. Tauscher
- [47] Millipore paper type HAWP pore size 0.45 made by MILLIPORE Corp., Bedford, Ma 01730 USA.
- [48] L. Afanasyev, V. Karpukhin, NIM A492 351 (2002).
- [49] B. Adeva et al., Nucl. Inst. and Meth. A491, 41 (2002).
- [50] M. Bragadireanu et al., NIM 426, 254 (1999).
- [51] DIRAC NOTE 99-03 : "Preshower detector commissioning along with DIRAC set-up", M. Pentia, Gh. Caragheorgheopol, M. Ciobanu, D. Pop and C. Rusu (IAP).
- [52] A. Lanaro, DIRAC Note 02-02, "DIRAC beam parameters" (2002).
- [53] L. Afanasyev et al., NIM A491, 376 (2002).
- [54] L. Afanasyev, M. Gallas, V. Karpukhin and A. Kulikov, NIM A479, 407 (2002).
- [55] G.D. Badhwar, S.A. Stephens, R.L. Golden Phys Rev. D15, 820 (1977).

- [56] A. Lanaro, DIRAC Note 01-01, "Parameterisation of correlated and accidental particle spectra" (2001).
- [57] DIRAC note 03-08, "A tracking system for upstream detectors in DIRAC", B. Adeva, A. Romero, O. Vazquez Doce.
- [58] DIRAC Note 05-15: "Full-Tracking Resolution in DIRAC with 2001 Data",
B. Adeva, A. Romero and O. Vázquez Doce.
DIRAC Note 05-19: "Addendum to Full-Tracking Resolution in DIRAC with 2001 Data", B. Adeva, A. Romero and O. Vázquez Doce.
- [59] DIRAC note 04-02: "DIRAC events generator", C. Santamarina.
- [60] DIRAC DIRAC Note 02-10: "Proton to pion ratio in accidental coincidences", S. Trusov.
- [61] DIRAC note 98-08. "The GEANT-DIRAC Simulation Program Version 2.5", P. Zrelov and V. Yazkov.
<http://zrelov.home.cern.ch/zrelov/dirac/montecarlo/instruction/instruct26.html>
- [62] D. Drijard, M. Hansroul, V. Yazkov,
<http://www.cern.ch/dirac/ariane.html>
- [63] L. Afanasyev, Observation of $\pi^+\pi^-$ atoms, Ph. D. Thesis, JINR, Dubna (1997).
Afanasyev L G et al. Phys. At. Nucl. 60 938 (1997).
L.G. Afanasyev. O.O. Voskressenskaya, V.V.Yazkov, Communication JINR P1-97-306, Dubna, 1997.

- [64] DIRAC note 03-09: "Determination of the experimental k-factor", C. Santamarina and C. P. Schutz.
- [65] DIRAC note 05-01: "Dependence of break-up probability estimation on K^+K^- and $p\bar{p}$ background", O. Gortchakov and V.V. Yazkov .
- [66] DIRAC Note 06-03: "Measurement of ponium lifetime", B.Adeva, A.Romero, O.Vazquez Doce.
- [67] DIRAC note 06-05 : "Experimental Measurement of a K^+K^- Signal at $p = 2.9\text{GeV}/c$ in Ni 2001 Data", B. Adeva, A. Romero and O. Vázquez Doce.
- [68] DIRAC note 07-02 : "Study of $K^\pm\pi^\mp$, K^+K^- and K^-p production in DIRAC using time-of-flight measurements" , B. Adeva, A. Romero, O. Vázquez Doce, C. Mariñas and J. L. Fungueiriño.
- [69] UrQMD manual. <http://th.physik.uni-frankfurt.de/~urqmd/>
M. Bleicher et al., J. Phys. G25 (1999) 1859; hep-ph/9909407.
- [70] C. Santamaria, M. Schuman, L.G. Afanasyev, T. Heim, A Monte-Carlo Calculation of the Ponium Breakup Probability with Different Sets of Ponium Target Cross Sections, J. Phys. B. At. Mol. Opt. Phys. 36 4273 (2003), arXiv:physics/0306161 v1.
- [71] DIRAC report "DIRAC targets", by A. Kuptsov, 5 March 2005.
- [72] T. Núñez-Pardo, *Desarrollo de un detector de micropistas de gas para el experimento DIRAC*, doctoral thesis presented at University of Santiago de Compostela, May 1999.
- [73] P. Vázquez, *Development and Construction of Electronics for Microstrip Detector Readout* , doctoral thesis presented at University of

Santiago de Compostela, June 2000.

- [74] DIRAC note 2005-04, V.V. Yazkov, *Experimental and simulated response of ScFi detector*
- [75] DIRAC note 2003-02, D. Goldin and L. Tauscher, *Scintillating Fiber Detector Efficiency Study*
- [76] *GEANT - Detector Description and Simulation Tool*
http://wwwasdoc.web.cern.ch/wwwasdoc/geant_html3/geantall.html
- [77] B. Rossi and K. Greisen, *Rev. Mod. Physics*, 13:240, 1941.
- [78] Particle Data Group, *Phys. Rev. D* 66 (2002) 010001.
- [79] DIRAC note 05-02, *Pion multiple Coulomb scattering in the DIRAC experiment*. A. Dudarev, V. Kruglov, L. Kruglova, M. Nikitin
- [80] DIRAC note 05-11, *Study of SFD efficiency using MSGC detector for 2001 data*, B. Adeva, A. Romero, O. Vázquez Doce
- [81] DIRAC note 02-02, *DIRAC beam parameters* A. Lanaro.
- [82] B. Adeva et al., *The time-of-flight detector of the DIRAC experiment*, *Nucl. Instr. Meth. A* 491 (2002) 41.
- [83] DIRAC Note 02-09: *New ionization hodoscope: design and characteristics*, V. Brekhovskikh, M. Jabitski, A. Kuptsov, V. Lapshin, V.

Rykalin, L. Tauscher.

- [84] Nucl. Instr. Meth. A491 (2002) 376. [hep-ex/0202045]

- [85] DIRAC note 04-06 : Experimental determination of momentum resolution in DIRAC using Lambda events, B. Adeva, A. Romero and O. Vázquez Doce.

- [86] DIRAC Note 07-07: Final Results for Pionium Lifetime Measurement with 2001 Data, A. Romero, B. Adeva, J. L. Fungueiriño and O.Vázquez Doce.

- [87] DIRAC Note 07-15: Pionium Lifetime Measurement with DIRAC 2002 and 2003 Ni Data, A. Romero, B. Adeva, J. L. Fungueiriño, O.Vázquez Doce

- [88] DIRAC Note 05-16: Study of Multiple Scattering in Upstream Detectors in DIRAC, B. Adeva, A. Romero and O. Vázquez Doce.

- [89] DIRAC Note 06-02: Evaluation of the measurement of multiple scattering for DIRAC set-up using standard DIRAC analysis tools, A. Benelli, D. Drijard, O. Gorchakov, L. Tauscher, V. Yazkov.